



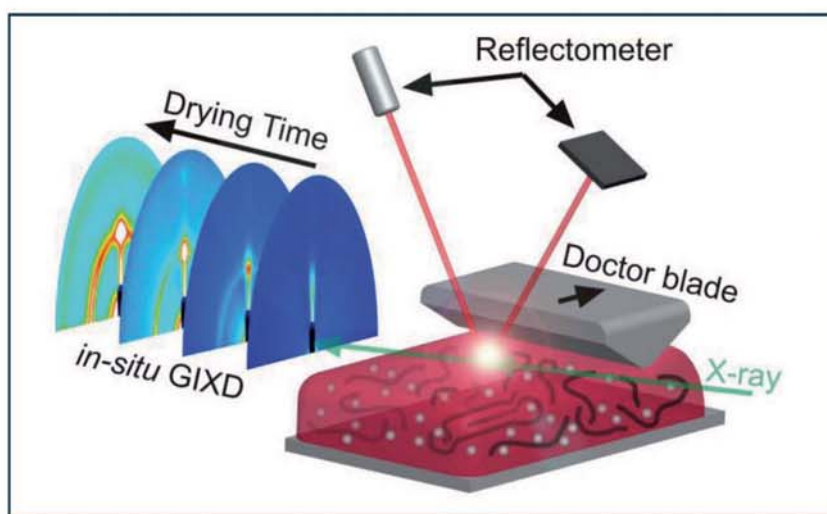
INNOVATION
LAB

FORUM
ORGANIC
ELECTRONICS

Benjamin Schmidt-Hansberg

Process-structure-property relationship of polymer- fullerene bulk heterojunction films for organic solar cells

Drying process, film structure and optoelectronic properties



Volume 2 | Forum Organic Electronics Science Series
Edited by Prof. Dr.-Ing. Wolfgang Kowalsky and Dr. Martin Raditsch



Cuvillier Verlag Göttingen
Internationaler wissenschaftlicher Fachverlag

Forum Organic Electronics Science Series

Volume 2

Editor's preface

We are pleased to present you the second volume of the Forum Organic Electronics Science Series.

The initiator of the series, Forum Organic Electronics, is a Leading-Edge Cluster centered in the Rhine-Neckar Metropolitan Region set off by the German Federal Ministry of Education and Research (BMBF). It is a powerful cooperative network of science and business comprising 26 companies, universities and research institutes with a major research focus on Organic Electronics enabling interdisciplinary research and development.

We are pleased to award the 2011 Forum Organic Electronics Science Series Publication Prize to Benjamin Schmidt-Hansberg, whose work responds to considerable questions in the field of organic electronics. His dissertation thesis "Process-structure-property relationship of polymer-fullerene bulk heterojunction films for organic solar cell" was selected by an interdisciplinary jury of cluster partners. In his thesis, Benjamin Schmidt-Hansberg investigated, how the understanding of drying process parameters can be employed for the generation of optimized structures with improved photovoltaic performance. This understanding is transferable to other material systems as shown within the scope of this work.

The research was supervised by Prof. Dr.-Ing. Wilhelm Schabel, head of Thin Film Technology, a research network within the Karlsruhe Institute of Technology (KIT). Currently, Benjamin Schmidt-Hansberg pursues his research with Prof. Neil Greenham at the Department of Physics, University of Cambridge (UK) in close cooperation with Eight19, a British company that designs printed plastic solar technology in order to deliver flexible, lightweight, robust and lower cost solar cells for a variety of solar-powered applications.

We would like to thank the author for his successful research contribution and we are convinced that his work will be a motivation for following young researchers in this field.

We hope that you will enjoy reading this work and we are already looking forward to the third volume.

Heidelberg, March 2012



Prof. Dr.-Ing. Wolfgang Kowalsky



Dr. Martin Raditsch

Managing Directors, InnovationLab GmbH

**Process-structure-property relationship of polymer-fullerene
bulk heterojunction films for organic solar cells**

- Drying process, film structure and optoelectronic properties -

zur Erlangung des akademischen Grades eines

DOKTORS DER INGENIEURWISSENSCHAFTEN (Dr.-Ing.)

der Fakultät für Chemieingenieurwesen und Verfahrenstechnik des
Karlsruher Instituts für Technologie (KIT)

genehmigte

DISSERTATION

von

Dipl.-Ing. Benjamin Schmidt-Hansberg

aus Frankfurt am Main

Referent:	Prof. Dr.-Ing. Wilhelm Schabel
Korreferent:	Prof. Dr. rer. nat. Uli Lemmer
Tag der mündlichen Prüfung:	03. Februar 2012

Bibliografische Information der Deutschen Nationalbibliothek

Die Deutsche Nationalbibliothek verzeichnet diese Publikation in der Deutschen Nationalbibliografie; detaillierte bibliografische Daten sind im Internet über <http://dnb.d-nb.de> abrufbar.

1. Aufl. - Göttingen : Cuvillier, 2012

Zugl.: Karlsruhe (KIT), Univ., Diss., 2012

978-3-95404-073-5

© CUVILLIER VERLAG, Göttingen 2012

Nonnenstieg 8, 37075 Göttingen

Telefon: 0551-54724-0

Telefax: 0551-54724-21

www.cuvillier.de

Alle Rechte vorbehalten. Ohne ausdrückliche Genehmigung des Verlages ist es nicht gestattet, das Buch oder Teile daraus auf fotomechanischem Weg (Fotokopie, Mikrokopie) zu vervielfältigen.

1. Auflage, 2012

Gedruckt auf säurefreiem Papier

978-3-95404-073-5

Preface

This thesis was conducted during my activity as research assistant at the Institute of Thermal Process Engineering at the Karlsruhe Institute of Technology from 2007 to 2011. I am grateful for the time at the institute which I enjoyed a lot.

First of all I especially thank Professor Wilhelm Schabel for the supervision of this thesis and his confidence. Professor Matthias Kind I thank for the opportunity of this thesis and Philip Scharfer for his strong support. All colleagues of the Institute of Thermal Process Engineering I want to thank for the great time we had together at the institute. Furthermore I thank the lab and workshop staff Annette Schucker, Michael Wachter, Markus Keller, Stefan Fink, Steffen Haury, Stefan Knecht as well as Andreas Burkart.

For their restless efforts and creativity I thank Michael Baunach, Benedikt Brenneis, Natalie Schnabel and Katharina Peters who conducted their diploma thesis with me. Timo Basile, Mareike Kowalski, Felix Buss, Stefan Jaiser, Helge Geisler, Jens Buzengeiger and Dieter Korp who conducted their student research project with me and the research students Tina Fromm, Daniel Griese, Tommy Mathieu, Gerhard Selle and Marcel Schmitt deserve the same appreciation.

Professor Uli Lemmer, Alexander Colsmann, Michael Klein and the organic photovoltaic group of the Light Technology Institute I thank for bringing me into the field of organic photovoltaics and for their continual strong support and confidence which was fundamental for this work.

Esther Barrena, Carmen Munuera and Monamie Sanyal of the Max-Planck-Institute for Metals Research I want to thank for the very inspiring and successful collaboration in the field of X-ray diffraction. I enjoyed the friendly and multicultural atmosphere in our joint research a lot.

Particular thanks go to Stefan Walheim, Cheng Huang and Jörg Pfeifer of the Institute of Nanotechnology for providing the reflectometry setup and many fruitful discussions. Also Norman Mechau is to thank for the generous usage of the ink-jet printer and surface profiler. I also thank Robert Maul for his commitment in the field of atomistic simulations.

Professor Dagmar Gerthsen, Erich Müller and Marina Pfaff I thank for their interest in our work and their support with electron microscopy measure-

ments. Hendrik Hölscher and the Karlsruhe Nano Micro Facility (KNMF) deserve special appreciation for the frequent usage of the AFM.

Alexei Vorobiev I want to thank for his strong commitment during our beamtimes at the European Synchrotron Radiation Facility (ESRF). Ralf Weigel deserves the same appreciation for his support at Ångströmquelle Karlsruhe (ANKA). Björn Bräuer of the Stanford Synchrotron Radiation Lightsource (SSRL) I thank for X-ray microscopy and NEXAFS measurements.

Hans-Joachim Egelhaaf and Mauro Morana of Konarka Technologies I owe many thanks for their interest in our work and for their generous supply of low band gap polymers. Christine Walsh and Jean-Philippe Piel of Sopralab I thank for the joint experiments on real time spectroscopic ellipsometry.

Felix Pasker of the Kekulé-Institute of Organic Chemistry and Biochemistry (University of Bonn) I thank for characterizing several P3HT batches.

In particular I want to thank my parents for their infinite confidence and support throughout my entire university career and my girlfriend for much more than distracting me from this thesis and for her patience.

Final thanks go to the German Research Foundation (DFG) for their financial support within the priority program SPP1355 and the Federal Ministry of Education and Research (BMBF) within the project NanoPolySol. Furthermore I thank the Karlsruhe House of Young Scientists (KHYS) for their financial support.

Karlsruhe, August 2011
Benjamin Schmidt-Hansberg

Abstract

Photovoltaic (PV) is attracting increasing interest as an important contribution to renewable energy supply. Organic photovoltaic (OPV) is a comparable young PV technology with a great potential towards low cost solar power. This is due to the intrinsic advantage of the incorporated organic semiconductors which are soluble. Solution processing allows high throughput coating and printing processes. Hence, energy intensive high temperature and vacuum steps can be avoided which reduces the fabrication costs and keeps energy payback times low. The performance of organic solar cells strongly depends on the structure of the solution cast photoactive layer which comprises a polymer-fullerene blend. The blend structure evolves during the film drying step which has been studied in this thesis.

Starting point of this work was the hypothesis that drying process parameters are suitable for systematically tuning the structure formation during drying of solution cast polymer-fullerene films in order to generate optimized structures with improved photovoltaic performance. For the evaluation of this hypothesis the structure formation of the polymer-fullerene system Poly(3-hexylthiophene-2,5-diyl):[6,6]-Phenyl C₆₁-butyric acid methyl ester (P3HT:PCBM) was investigated incorporating i) thin film drying kinetics, ii) phase behavior of polymer-fullerene solutions, iii) structure formation and iv) the drying process-structure-property relationship of solar cells. The generality of the obtained results has been studied in comparison with the behavior of Poly{[4,40-bis(2-ethylhexyl)dithieno(3,2-b;20,30-d)silole]-2,6-diyl-alt-(2,1,3-benzothiazole)-4,7-diyl} (PSBTBT).

i) Within this thesis a dedicated coating and drying setup was developed which afforded precisely defined coating and drying process conditions as prerequisite for all obtained results. For the first time, the drying behavior of finally a few hundred nanometer thin films could be investigated at five measurement positions with laser reflectometry simultaneously. This allowed the elaboration of a spatially resolved numerical thin film drying model.

ii) In conjunction with the measurement and simulation of the evolution of film composition it was required to determine important instants of phase transitions such as solubility limits. Therefore the binodal region of P3HT solutions has been determined in the temperature range of 0°C-60°C. Within

the unstable region P3HT solutions phase separate into a sol and a gel phase. The fullerene PCBM exhibits only a single solubility limit.

iii) In order to correlate the expected phase transitions according to the phase diagrams with the real structure formation, the above mentioned coating and drying setup was combined with synchrotron based in situ grazing incidence X-ray diffraction (GIXD) measurements. This gave unique insights into the mechanisms and dynamics of polymer-fullerene blend crystallization. After reaching P3HT solubility the crystallization proceeded with well-oriented interface-induced P3HT nucleation followed by P3HT crystal growth with increasing orientation distribution of the crystallites and PCBM aggregation in the final drying period. Furthermore strong polymer-fullerene interaction forces could be derived. By increasing the PCBM fraction it could be shown for the 1:2 P3HT:PCBM ratio that PCBM molecules brake the (020) π - π -stacking of P3HT lamellae which signifies a dramatic loss of hole mobility and consequently reduced device performance. It is further notable that increasing drying temperatures reduce the amount of (020) π - π -stacked P3HT molecules but lead to an increased amount of P3HT (100) crystallinity. Hence, drying temperature determines the preferred direction of crystal growth.

iv) Besides a finer degree of phase separation, reduced drying temperatures also cause a higher amount of π - π -stacked polymers, longer effective polymer conjugation length, increased amount of vertical charge transport pathways and an increasingly rough topography due to larger polymer aggregates. Jointly this leads to improved power conversion efficiency at lower drying temperatures. Based on the elaborated knowledge a strategy for a 40% reduction of drying time with only small drawbacks in solar cell performance could be developed.

Finally it was important to investigate the transferability of the obtained knowledge to other material systems. PSBTBT:PC₇₁BM blends show similarities to that of P3HT:PCBM with partly interface induced polymer nucleation and subsequent fullerene aggregation in the final drying stage. The kinetics of molecular ordering however proceed fast enough such that the drying process under the investigated conditions cannot limit the structure formation. Hence, P3HT:PCBM is a suitable model system due to its sensitivity to many process parameters. According to the process influence on novel materials the results of this thesis can serve as a source for appropriate process strategies.

Zusammenfassung

Im Zuge des Ausbaus erneuerbarer Energien wächst das Interesse an Photovoltaik (PV). Organische Photovoltaik (OPV) ist eine vergleichsweise junge Technologie mit großem Potential zu kostengünstiger Solarenergie. Dabei stellt die Löslichkeit der verwendeten organischen Halbleiter einen intrinsischen Vorteil dar. Beschichtungs- und Druckprozesse von organischen Lösungen ermöglichen eine großflächige Herstellung mit hohen Durchsätzen. Dadurch können energieaufwändige Hochtemperatur- und Vakuumschritte vermieden werden, was Kosten und Energierücklaufzeiten gering hält. Die Leistung organischer Solarzellen hängt wesentlich von der Struktur der fotoaktiven Schicht ab, die ein Polymer-Fulleren-Gemisch enthält. Diese Struktur bildet sich während der Filmtrocknung aus, was im Rahmen dieser Arbeit untersucht wurde.

Startpunkt dieser Arbeit war die Hypothese, dass der Trocknungsprozess systematisch zur Beeinflussung der Strukturbildung in Polymer-Fulleren-Gemischen genutzt werden kann, um damit optimierte Strukturen mit gesteigerter PV Leistung zu erzeugen. Zur Evaluation dieser Hypothese wurde die Strukturbildung des Systems Poly(3-hexylthiophene-2,5-diyl):[6,6]-Phenyl C₆₁-butyric acid methyl ester (P3HT:PCBM) untersucht. Dies umfasste die Bereiche i) Filmtrocknung dünner Schichten, ii) Phasenverhalten von Polymer-Fulleren-Lösungen, iii) Strukturbildung und iv) Prozess-Struktur-Eigenschaftsbeziehung der fotoaktiven Schicht. Die Übertragbarkeit der gewonnenen Erkenntnisse wurde mit dem Verhalten von Poly{[4,40-bis(2-ethylhexyl)dithieno(3,2-b;20,30-d)silole]-2,6-diyl-alt-(2,1,3-benzothiazole)-4,7-diyl} (PSBTBT) untersucht.

i) Als Grundvoraussetzung für diese Arbeit wurde ein Trocknungskanal mit automatisierter Beschichtungseinheit entwickelt, was definierte und reproduzierbare Prozessbedingungen gewährleistete. Darin konnte mit Laserreflektometrie erstmalig das Trocknungsverhalten von letztendlich wenige hundert Nanometer dicken Schichten simultan an fünf Positionen gemessen werden. Anhand der gewonnenen Messdaten konnte ein lateral aufgelöstes Filmtrocknungsmodell erarbeitet werden.

ii) Zusammen mit der Messung und Simulation der Filmtrocknung war es nötig die während der Trocknung durchschrittenen Phasenübergänge wie z.B. Löslichkeitsgrenzen zu bestimmen. Für P3HT Lösungen wurde die Binodalkurve im Bereich von 0°C-60°C bestimmt. Innerhalb des instabilen

Bereichs phasensepariert die Lösung in eine Sol und Gel Phase. PCBM Lösungen zeigten hingegen nur eine einfache Löslichkeitsgrenze.

iii) Um die anhand der Phasendiagramme erwarteten Phasenübergänge mit der realen Strukturbildung korrelieren zu können, wurde der Trocknungskanal mit Synchrotron basierter in situ Röntgenbeugung im streifenden Einfall (GIXD) für Echtzeitmessungen während der Trocknung kombiniert. Somit konnten erstmalig die Mechanismen und die Dynamik der Polymer-Fulleren-Kristallisation während der Trocknung beobachtet werden. Mit der Überschreitung der P3HT Löslichkeit kam es zur grenzflächeninduzierten P3HT Keimbildung gefolgt von kristallinem P3HT-Wachstum mit steigender Orientierungsverteilung und abschließender Fulleren Aggregation. Des Weiteren wurden starke Polymer-Fulleren Wechselwirkungen nachgewiesen.

Unter erhöhtem PCBM Anteil konnte für eine P3HT:PCBM (1:2) Mischung nachgewiesen werden, dass PCBM Moleküle die (020) π - π -Stapelung der P3HT Lamellen unterbrechen, was starke Einbußen in der Lochmobilität und somit einen Leistungsverlust der Solarzelle bewirkt. Außerdem wurde mit ansteigender Trocknungstemperatur ein verringerter Anteil π - π -gestapelter Polymere, aber ein erhöhter Anteil an P3HT (100) Kristallinität nachgewiesen. Demzufolge eignet sich die Trocknungstemperatur zur Steuerung der bevorzugten Kristallisationsrichtung

iv) Neben einer feineren Phasenseparation bewirkt die Absenkung der Trocknungstemperatur einen Anstieg π - π -gestapelter Polymere, eine längere effektive Konjugationslänge, einen erhöhten Anteil vertikaler Ladungstransportpfade und eine erhöhte Oberflächenrauigkeit. Gemeinsam führt dies zu einer erhöhten Leistungsfähigkeit für niedrige Trocknungstemperaturen. Anhand der erarbeiteten Erkenntnisse konnte eine Strategie zur Reduktion der Trocknungszeit um 40% mit nur geringen Leistungseinbußen entwickelt werden.

Abschließend wurde die Übertragbarkeit der gewonnenen Erkenntnisse auf andere Stoffsysteme untersucht. PSBTBT:PC₇₁BM zeigt ebenfalls eine grenzflächeninduzierte Kristallisation mit abschließender PCBM Aggregation. Die Kinetik der Molekülanordnung verläuft jedoch schnell genug, sodass der Trocknungsprozess nicht limitierend auf die Strukturbildung wirkt. Aufgrund seiner hohen Sensitivität gegenüber der Prozessierung erwies sich P3HT:PCBM somit als ein geeignetes Modellsystem. Die Ergebnisse dieser Dissertation können je nach Prozesseinfluss bei neuen Materialien als Quelle zur Entwicklung passender Prozessstrategien genutzt werden.

Content

List of symbols	VII
1 Introduction	1
1.1 Principles of organic solar cells	3
1.2 Organic semiconductors.....	7
1.3 Morphology of polymer-fullerene blends.....	10
1.4 Aim of this work	15
2 Drying kinetics of thin films.....	19
2.1 State of the art	20
2.2 In situ measurement of drying kinetics.....	21
2.2.1 Basics of in situ reflectometry	23
2.2.2 Experimental approach and data analysis	26
2.2.3 Spatially resolved measurements	32
2.3 Model of mass transfer for thin film drying	37
2.3.1 Mass transfer in the gas phase.....	38
2.3.2 Phase equilibrium at the gas-liquid interface.....	42
2.3.3 Diffusion in the film.....	44
2.3.4 Summary of the chosen model.....	44
2.4 Evaluation of the drying kinetics model.....	46
2.4.1 Drying kinetics of a single solvent.....	46
2.4.2 Drying kinetics of solvent mixtures	49
3 Solution behavior of organic semiconductors	53
3.1 State of the art	54
3.2 Thermodynamics of polymer solutions	54
3.2.1 Flory-Huggins theory	55
3.3 Experimental method.....	59
3.4 Fullerene solution.....	61
3.5 Polymer solution	62

4	Morphology formation in polymer-fullerene films.....	67
4.1	State of the art	67
4.2	Experimental Methods used in this thesis.....	69
4.2.1	Grazing Incidence X-ray Diffraction (GIXD)	70
4.3	Real time observation of morphology formation.....	76
4.4	Influence of polymer-fullerene blending ratio.....	86
4.5	Influence of drying temperature.....	91
4.5.1	In-situ observation of molecular ordering.....	91
4.5.2	Ex-situ characterization of film structure.....	95
4.5.3	Optoelectronic properties	102
5	Influence of solvent mixtures on film properties	109
5.1	Low volatile and selectively solvating additives	109
5.2	Mixture of solvents with different volatility	114
5.2.1	Solvent mixture drying kinetics	114
5.2.2	Impact of solvent mixtures on film structure	117
5.2.3	Impact of solvent mixtures on optoelectronic properties.....	119
6	Structure formation of low band gap polymers	123
6.1	In-situ observation of molecular ordering	123
6.2	Film structure and optoelectronic properties	133
7	Conclusion.....	139
7.1	Summary of the obtained results.....	139
7.2	Outlook.....	144
8	References	147
9	List of Publications.....	167
10	Appendix	173

List of symbols

Latin letters

a_i	-	Activity of component i
Bi	-	Biot number
\tilde{c}_i	mol/m ³	Molar concentration of component i
$d, \Delta d$	m	Film thickness, thickness difference
D_{ij}	m ² /s	Stefan-Maxwell diffusion coefficient of i in j
E_{coh}	J	Cohesive energy
ΔG_M	J	Free enthalpy of mixing
Δh_M	J	Volume related enthalpy of mixing
ΔH_M	J	Enthalpy of mixing
I	A	Current
J_{sc}	A/m ²	Short-circuit current density
k_B	J/K	Boltzmann constant
k	-	Number of interference condition
L	m	Length
m	kg	Mass
M_w	kg/mol	Weight average molecular weight
n_i	-	Refractive index of component i
\dot{n}_i	mol/(m ² ·s)	Area related molar flux of component i
N_i	-	Number of lattice spaces occupied by component i
N_A	1/mol	Avogadro number
p	-	Number of contact points
p	Pa	Pressure
p_i	Pa	Partial pressure of component i
p_i^*	Pa	Saturated vapor pressure of component i
P	-	Number of polymer segments
P_{light}	W	Light power
q_{xy}	1/Å	In-plane vector

List of symbols

q_z	1/Å	Out-of-plane vector
\dot{r}_i	-	Relative flux of component i
R	J/(mol·K)	Ideal gas constant
R_q	nm	Root mean square roughness
Re	-	Reynolds number
ΔS_M	J/K	Entropy of mixing
Sc	-	Schmidt number
Sh	-	Sherwood number
$t, \Delta t$	s	Time, time interval
T	°C or K	Temperature
ΔU_M	J	Internal energy of mixing
v_{knife}	m/s	Knife coating velocity
ΔV_M	m ³	Excess volume of mixing
V	m ³	Volume
V	V	Voltage
w	m/s	Gas flow velocity
x	m	Length coordinate
x_0	m	Offset of concentration boundary layer
x_i	-	Mass fraction of component i in the liquid phase
\tilde{x}_i	-	Molar fraction of component i in the liquid phase
X_i	-	Mass content of component i (e.g., g_{liquid}/g_{solid})
\tilde{y}_i	-	Molar fraction of component i in the gas phase
Y	-	Volume fraction of crystalline component
z	m	Length coordinate
z	-	Lattice coordination number

Greek letters

α	$^{\circ}$	Angle of incidence
β_{ij}	m/s	Mass transfer coefficient of component i in j
γ_i	-	Activity coefficient of component i
δ	m	Boundary layer thickness
δ	$(\text{J}/\text{cm}^3)^{1/2}$	Solubility parameter
Δ	m	Optical pathway difference
Δ	-	Phase shift
ε_{ij}	J	Interaction energy between components i and j
$\Delta\varepsilon$	J	Interaction energy difference
φ_i	-	Volume fraction of component i
λ	m	Wavelength
Θ	$^{\circ}$	Angle of incidence
ρ_i	kg/m^3	Mass density of component i
$\tilde{\rho}_i$	mol/m^3	Molar density of component i
η	-	Power conversion efficiency
$\Delta\mu_i$	J/mol	Chemical potential of component i in the mixture
ν	m^2/s	Kinematic viscosity
$\tilde{\nu}_i$	m^3/mol	Specific molar volume
$\tan(\Psi)$	-	Polarized light amplitude ratio upon reflection
χ_{ij}	-	Flory-Huggins interaction parameter between i and j
χ_{ij}^*	-	Integrated Flory-Huggins interaction parameter

Subscript indices

0	Initially
∞	Bulk
<i>conc.</i>	Concentration
<i>d</i>	Disperse
<i>diode</i>	Reflectometer photodiode
<i>dry</i>	Dry state
<i>ext</i>	Extended correlation
<i>fit</i>	Fitted correlation
<i>g</i>	Gas
<i>h</i>	Hydrogen bonding
<i>hkl</i>	Miller indices of crystal lattice spacing
<i>k</i>	Number of interference condition
<i>l</i>	Liquid
<i>max</i>	Maximum
<i>MPP</i>	Maximum power point
<i>oc</i>	Open-circuit
<i>p</i>	Polymer
<i>p</i>	Polar
<i>ph</i>	Phase interface
<i>s</i>	Solid
<i>sc</i>	Short-circuit

Abbreviations

ADF	Annular dark field
AFM	Atomic force microscopy
AM 1.5	Air mass 1.5
bp	Boiling point
BF	Bright field
Cf	Chloroform
DCB	o-Dichlorobenzene
FF	Fill factor
FH	Flory-Huggins
FWHM	Full width at half maximum
GIXD	Grazing incidence X-ray diffraction
HAADF	High-angle annular dark-field
HOMO	Highest occupied molecular orbital
IMRS	Inverse micro Raman spectroscopy
In	Indane
ITO	Indium tin oxide
LCOE	Levelized cost of electricity
LUMO	Lowest unoccupied molecular orbital
MPP	Maximum power point
NEXAFS	Near edge X-ray absorption fine structure spectroscopy
ODT	1,8-Octanedithiol
OLED	Organic light emitting diode
OPV	Organic photovoltaic
OSC	Organic solar cells
P3HT	Poly(3-hexylthiophene-2,5-diyl)
pBTTT	poly(2,5-bis(3-hexadecylthiophen-2-yl)thieno[3,2-b]thiophene
PC ₆₁ BM	[6,6]-Phenyl C ₆₁ -butyric acid methyl ester
PC ₇₁ BM	[6,6]-Phenyl C ₇₁ -butyric acid methyl ester
PCE	Power conversion efficiency

List of symbols

PCPDTBT	Poly {[4,4-bis(2-ethylhexyl)-cyclopenta-(2,1-b;3,4-b')dithiophene]-2,6-diyl-alt-(2,1,3-benzothiadiazole)-4,7-diyl}
PDI	Polydispersity
PEDOT:PSS	Poly(3,4-ethylenedioxythiophene):poly(styrenesulfonate)
PSBTBT	Poly {[4,40-bis(2-ethylhexyl)dithieno(3,2-b;20,30-d)silole]-2,6-diyl-alt-(2,1,3-benzothiadiazole)-4,7-diyl}
PV	Photovoltaic
R2R	Roll-to-roll
rms	Root mean square
SANS	Small angle neutron scattering
SAED	Selective area electron diffraction
SE	Spectroscopic ellipsometry
SEC	Size exclusion chromatography
SEM	Scanning electron microscopy
STEM	Scanning transmission electron microscopy
STXM	Scanning transmission X-ray microscopy
TEM	Transmission electron microscopy
Tol	Toluene
UNIFAC	UNIQUAC functional group activity coefficients
VASE	Variable angle spectroscopic ellipsometry
oXyl	o-Xylene
XPS	X-ray photoelectron spectroscopy

1 Introduction

Photovoltaic (PV) is attracting increasing interest as an important contribution to renewable energy supply. This trend is getting strengthened by increasing price of fossil fuels, concerns over vast amounts of green house gases and upcoming discussions about the back out of the nuclear energy supply. In 2009, the world consumed in total 11164.3 million tons oil equivalent of fossil fuels corresponding to about 4.675×10^{20} J of primary energy consumption. [1] The total annual solar energy available to the earth is approximately 3.9×10^{24} J/a which is equivalent to 1.08×10^{18} kWh [2] with a global mean of about 170 W/m^2 [3]. This is more than 8000 times the world primary energy consumption. So if harnessed properly, solar energy can be used to cover the global energy needs. Presently, commercially dominating photovoltaic modules are based on crystalline silicon (first generation PV) or thin film techniques (second generation PV) as for instance copper indium gallium selenide (CIGS) or cadmium telluride (CdTe) solar cells. Silicon solar cells require energetically intensive high temperature processes, which leads to energy payback times in the range of 2-5 years [4-6]. On the other hand thin film solar cells like CIGS and CdTe can be fabricated more efficiently by vapor deposition, which reduces the energy payback time to about 1 year for CdTe. However, such thin film solar cells commonly require processing under high vacuum which still demands high needs of energy if the vapor deposition rates limit the fabrication throughput. Particle based printing processes and evaporation under ambient conditions are therefore under development for thin film PV.

In addition to the mentioned inorganic PV technologies organic photovoltaics (third generation PV) could make solar energy more affordable with energy payback times potentially in the order of months or weeks. No high temperature or high vacuum processes are required and the fabrication process can be conducted in a large area, so called roll-to-roll (R2R) coating process, from solution. Solution processing is an intrinsic advantage of soluble organic semiconductors¹. The mechanical flexibility of the active

¹ In 2000 A.J. Heeger, A.G. MacDiarmid and H. Shirakawa received the Nobel Prize for Chemistry “for their discovery and development of conductive polymers”.

1 Introduction

layer with thicknesses below 500 nm allows for the realization of flexible [7-10], stretchable [11] or solar cells on paper [12] or as textile fibers [13, 14]. Although light weight and mechanical flexibility offers many interesting applications for organic photovoltaic (OPV) their efficiency is not yet competitive with the inorganic counterparts. Table 1.1 depicts the current state of some exemplary photovoltaic technologies.

Table 1.1: Selected record efficiencies for different organic and inorganic solar cell devices [15, 16].

Classification	Efficiency	Test Center (Date)	Manufacturer
Organic polymer	8.3%	NREL (11/10)	Konarka
Organic (tandem)	8.3%	FhG-ISE (10/10)	Heliatek
Dye sensitized	10.4%	AIST (08/05)	Sharp
Silicon (crystalline)	25%	Sandia (03/99)	UNSW PERL
Silicon (multicryst.)	20.4%	NREL (05/04)	FhG-ISE
Silicon (amorphous)	10.1%	NREL (07/09)	Oerlikon Solar Lab
GaAs (thin film)	27.6%	NREL (11/10)	Alta Devices
CIGS	20.3%	FhG-ISE (08/10)	ZSW
CdTe	16.7%	NREL (09/01)	NREL

However, the advantage of OPV is the considerable reduction of fabrication costs which would make this technology competitive even at PCE below those of inorganic solar cells. Reduced fabrication costs of the solution cast layers of the OSC can be reached by large area coating and printing processes. For this purpose different coating techniques like knife over roll [17], slot die [17-20], screen printing [10, 17-19, 21, 22] and gravure coating [18, 23] have been proven to be suitable for large area fabrication of organic solar cells (OSC). Further large area deposition techniques are spray coating [24-28] and ink-jet printing [29, 30]

Recently, Krebs et al. have evaluated the cost of their R2R fabricated OSC to be 89 €/m² and 8.1 €/W_p [19], where the latter depicts the costs per generated electric power at standardized 1000 W/m² illumination and Air Mass 1.5 (AM 1.5) light spectrum. Even though the cost in €/W_p is comparable to the cost for electricity using existing technologies the levelized cost of

electricity (LCOE) is expected to be significantly higher than the existing technologies due to the inferior operational lifetime. Currently available OPV devices are thus competitive for consumer electronics but ill-suited for on-grid electricity production [19]. Dennler et al. estimated that OPV can become competitive at 7% efficiency and a lifetime of 7 years [31]. Although the maximum power conversion efficiency shows a fast progress and has reached presently a record efficiency of 9.2% at laboratory scale [32], many details from physical fundamentals up to the influence of the fabrication process on the device properties remain unclear. This thesis focuses therefore upon the fabrication process-device property relationship in order to facilitate the transfer from laboratory results to large scale manufacturing.

1.1 Principles of organic solar cells

In photovoltaic devices sunlight is absorbed in the photoactive layer, which excites electrons. Subsequently electrons and defect electrons, so called holes, are separated and collected at the electrodes. By this process a voltage in-between both electrodes is generated, which serves as power source.

In inorganic photovoltaic devices thermal energy at room temperature is sufficient for the dissociation of the photo-induced electron-hole pair within a single material (homojunction). In contrast to inorganic PV, organic semiconductors exhibit higher binding energies of the electron-hole-pair, also called exciton [33] which requires the incorporation of a second material in a so called heterojunction [34]. In this concept two materials with differing HOMO and LUMO energy levels are brought into contact with each other (Figure 1.1).

If electrons are excited at the light absorbing electron donator by photon absorption from the HOMO to the LUMO level, they leave a positive charge (hole) at the HOMO. Subsequently the excitons have to diffuse within the electron donating material to the interface with the electron accepting material. The diffusion distance is limited by the exciton lifetime to about 5-10 nm before recombination [35-37]. At the donator-acceptor interface the lower LUMO energy level of the electron acceptor is energetically preferred. If the LUMO-LUMO energy level difference exceeds the electron-hole binding energy, the charge carriers can be separated at the interface. LUMO positions of the polymer and acceptor separated by roughly 0.3 eV are expected to yield satisfactory charge separation and prevent charge recombination. [38-40]

Subsequently, the charges travel within the appropriate phases to the electrodes: holes within the electron donor phase (here polymer) and electrons within the electron acceptor phase (here fullerene). The theoretical voltage maximum of the solar cell device at open-circuit conditions (no current) V_{oc} can be determined from the difference of $LUMO_{acceptor} - HOMO_{donor}$.

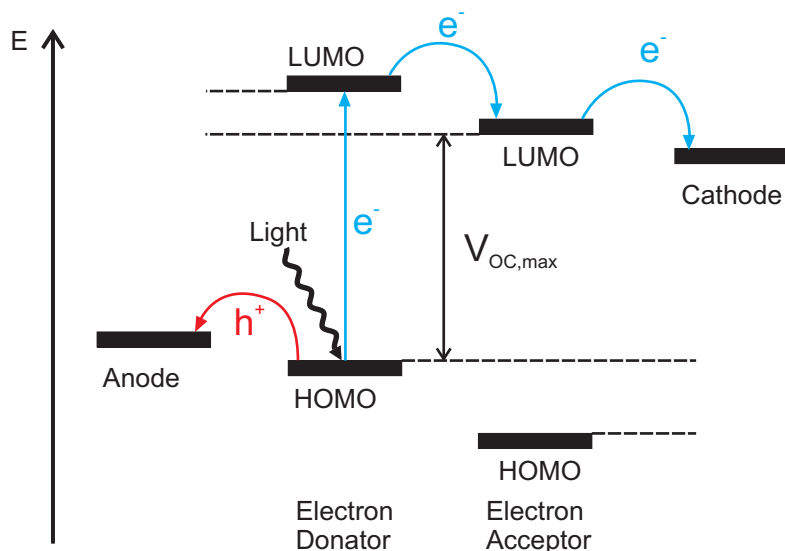


Figure 1.1: Energy level scheme of the steps of exciton generation, diffusion, dissociation and charge transport to the electrodes within each phase for the heterojunction concept. (According to [38])

For efficient solar cells it is worthwhile to generate short diffusion paths to the donor-acceptor interface, because of the very limited exciton diffusion length. Another important fact is the correlation of the amount of separated excitons with the donor-acceptor interface area, which should be as high as possible. Short exciton diffusion paths and an increased donor-acceptor interface can be achieved by the mixture of both phases. Figure 1.2 depicts a simplified scheme of the intermixed donor-acceptor structure of the bulk heterojunction (BHJ) concept [41, 42] and the typical architecture of a polymer solar cell. The challenge of the BHJ structure is to optimize the maximized interface area on the one hand, by providing sufficient interpenetrating charge transport pathways to the electrodes [43]. Charges that are generated at isolated domains remain trapped and cannot contribute to solar energy harvesting. It should be mentioned, that the image of clearly separated pure phases does not reflect the real character of interpenetrating morphology [44]. Additionally the crystallinity and the orientation of crystallites within the phases are of importance for the charge carrier mobility [45-47]. The solar

cell architecture comprises a transparent indium tin oxide (ITO) anode on top of the substrate (glass slides or plastic foils), followed by the solution processed hole conductive layer Poly(3,4-ethylenedioxythiophene):Poly(styrenesulfonate) (PEDOT:PSS) and the active layer (here P3HT:PCBM). On top of the active layer it is common to deposit a calcium/aluminum cathode¹ by evaporation through a shadow mask.

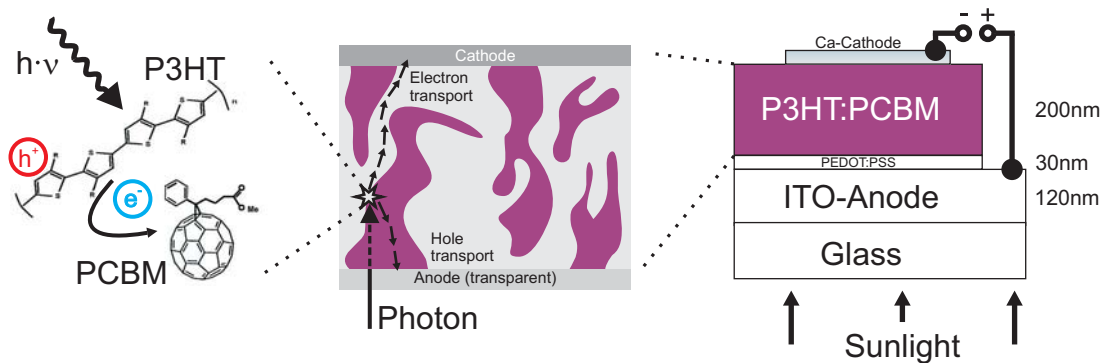


Figure 1.2: Structure of the polymer solar cell with approximate film thicknesses. Electron donor (P3HT) and acceptor (PCBM) are blended together to maximize the interface area where exciton dissociation into electrons and holes takes place. For an efficient photocurrent, each material must provide a continuous path for electron and hole transport to the respective contact. Isolated domains can collect charges and cause recombination.

For the electrical description of organic photovoltaics, the two-diode-model is suitable [48]. The equivalent circuit scheme of this model is shown in Figure 1.3, where I_{sc} is the generated photocurrent, D_1 the diode that determines the dark current and D_2 represents recombination losses. R_S and R_P represent the series and parallel resistance.

¹ For large area coating applications the moisture and oxygen sensitive calcium layer has to be replaced [10, 263, 264][265].

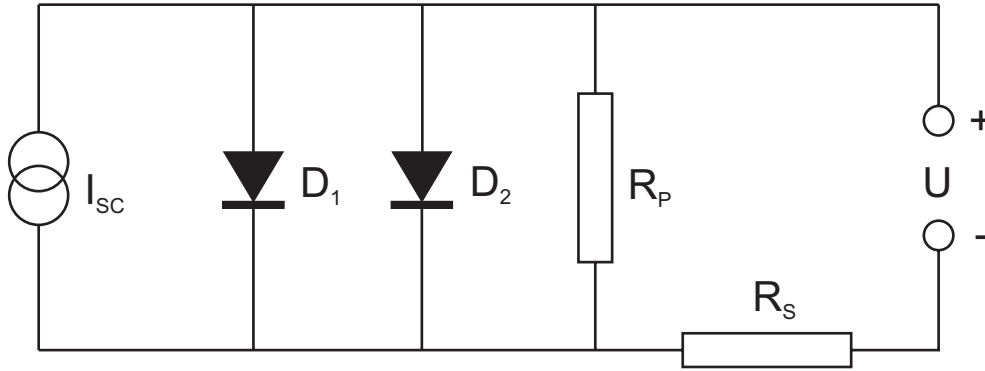


Figure 1.3: Equivalent circuit scheme of an organic solar cell.

The current density-voltage characteristics (JV-characteristics) describe the behavior of an organic solar cell and can be related to parameters of the equivalent circuit. The JV-curve of a solar cell corresponds basically to the characteristics of a diode shifted about the amount of the photocurrent (Figure 1.4a). This is the case if the resistances and recombination losses are independent from illumination of the device. The point at the JV-curve where the generated power ($P = V \cdot I$) reaches a maximum is called maximum power point (MPP). The highest voltage at the solar cell is reached at open-circuit conditions ($I = 0$) and is denoted as V_{oc} or U_{oc} . The highest current is reached under short-circuit conditions ($V = 0$) and denoted as I_{sc} or as J_{sc} for the area related current density. The power conversion efficiency η (PCE) of a solar cell is determined by the ratio of generated electric power to the incident light power.

$$\eta = \frac{V_{MPP} \cdot I_{MPP}}{P_{light}} = \frac{V_{oc} \cdot I_{sc} \cdot FF}{P_{light}} \quad 1.1$$

The fill factor FF describes the ratio between the power at MPP and the product of V_{oc} and I_{sc} .

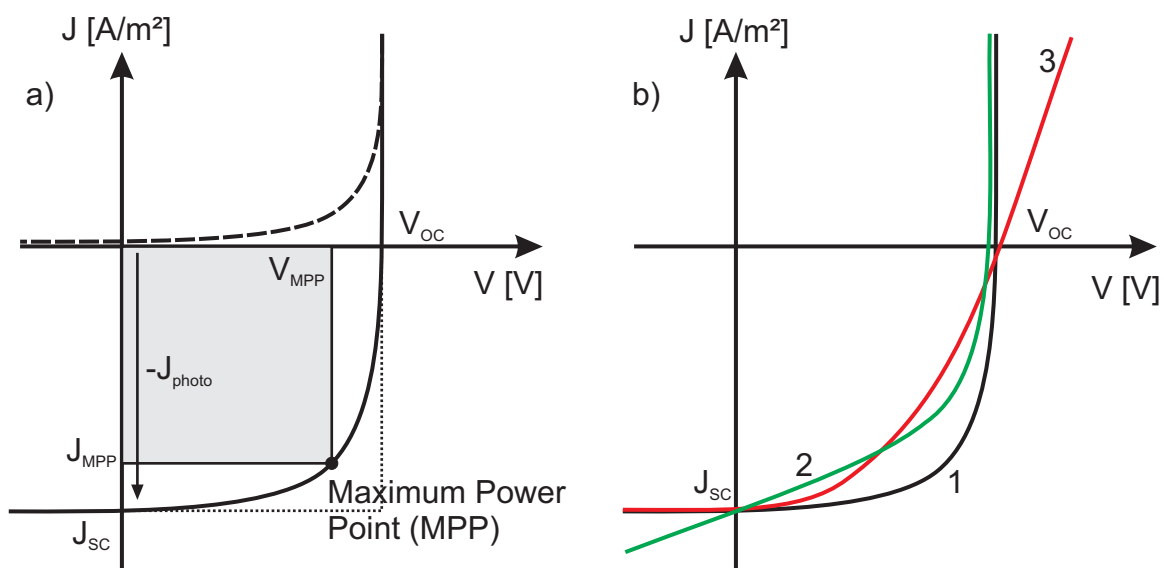


Figure 1.4: a) Current density-voltage (JV) characteristics of a solar cell. Dark curve (dashed line) and under illumination (solid line). b) JV -characteristics for an "ideal" solar cell (1) with negligible series resistance and almost infinite parallel resistance. Case (2) exhibits a finite parallel resistance and case (3) an increased series resistance. [49]

The series and parallel resistance are important for the performance of solar cells. An ideal solar cell exhibits an infinite parallel resistance and a negligible series resistance (case 1 in Figure 1.4b). This ideal case is usually not reached. The parallel resistance is proportional to the reciprocal slope of the JV -curve for $V \leq 0$ before the diode breaks through. Decreasing parallel resistance is expressed by an increasing slope in forward regime at high voltage (case 2 in Figure 1.4b). The series resistance can be derived from the reciprocal slope at comparatively high voltages, since it is the determining parameter in that range. An increased series resistance is expressed by a decreasing slope at V_{oc} (case 3 in Figure 1.4b).

1.2 Organic semiconductors

For the investigation of the impact of fabrication scenarios on the solar cell properties of organic solar cells, the well-established electron donating polymer poly-(3-hexylthiophene) (P3HT, Figure 1.5) was mainly investigated in this thesis. The transferability of the observed mechanisms and correlations as obtained for P3HT was accomplished for the low band gap polymers poly{[4,4-bis(2-ethylhexyl)-cyclopenta-(2,1-b;3,4-b')dithiophene]-2,6-diyl-

1 Introduction

alt-(2,1,3- benzothiadiazole)-4,7-diyl} (PCPDTBT, Figure 1.5) and the similar polymer containing a silicon bridging atom poly{[4,40-bis(2-ethylhexyl)dithieno(3,2-b;20,30-d)silole]-2,6-diyl-alt-(2,1,3-benzothiadiazole)-4,7-diyl} (PSBTBT¹, Figure 1.5).

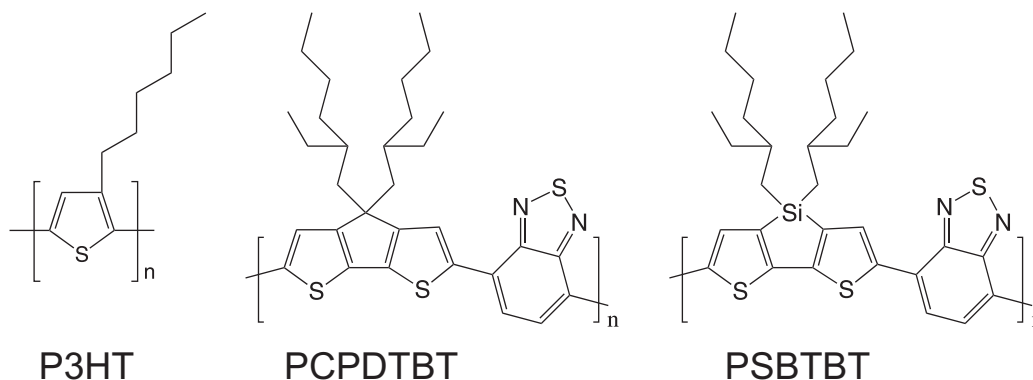


Figure 1.5: Structures of the investigated electron donating polymers.

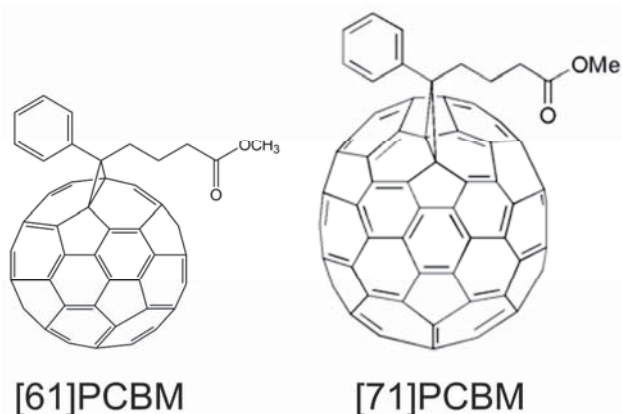


Figure 1.6: Structures of the investigated electron accepting fullerene derivatives. [50]

In the photoactive layer, these electron donating polymers are combined with electron accepting fullerene² derivatives like [6,6]-phenyl C₆₁-butyric acid methyl ester (PC₆₁BM, Figure 1.6) and [6,6]-Phenyl C₇₁-butyric acid methyl ester (PC₇₁BM, Figure 1.6). Reasons for the incorporation of these two

¹ In literature the abbreviation Si-PCPDTBT is also common.

² Harold Kroto, Robert Curl and Richard Smalley were awarded the 1996 Nobel Prize in Chemistry for their roles in the discovery of buckminsterfullerene and the related class of molecules, the fullerenes.

types of materials and the concept of organic solar cells shall be explained below in section 1.1

One property which all organic semiconductors have in common is the conjugated π -electron system, i.e. alternating single and double bonds, along the entire molecule of the organic semiconductor. In this configuration all carbon atoms exhibit a sp^2 -hybridization state. While the three sp^2 -orbitals are ordered planar as indicated in Figure 1.7 (right), the unhybridized p_z -orbital stands normal to the sp^2 -orbital plane. Within the sp^2 -orbital plane, single bonds (σ -bonds) are formed. Overlapping p_z -orbitals of neighboring carbon atoms can additionally form a weaker π -bond, which leads in sum to a double bond. For the case of alternating single and double bonds, p_z -orbitals can either overlap with one or the other neighboring carbon atom which is a dynamically changing process. In time average this leads to the delocalization of π -electrons in one large π -orbital over the entire conjugated electron system. This interaction of p_z -orbitals within one molecule leads to the formation of a multitude of possible electronic states. In the non-excited ground state electrons will occupy energetically favorable states, which is the Highest Occupied Molecular Orbital (HOMO). This molecular orbital is the analogue of the valence band in inorganic semiconductors. The Lowest Unoccupied Molecular Orbital (LUMO) represents the analogue of the conductive band in inorganic semiconductors.

In this work polymers are used as hole conducting (p-type) electron donating materials and fullerene derivatives as electron accepting and conducting (n-type) compounds. Figure 1.7a exemplarily depicts the unit cell of the hole (h^+) conducting polymer P3HT, which exhibits a conjugated electron system along the polymer backbone. Hence, charges can travel along the polymer backbone within the plane of sp^2 -orbitals due to overlapping p_z -orbitals.

The charge transport from one polymer backbone to the other, where the distance of the hexyl-side chains must be overcome is not possible, since the side chains are not part of the conjugated electron system [51]. Because p_z -orbitals protrude out of the plane of σ -bonds which are formed by sp^2 -orbitals (indicated as grey planes in Figure 1.7), polymers tend to stack in a manner such that p_z -orbitals additionally overlap in the (020) stacking direction according to the crystallographic nomenclature. This effect is called π - π -stacking and it provides additional charge transportation in p_z -orbital direction normal to the plane of σ -bonds.

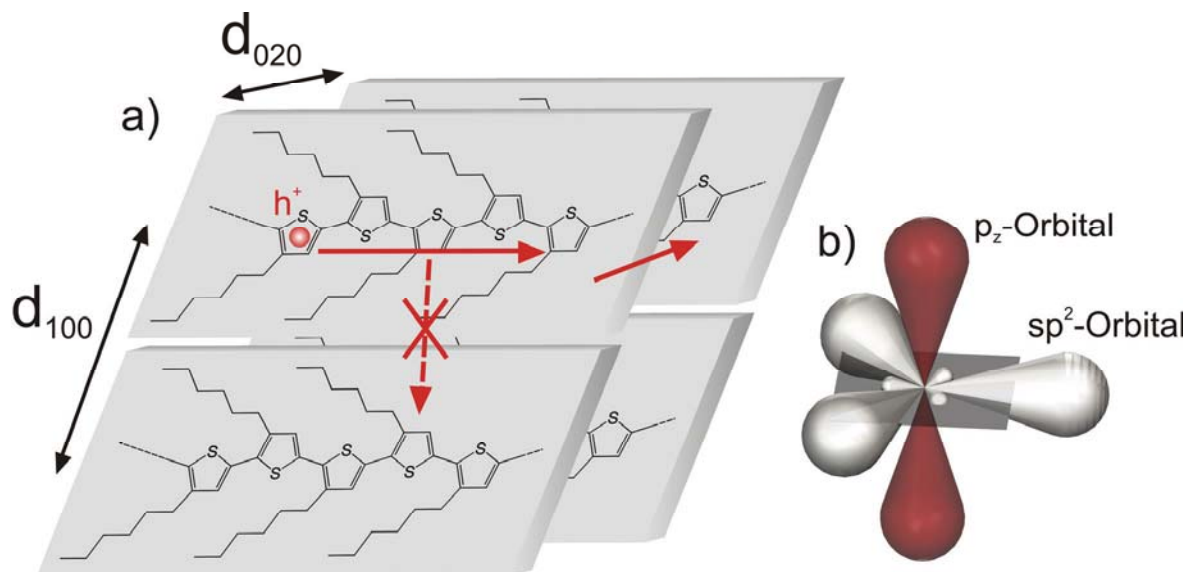


Figure 1.7: a) Scheme of hole (h^+) transport in P3HT along the polymer backbone and in π - π -stacking direction indicated by red arrows. The spacing in intra layer (100) and inter layer (020) π - π -stacking are denoted as d_{100} and d_{020} respectively. b) Drawing of sp^2 -hybridized orbitals.

The average chain length of P3HT investigated in this thesis ($M_w \approx 40.000 - 60.000$ g/mol, polydispersity $\approx 1.7-1.9$) is in the order of several hundred thiophene units. The effective conjugation length of polythiophene, which is the length of continuously delocalized π -electron system along the polymer backbone, is typically in the range of ≈ 10 thiophene units [52, 53]. Reasons for the low conjugation length can be distorted polymers and kinks along the backbone [54]. These barriers must be overcome by so called hopping processes of the charge carriers. In amorphous materials hopping processes are the dominating charge transport mechanism, which usually leads to lower charge carrier mobility in comparison to semi-crystalline materials.

1.3 Morphology of polymer-fullerene blends

The performance of organic solar cells strongly depends on the phase separated polymer-fullerene structure which forms by self assembly during the solvent evaporation step subsequent to the coating process [55-58] and can further be modified by post process treatments, such as thermal [59-63] or solvent annealing [64-66]. Domain sizes, degree of crystallinity, molecular orientation and the interpenetrating network geometry are important morpho-

logical parameters for the optimization of solar cell performance. Several review articles discuss the crucial importance of morphology for the efficiency of OPV and demand an improved understanding of the driving assembly mechanisms [67-70]. Due to the paramount relevancy of this topic it has been of great research interest worldwide over the past years. The knowledge about morphology and its relation to the physical properties of solar cells are still under progress.

At the beginning of this thesis the image of morphology was basically a three dimensional phase separated structure of pure donor and acceptor domains. Since the structures are very small (desired in the range of a few tens of nanometers) and the optical contrast is very low for the predominantly carbon containing materials, it has been very challenging to obtain reliable images of the film structure by common microscopy methods. This section gives a brief overview about common methods for the structural investigation of BHJ blends. Several review articles give a broader overview of appropriate experimental techniques [51, 71-73]. Morphology aspects are discussed in more detail in chapter 4 in conjunction with results obtained in this work, which contributed to an improved and more detailed image of the polymer-fullerene blend structure. In the following, the presently most relevant techniques and reported results are exemplarily discussed with some selected publications.

Molecular scale: X-ray diffraction and scattering X-ray techniques are in general suitable for the investigation of crystalline structures. For the determination of crystallographic structures in thin films they are commonly operated at very low angles of the incident beam close to total reflection in the order of 0.1-0.2 degree, which is called grazing incidence [74]. Grazing incidence X-ray diffraction (GIXD) or similar techniques have been used in numerous publications for the determination of the crystalline polymer structure and their orientation with respect to the substrate [75, 76]. Recent works exploited the advantage of bright synchrotron¹ based X-ray sources for in-situ measurements during thermal [63, 77, 78] or solvent annealing [79]. By changing the angle of incidence it is even possible to adjust the penetra-

¹ A synchrotron is a type of cyclic particle accelerator in which the magnetic field and the electric field (to accelerate the particles) are synchronized with the travelling particle beam.

tion depth of the X-ray beam and probe the structure vertically resolved. In this work GIXD could be applied for the first time for monitoring the molecular ordering of polymer-fullerene blends during film drying in real time [58, 80, 81], which is explained in more detail in section 4.2.1. This technique provides quantitative information on polymer chain spacing, their orientation with respect to the substrate, domain size (correlation length) and the relative amount of crystallites (related to signal intensity). The detectable structure scale ranges from the molecular scale to the size of crystalline domains.

Cluster and domain scale: Neutron scattering Kiel et al. demonstrated by the application of small angle neutron scattering (SANS) at polymer-fullerene blend films that small scale crystallites form superior aggregate structures [82, 83]. Thermal annealing leads to increasing PCBM cluster sizes. This method is very useful, since it covers the intermediate structural scale between X-ray and electron microscopy techniques.

Domain and topography scale: Electron microscopy Typical electron microscopic methods for transmission measurements are transmission electron microscopy (TEM), scanning transmission microscopy (STEM) [84, 85] and selected area electron diffraction (SAED). While TEM is sensitive to the local density of the sample, STEM can provide higher sensitivity to material contrast, i.e. the atomic number, if operated with a high-angle annular dark-field (HAADF) detector. SAED diffraction patterns give information about the crystallographic film structure.

The difficulty of TEM measurements at BHJ layers [60, 86-88] is the low contrast between both mainly carbon containing materials and the small structure scale of a few tens of nanometers. A trick is to slightly defocus the microscope. Excessive defocusing falsifies the structure scale. 50-100 nm thin films must be prepared, in order to prevent shadow effects. The smoothness of the film is important, since high roughness causes additional contrast due to lateral deviations in electron penetration length through the sample. Usually the BHJ film is lifted off the water soluble PEDOT:PSS layer and is transferred to a common TEM copper grid. This device destructive, but not film destructive procedure is the same for all measurements mentioned in this section that are operated in transmission. If used properly, TEM can reveal the fibril structure of P3HT in the BHJ blend and also depicts the larger scale film

topography [60]. The dimensions of such P3HT whiskers are about 3-7 nm in height, 15 nm in width and about 0.2-5 μm in length [45, 89]. A more comprehensive image of the three dimensional (3D) morphology can be obtained by electron tomography [66, 85, 90]. This is basically done by a series of TEM measurements at different angles of incident (i.e. from $+70^\circ$ to -70°). It should be noted that the image contrast of this technique originates mainly from the density difference of crystalline and amorphous regions. Polymer and fullerene phases can hardly be deciphered. These structural 3D measurements furthermore deliver information of the vertical distribution of crystalline volume fraction.

Vertical gradients The vertical donor-acceptor ratio is crucial for charge carrier transport, since electrons are collected at the top electrode and holes at the bottom electrode in regular device architecture. Hence, polymer enrichment close to the top electrode would cause a barrier for electron extraction. A method that is very sensitive to vertical gradients in BHJ layers is neutron reflectivity [82, 91, 92]. The difference in scattering length density (SLD) of P3HT ($0.80 \pm 0.01 \times 10^{-6} \text{ \AA}^{-2}$) and PCBM ($4.34 \times 10^{-6} \text{ \AA}^{-2}$) provides sufficient contrast between both materials [92]. The vertical gradient is determined indirectly by model fits to the reflectivity measurements where the angle of incident is scanned. Another way for the determination of the vertical gradient is variable angle spectroscopic ellipsometry (VASE). In VASE, changes in the polarization state are utilized for model fits of the complex refractive index of the investigated film, which can also provide vertical information [93, 94]. A destructive method for the determination of vertical concentration gradients is secondary ion mass spectrometry (SIMS) [95-98]. Here the film is sputtered with typically Ga^+ ions and subsequently analyzed by mass spectrometry. A critical issue is the sputtering rate, which might be very different for multi component systems. Another possibility to investigate the vertical gradient is to lift off the BHJ layer and measure the chemical composition on the top and bottom surface of the film with surface sensitive techniques.

Surface sensitive techniques X-ray photoelectron spectroscopy (XPS) is capable of measuring the chemical composition at surfaces. An incident X-ray beam generates photoelectrons close to the surface which are detected with respect to their kinetic energy and intensity. This results in spectra that are

characteristic for a distinct composition. After initial pure substance calibration XPS allows for a quantitative determination of the chemical composition at the surface. Due to the short mean free path of the photoelectrons, the probing depth of XPS is only 6–8 nm [99]. XPS could be exploited for the comparison of the composition at the top and bottom interface of the BHJ layer [53, 100, 101]. In combination with ion sputtering it is used to investigate depth profiles in bulk materials and buried interfaces. Another technique for the determination of the surface composition is near-edge X-ray absorption fine structure spectroscopy (NEXAFS) which is more sensitive to structural features than XPS [71]. With NEXAFS, composition specific spectra are utilized for concentration determination [94, 102, 103]. Germack et al. measured the chemical composition at the bottom and top interface of the BHJ layer with NEXAFS and could proof the influence of substrate surface energy on the vertical polymer-fullerene-ratio gradient [102].

Another class of surface sensitive techniques is scanning probe microscopy (SPM) [72] whereby atomic force microscopy (AFM) [104] is the prevalent method. In AFM, the sample surface is scanned with a sharp tip providing mainly the surface topography and a sort of mechanical property mapping which is explained in more detail in section A 3.2.

Lateral chemical mapping In combination with scanning transmission X-ray microscopy (STXM) NEXAFS has been shown to be very utile for lateral chemical mapping when operated in transmission [44, 71, 105-107]. In this combined method the sample is first of all scanned by STXM for the identification of structures revealed by lateral contrast. Subsequently these lateral contrast features are investigated by NEXAFS analysis which provides the chemical composition after prior calibration and structure information with a spatial resolution of about 20-50 nm [71, 105]. If operated with polarized X-rays the polymer backbone or crystalline plane orientation can be determined according to interactions between the X-ray electric field and the delocalized electrons along the delocalized π -electron system [108].

1.4 Aim of this work

This work was encouraged by the observation of the drying process influence on the light absorption behavior of the photoactive layer of OSC. Initial drying experiments have been conducted in collaboration with Hung Do and Alexander Colsmann of the Light Technology Institute (LTI, Karlsruhe). This observation was supported by Li et al. [109] and Mihailetschi et al. [110] who demonstrated that the drying process of the photoactive layer in OPV devices influences the solar cell performance. This led to the hypothesis, that the drying process can be utilized for a systematic optimization of solar cell performance due to systematically induced morphological changes in the photoactive layer. The evaluation of the hypothesis requires the elaboration and investigation of different topics:

- Drying kinetics (evolution of thickness or composition) measurement and simulation of μm to nm thin multi component films
- Phase diagrams of organic semiconductor solutions
- Determination of driving mechanisms for film morphology
- Exploitation of the process-structure-property relationship in order to realize an optimized fabrication of solar cells (higher efficiency and faster production)

For the exploitation of the drying process in order to generate a favorable film structure it is mandatory to be able to describe the drying kinetics of the solution cast film. Therefore, new methods for the measurement of film drying kinetics from several micrometers to the nanometer scale have to be developed. This requires the elaboration of an experimental setup which allows for an accurate coating of wet film thicknesses below 10 μm combined with well-defined and reproducible drying conditions to obtain dry film thicknesses of 20-300 nm. In combination with this experimental setup a technique for the measurement of the drying kinetics of such thin films shall be elaborated.

In the theoretical part of this thesis, an appropriate model shall be developed, which is capable to describe the drying kinetics of such thin films for single and multiple solvent systems. This part can be conducted in continuation to previous work on film drying [111] and mass transport in polymeric membranes [112] which show many similarities. The validation shall be conducted with experimental data obtained from solution cast blends of organic semiconductors.

1 Introduction

In the morphology and optoelectronic part of this thesis, the governing mechanisms of molecular ordering and their influencing parameters are the mayor interest. For a systematic exploitation of the self-assembly mechanisms their influencing parameters shall be explored. This requires new experimental approaches for in situ observations of the assembly process during film drying. A simultaneous measurement of the evolving film structure and film composition is required for this purpose.

The influence of drying time on solar cell device performance is expected to originate from differences in molecular assembly time induced by crossing solubility limits or entering thermodynamically unstable states. This assumption demands the comparative investigation of two competitive mechanisms: thermodynamic equilibrium and film formation kinetics. This requires on the one hand the determination of the solutions phase diagram (Figure 1.8a), which depicts the preferred thermodynamically equilibrium state at a distinct composition. On the other hand film drying kinetics (Figure 1.8b) can hinder that this state is reached, if kinetic limitation is given.

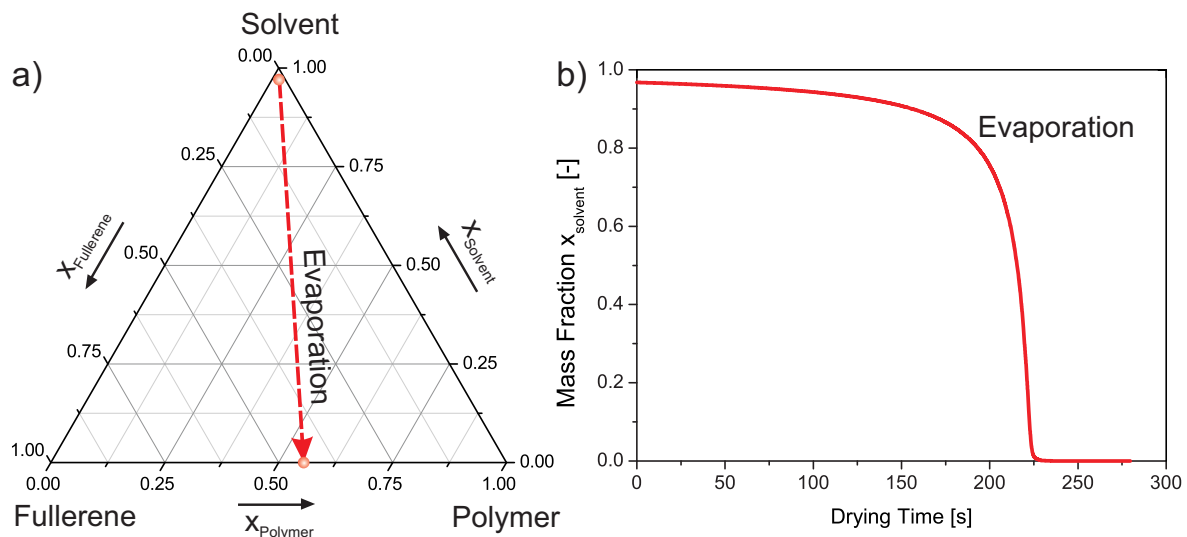


Figure 1.8: a) Schematic ternary phase diagram comprising the drying path of a polymer-fullerene (1:0.8) solution (Details see section 3). b) Exemplary drying curve of a thin film with initially 3 wt.% solid fraction (Details see section 2).

Finally, it is important to investigate the systematic impact of different drying conditions on the blend film structure. If parameters such as drying temperature and drying gas velocity (gas phase mass transfer coefficient) are suitable for generating different film structures, the process-structure-property

relationship of solar cell devices will be investigated. Therefore suitable measurement techniques for the determination of the molecular, nanometer and micrometer scale structure have to be chosen or developed. The comparison with solar cell devices requires the elaboration of a solar cell fabrication process within the experimental setup of controlled drying kinetics.

2 Drying kinetics of thin films¹

As previously mentioned, the drying kinetics of the solution processed active layer of organic solar cells determines the performance of the final solar cell device. Hence, it is of great interest to augment the knowledge of the film formation process in the course of film drying. The first step of a quantitative understanding signifies the development of an accurate method for the measurement of the film composition versus drying time. The second step requires a fundamental knowledge on those mechanisms that govern molecular ordering during solvent evaporation, which results in different film structures corresponding to different drying scenarios. The third step is correlating these film structures with their optoelectronic properties and final solar cell efficiency in order to elaborate the appropriate drying conditions for highest solar cell efficiency.

Because of the multi scale character of film morphology, which ranges from single molecule to macroscopic bulk effects with dimensions from the angstrom to the micrometer scale, many parameters are in principle suitable for describing the film structure. These different structural features originate from self-assembly mechanisms in the course of film drying. It was part of this thesis to identify those parameters, that can be systematically tuned by the drying process in order to design suitable drying conditions for efficient solar cells. Therefore, simulation of the drying kinetics is of crucial importance. Furthermore, the drying kinetics-film property relationship can subsequently be transferred to a large area so called roll-to-roll processes by exchanging the boundary conditions for heat and mass transfer. This chapter shows a suitable method for the measurement and simulation of thin film drying kinetics suitable for the required film thickness range from several micrometers down to a few tens of nanometers.

¹ Katharina Peters [266] and Michael Baunach [139] dedicated their diploma thesis and Felix Buss [267] his student research project to the drying kinetics of thin films. The essence of this chapter is published in [56, 135]

2.1 State of the art

Organic solar cells comprise different solution cast layers in the sub micrometer scale. For the elaboration of appropriate drying kinetics models of these layers, suitable measurement techniques for the film shrinkage during drying of such thin films are required. In thin films the mass loss due to solvent evaporation is very low according to low film thicknesses. This demands very sensitive measurement techniques for monitoring the film shrinkage during the drying process. A measuring technique which is capable of detecting very low changes in mass during the solvent evaporation in thin films is quartz crystal micro balance [113-116]. A limitation of this technique is that the wet film has to be coated directly on top of the microbalance surface in order to achieve an accurate measurement. Furthermore, forced convection as it is required for a controlled drying process worsens the signal to noise ratio.

Optical methods can be operated without contact which is preferred for thin films in this case. A method that is appropriate for monitoring the film composition during film drying is the Inverse Micro Raman Spectroscopy (IMRS) [117, 118]. This technique has been used for characterizing the mass transfer in drying thin polymer films [111, 117, 119] and membranes [112, 120, 121]. Requirements for this technique are a sufficient transparency in the spectral range of the applied laser wavelength (e.g., 532 nm, 633 nm) and a Raman activity of the material system. If the film is sufficiently thick (10-200 μm), it is possible to determine the profile of film composition in the vertical film coordinate normal to the substrate. Since the used film thickness in this thesis ranges from several μm (wet film) to a few tens of nanometers (dry film) IMRS could not resolve the vertical concentration. A further drawback is the high extinction coefficient of the organic semiconducting materials in the spectral visible range, which causes a predominating photoluminescence making the Raman signal hardly recognizable in the drying film. Hence, reproducible quantitative Raman measurements were difficult to accomplish in situ during film drying.

A promising optical technique is spectroscopic ellipsometry (SE) [122], which is capable of resolving thickness changes up to the sub nanometer range [123]. The data acquisition time for a wide spectral range is fast enough to follow film drying processes in-situ. This makes SE appropriate for monitoring the film thickness during film drying [57]. This was done at drying P3HT:PCBM films in collaboration with Sopralab (Semilab group, France), which is shown in the appendix in section A 1.4. However, film thickness is

measured indirectly with SE and requires the modeling of optical film properties. This signifies a modeling of the complex refractive index of the film [124, 125] at each instant of measurement. In the course of drying, the optical properties of the drying film change continuously. Since this technique is also sensitive to vertical gradients and optical/structural anisotropies, the optical modeling is consistently challenging for each drying experiment.

Another contactless optical technique is reflectometry based on interference effects which are related to the optical film thickness. Reflectometry can be conducted with a spectral light source allowing for an optical modeling of film properties [79]. A similar challenge for this method is the continuously changing spectral refractive index of the film. An easy way to handle the evolution of refractive index is to use a monochromatic light source, e.g. laser light, in a spectral range, where the changes of refractive index correlate in a simple way with the film composition. Jukes and Heriot et al. introduced this technique for monitoring the evolution of film thickness during spin coating [126, 127]. Based on the work of Jörg Pfeifer, Cheng Huang and Stefan Walheim of the Institute of Nanotechnology (INT, Karlsruhe) reflectometry was developed further to spatially resolved measurements in this thesis. This afforded the elaboration of mass transfer models for spatially resolved film drying simulations at dry film thicknesses in the nanometer range.

A challenging part in the simulation of film drying is the evaporation of the last few weight percent of solvent, which is in most cases determined by the kinetics of solvent diffusion in the solid matrix of the film [111, 117, 119, 128-134]. In order to simulate this drying regime, the diffusion coefficient must be considered as a function of solvent concentration and drying temperature, which is very difficult to access for the material system used in this thesis.

2.2 In situ measurement of drying kinetics

For the investigation of thin film drying of OPV layers, a dedicated coating and drying setup had to be developed within this thesis. Therefore, a drying channel with integrated knife coater (doctor blade) and five monochromatic reflectometers as illustrated in Figure 2.1 was built. Using this setup, thin films in the range of several μm to nm dry film thickness can be coated and subsequently dried under defined drying conditions (more details in section 2.2.2). In order to control the drying kinetics, the temperature and the drying

2 Drying kinetics of thin films

gas flow in the drying channel can be adjusted. Drying kinetics were investigated at temperatures of 15, 25 and 40°C and gas flow velocities in the range from 0.1 to 0.65 m/s. The drying process was monitored in-situ with five monochromatic reflectometers (635 nm or 650 nm wavelength).

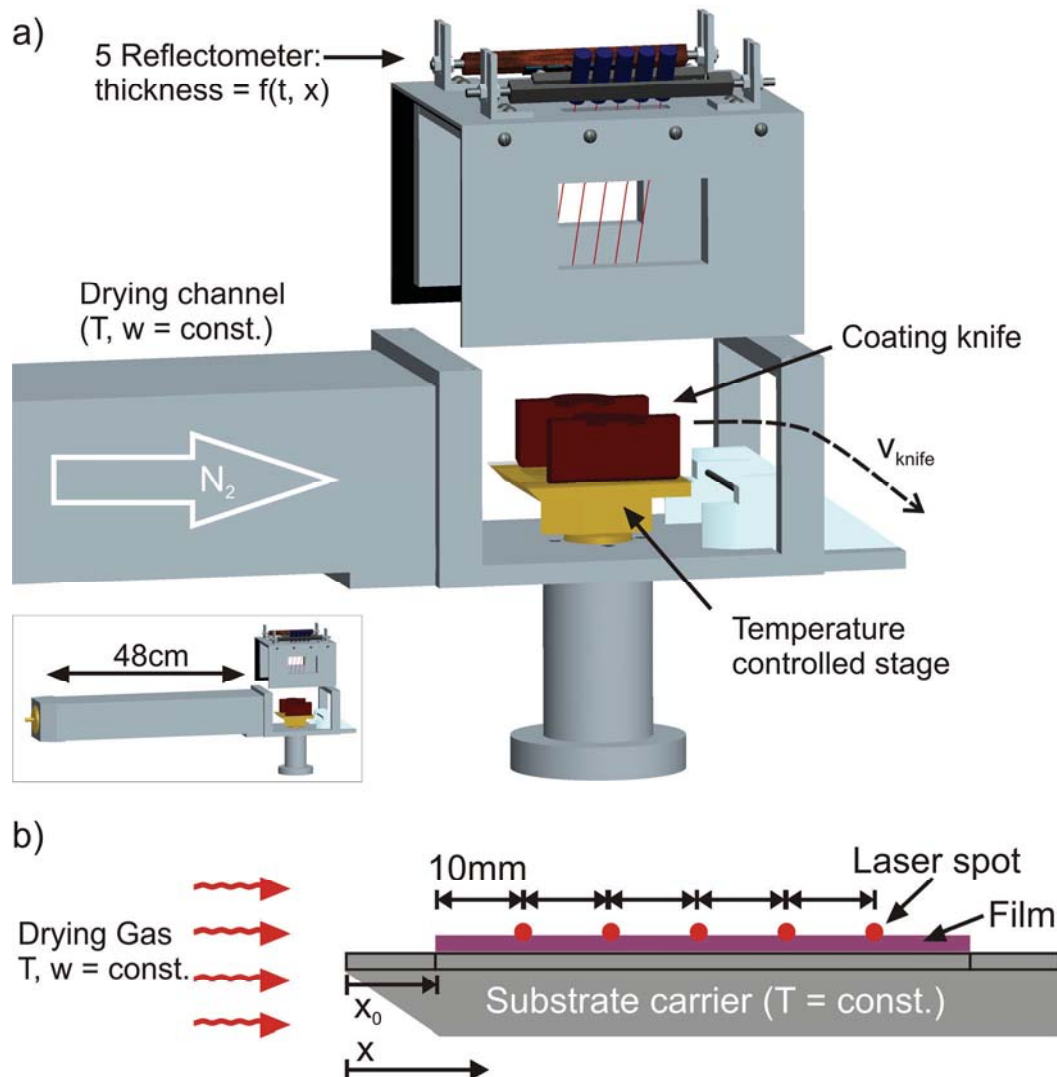


Figure 2.1: a) Schematic drawing of the drying channel with integrated knife coater and linear array of five laser reflectometers. The inset shows the 48 cm long channel for horizontal, laminar gas flow distribution in front of the coating stage (flat plate). The coating knife is moved horizontally over the substrate with the speed v_{knife} and leaves the drying channel by sliding down a plastic chute (dashed arrow). b) Position of the substrate fixed in-between two silicon slices on the overflowed plate with 45° angle at the left edge and the position of the laser spots. [135]

The substrate carrier plate dimensions (see appendix Figure 10.3) were $7 \times 77 \times 70 \text{ mm}^3$ (thickness \times length \times width) with a 45° angle at the upstream edge, mounted on top of a 7 mm thin fin and a channel cross section of $110 \times 80 \text{ mm}^2$ (width \times height). To monitor the drying kinetics in situ, laser light (635 nm or 650 nm) was reflected at 5 distinct positions as shown in Figure 2.1 under an incident angle of 30° and detected by a Si photodiode during coating and the following drying period. Hence the film thickness was monitored directly after film casting at 5 distinct positions simultaneously.

2.2.1 Basics of in situ reflectometry

Laser reflectometry is based on the interference of the laser beam after being reflected at two parallel interfaces. In our case these two interfaces are the air-film and the film-substrate interface. Depending on the film thickness, conditions of constructive or destructive interference are reached. In the course of solvent evaporation and film shrinkage, constructive and destructive interference conditions are passed through, which are detected by high and low light intensity respectively at the photo diode. With the knowledge of the refractive index and the dry film thickness one can reconstruct the evolution of film thickness based on the observed interference fringes during film drying. For such an analysis of the reflectometer measurements, one must consider the geometry of the laser beam in the shown experimental setup as depicted in Figure 2.2.

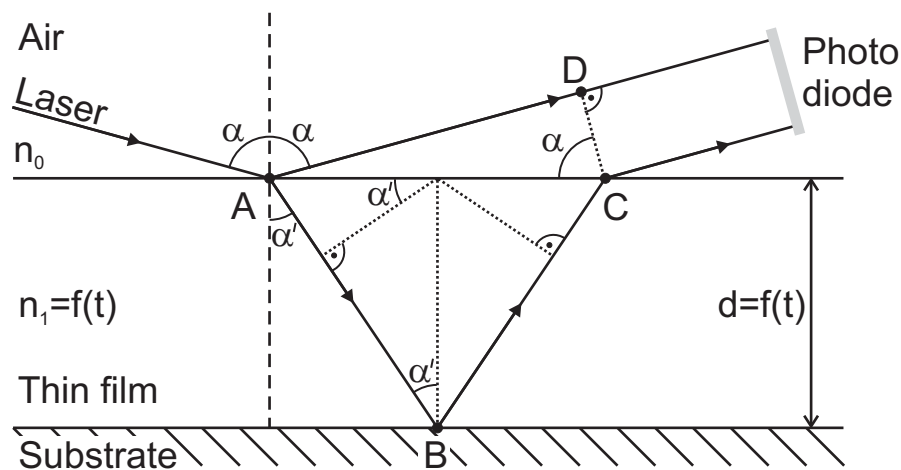


Figure 2.2: Optical pathway of the reflectometer laser beam through the drying film with the continuously changing refractive index n_1 .

2 Drying kinetics of thin films

Laser light hits the wet film surface under the incident angle α and is partly reflected under the same angle, while the beam penetrates partly the wet film under the refracted angle α' due to an increasing refractive index of the drying film. The refracted part of the beam is reflected at the film substrate interface under the same angle α' . After leaving the wet film, both parts of the laser beam interfere with each other after the common laws of optics [136, 137]. Hence, the optical path difference Δ can be written as

$$\Delta = n_1[(\overline{AB}) + (\overline{BC})] - n_0(\overline{AD}) \quad 2.1$$

Where n_1 is the refractive index of the film during drying as a function of drying time, n_0 the refractive index of the gas phase ($n_0=1$) and Δ is the optical path difference. With Snell's law (eq. 2.2), equation 2.1 and the law of Pythagoras the optical path difference can be expressed as follows

$$\sin \alpha \cdot n_0 = \sin \alpha' \cdot n_1 \quad 2.2$$

$$(\overline{AB}) = (\overline{BC}) = \frac{d}{\cos \alpha'} \quad 2.3$$

$$(\overline{AD}) = \sin \alpha \cdot (\overline{AC})$$

$$(\overline{AC}) = 2d \cdot \tan \alpha'$$

$$\Delta = 2n_1 \cdot d \cdot \cos \alpha' \quad 2.4$$

with d as the film thickness, α as the angle of incidence and α' as the angle of the refracted beam. Since α' changes in the drying process due to a continuously increasing refractive index n_1 caused by the evaporation of the optically lower dense solvent, it is more feasible to replace α' with an expression of the constant angle α . With Snell's law and the assumption of an ambient refractive index $n_0=1$ we can derive

$$\cos \alpha' = \sqrt{1 - \left(\frac{n_0}{n_1}\right)^2 \sin^2 \alpha} = \sqrt{1 - \left(\frac{1}{n_1}\right)^2 \sin^2 \alpha} \quad 2.5$$

As a function of the film refractive index n_1 we subsequently receive for the optical path difference

$$\Delta = 2d \sqrt{n_1^2 - \sin^2 \alpha} \quad 2.6$$

Herein the refractive index of the film n_1 is a function of drying time. The refractive index can be expressed as a mixture of the blended components according to their volume fractions φ_i [138]

$$n_1 = \sum_{i=1}^K \varphi_i \cdot n_i \quad 2.7$$

The solution is treated as a mixture of one or more solvents and the solid compounds. Solid fractions of the cast solutions are commonly below 5 wt.%. In the course of further drying we also apply equation 2.7 for the calculation of blend refractive index. With the volume fractions φ of each component we can calculate the overall film refractive index in relation to the film thickness

$$\varphi_l = \frac{V_l}{V_l + V_s} = \frac{d - d_{dry}}{d} \quad 2.8$$

$$\varphi_s = \frac{d_{dry}}{d} \quad 2.9$$

with V as the volume of each component (l for the summarized liquid and s for the summarized solid components in the film), d_{dry} as the dry film thickness and the film thickness d , which is the parameter we want to measure against drying time.

Repeating instants of constructive and destructive interference are determined out of high and low extreme values of the detector voltage signal. Interference conditions occur for

$$\Delta = \frac{k}{2} \cdot \lambda \quad 2.10$$

with the values [1, 2, 3, ...] for k and λ as the laser wavelength. Destructive interference (dark – low photovoltage) occurs at odd values for k and constructive interference (bright – high photovoltage) at even values. Inserted in the equation of optical path difference (eq. 2.6) we receive a quadratic equation

$$0 = \underbrace{[n_l^2 - \sin^2 \alpha]}_A \cdot d^2 + \underbrace{[2d_{dry} n_l (n_s - n_l)]}_B \cdot d + \underbrace{\left[d_{dry}^2 (n_s - n_l)^2 - \frac{k^2 \cdot \lambda^2}{4} \right]}_C \quad 2.11$$

$$d = \frac{-B \pm \sqrt{B^2 - 4AC}}{2A} \quad 2.12$$

For all material combinations used in this work the addition of the root term gave reasonable results in contrast to the subtraction. Neglecting excess volume of the mixture, we can calculate the solvent mass fraction x_l and solvent content X_l (capital letter) for a single solvent out of the thickness evolution during film drying as follows

$$x_l = \left(1 + \frac{d_{dry}}{d - d_{dry}} \cdot \frac{\rho_s}{\rho_l} \right)^{-1} \quad 2.13$$

$$X_l = \frac{d - d_{dry}}{d_{dry}} \cdot \frac{\rho_l}{\rho_s} \quad 2.14$$

where ρ is the density of s the solid and l the solvent.

2.2.2 Experimental approach and data analysis

For the measurement of the drying kinetics a 3 wt-% solution of a P3HT ($M_w \approx 43$ kg/mol, Rieke Metals) and PCBM (Solenne) blend (1:1 by wt.) in 1,2-dichlorobenzene (DCB) was deposited in front of the coating knife (Figure 2.1a). Subsequently a wet film was cast evenly underneath the knife with a gap of 70 μm to the substrate and a constant knife speed of 5 mm/s. Afterwards, the film dried at a previously adjusted temperature (15-40°C) and drying gas velocity (0.1-0.65 m/s). To monitor the drying kinetics in situ, laser light (635 nm) was reflected under an incident angle of 30° and detected by a Si photodiode during coating and the following drying period. Laser and photodiode were mounted at the channel cover. At the air/film interface reflected light interfered with light that was reflected at the film/substrate interface. To achieve high optical contrast between the wet film and the substrate, silicon substrates with about 2-4 nm silicon oxide on top were used. The 60×35 mm² silicon substrates were cleaned by sonication in acetone and isopropanol followed by an oxygen plasma treatment for 120 s at 160 W

(Pico, Diener electronic) in order to achieve reproducible and homogeneous solution spreading.

The drying gas (nitrogen) and the substrate holder were liquid temperature-controlled with a Lauda RC6 cryostat. The channel wall was temperature-controlled by electrical heating (turned off at 15°C conditions). The gas flow speed of the drying gas was measured in front of the substrate holder by a hot-wire anemometer which was removed after the adjustment.

For interference analysis, the composition-dependent refractive index of the polymer-fullerene-solution was determined from concentration series using a Kernchen refractometer at 589 nm. According to Ng et al. [124] the refractive index of P3HT:PCBM films does not change significantly from 589 nm (refractometer wave length) to 635 nm (reflectometer wave length). The density of polymer-fullerene-solutions was obtained by determining the liquid density of concentrations series with an Anton Paar DMA 4500 density meter.

The steps of the drying experiments accomplished in the drying channel are illustrated in Figure 2.3. Laser light is reflected on the bare substrate before coating and detected by a Si photo diode. The light is scattered by the coating knife during coating and subsequently reflected at the wet film interfaces directly after coating. Figure 2.3d shows the photovoltage a) before and b) during solution casting where the coating knife crosses the laser beam followed by c) the drying process.

2 Drying kinetics of thin films

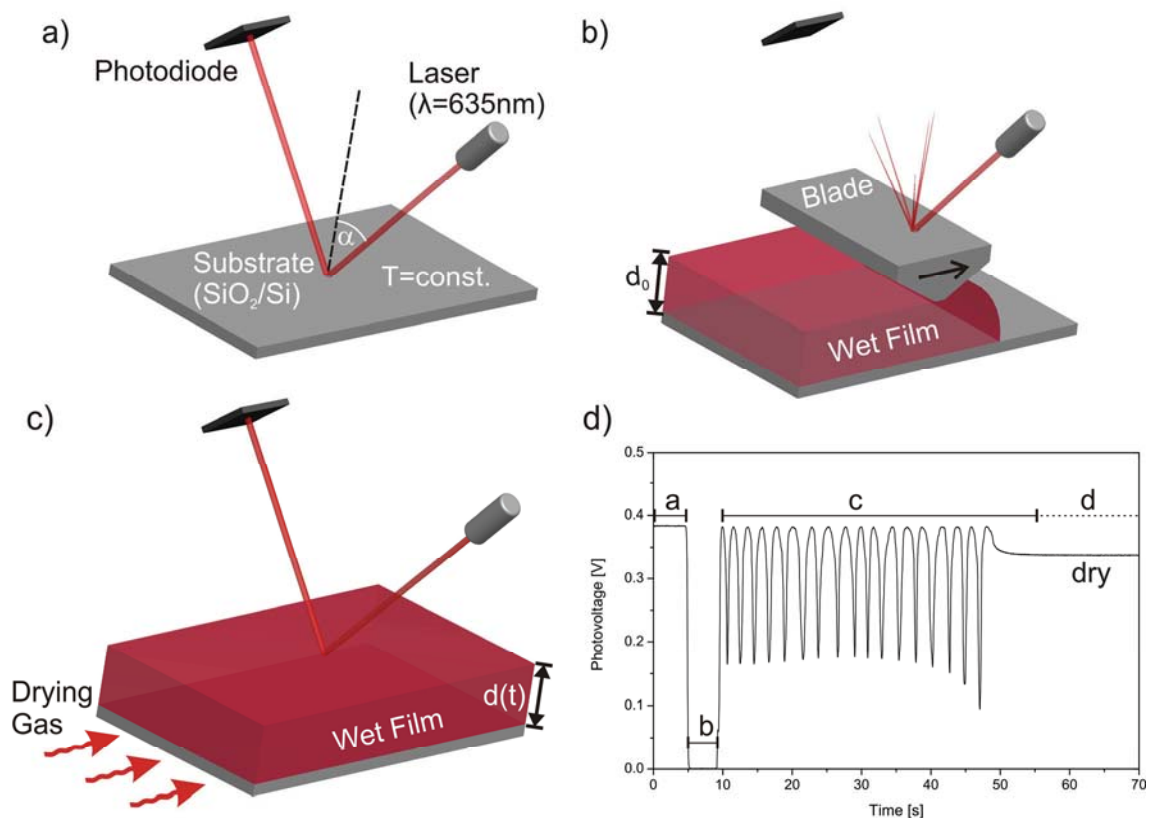


Figure 2.3: Experimental process scheme of the reflectometer/knife coater unit with a) the blank SiO₂/Si substrate, b) the coating step and c) the drying process. d) Photovoltage during the three processing steps as shown in a)-c) with the measurement of the shrinking film instantly after solution casting and d) the dry film. [56]

During drying, the detector voltage (Figure 2.3d) exhibits a series of peaks related to constructive and destructive interference conditions of the reflected light as the film thickness decreases. When the photovoltage remains constant, the optical properties are settled and the film is declared to be dry.

Figure 2.4 shows the photovoltage evolution during the drying experiments for the films dried at different conditions. Especially the interference curves at 15 and 25°C drying temperature exhibit a long final drying phase with decreased drying speed after the last interference peak (Figure 2.4 a-d). Changes in the amplitude of the interference curves of Figure 2.4 are reproducible for each drying conditions. Jukes and Heriot et al. have demonstrated that distinct effects in the interference fringe appearance can correspond to phase separation processes [126, 127], which do not appear in the measurements at drying P3HT:PCBM films. The dry film thickness increases in our

2.2 In situ measurement of drying kinetics

experiments with decreasing temperature but constant knife coating conditions. This is due to an increasing viscosity by decreasing temperature causing a thicker wet film during coating, which additionally increases drying time.

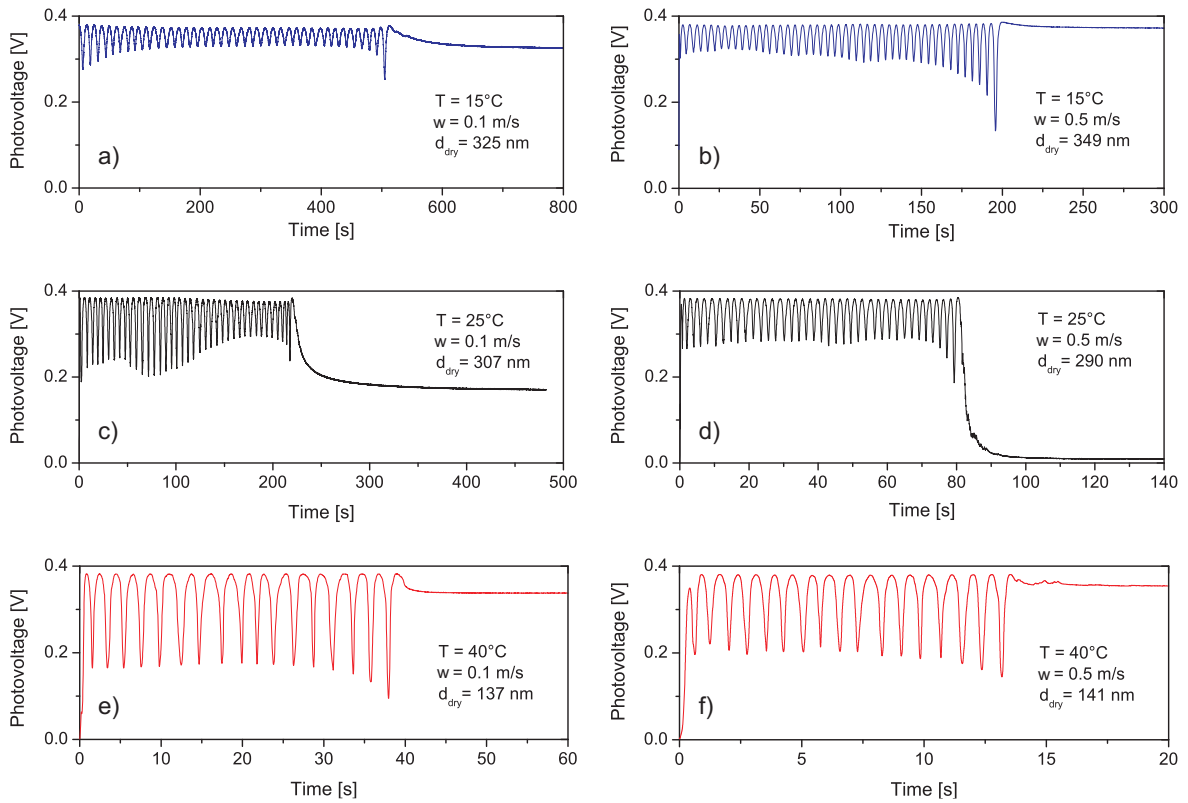


Figure 2.4: Photovoltage versus time showing interferences during drying. a) and b) show two drying experiments at 15°C and 0.1 m/s air speed in front of the substrate carrier (left) and 0.5 m/s (right). c) and d) show drying experiments at 25°C and same gas flow rates and e) and f) at 40°C. The dry thicknesses are mentioned in the graphs. [56]

As discussed in section 2.2.1 the film thickness related to each instant of constructive or destructive interference condition can be calculated, if the dry film thickness and the refractive index of the pure components are known. After determining the dry film thickness with a surface profiler (Dektak 6M, Veeco), we deduce the position of maxima and minima in order to determine the evolution of film thickness using the standard interference condition eq. 2.6. In contrast to prior work of Jukes and Heriot et al. [126, 127], who measured the film shrinkage during spin coating of polymer blends, we do not spin off the solution. This advantage of knife coating affords mass balancing and a calculation of the refractive index, angle of refraction and density during drying by using the values given in Table 2.1.

2 Drying kinetics of thin films

Table 2.1: Material properties of the used 1:1 blend of P3HT:PCBM and the solvent 1,2-dichlorobenzene given at 25°C, since temperature dependency was not significant from 15°C to 40°C. The refractive indices are given at 589 nm. [56]

Material Property	Unit	15°C	25°C	40°C
Density P3HT:PCBM	[g/cm]		1.222	
Density DCB	[g/cm ³]		1.302	
$n_{\text{P3HT:PCBM}}$	[-]	1.866	1.849	1.827
n_{DCB}	[-]	1.554	1.549	1.541
Vapor pressure DCB	[mbar]	1.58	2.79	6.14

Based on the known dry film thickness and material properties, the drying process can be reconstructed. The transient film composition during drying, i.e. the drying curve, can be calculated from the thickness difference between the dry film and the current film height as calculated with the interference conditions. For the analysis it is assumed that the volumes (or heights) of dry film and solvent can be summed up. Excess volume is neglected. Therefore, the thickness development during drying can be calculated as depicted in Figure 2.5b. This is done in a self-written Matlab routine [139].

The representative drying curve in Figure 2.5 shows a linearly decreasing thickness over the first drying period which is called “constant rate period” followed by a second slower drying period called “falling rate period”. The thickness evolution during the falling rate period cannot be resolved by this experimental setup due to the limited resolutions.

The thickness evolution over drying time is calculated into the evolution of solvent mass fraction $x_{\text{DCB}} = m_{\text{DCB}} / (m_{\text{DCB}} + m_{\text{solid}})$. With common density mixing rules and the pure component densities depicted in Table 2.1 the evolution of solvent mass fraction is calculated based on the experimental data as shown in Figure 2.5c. Because of the low solid content, the solvent mass fraction x_{DCB} initially decreases slowly until the solid content becomes significant. Subsequently, this leads to a fast drop of the solvent fraction at the end of the constant rate period. The shifted point at $x_{\text{DCB}} = 0$ indicates the dry state where the photovoltage remains constant.

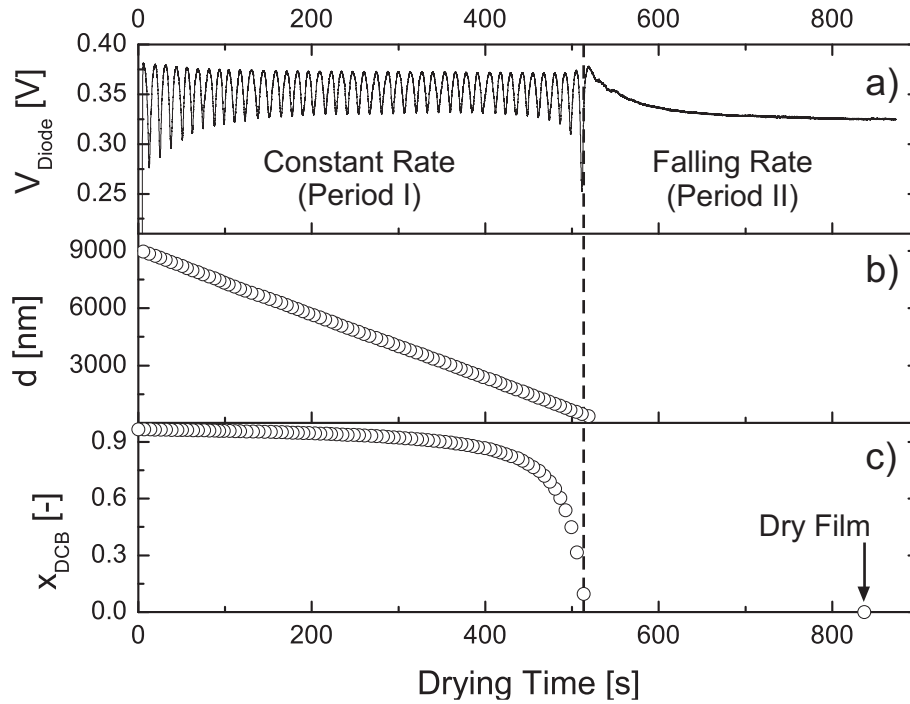


Figure 2.5: a) Voltage of the reflectometer photo diode against drying time at 15°C and $v=0.1$ m/s. The range of constant rate and falling rate period of drying are indicated. b) Thickness and c) solvent mass fraction evolution over drying time. The film is declared to be dry when the photovoltage remains constant.

The analysis of experimental data leads to an average initial solvent mass fraction of $x_{0,\text{DCB}} = 96.74 \pm 0.12$ wt-%, whereas the initial solution was prepared with a solvent mass fraction of about $x_{0,\text{DCB}} = 97$ wt-%, indicating a high accuracy of the interference analysis method. Within the scope of this thesis, the diffusional limitation of solvent mass transport in the film, which is responsible for the transition from constant to falling rate period, is not incorporated into the drying model. The reflectometry setup cannot resolve the low thickness changes, since the thickness change between two interference conditions is about 100 nm. In principal spectroscopic ellipsometry can resolve such low thickness changes in real time (see appendix section A 1.4 and [57]) but requires the modeling of the complex refractive index of the thin film. However, the time period of this final drying stage can be estimated by the subsequent period after the last interference peak (Figure 2.5a) until the photovoltage V_{diode} remains constant. This is the case when the optical properties of the film (thickness and refractive index) are settled. Experimental data, e.g., Figure 2.5b-c indicates, that film drying proceeds with an

almost constant evaporation rate up to solvent mass fractions of about 10 wt.%.

Further reduction of the solvent mass fraction reduces solvent mobility and consequently the solvent diffusion coefficient in the swollen polymer-fullerene matrix. Additionally, organic semiconductors are commonly rigid semicrystalline materials that comprise glass transition temperatures above room temperature [140-142]. Due to the evaporation of plasticizing solvent the film can cross the glass transition during drying at temperatures close to room temperature. This can complicate the description of the diffusional mass transport but is not necessarily the case. For P3HT glass transition temperatures, which depend on the molecular weight and the fabrication history, have been reported in the range from -14 to 110°C [140, 142-147]. However, diffusional limitations and glass transition effects on the drying behavior are not the scope of this work and therefore not considered in this thesis.

2.2.3 Spatially resolved measurements

As explained in the previous chapter we are now capable of measuring the film shrinkage at a distinct position of the much larger wet film. The applied horizontal forced convection causes a faster drying at the upstream edge of the substrate for the investigated solutions. This will be explained in more detail below (see Figure 2.12). This effect leads to an inhomogeneous drying which can be observed by a moving drying front as shown in Figure 2.6. The dashed line in Figure 2.6a indicates the drying front at different stages of the drying process of a P3HT:PCBM film at a silicon substrate. The interference colors reveal a steeper thickness gradient in the beginning. In order to describe the drying kinetics of such knife coated thin films this effect must be considered and quantitatively investigated. Therefore multiple measurement spots in a linear ordered array of 5 reflectometers (Figure 2.1) were used for spatial resolved drying kinetics measurements.

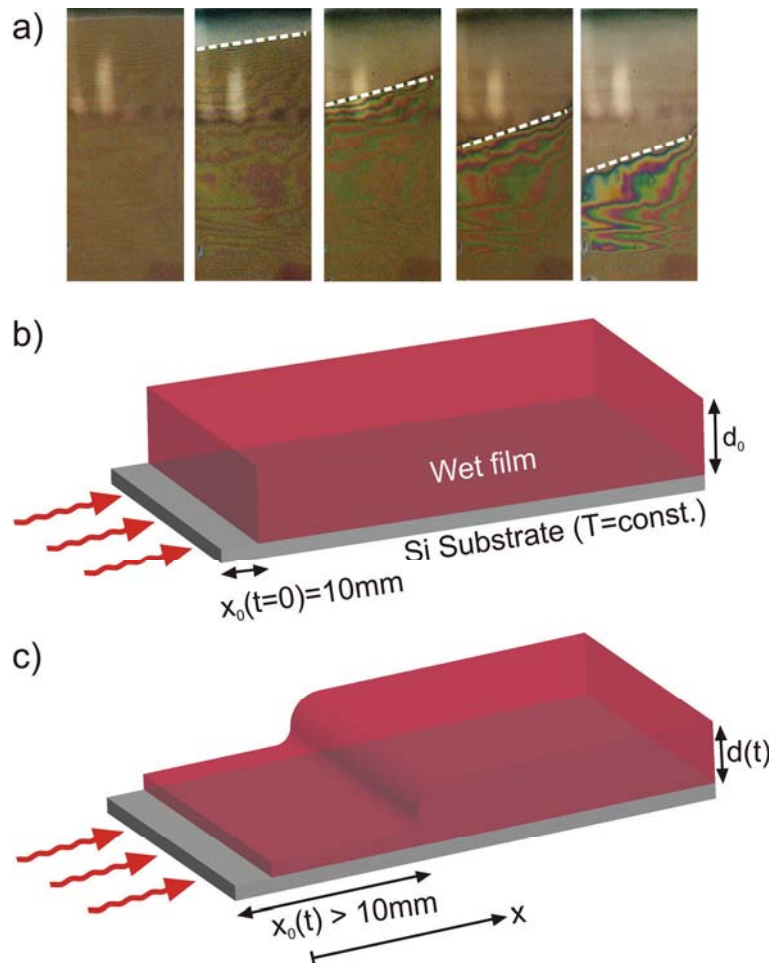


Figure 2.6: a) Photographs of the moving drying front in the opened channel. Gas flow direction is from top to bottom of the images. b) Scheme of the process conditions for film drying with uncoated offset x_0 at the beginning and c) increasing offset due to the moving drying front. [135]

First of all, the drying characteristics of a single local reflectometry measurement are discussed in more detail. The drying curve exemplarily depicted in Figure 2.7a was locally measured by reflectometry in the centered position of the plate. The shrinkage seems to remain linear until it accelerates (increasing negative slope) in the final stage of film drying. Figure 2.7b depicts the slope of the drying curve given in Figure 2.7a which decreases from the beginning on and drops rapidly at the final stage of drying. The reason for this behavior is the moving drying front due to a faster drying at the upstream edge of the plate which is shown in Figure 2.6. As this drying front approaches the spot of local measurement, the drying process accelerates which shall be explained in the following.

2 Drying kinetics of thin films

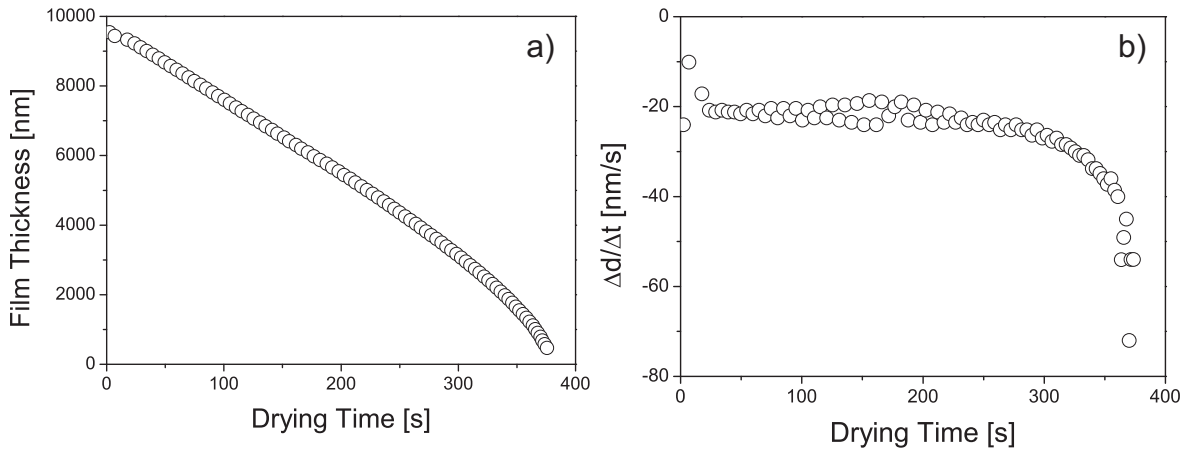


Figure 2.7: a) Measurement of the film shrinkage during drying of a P3HT:PCBM solution in DCB at $x_s=3$ wt.%, 20°C and 0.3 m/s gas flow speed. b) The slope of the film shrinkage is averaged in-between two data points and plotted against drying time. [135]

The film was cast at the substrate with a distinct off-set x_0 to the front edge of the substrate for practical reasons. The hydrodynamic boundary layer starts to form at the front edge of the substrate carrier. In contrast to the hydrodynamic boundary layer the concentration boundary layer starts to form at the front edge of the wet film after the offset distance x_0 (Figure 2.8). The mass transfer coefficient decreases from the beginning of the concentration boundary layer ($x = x_0$) in airflow direction x . This is due to an increasing boundary layer thickness with x and consequently a less steep concentration gradient as driving force for the solvent evaporation in downstream direction of the wet film.

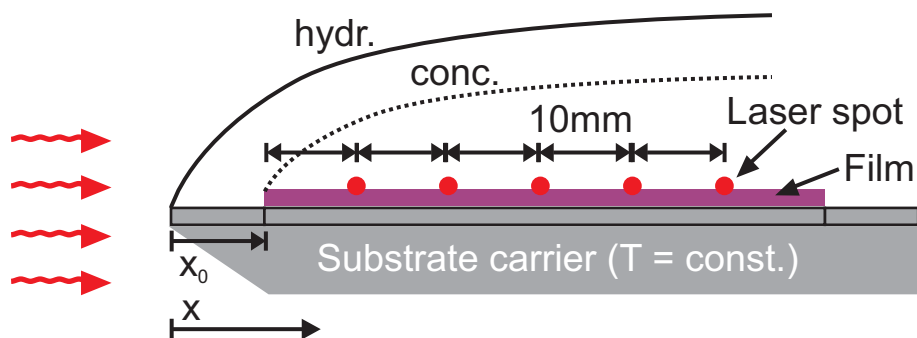


Figure 2.8: Position of the film at the stage and the laser spots for thickness measurement. Each scale bar represents 10mm. [135]

However, the position of the drying front is not static. Since the concentration boundary layer starts to form at the position of the front, the movement towards a measurement spot causes a local acceleration of evaporation rate/film shrinkage as the front approaches. The effect of the moving drying front was quantitatively investigated by spatially resolved drying kinetics measurements at five positions simultaneously (Figure 2.8). For a comparison with model calculations mass transfer coefficients must be obtained from the experimental data.

The used low volatile solvents the solvent vapor diffusion in the gas phase governs the mass transfer after the liquid-vapor phase transition in the constant rate period. For this case (low partial pressure and low mass flux of the evaporating component) a linear gas phase mass transfer kinetic (eq. 2.21) is appropriate and the isothermal solvent evaporation out of the drying thin film (thickness $< 10 \mu\text{m}$) can be described as

$$\frac{dn_i}{dt} = -\dot{n}_i \quad \text{component balance} \quad 2.15$$

$$\dot{n}_i = \beta_{i,g} \cdot \tilde{\rho}_g (\tilde{y}_{i,ph} - \tilde{y}_{i,\infty}) \quad \text{mass transfer kinetics} \quad 2.16$$

$$\frac{dn_i}{dt} = \tilde{\rho}_{l,i} \cdot \frac{dd}{dt} \quad 2.17$$

with \dot{n}_i as molar mass flux of component i , β_{ij} as mass transfer coefficient of component i in j , $\tilde{\rho}_g$ as molar gas density, $\tilde{\rho}_{l,i}$ as the liquid density of component i , $\tilde{y}_{i,\infty}$ and $\tilde{y}_{i,ph}$ as the molar fraction of component i in the bulk and at the phase interface respectively and d as film thickness. The mass transfer coefficient β_g can be determined from the slope of the evolution of film thickness over drying time for each measuring position. The slope of film shrinkage over time dd/dt can be discretized into appropriate intervals, i.e. two subsequent interference conditions. Based on the time resolved thickness measurements the local mass transfer coefficient can be determined as

$$\beta_{i,g} = \frac{\tilde{\rho}_{l,i} \cdot \frac{\Delta d}{\Delta t} \cdot R \cdot T}{p_i} \quad 2.18$$

2 Drying kinetics of thin films

with p_i as partial pressure of component i , R as ideal gas constant and T as absolute temperature. In Figure 2.9a the evolution of the normalized film thickness¹ is depicted for 5 different positions in airflow direction. It gets clear that the overall drying time increases in gas flow direction because of the increasing boundary layer thickness in gas flow direction. Furthermore, the drying curve at each position accelerates with proceeding drying time, which is due to the approaching drying front. This is more quantitatively depicted in the evolution of the slope of film shrinkage over time in Figure 2.9b.

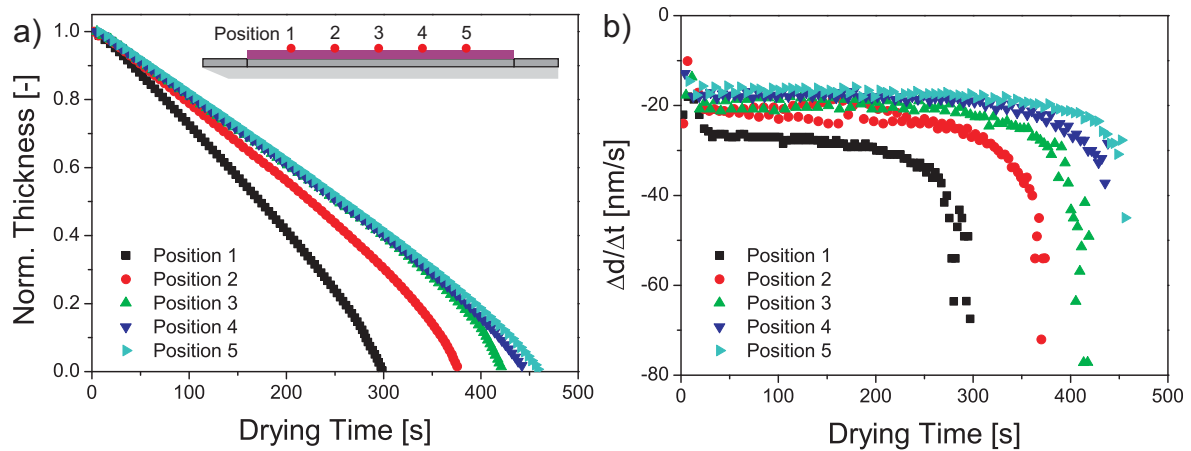


Figure 2.9: a) Evolution of normalized thickness during film drying of P3HT:PCBM solution in DCB at $x_s=3$ wt.%, 20°C and 0.4 m/s airflow compared for 5 different measurement positions. The corresponding slope of the film shrinkage of these 5 different positions is plotted in b). [135] Here $x_0 = 10$ mm and further positions are according to Figure 2.8.

The slope of film shrinkage $\Delta d/\Delta t$ initially decreases due to the coating knife which disturbs the fluid dynamics at the beginning (first few data points). After this phase the next 10 data points of the slope are averaged and used for the determination of the initial local mass transfer coefficient (at each laser position) as shown in equation (2.18). In this range the initial coating offset x_0 is almost constant. The experimentally derived local mass transfer

¹ Normalized film thickness = $(d(t)-d_{dry})/(d_{wet}-d_{dry})$. Film thickness is not perfectly constant over the substrate which requires a normalized presentation of the data for an improved readability.

coefficients are compared in section 2.4 with those of model calculations that will be derived in the following section.

2.3 Model of mass transfer for thin film drying

In order to calculate the drying kinetics an appropriate model, which should be sufficiently accurate for describing the real film drying behavior must be developed. In general, one must consider i) the mass transfer of solvent within the film, ii) the liquid-vapor phase change at the film surface and iii) the mass transport of solvent in the gas phase.

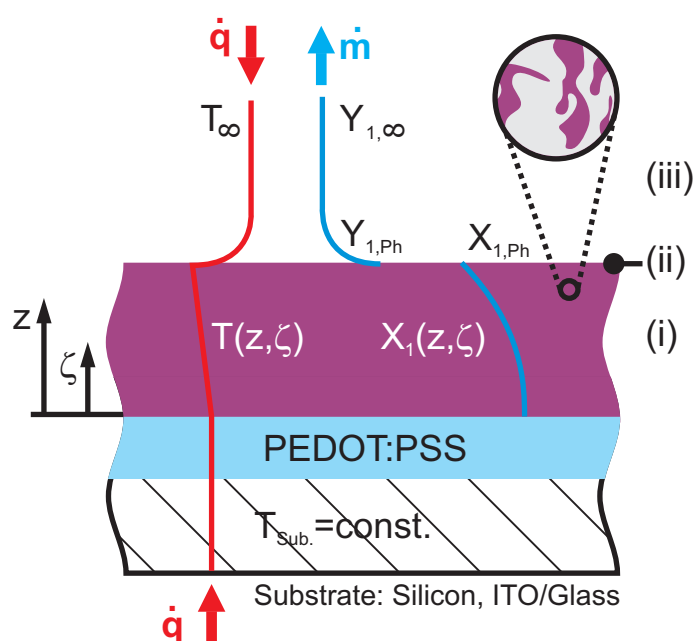


Figure 2.10: Scheme of all possible gradients of temperature and concentration during polymer-fullerene film drying with mass transfer limitation in the film i) and the gas phase iii). The vapor-liquid phase interface is denoted as ii).

Figure 2.10 depicts schematically a case where all the mentioned factors including temperature gradients are taken into account. In the case of this work isothermal conditions could be realized due to very low film thicknesses ($<10 \mu\text{m}$), highly heat conducting silicon substrates ($600 \mu\text{m}$ thin) and accurately temperature controlled drying conditions in the experimental setup (see chapter 2.2). Furthermore most of the used solvents exhibit a low vapor pressure, causing very slow consumption of vaporization enthalpy. In the following, the chosen model will be elaborated in detail.

2.3.1 Mass transfer in the gas phase

The mass transfer in the gas phase can be described with the Stefan-Maxwell equation 2.19 [148]. The approach after Josef Stefan and James Maxwell is based on a molecular friction and collision theory.

$$\frac{d\tilde{c}_i}{dz} = \tilde{\rho}_g \frac{d\tilde{y}_i}{dz} = \sum_{j=1}^n \frac{1}{D_{ij}} (\tilde{y}_i \cdot \dot{n}_j - \tilde{y}_j \cdot \dot{n}_i) \quad 2.19$$

with n as the number of components, \tilde{c}_i as the concentration of component i , z as length coordinate in mass transfer direction and D_{ij} as Stefan-Maxwell diffusion coefficient. For binary systems ($n = 2$) with unidirectional mass transfer equation 2.19 can be solved exactly [149] leading to the following expression for the area-related mass flux of species i

$$\dot{n}_i = \underbrace{-D_{12} \cdot \tilde{\rho}_g \frac{d\tilde{y}_1}{dz}}_{diffusion} + \underbrace{\tilde{y}_1 \cdot \dot{n}}_{convection} \quad 2.20$$

with \dot{n} as the overall mass flux. For low molar fractions in the gas phase of species i or low overall mass flux the convection term in equation 2.20 can be neglected leading to the linear expression for the area related mass flux

$$\dot{n}_i = \beta_{ij} \cdot \tilde{\rho}_g \cdot (\tilde{y}_{i,Ph} - \tilde{y}_{i,\infty}), \quad \beta_{ij} = \frac{D_{ij}}{\delta_{conc}} \quad 2.21$$

with δ_{conc} as the concentration boundary layer thickness. More general is the following expression 2.22 also appropriate for high molar fractions in the gas phase and high overall mass flux as it occurs for drying of highly volatile solvents at comparatively high temperatures close to the boiling point.

$$\dot{n}_i = \beta_{ij} \cdot \tilde{\rho}_g \cdot \ln \frac{1 - \tilde{y}_{i,\infty}}{1 - \tilde{y}_{i,Ph}} \quad 2.22$$

Equation 2.22 can also be used for simultaneously evaporating solvent mixtures under the assumption that the gas phase diffusion of one solvent is unaffected by the diffusion of the other solvents. Gas phase diffusion coefficients D_{ij} are calculated by the group contribution method after Fuller et al. [150].

2.3 Model of mass transfer for thin film drying

For the determination of the mass transfer coefficient β_{ig} (in the drying context component j usually represents the gas phase denoted with the index g) Sherwood correlations in the form $Sh = f(Re, Sc, geometry)$ are used. In our case we use the case of a horizontal plate in a horizontal forced convection flow. As depicted in Figure 2.11 the hydrodynamic boundary layer thickness δ increases with the length coordinate x in airflow direction. Likewise increases the concentration boundary layer $\delta_{conc.}(x)$ of the evaporating constituents.

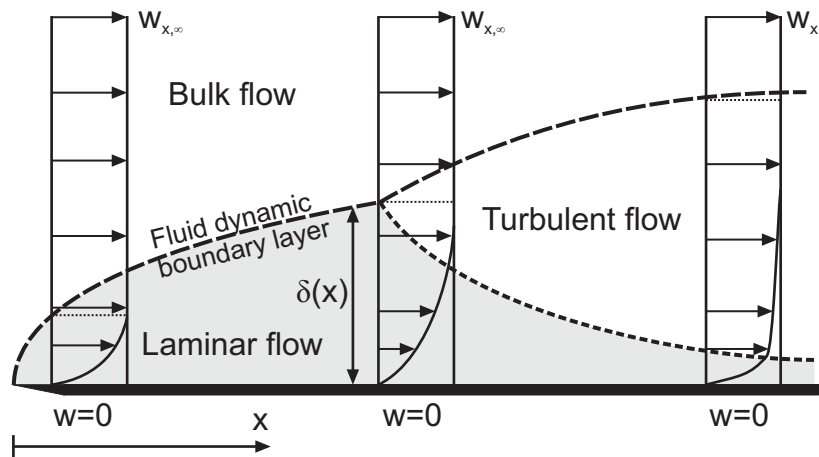


Figure 2.11: Dependency of velocity profile w and boundary layer thickness $\delta(x)$ on plate length coordinate x . [151]

Mass transfer in the gas phase is governed by the concentration gradient, which decreases with increasing concentration boundary layer thickness $\delta_{conc.}(x)$. The concentration boundary layer forms analog to the fluid dynamic boundary layer $\delta(x)$ at the beginning of the wet film area in airflow direction. Hence, the driving force for mass transfer in the gas phase decreases with the length coordinate x in the case of uniform interface conditions at the entire plate surface (equally distributed molar solvent fraction at the interface). This demands the application of a local Sherwood number Sh_x leading to a local mass transfer coefficient $\beta_{g,x}$.

$$Sh_x = \frac{\beta_{g,x} \cdot x}{D_{ij}} = 0.332 \cdot Sc^{1/3} \cdot Re_x^{1/2} \quad 2.23$$

with $Sc = \frac{\nu}{D}$ Schmidt number

2 Drying kinetics of thin films

$$Re_x = \frac{w \cdot x}{\nu} \quad \text{Reynolds number}$$

with ν as the kinematic viscosity. For the integrated mass transfer of the entire plate surface length L we receive

$$\beta_g = \frac{1}{\Delta L} \int_{L_0}^{L_1} \beta_{g,x} dx \quad 2.24$$

$$Sh = \frac{\beta_g \cdot L}{D_{ij}} = 0.664 \cdot Sc^{1/3} \cdot Re^{1/2} \quad 2.25$$

Figure 2.12 depicts both, the local mass transfer coefficient $\beta_{g,x}$ as a function of plate length coordinate and the integrated coefficient β_g . The experimental setup in this work comprises a plate of 77 mm length. Mathematically the local mass transfer coefficient $\beta_{g,x}$ exhibits a singularity at the front edge of the plate ($x = 0$ mm). It decreases dramatically over the first few millimeters and exhibits a moderate decrease up to the downstream end of the plate for the classical boundary layer theory of infinite long plates. Fluid dynamic effects at the downstream end of the plate ($x = L$) can cause a further increase of mass transfer at the end of the plate. This topic is discussed in references [152, 153], but is not taken into account within this work.

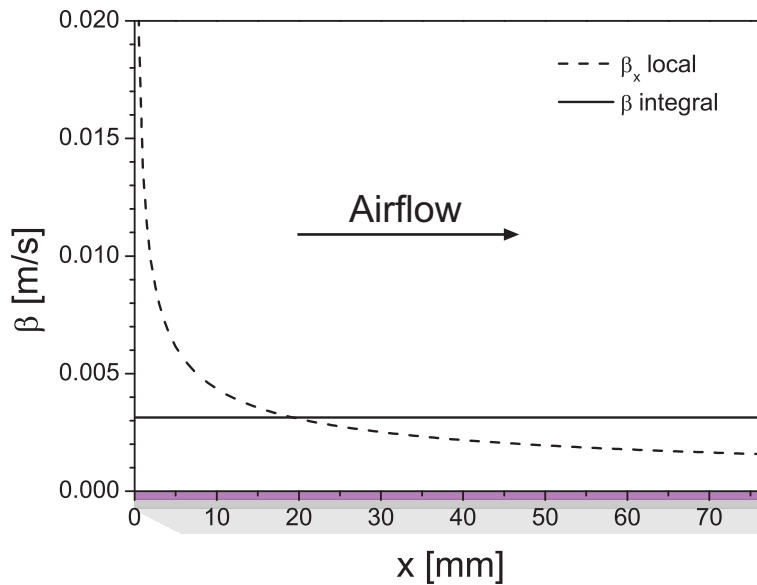


Figure 2.12: Local and integral mass transfer coefficient at 20°C, $w=0.3$ m/s, $L=77$ mm.

In contrast to Figure 2.12 we cannot apply a wet film up to the front edge of the substrate at $x = 0$. Therefore we have to take the initially uncoated off-set distance x_0 into account (Figure 2.8), which does not contribute to the formation of the concentration boundary layer (equation 2.26). This initial off-set is due to practical reasons of the knife coating process. In heat transfer, this off-set topic is discussed by Brauer et al. [154] and Ameel et al. [155, 156]. In analogy to heat transfer, the Sherwood correlation 2.23 must be formed with the offset distance x_0 and the length coordinate x

$$Sh_{x,ext} = \frac{0.332 \cdot Sc^{1/3} \cdot Re_x^{1/2}}{\left[1 - \left(\frac{x_0}{x}\right)^{3/4}\right]^{1/3}} \quad 2.26$$

Furthermore, the profile of the local mass transfer coefficient in Figure 2.12 results in an increased solvent evaporation rate at the front of the wet film. Accordingly, the film dries faster at the front with a decreasing drying rate with the length coordinate x . This effect causes inhomogeneous drying with a moving drying front as observed by Scharfer et al. [157]. Therefore the increasing offset distance $x_0(t)$ during film drying must be considered for the numerical simulation of the drying process.

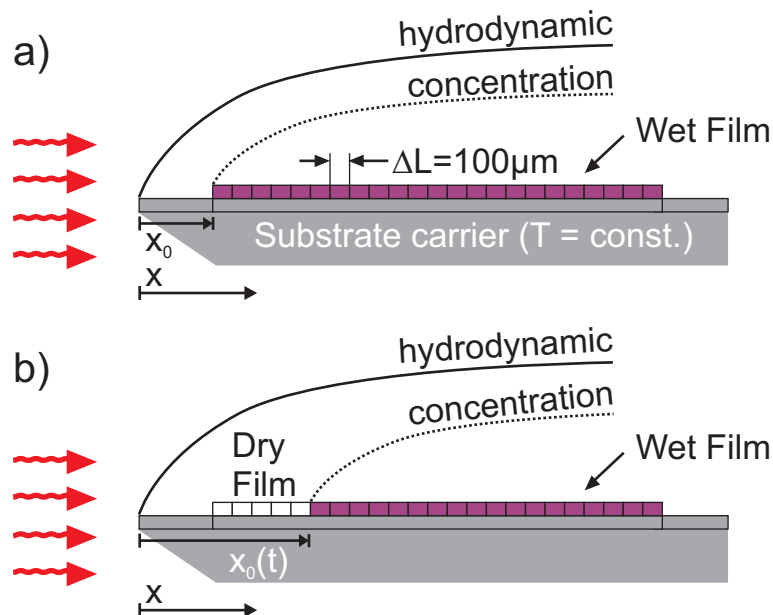


Figure 2.13: a) Scheme of the in $100 \mu\text{m}$ slices discretized wet film cast with an initial off-set length x_0 . b) Effect of moving drying front that leads to an increase of x_0 and a moving concentration boundary layer.

Hence, the gas phase mass transfer coefficient must be formed as a function of space and time. This is done as illustrated in Figure 2.13 with a discretization of the wet film into slices of 100 μm width cast with an initial off-set length x_0 . Under these preconditions the gas phase mass transfer is calculated for a distinct period of time with equation 2.26. The faster drying rates at the wet film front results in a dry film at the very beginning after a distinct drying time. If this is the case, this dry film length does not contribute to the formation of the concentration boundary layer anymore. The film is declared to be dry, at solvent fractions below 0.001. Hence the off-set length $x_0(t)$ is increased about this dry film length.

2.3.2 Phase equilibrium at the gas-liquid interface

To describe the solvent evaporation at the phase interface, ii) in Figure 2.10, the vapor-liquid phase equilibrium of absorbed solvent in the polymer-fullerene matrix is needed for considering non-ideal vapor pressure of the mixture. Solvent-polymer-fullerene interaction forces can cause non ideal phase equilibrium states with increased (repulsive forces) or reduced (attractive forces) vapor pressure in comparison to the pure solvent. In general this can be described for moderate absolute pressures below about 10 bar and ideal gas phase behavior after the law of Raoult-Dalton

$$\tilde{y}_i \cdot p = \tilde{x}_i \cdot \gamma_i \cdot p_i^* \quad 2.27$$

where p_i^* is the pure component vapor pressure. The product of the molar fraction of the volatile component i in solution and the activity coefficient is known as the activity of component i which correlates the real partial pressure with the pure component vapor pressure.

$$a_i = \tilde{x}_i \cdot \gamma_i = \frac{p_i}{p_i^*} \quad 2.28$$

In the case of polymer solutions, the Flory-Huggins equation (eq. 2.29) is commonly used for describing the solutions activity. In the scope of this thesis, the vapor-liquid equilibrium was exemplarily determined from sorption experiments of P3HT:PCBM (1:1) films in a Rubotherm magnetic-suspension-balance (MSB) at 40°C sorption temperature with the solvent DCB. This was done analog to the method described in reference [158]. Polymer-fullerene films were mounted in a sorption chamber where the solvent “humidity” (solvent activity) can be adjusted. With increasing activi-

ty, the solvent sorbs into the solid polymer-fullerene-film and the mass gain is gravimetrically monitored with the MSB. In order to get a higher mass signal due to an increased amount of solvent absorption, gravimetric sorption experiments have been accomplished at comparatively thick films (around 20 μm) in contrast to usually 100-200 nm thin films as used in polymer solar cells. These measurements enable correlating the solvent fraction of absorbed solvent in the film with the solvent activity in the gas phase (Figure 2.14).

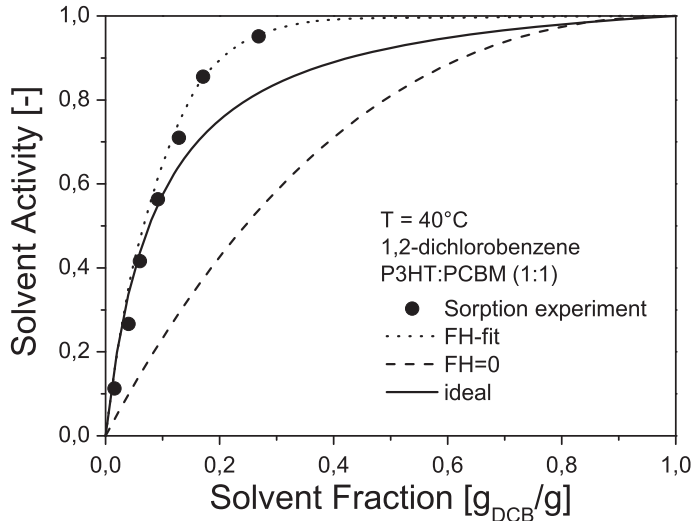


Figure 2.14: Sorption isotherm of DCB and P3HT:PCBM (1:1) measured with a magnetic suspension balance at 40°C. Symbols indicate sorption measurements, the dotted line represents the FH-fit, the dashed line the FH approach with $\chi = 0$ and the solid line as the ideal calculation according to Raoult-Dalton [56].

Flory-Huggins (FH) interaction parameters can be determined in order to describe the in our case reduced vapor pressure at the interface. Therefore the solvent activity is given by (see chapter 3.2.1)

$$\ln a_i = \ln \frac{p_i}{p_i^*(T)} = \ln \varphi_i + \left(1 - \frac{\tilde{v}_i}{\tilde{v}_p}\right) \varphi_p + \chi_{i,p} \cdot \varphi_p^2 \quad 2.29$$

with $\chi_{i,p}$ as the FH-parameter, $\varphi_{i,p}$ as volume fraction (i : solvent, p : solid) and \tilde{v} as specific molar volume ($\tilde{v}_p \gg \tilde{v}_i$). The solid blend is treated as one effective medium. Following, the concentration-dependent FH-parameter (eq. 2.30) can be fitted to the sorption measurements for the material system DCB and the blend of P3HT:PCBM (1:1 by wt.)

$$\chi_{DCB,blend}(\varphi_{DCB}) = 0.8521 \cdot \varphi_{DCB}^2 + 1.804 \cdot \varphi_{DCB} + 1.444 \quad 2.30$$

The definition of the solvent activity a_i leads to the vapor pressure p_i at the interface of absorbed solvent in the polymer-fullerene-matrix. Hence, the molar fraction of solvent at the interface $\tilde{y}_{i,0} = p_i/p$ in equation 2.22 can be calculated based on FH-parameters from equation 2.29. However, sorption experiments are time consuming with measurement times of up to several months for a single sorption isotherm, as it was the case for the above shown data.

If no sorption experiments or FH-parameters are available, one can assume an ideal solid-liquid interaction behavior with $\chi = 0$ (pure entropic contributions) or according to the equation of Raoult Dalton with $\gamma_i = 1$. In the latter case the solvent activity is equal to the molar fraction of solvent and approaches the sorption experiment more accurate as for the case of the neglected enthalpic term in the FH-equation as compared in Figure 2.14. The averaged molecular weight of the P3HT:PCBM blend was 1785g/mol.

The non ideality of solvent mixtures can be estimated with group contribution methods such as UNIFAC (Universal Quasichemical (UNIQUAC) Functional Group Activity Coefficients) [159, 160]. Activity coefficients obtained by this method for the used solvent mixtures can be found in section A 4.5.

2.3.3 Diffusion in the film

Low solid contents at the beginning of the drying process (2-5wt.%) and low dry film thicknesses (<1 μm) that lead to short diffusion paths at higher solid contents diminish the influence of diffusional limitation over a wide range in the drying process (see section A 1.1). An accurate determination of the solvent diffusion coefficient as a function of film composition is challenging for this material system and this range of film thicknesses. Additional effects can originate from the glass transition [140-142] which is crossed in the course of film drying.

2.3.4 Summary of the chosen model

In conclusion, a model with isothermal conditions and full mass transfer limitation in the gas phase was chosen for the drying kinetics calculations in this thesis as depicted in Figure 2.15b. Due to the low film thickness

2.3 Model of mass transfer for thin film drying

(<10 μm) and the low vapor pressure of the used solvents we assume the gas phase mass transfer as the dominating process. Isothermal conditions could be realized due to low film thicknesses, highly heat conducting silicon substrates (600 μm) and accurately temperature controlled drying conditions in the experimental setup (see chapter 2.2). Furthermore most of the used solvents exhibit low vapor pressure, causing low consumption of vaporization enthalpy. The gas phase mass transfer coefficient is assumed to depend on both, time and space.

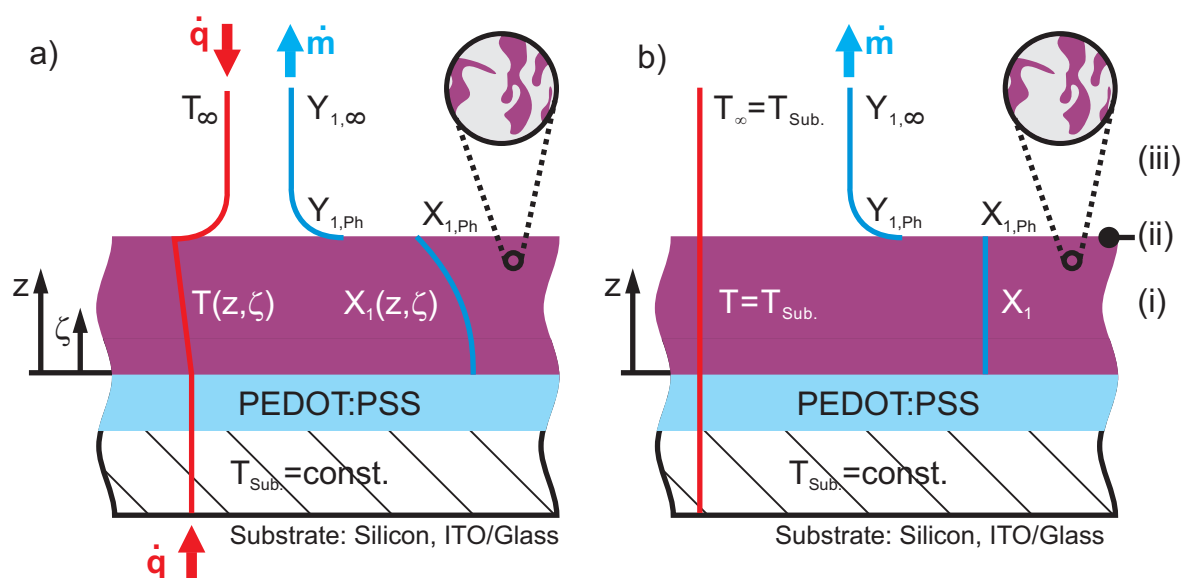


Figure 2.15: a) Scheme of all possible gradients of temperature and concentration during polymer-fullerene film drying with mass transfer limitation in the film i) and the gas phase iii). The phase interface is denoted as ii). b) Scheme of the chosen model with isothermal conditions and full mass transfer limitation in the gas phase.

For the comparison of the drying kinetics model calculations with experimental data, the phase equilibrium is assumed to be ideal in terms of solid-liquid interactions and also in terms of liquid-liquid interactions for the usage of solvent mixtures. The vapor pressure of each component is calculated according to the molar fractions of the incorporated components. The average molecular weight of the fullerene and the weight average molecular weight of the polymer according to size exclusion chromatography was used. For the solvent mixtures no sorption data was available and for consistency in the calculation strategy ideal solution behavior ($\gamma = 1$) was also applied for the single solvent measurements according to Raoult-Dalton. The assumed

simplifications will be evaluated in comparison with experimental data in the following.

2.4 Evaluation of the drying kinetics model

2.4.1 Drying kinetics of a single solvent

For a normalized comparison between the correlation of Brauer et al. (eq. 2.26) and the experimentally determined mass transfer coefficients, the local Sherwood number Sh_x (eq. 2.23) is plotted against the local Reynolds number Re_x for both (Figure 2.16).

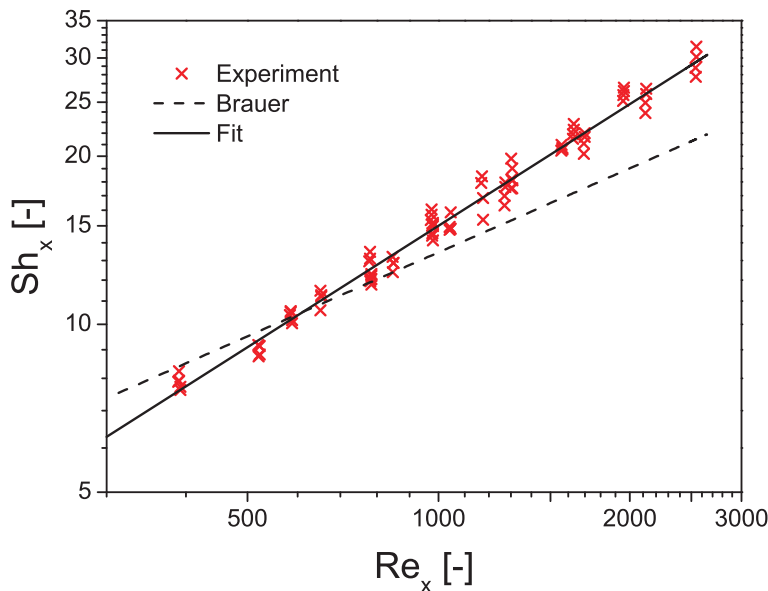


Figure 2.16: The local Sherwood number is plotted for the experimental data against the local Reynolds number for distinct airflow rates (0.3-0.65 m/s) which is compared with the correlation of Brauer et al. and the adapted correlation. [135]

Since the experiments deliver data for the local mass transfer coefficient $\beta_{i,g,x}$ which is converted to the local Sherwood number $Sh_{x,ext}$ (eq. 2.26) including the off-set effects, the experimentally derived $Sh_{x,ext}$ must be multiplied with the denominator of equation 2.26 in order to receive Sh_x . In a log-log plot both relations show linear behavior (Figure 2.16). The slope of the analytically derived correlation deviates from the experimental data but both agree in the linear character. A comparison of both curves allows fitting the correlation with two parameters to the experimental data:

$$Sh_{x,ext}^{fit} = \frac{0.07919 \cdot Sc^{1/3} \cdot Re_x^{0.7234}}{\left[1 - \left(\frac{x_0}{x}\right)^{3/4}\right]^{1/3}} \quad 2.31$$

The fitted exponent of the Reynolds number rather approaches the value of 0.8 for turbulent conditions than the value of 0.5 for laminar flow. This indicates that unexpected turbulent conditions might cause the mismatch with the analytical correlation. In the meantime it could be verified by comparative simulations of the fluid dynamics for this geometry [161] that the chosen 45° angle at the edge of the plate (see Figure 2.1) is responsible for this effect. This can be improved by using a 10° angle at the edge of the plate.

Based on the fitted correlation we can now calculate the mass transfer coefficient and related parameters as a function of the position x and time for this geometry. Figure 2.17a depicts for some exemplary scenarios of x_0 the mass transfer coefficient over the whole plate length. The transition from the steep drop of β at the beginning of the concentration boundary layer to the flat plateau gets broader with an increasing off-set length x_0 .

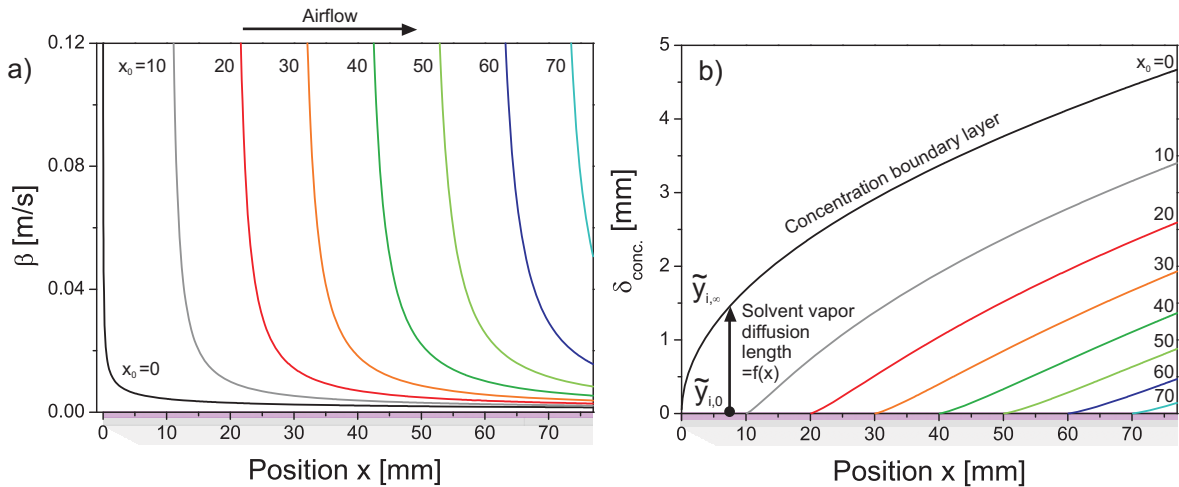


Figure 2.17: a) Mass transfer coefficient of DCB in the gas phase for offset lengths from 0-70mm at $x_s = 3$ wt.%, 20°C and 0.3 m/s airflow. The results are obtained from the fitted correlation. High values for the mass transfer coefficient signifies high solvent evaporation rate close to the edge of the drying front ($x = x_0$). Corresponding concentration boundary layer thicknesses $\delta_{conc.}$ are shown in b). [135]

2 Drying kinetics of thin films

Also the concentration boundary layer grows slower with increasing x as shown in Figure 2.17b for the corresponding cases of x_0 . With increasing concentration boundary layer thickness, the constant solvent vapor concentration gradient, which is the driving force for mass transfer, is getting less steep (lower driving force).

Subsequently a spatial resolved calculation of the film drying process was realized. Therefore the film (60 mm length) was discretized into slices of 100 μm width in airflow direction as illustrated in Figure 2.13. For each slice the mass transfer kinetics and mass balance was calculated for each time step of 0.05 s. Once the first slice reached the solvent mass fraction of $x_{DCB} \leq 0.001$ the contribution to the formation of the concentration boundary layer is assumed to get negligible and the initial off-set is shifted to the next slice and so on.

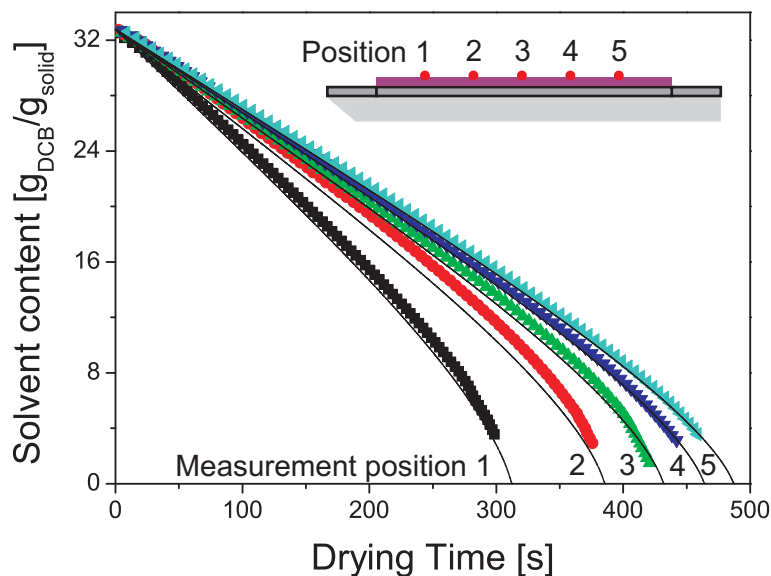


Figure 2.18: Spatial resolved (in airflow direction) film drying of experimental data and the adopted correlation at schematically indicated positions. The initial solvent content (solvent mass/solid mass) is equal for all positions on the wet film. [135] Here $x_0 = 10$ mm and further positions are according to Figure 2.8.

In Figure 2.18 calculations based on equation 2.31 are compared with experimental data for the drying process of a P3HT:PCBM solution in DCB at 3 wt.%, 20°C and a gas flow velocity of 0.4 m/s measured in front of the plate. Both, the increasing drying time with x and the acceleration of drying (increasing negative slope) are reasonably described by the calculations. For

this comparison, it was most practical that all curves originate from the same position in the diagram. Because film thickness is not absolutely constant over the substrate length, the solvent loading ($X_{DCB}=m_{DCB}/m_{solid}$) was chosen as parameter. Furthermore the analysis of the interference conditions was not started at the dry film, but at the freshly cast wet film. At this instant the film composition is known and should be equal at all positions. Uncertainties in the sample preparation and potentially missed interference peaks have the effect, that the dry film state of $X_{DCB}=0$ is not reached. However, this does not affect the fitting quality of the correlation which is adapted to the initial evaporation rate that is independent from absolute values of film thickness. A more comprehensive error discussion of reflectometry can be found in the appendix in section A 1.2.

At this point it should be mentioned that the effect of the moving drying front (decrease of “wet” area where solvent evaporates) must also be taken into account for integral measurements over the whole plate, such as gravimetric experiments. Neglecting this effect leads to tremendous misinterpretation for drying measurements with limitations in the gas phase mass transfer.

2.4.2 Drying kinetics of solvent mixtures

With regard to a large scale production of organic photovoltaics, environmentally friendly solvents should preferably be used. Appropriate solvent combinations of two or more solvents can provide a wider scope of optimized properties, such as solubility, wetting behavior and drying time. The usage of solvent mixtures can furthermore be beneficial for tuning molecular ordering during drying due to specific solubility and solvent-solid interactions which can have been reported to lead to different film structures [55, 162, 163]. In this work we replaced the common solvent 1,2-dichlorobenzene with the solvent mixtures toluene-indane and o-xylene-indane. Indane exhibits a comparable vapor pressure to DCB, is a suitable solvent for P3HT and PCBM and due to its non-halogenated character appropriate for large scale fabrication processes. The wetting properties of the pure solvent can be improved by mixing with toluene or o-xylene. The impact on film structure due to the exchanged solvents is discussed later in chapter 5.2.

2 Drying kinetics of thin films

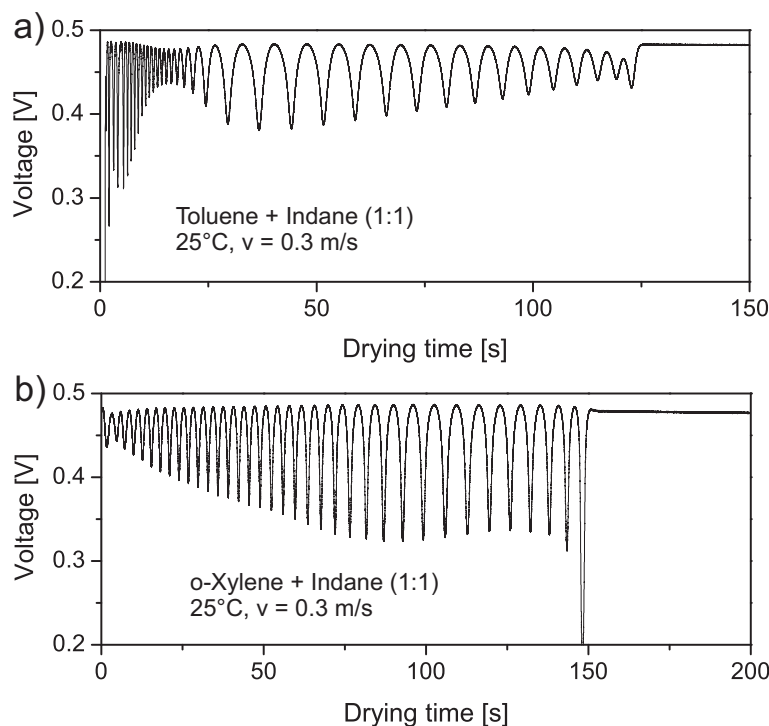


Figure 2.19: Reflectometer raw data at centered position (pos. 3) for the solvent mixture toluene-indane a) and o-xylene-indane b). The solution contained 2wt.% P3HT:PCBM (1:0.8) and was dried after knife coating at 25°C and 0.3m/s airflow. [135]

The reflectometer raw signal of both solvent mixtures is shown in Figure 2.19 for the centered position. The peak to peak distance, which is related to the film shrinkage, is increasing after an initial fast evaporation of the higher volatile component. This transition is of course less pronounced for the combination o-xylene-indane (Figure 2.19a) than for the system toluene-indane, because of the higher difference in vapor pressure of the latter (Table 2.1). For the analysis of the optical measurement, the changing refractive index is taken into account again by mixing the refractive indices of the solid constituents and the solvent mixture with respect to their changing volume fraction. The refractive index of the solvent mixture (Table 2.1) is set constant over the whole drying process to the initial solvent composition averaged by volume fractions. This signifies one effective refractive index for the solid components and one effective refractive index for the solvent components. These two effective refractive indices are subsequently averaged with the respectively changing volume fractions over the drying process. The curve shape shall not be interpreted in terms of phase behavior or layer formation, but shows further potential of this method [126, 127].

2.4 Evaluation of the drying kinetics model

Table 2.2: Material properties of the used solvents at 25°C. The refractive indices are given at 589 nm. [135, 164]

Solvent	Vapor pressure	Density	Refractive index
	mbar	g/cm ³	-
1,2-Dichlorobenzene	1.81	1.301	1.549
Toluene	37.9	0.865	1.494
o-Xylene	8.84	0.858	1.503
Indane	2.05	0.960	1.532

In order to design the transition from the fast to the slow evaporating solvent at a distinct film composition, e.g. for solubility reasons or the overall drying time, a drying kinetics model of this multi-component systems is required. This was done under the assumption of an ideal mixture of both solvents and an ideal solution of both dissolved compounds P3HT and PCBM. In this case the activity coefficient $\gamma_i = 1$ (eq. 2.27) and the vapor pressure of each solvent can be calculated according to the changing molar fraction of each component (see Figure 2.15). The non-ideality of the solvent mixture can be neglected for these two cases according to activity coefficients close to unity determined with UNIFAC (see section A 4.5).

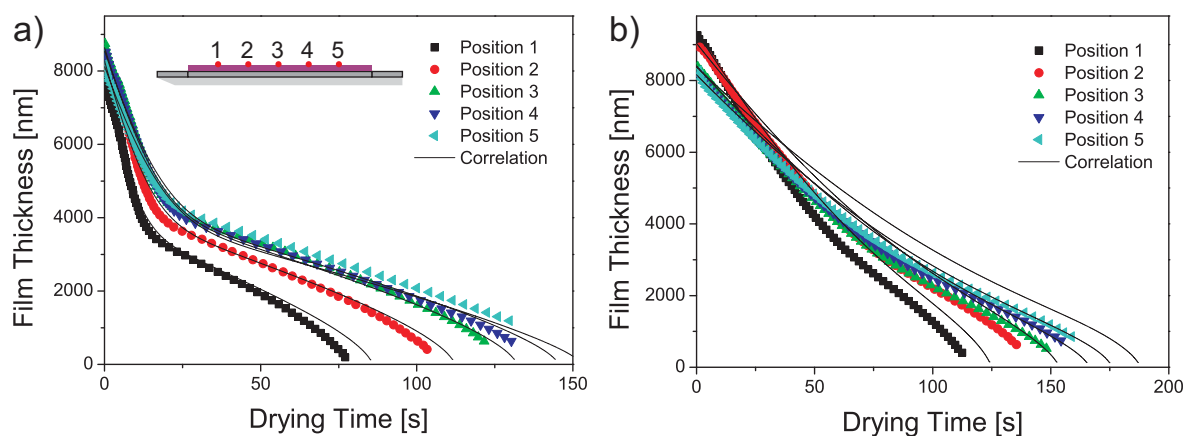


Figure 2.20: a) Calculated and measured evolution of film thickness for the solvent mixture toluene-indane and b) o-xylene-indane. The film composition can be obtained from the numerical simulation of film drying by the fitted correlation. [135] Here $x_0 = 10$ mm and further positions are according to Figure 2.8.

The mass transfer kinetics are assumed to be dominated by the mass transfer in the gas phase as a function of time and space. The comparison of model based calculation and experimental data (Figure 2.19) is given in Figure 2.20. Position 1 represents the measurement in 10 mm distance to the front of the wet film. The distance between each measurement position is 10 mm.

The numerical calculation is in sufficient agreement with the experimental data although the correlation for gas phase mass transfer was fitted to a different material system (pure 1,2-dichlorobenzene). This confirms the validity of the undertaken simplifications. The numerical approach can aid the design of solvent blending ratios in order to change the transition from fast to slow drying at distinct film compositions. Further the overall drying time can be optimized by temperature and gas flow rate to a desired value. By changing the Sherwood correlation to, e.g. slot nozzle driers for suitable conditions in roll-to-roll dryers, lab scale results of the drying process-film property relationship can be transferred to appropriate process conditions of a roll-to-roll manufacturing process.

In conclusion, within this thesis an experimental setup for spatially resolved thin film drying kinetics measurement could successfully be developed. The spatially resolved measurement was accomplished for single and binary solvent systems of polymer-fullerene (P3HT:PCBM) solutions as used in OPV. The effect of a moving drying front in gas flow direction has been quantitatively investigated. It leads to a local acceleration of the film shrinkage as the drying front approaches and to an increased overall drying time in gas flow direction. The analytical approach of Brauer et al. (solvent mass transfer coefficient as a function of time and space) shows a very similar behavior, but needed to be adapted in two parameters to the experimental drying kinetics data. The fitted correlation allows a spatially resolved calculation of thin film drying kinetics with full mass transfer limitation in the gas phase for single and also for multiple solvent systems. This was demonstrated for two solvent mixtures in a comparative study with experimental data. This work could proof, that neglecting this effect leads to tremendous misinterpretation of local and integral drying kinetics measurements with limitations in the gas phase mass transfer.

3 Solution behavior of organic semiconductors¹

In the previous chapter the kinetics of film drying were discussed. The origin of the influence of drying kinetics on solar cell efficiency is unclear and shall be investigated in this work. Film crystallinity and nanomorphology, which form during film drying, play an important role for solar cell performance and are assumed to be the decisive link between device performance and film formation kinetics. In order to investigate the competitive interplay between thermodynamic equilibrium and kinetic limitations, we now focus on the thermodynamic behavior of the polymer-fullerene solution. Since crystallization during solvent evaporation is solubility driven, we initially focus on the solubility and phase behavior of PCBM and P3HT solutions. Up to now, the polymer-fullerene phase diagram is only known for crystallization from melt of P3HT:PCBM measured by calorimetry [147, 165] and dynamic mechanical analysis [141]. In this work the phase diagrams of the binary PCBM-DCB and P3HT-DCB solutions were determined. This was done by preparing a slightly oversaturated state, whereupon, in a subsequent step after centrifugation, the composition of the coexisting phases was determined for each temperature. For comparison few solubility data is available in literature which is listed in Table 3.1.

Table 3.1: Solubility data of P3HT and PCBM in o-dichlorobenzene. All data is given in mg/ml and was converted to mass fraction in weight percent.

Substance	Solubility	Temperature	Reference
P3HT	2.3wt.% (30mg/ml)	18-22°C	[166]
PC ₆₁ BM	>3.8wt.% (>50mg/ml)	18-22°C	[166]
PC ₆₁ BM	7.7wt.% (100mg/ml)	room temperature	[100]
PC ₇₁ BM	15.5wt.% (203mg/ml)	room temperature	[167]

¹ Natalie Schnabel [191] dedicated her diploma thesis and Stefan Jaiser [190] his student research project to the solution behavior of organic semiconductors. The essence of this chapter is published in [81]

3.1 State of the art

A simple approach towards the description of the solubility of a substance is the cohesive energy density (CED) theory developed by Hildebrand and Scott [168] which was extended in 1967 by Hansen [169-171] with distinction between dispersive, dipole-dipole and hydrogen-bonding forces. With this group contribution approach Kim et al. determined the solubility limit of a ternary solid-solid-solvent system of organic semiconductors [101]. The phase diagram aided the interpretation of the observed final film structures which are assumed to arise in a spinodal phase separation process [172]. Walker et al. applied solubility parameters in the search for appropriate solvents and for device optimization of a novel polymer-fullerene blend [167]. However, this method is limited to the accuracy of group contribution methods.

Jukes and Heriot et al. investigated the drying film of pure polymer and polymer blend solutions whereby they observed a bilayer formation due to phase separation with subsequent stratification of one component at a distinct composition [126, 127]. To further extend the image of undergoing processes during film drying and simultaneous phase separation Michels [173] simulated this process based on an approach of combined Flory-Huggins [174-176] and Cahn-Hilliard theory [177, 178]. The simulations of the macroscopic film structure evolution of a binary organic semiconductor blend solution show surface-directed spinodal decomposition, being triggered by small differences in substrate- and/or air-interface interaction energies of the separating phases. Hence, solubility limits and unstable spinodal regions in the phase diagram are crucial for understanding the driving forces of structure evolution. However, it has finally to be evaluated if this type of phase separation coincides with the polymer-fullerene segregation which is relevant for OPV.

3.2 Thermodynamics of polymer solutions

In this thesis the phase diagrams of the established organic photovoltaic material system P3HT and PCBM was elaborated for the binary solutions of different solvents. Flory-Huggins parameters are determined from the experimental phase diagram data as prerequisite for future work of simulations as accomplished by Michels. The relevance of the binary phase diagrams of P3HT and PCBM solutions in terms of the phase separated P3HT-PCBM

structure is discussed in chapter 4.5, where the structure formation of the ternary system is observed in-situ as the structure evolves.

3.2.1 Flory-Huggins theory

A thermodynamic system is striving for a minimum of free enthalpy of mixing in order to reach thermodynamic equilibrium. Negative free enthalpy of mixing is necessary for the miscibility of two components, but not a sufficient condition. Within the Flory-Huggins theory¹ the free enthalpy of mixing ΔG_M for non-ideal polymer solutions can be described by

$$\Delta G_M = \Delta H_M - T \cdot \Delta S_M \quad 3.1$$

with T as temperature of the system. The enthalpy of mixing ΔH_M and entropy of mixing ΔS_M are discussed in the following. In statistic thermodynamics the lattice theory [176, 179, 180] can be applied for describing ΔS_M . Herein, a lattice is filled by the number N_1 of solvent molecules and $N_2 = P \cdot N_1$ polymer molecules. N_i is equivalent to the relative molar volume of component i . Polymer chains are divided into P segments equivalent to the size of solvent molecules (lattice size). For the used type of P3HT $P \approx 300$. Statistic considerations for the occupation of lattice spaces lead to the expression of the entropy of mixing ΔS_M as a function of volume fraction

$$\Delta S_M = -R[\tilde{x}_1 \cdot \ln \varphi_1 + \tilde{x}_2 \cdot \ln \varphi_2] \quad 3.2$$

$$\text{with } \varphi_1 = \frac{N_1}{N_1 + P \cdot N_2} \quad \varphi_2 = \frac{N_2 \cdot P}{N_1 + P \cdot N_2}$$

with the ideal gas constant $R = k_B \cdot N_A$, the molar fraction $\tilde{x}_i = N_i/N_A$ and φ_i as volume fraction of each component. Following, we want to consider interaction forces between the lattice segments of the next lattice neighbors. Long range interaction over larger distances is neglected. In the case of a polymer solution there are three types of interactions associated with the expression of a characteristic energy ε_{ij} . Solvent-solvent interactions are denoted as ε_{11} , polymer-polymer interactions as ε_{22} and solvent-polymer

¹ Paul John Flory was awarded the Nobel Prize in Chemistry in 1974 "for his fundamental achievements, both theoretical and experimental, in the physical chemistry of macromolecules." Together with Maurice Loyal Huggins he elaborated the Flory-Huggins solution theory.

3 Solution behavior of organic semiconductors

interactions as ε_{12} . For the dissolution of each polymer segment a polymer-polymer contact and solvent-solvent contact is broken followed by the generation of a polymer-solvent contact. Hence, the generated energy difference $\Delta\varepsilon$ can be expressed by

$$\Delta\varepsilon = \varepsilon_{12} - \frac{1}{2}(\varepsilon_{11} + \varepsilon_{22}) \quad 3.3$$

With the number of contact points p

$$p = x \cdot N_2 \cdot z \cdot \varphi_1 = N_1 \cdot z \cdot \varphi_2 \quad 3.4$$

with $x \cdot N_2$ as the number of lattice spaces occupied by the polymer molecule and z as the coordination number of the lattice. Neglecting excess volume of mixing $\Delta V_M = 0$ leads to

$$\Delta H_M = \Delta U_M + p\Delta V_M = \Delta U_M \quad 3.5$$

Subsequently we can define the enthalpy of mixing as

$$\Delta H_M = \Delta U_M = p \cdot \Delta\varepsilon = N_1 \cdot z \cdot \varphi_2 \cdot \Delta\varepsilon = \tilde{x}_1 \cdot \varphi_2 \cdot \chi^* \cdot R \cdot T \quad 3.6$$

with the polymer-solvent interaction parameter

$$\chi^* = \frac{z \cdot \Delta\varepsilon}{k_B \cdot T} \quad 3.7$$

Combining equations 3.1, 3.2 and 3.6 we receive the Flory-Huggins-equation

$$\Delta G_M = R \cdot T [\tilde{x}_1 \cdot \ln \varphi_1 + \tilde{x}_2 \cdot \ln \varphi_2 + \tilde{x}_1 \cdot \varphi_2 \cdot \chi^*] \quad 3.8$$

Strictly seen, this equation is only suitable for athermal solutions. However, it is common to incorporate additional contributions of ΔS_M , which originate from the interactions between lattice segments, into χ^* . The derivative of equation 3.8 over \tilde{x}_1 and \tilde{x}_2 delivers an expression of the chemical potential $\Delta\mu_i$ and the activity for each component in the mixture.

$$\ln a_1 = \frac{\Delta\mu_1}{RT} = \frac{1}{RT} \frac{\partial \Delta G_M}{\partial \tilde{x}_1} = \ln \varphi_1 + \left(1 - \frac{1}{P}\right) \cdot \varphi_2 + \varphi_2^2 \cdot \chi \quad 3.9$$

$$\ln a_2 = \frac{\Delta\mu_2}{RT} = \frac{1}{RT} \frac{\partial \Delta G_M}{\partial \tilde{x}_2} = \ln \varphi_2 + (1 - P) \cdot \varphi_1 + P \cdot \varphi_1^2 \cdot \chi \quad 3.10$$

Commonly χ is fitted to measurements of the chemical potential. For the calculation of ΔG_M which requires χ^* , the first derivative of χ must be formed. If the interaction parameter $\chi(T)$ is only a function of temperature, both definitions of the interaction parameter are equal ($\chi^* = \chi$). If $\chi(T, \varphi)$ also is a function of volume fraction the definitions of the interaction parameters differ ($\chi^* \neq \chi$) and the derivative of $\chi(T, \varphi)$ depends on the chosen empirical function. In chapter 3.5 the Flory-Huggins-equation is applied to phase separating polymer solutions. In thermodynamic equilibrium the chemical potential and activity is alike for coexisting phases. After determining the composition for both phases, such as “sol” which is denoted as ' (prime) and “gel” phase denoted as '' (double prime), the interaction parameter can be derived from equation 3.9 with $\Delta\mu_1' = \Delta\mu_1''$ and equation 3.10 with $\Delta\mu_2' = \Delta\mu_2''$ giving

$$\chi = \frac{\ln \varphi_1'' + (1 - 1/P) \cdot \varphi_2'' - \ln \varphi_1' - (1 - 1/P) \cdot \varphi_2'}{\varphi_2'^2 - \varphi_2''^2} \quad 3.11$$

$$\chi = \frac{\ln \varphi_2'' + (1 - P) \cdot \varphi_1'' - \ln \varphi_2' - (1 - P) \cdot \varphi_1'}{P(\varphi_1'^2 - \varphi_1''^2)} \quad 3.12$$

The interaction parameter $\chi(T, \varphi)$ is usually fitted to experimental data and can be a function of temperature, volume fraction or other influencing parameters. Several models comprise these dependencies [172, 181-185].

For the calculation of the phase diagram the free energy of mixing is plotted against the volume fraction of polymer φ_2 for different temperatures (Figure 3.1). Both coexisting phases ' and '' exhibit the same chemical potential

$$\Delta\mu_1' = \Delta\mu_1'' \quad \text{and} \quad \Delta\mu_2' = \Delta\mu_2'' \quad 3.13$$

Points that comply with these conditions are on the common tangent and depict the binodal curve of coexisting phases. The inflection points of ΔG_M enclose the unstable spinodal region. The condition for the spinodal curve is

$$\partial^2 \Delta G_M / \partial \phi_1^2 = 0$$

3.14

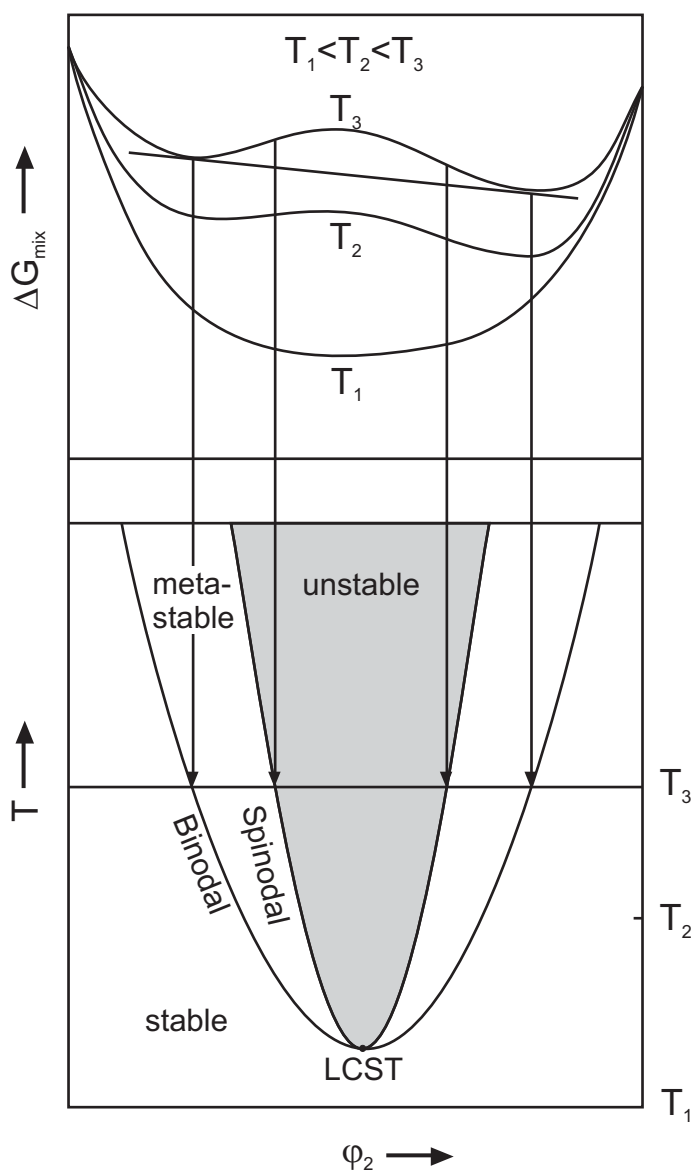


Figure 3.1: Construction of a polymer solution phase diagram (bottom) based on the plot of the free energy of mixing (top).

Binodal and spinodal curve enclose the metastable area where nucleation and growth are the governing mechanisms of phase separation. By crossing the spinodal curve the system undergoes spontaneous phase separation. Further details on thermodynamics of polymer solutions can be found elsewhere [186-188]. The solubility parameter concept is presented in the appendix (see A 2.1).

3.3 Experimental method

For the polymer P3HT (Rieke Metals 4002E, $M_w \approx 48900$ g/mol, polydispersity 1.7) and the fullerene derivative PCBM (Solenne, purity >99%) no thermodynamic data was available and had to be determined within this thesis. Common methods for the determination of the chemical potential of a solution are such as osmotic pressure, vapor pressure, gas-liquid chromatography, freezing-point depression, swelling equilibria, intrinsic viscosity, light scattering, and other methods [187, 188]. Both substances are highly light absorbing which excludes optical methods as remedy of first choice. Commonly low volatile aromatic solvents, such as 1,2-dichlorobenzene ($p_{DCB}(25^\circ C) = 1.8$ mbar), chlorobenzene ($p_{CB}(25^\circ C) = 16$ mbar) and o-xylene ($p_{oXyl}(25^\circ C) = 8.8$ mbar) are used for this polymer-fullerene blend. At such low vapor pressures it is hard to determine the reduction of vapor pressure by the addition of a few weight percent of the low soluble solid substances to the solvent.

Hence, a method dealing with low material consumption had to be elaborated in this work for the determination of the phase diagrams of P3HT and PCBM. Oversaturated solutions were prepared in the phase separated state with a subsequent determination of the composition of each phase. This shall be explained in the following and is schematically depicted in Figure 3.2.

Slightly oversaturated solutions of the binary P3HT and PCBM solutions are prepared in 2 ml safe-lock tubes (Eppendorf). This was done in iterative steps in order to prevent excessive amounts of insoluble solid substance, which would falsify the solid fraction in the solid rich phase. For statistical reasons 4 samples were prepared for each temperature independently in different vials. The solution was stored for about 18 hours at a defined temperature under agitation. Koppe et al. observed completed gelation after not more than 16 hours for several molecular weights of P3HT [189]. After this period of time, it was checked if the samples showed two coexisting phases. If not, further solid was added and further 18 hours of agitation under controlled temperature followed. This was done until the amount of both phases was sufficient for the further analysis. The phases can be distinguished in a solid rich, higher viscous gel phase and a lower viscous solution phase. The purity of both phases is promoted by centrifugation, whereby a temperature controlled centrifuge (Sigma 2-16KCH) was used at the equilibrium temperature. In order to diminish the influence of shearing forces during centrifugation, samples rested for further 2 hours without agitation in a

3 Solution behavior of organic semiconductors

temperature controlled environment. Subsequently samples of each phase are extracted by a syringe.

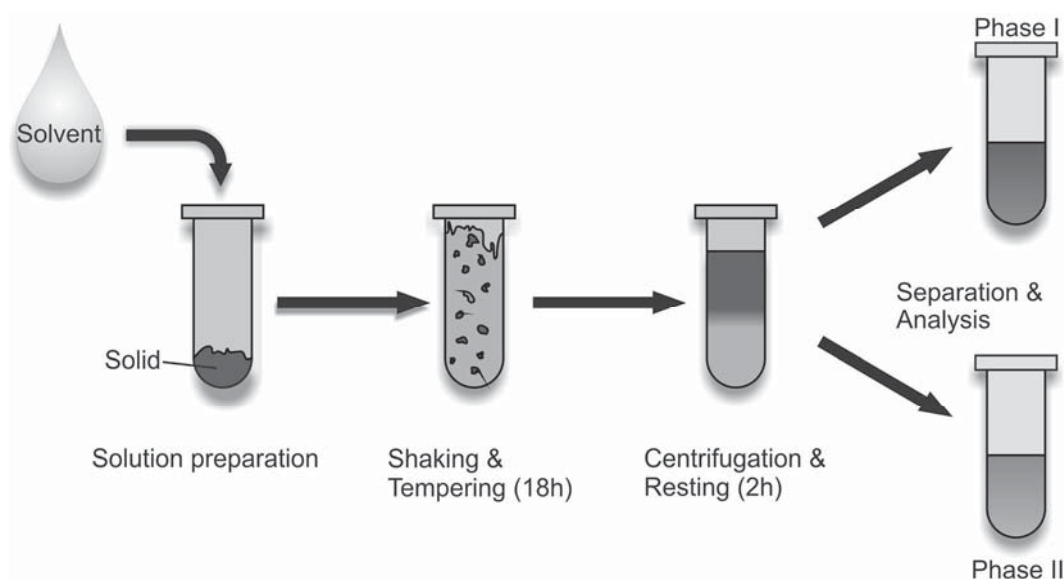


Figure 3.2: Scheme of processing steps for the preparation of a two phase solution with subsequent concentration analysis of each phase. [190]

Both extracted phases are diluted afterwards (100 μl sample added to 900 μl solvent) in order to prevent a repeated phase separation due to cooling at room temperature, which is the case for samples investigated at elevated temperatures. The dilution ratio is checked gravimetrically assuring high accuracy. Afterwards the solid mass fraction of each semiconducting compound is determined by means of refractive index measurements of the diluted solution (calibration see appendix Figure 10.7). For the analysis an Abbe refractometer (Dr. Kernchen) was used with a wavelength of 589 nm.

For ternary P3HT-PCBM-solvent the separation of both dissolved solid constituents are required. Therefore the extracted samples were processed by size exclusion chromatography (SEC) and quantitatively analyzed with a diode array detector (see appendix Figure 10.8). Although the analysis method could be elaborated for this ternary system, difficulties of sample extraction out of low amounts of dark and turbid solution prevented reliable data of the ternary phase diagram.

3.4 Fullerene solution

The C₆₁ fullerene derivative PCBM is commonly used as electron acceptor in organic solar cells. It exhibits a single solubility limit in all investigated solvents which is depicted for 1,2-dichlorobenzene in Figure 3.3. The solubility increases with temperature. An increased solubility expresses stronger solvent-PCBM interactions which can be fortified with increasing temperature. By crossing the solubility limit due to solvent evaporation (film drying), solid PCBM aggregates form and precipitate. The residual solution maintains at the solubility limit as shown schematically in Figure 3.3a).

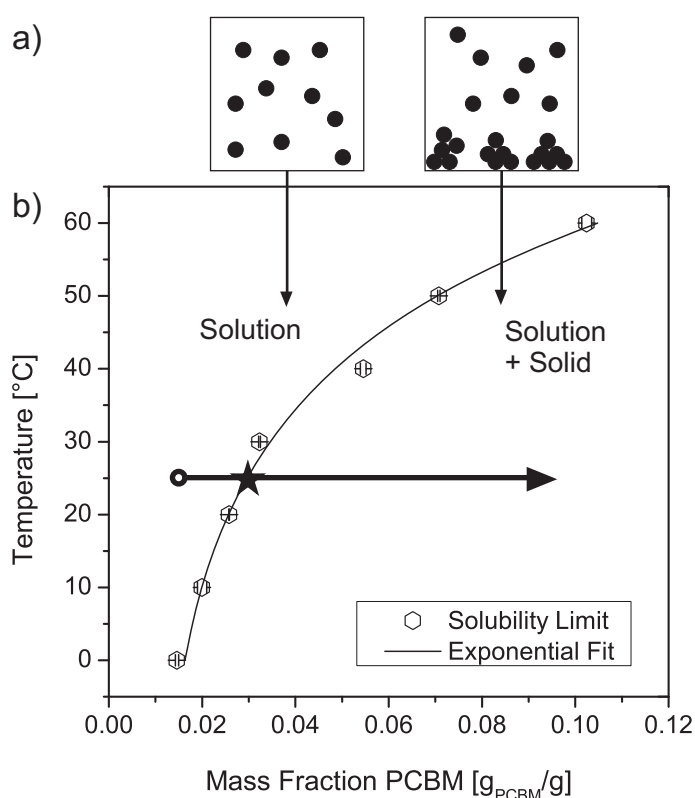


Figure 3.3: a) Scheme of PCBM aggregation after crossing the solubility limit. b) Solubility of PCBM in DCB as a function of temperature. Error bars are mostly smaller than the symbol size. The arrow indicates the drying process at 25°C and the star symbol the instant of phase transition. [81]

The temperature dependence of PCBM solubility can empirically be described by the following exponential approach

$$x_{PCBM,max} = 3.034 \cdot 10^{-8} \cdot \exp\left(\frac{T}{22.267}\right) + 9.932 \cdot 10^{-3} \quad 3.15$$

$$\bar{R}^2 = 0.9903$$

with the temperature T as the absolute temperature and \bar{R}^2 as the corrected determination coefficient. Additional data for other solvents can be found in chapter A 2.3.

3.5 Polymer solution

In contrast to PCBM solutions which exhibit a single solubility limit polymers tend to phase separate in solution into a sol and a gel phase (Figure 3.4). This happens if the polymer concentration is situated in a thermodynamic unstable region. Figure 3.4b shows the phase diagram of P3HT in DCB solution with the binodal curves of coexisting solution and gel phase. The dashed line is just a guide to the eye. The solution is stable in the concentration range usually used for coating of such solutions for organic solar cells at room temperature ($x_s \leq 3$ wt.%, or ≤ 40 mg/ml). With solvent evaporation at a constant temperature (arrow indicates evaporation at 25°C) the P3HT solution reaches the solubility limit at a solid mass fraction of, e.g. $x_s=5.1$ wt.% (interpolated for 25°C) and enters the unstable area. The demixing in this unstable area usually originates from strongly differing dynamics of the small solvent and comparatively big and in this case also rigid polymer molecules.

As illustrated above the phase diagram in Figure 3.4a, the demixing process, which is thermodynamically preferred, leads to an aggregation of polymer chains and ends in a physically cross-linked network. These solid rich aggregates comprise a solid fraction of $x_s=10.2$ wt.% compared to 5.1 wt.% in the residual solution. Aggregates grow as long as the solution (in our case the drying film) remains in this unstable area, until the whole film turns into a higher viscous gel phase. The width of the unstable two phase region is almost zero at 50°C (overlapping error bars) indicating an almost continuous increase of viscosity without phase separation at this drying temperature. At higher temperatures, the dynamics of the large polymer and small solvent molecules differ strongly due to increasing thermal energy causing the expansion of the two phase region. Although gravity and density effects might not have an effect in thin films below 20 μm , it is noteworthy that the gel phase (solid rich) density is lower than the solution phase (solid poor) density due to the lower density of P3HT ($\rho_{P3HT} = 1.1$ g/ml) in comparison to DCB ($\rho_{DCB} = 1.3$ g/ml). Macroscopically, after centrifugation, this leads to a floating gel phase on top of the solution phase.

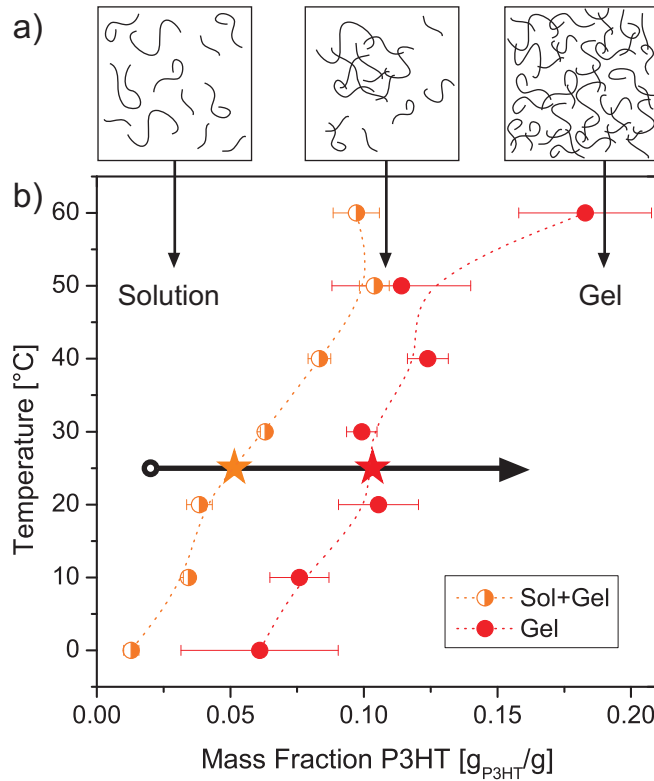


Figure 3.4: a) Scheme of the transition from solution to gel state with polymer aggregation in the unstable two-phase region, before the solution turns into a higher viscous gel during solvent evaporation. b) Phase diagram of P3HT solution in DCB with unstable two phase region between the solution and gel state. Dashed lines are just a guide to the eyes. The arrow indicates the drying process at 25°C and the star symbols the instant of phase transition. [81]

The mass fraction is chosen as concentration unit for comparison reasons with data in the succeeding sections. Neglecting excess volume, it can be converted into volume fractions by

$$\varphi_i = \left(\sum_{k=1}^K \frac{x_k}{x_i} \cdot \frac{\rho_i}{\rho_k} \right)^{-1} \quad 3.16$$

with φ_i as volume fraction, x_i as mass fraction, ρ_i as density of component i and K the number of components.

The chemical potential is equal for the coexisting sol (half filled circles in Figure 3.4) and gel phase (s. eq. 3.13, filled circles in Figure 3.4). The comparison of the polymer volume fraction of both phases, according to

3 Solution behavior of organic semiconductors

equation 3.10, delivers the associated interaction parameter χ of the coexisting phases in thermodynamic equilibrium. This was done for different temperatures and solvents. The main focus was on the mainly used solvent DCB wherefore each point in the phase diagram was determined at four independent samples. For all other solvents each sample was only accomplished twice. The resulting interaction parameters are given in Table 3.2.

Table 3.2: Flory-Huggins interaction parameter χ for P3HT solutions in the given solvents. χ is derived from the averaged polymer volume fraction of the coexisting sol and gel phases. [190, 191]

Temp. [°C]	o-DCB	Chloroform	p-Xylene	Toluene	Tetralin	Mesitylene
0	0.581	0.570		0.567	0.569	0.577
10	0.561	0.565	0.570	0.571	0.565	0.570
20	0.564	0.560	0.567	0.565	0.567	0.569
30	0.562	0.571	0.564	0.562	0.569	0.569
40	0.567	0.569	0.561	0.561	0.568	0.568
50	0.569		0.560	0.573	0.568	0.561
60	0.585					0.590

The low solubility and narrow two phase region complicates the calculation of the phase diagram close to a chemical potential and activity of the pure solvent. The focus of this work was to evaluate the relevancy of the solutions phase diagram in conjunction with the drying kinetics for the structure formation in polymer-fullerene blends.

Reliable data for the ternary polymer-fullerene-solvent system could not be obtained by the available amount of organic semiconducting material and techniques. Hence, up to this point, information on polymer-fullerene interaction forces is lacking. In the following chapter 4.3, the relevance of the phase transitions determined in this chapter shall be discussed in relation to the evolving film structure of the ternary system, which is observed in-situ. By this method, qualitative information about polymer-fullerene interaction forces in the ternary solution could be obtained.

In conclusion, the phase diagram of P3HT and PCBM solutions have been successfully determined in the temperature range 0-60°C which provides

a fundamental understanding of the macroscopic solutions behavior. In the following sections it will be elaborated how structure formation during drying proceeds by crossing the solubility limits determined in this section. The temperature influence on the mechanisms of structure formation can also be discussed in relation with the solutions phase diagrams.

4 Morphology formation in polymer-fullerene films

In chapter 2 new methods for the measurement of film thickness evolution during thin film drying have been introduced. In combination with simulations of film drying it is even possible to handle quaternary systems, such as polymer-fullerene blends dissolved in a mixture of two solvents. The preceding chapter 3 delivers the information of the solubility of each substance which is crossed in the course of solvent evaporation during film drying. Thus we are able to plot the drying path through the phase diagram and to determine the instants of expected phase transitions.

Hence, we are now at the starting point for the systematic investigation of the impact of film drying kinetics and phase behavior on the final film morphology. A strong influence of the kinetics of film drying on the final device properties have been reported [109, 110, 192]. Hence, we raise the hypothesis that this originates from differences in blend morphology. Understanding the driving mechanisms for molecular ordering during this process step is the key for systematically tuning the blend morphology and solar cell device properties with drying process parameters. The steps of the investigation in this thesis are divided as follows

- Understanding the mechanisms and dynamics of morphology formation during solvent evaporation
- Identification of key parameters for the manipulation of film morphology during film drying
- Exploitation of influencing parameters in order to generate a favorable morphology for optimized solar cell performance

The experimental methods for the characterization of the multi scale morphology, which ranges from the molecular level to micrometer scale, are discussed in section 4.2.

4.1 State of the art

The phenomenon of thermo reversible gelation of P3HT solutions was already observed by Malik et al. [193]. A gel state signifies a physical cross-linked state of polymer chains over macroscopic distances in comparison to

the contour length of the polymer, which is for example approximately 120 nm for 50 kg/mol weight average P3HT [46]. In the progress of this thesis Koppe et al. [189] investigated the effect of polymer gelation towards solar cell properties. They observed turbidity, but no color shift in a first step of aggregation followed by a color shift when the state of entire gelation was reached. This implies several successively proceeding structural changes in the process of gel formation. Remaining the concentration of the solution constant, it takes several hours for reaching the gel state. Koppe et al. could show that the P3HT:PCBM blend film morphology fabricated by solution casting of the gel state is beneficial for the device performance. However, the structural evolution in this process has not yet been investigated and it is not known how the dynamics of molecular ordering are affected by the kinetics of solvent evaporation in the drying film. Furthermore, it is not clear how the gel transition is related to the solubility of both solid substances and how it proceeds during film drying.

Peet et al monitored the evolution of absorption spectra for drying PCPDTBT:C₇₁-PCBM films cast from 1,2,4-trichlorobenzene [55]. This extreme low volatile solvent with a boiling point of about 214°C is required for reducing the drying process due to the comparatively slow data acquisition of spectrophotometers. Their work provides a correlation of optical transitions with approximated stages of drying, but does not afford a detailed insight into the evolution of structural ordering or quantitative information of film composition. Recently, Wang et al. [57] investigated the drying process of P3HT:PCBM films with spectroscopic ellipsometry (SE) and grazing incidence X-ray scattering (GIXS). In their approach, very similar to this thesis, a structure sensitive X-ray technique was combined with an optical technique in the spectral UV-vis range in order to obtain both, the structural information and the evolution of film composition (volume fraction of solvent). The experiments were accomplished with both techniques in the same setup but not simultaneously as it has been done in this thesis. Ellipsometry reveals the existence of a diffusional limitation in a final drying stage, although the diffusion path is short in films of about 100 nm thickness. The kinetics of crystallization as obtained by X-ray scattering are explored using the Avrami equation [194-196] in the form

$$Y = 1 - e^{-K \cdot t^n} \quad 4.1$$

where Y is the volume fraction of the crystalline component, and K and n are fitted constants [57].

A method for controlling morphology independently from film processing is the pre-aggregation of polymer fibers in solution even before film coating. This provides a possibility for long aggregation time in the order of hours or even days without drawbacks in fabrication speed, since aggregation time and processing time are decoupled. P3HT whiskers provide high hole mobility along the fiber direction [45], which is beneficial for hole extraction out of the BHJ structure. Basically these whiskers can be generated on two ways. First, solutions can be dissolved at elevated temperatures, which undergo whisker formation after crossing the solubility limit of the polymer during a cooling step [197-204]. The second manner is the addition of an “unfriendly” solvent for the polymer, such that whisker formation is induced [162, 205, 206]. By these methods whiskers are observed to form during gel formation.

The addition of selectively PCBM solvating low volatile additives has also been shown to effectively promote the formation of an overall more efficient film morphology [55, 87, 100, 207-210]. The effect of the additives is to dramatically increase aggregation and order within the polymer domains while excessive crystallization of the fullerene is avoided [211].

4.2 Experimental Methods used in this thesis

For the characterization of the in this thesis fabricated thin films atomic force microscopy (AFM) was used in tapping mode for the measurement of the film surface morphology (see A 3.2). Access to the AFM (Dimension Icon, Veeco) was provided by the Karlsruhe Nano Micro Facility (KNMF). For the characterization of the bulk morphology scanning transmission electron microscopy (STEM, see A 3.3) measurements were carried out by Marina Pfaff at the Laboratory for Electron Microscopy (LEM) at KIT. In collaboration with Monamie Sanyal and Esther Barrena of the Max Planck Institute of Metals Research, novel approaches of synchrotron based grazing incidence X-ray diffraction have been developed for to the dynamic crystallization process of drying thin films. By this method the self assembly of solution cast polymer-fullerene films could be studied for the first time in situ during solvent evaporation which is explained in the following.

4.2.1 Grazing Incidence X-ray Diffraction (GIXD)¹

X-ray diffraction is a common technique for the investigation of crystalline materials² since the wavelength is in the order of the crystalline lattice spacing. X-ray scattering from thin films of polymers is relatively weak due to the weak scattering strength of carbon, the small number of scattering planes, and also disorder in these films [212, 213]. Thus to achieve measurable scattering intensities, either long integration times or high flux X-ray sources are required [214]. Synchrotron sources provide the high flux required to examine the scattering over a larger dynamic range, as it is needed for the real time observation of blend crystallization during film drying in this work.

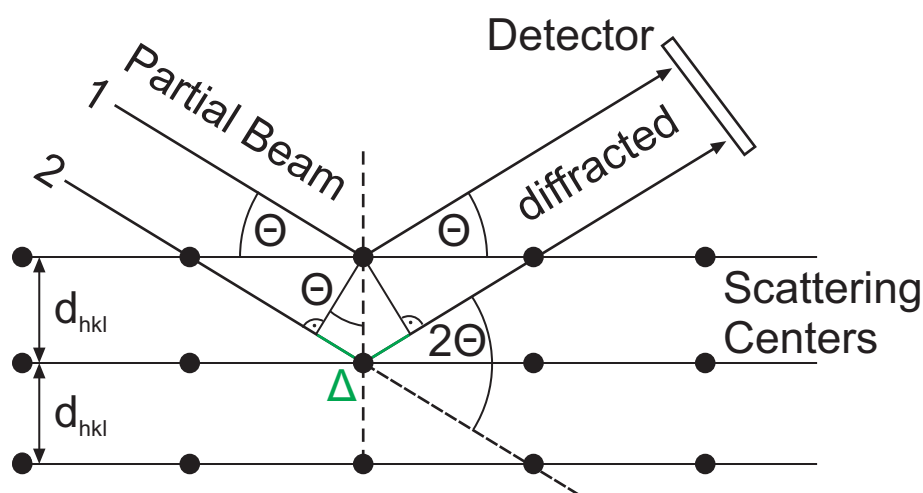


Figure 4.1: Reflection and interference at crystalline material according to Bragg with the beam angle of incidence Θ . The optical path difference is indicated as Δ .

The incident beam is getting diffracted at periodic repeating structures of crystalline substances and undergo coherent scattering (diffraction). In the case of X-ray scattering the electromagnetic wave interacts with electrons of the crystalline material, which spherically emit radiation of the same wave-

¹ Other common abbreviations for this technique are GID, GIXRD. Even grazing incidence X-ray scattering (GIXS) and grazing incidence wide angle X-ray scattering (GIWAXS) are accomplished in a similar way and deliver similar diffraction patterns. The manner of the diffraction/scattering pattern analysis is also determining the terminology in these cases.

² In 1912 Max von Laue, Walter Friedrich and Paul Knipping discovered X-ray diffraction at crystals. For this work von Laue was awarded the Nobel Prize in Physics in 1914.

length. Figure 4.1 depicts the pathway of the portion of emitted radiation under $\Theta_{out} = \Theta_{in}$.

The angle between direct and diffracted beam is 2Θ . The diffracted partial beams generate constructive interference at appropriate angles, if the optical path difference, denoted as Δ , is a multiple of the wavelength, as it is described by the Bragg condition 4.2

$$\sin \Theta = \frac{n \cdot \lambda}{2d_{hkl}} \quad 4.2$$

The angle Θ for Bragg condition ($n = 1, 2, 3, \dots$) depends on the lattice spacing d_{hkl} ¹ and the wavelength λ (e.g., 1-1.55 Å at 12.3-8 keV). For wide ranging crystalline ordered substances higher order Bragg conditions ($n = 2, 3, \dots$) of constructive interference can be observed. According to equation 4.2, smaller scattering plane spacing d_{hkl} results in a higher diffraction angle for observing constructive interference, which is later observed as Bragg peak.

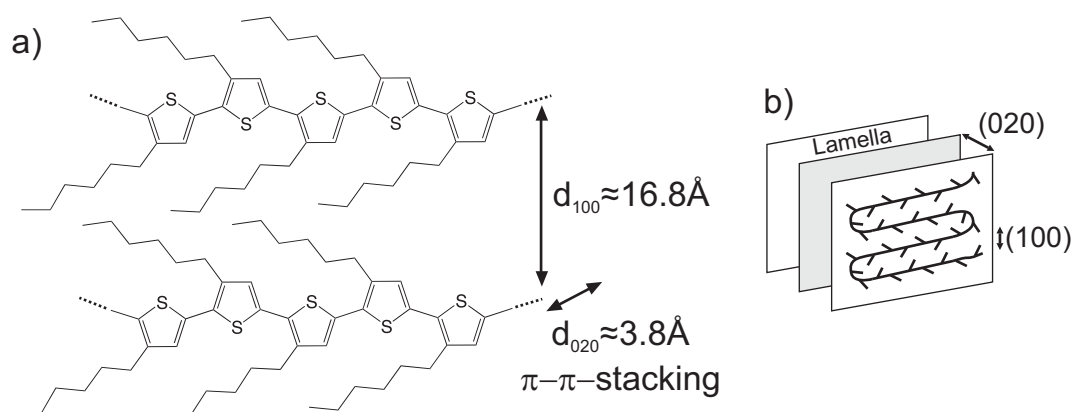


Figure 4.2: a) Stacking of P3HT molecules in edge on configuration. b) Simplified drawing of P3HT unit cell. (100) and (020) are the two crystalline directions. Chain folding occurs predominantly at higher molecular weight polymers while low molecular weight polymers tend to stack in the stretched linear form.

¹ HKL originates from the Miller indices which is a common notation system in crystallography for crystalline orientations. In the case of this work the directions (h00) and (020) are of importance.

Figure 4.2a and b depict a model of the common unit cell for crystalline P3HT domains. P3HT molecules are mainly oriented with their backbone parallel to the substrate and their alkyl side chains normal to the substrate. Polymer chain folding/stacking leads to lamella formation in (100) direction normal to the substrate. Interlayer stacking in (020) direction of such lamellae is driven by π -orbitals of sp^2 -hybridized carbon atoms in the conjugated backbone, which protrude normal to the lamella plane. This (020) interlayer stacking provides π - π -orbital overlapping in-between the lamellae layers and an additional direction of delocalized electrons, which results in high hole mobility in (020) direction (s. section 1.2).

As mentioned before, X-ray scattering at polymers is comparatively weak, especially at such thin films in the range from 20-500 nm. Operating at grazing incidence conditions (Figure 4.3) with low angles of incidence $\Theta < 0.2^\circ$ provides a maximized pathway through the film and a minimized effect of the substrate. The index of refraction of organic materials at X-ray wavelengths is slightly less than unity leading to total external reflection at small angles. The angle of total reflection is called critical angle. In the regime of total external reflection (i.e. for incidence angles less than the critical angle) a so-called evanescent X-ray wave field forms inside the less dense medium and propagates parallel to the surface. This establishes the basis of GIXD to probe the structural properties of the surface of the materials. With slightly increasing angle of incidence the penetration depth of the X-ray beam can finely be adjusted, allowing for a vertical probing of the thin film. An important requirement for a well-defined calculation of the penetration depth is a highly smooth surface, which is not always the case for the investigated films. Hence, this work focuses merely on the integral structure of the entire film.

In grazing incidence geometry, the incidence angle is kept below the critical angle of total reflection, preventing the penetration of the substrate which would cause strong diffraction and scattering effects. A disadvantage is the geometrical mismatch of the planar 2D detector with the spherical space (Laue sphere) of exact Bragg condition. Hence, with a 2D detector the Bragg condition is only met at a single spot and the specular rod ($q_{xy} = 0, q_z$) cannot be accessed in the reciprocal space. Therefore for a quantitative structural analysis of the out-of-plane structure (along q_z), ex-situ measurements by X-ray reflectivity were accomplished in this thesis. A more detailed explanation of this technique can be found in the thesis of Monamie Sanyal who conduct-

ed the GIXD analysis of all in this thesis mentioned experiments and in further references [214-217].

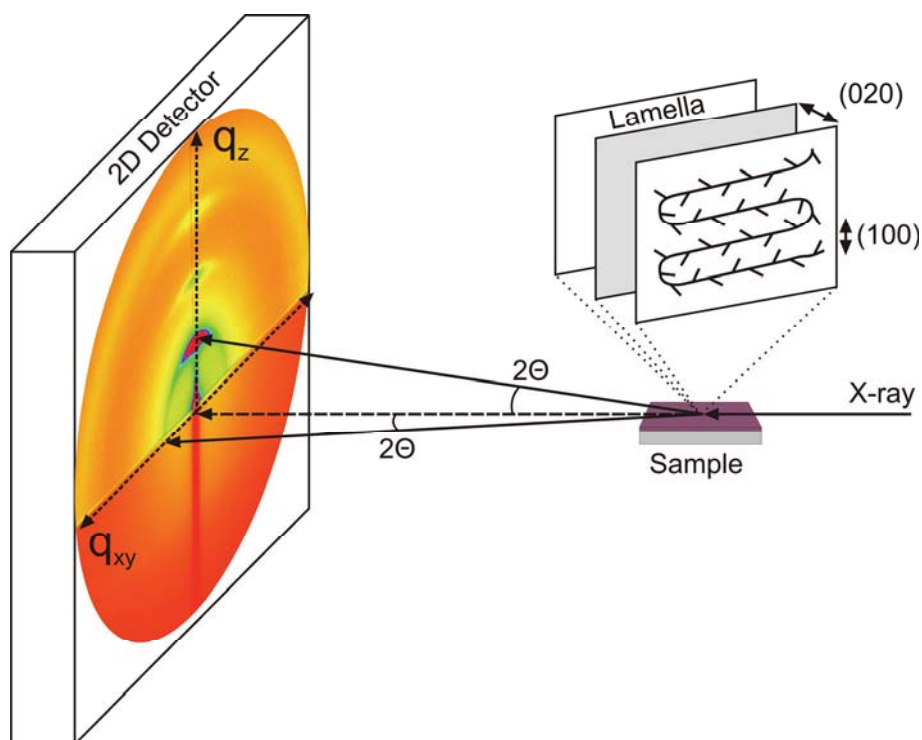


Figure 4.3: Grazing incidence geometry for X-ray diffraction and scattering at thin films. The inset depicts the typical unit cell of P3HT in edge on configuration (According to [214]).

The key advantage of a 2D X-ray detector is that it permits viewing of a large volume of reciprocal space within a single collection frame in very short time. The fast acquisition speed, in a time scale of seconds, enables a real-time study of the crystallization of the polymer-blend. Figure 4.4 depicts schematically several typical diffraction features on the left and the appropriate structures on the right. According to the ideal edge on orientation of P3HT as depicted in Figure 4.3, where the linear scattering centers (polymer backbones) are parallel to the substrate, we would observe a spot like diffraction pattern in out-of-plane direction q_z . This diffraction pattern is related to the (100) planes, which is denoted as (100) Bragg peak (Figure 4.4a). Increasing misalignment with respect to the substrate causes a wing-like spread of the Bragg peak as depicted in Figure 4.4b. Powder like materials exhibit randomly oriented crystallites which correspond to a diffraction ring (Figure 4.4c). A common expression for the amount of increasing misalignment, as it is the

4 Morphology formation in polymer-fullerene films

case in the order from Figure 4.4a-c, is the so called mosaicity¹, which is explained below.

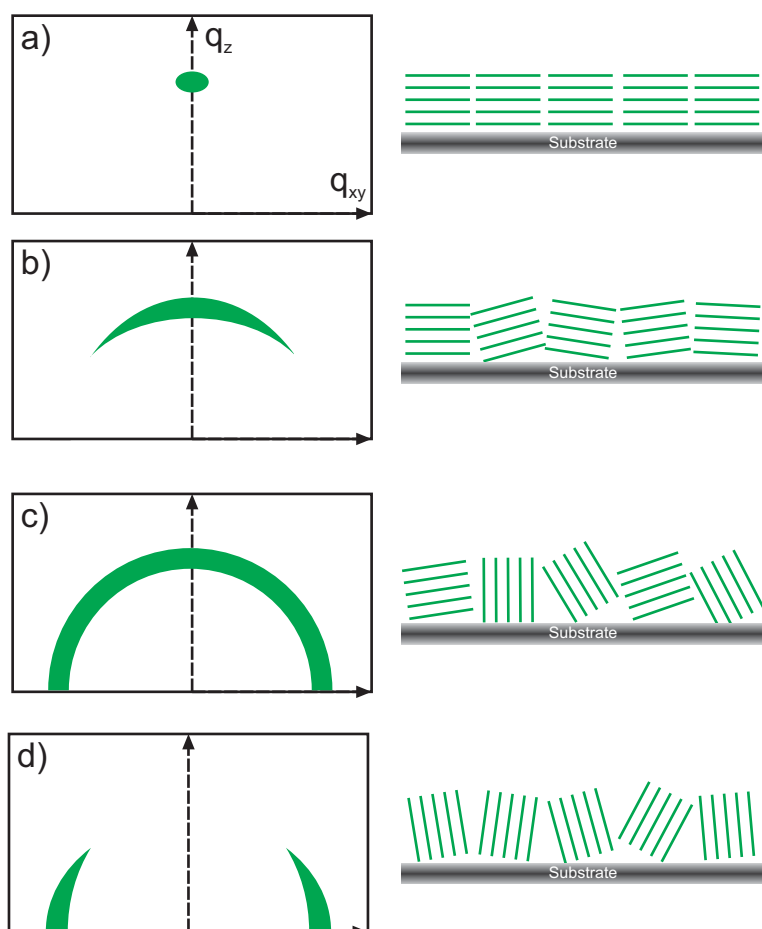


Figure 4.4: Illustrated diffraction features (left) of some exemplary scattering plane orientations (right). (According to [71])

For the case of (100) scattering planes mainly oriented normal to the substrate (Figure 4.4d), one would observe the (h00) peaks in the in-plane direction q_{xy} (Figure 4.4d). For P3HT films oriented in edge-on configuration, the (020) diffraction peak characteristic of the π - π -stacking is found in-the in-plane direction.

This work focuses on the blend of the conjugated polymer P3HT and the fullerene derivative PCBM. An exemplary 2D X-ray diffraction image is

¹ The expression originates from the analogue of crystalline mosaic pieces, which are not perfectly aligned to each other as mosaic stones.

shown in Figure 4.5. From Figure 4.4 we can already qualitatively derive several structural features of the investigated film.

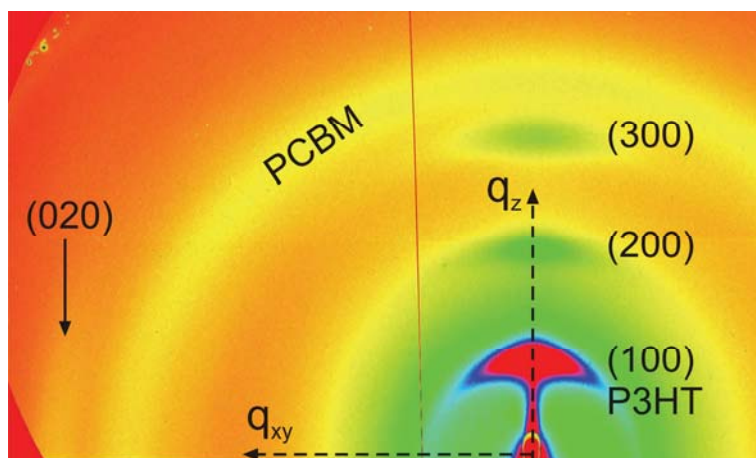


Figure 4.5: GIXD diffraction pattern of a P3HT:PCBM blend film at native silicon substrate fabricated by doctor blading.

First of all, the powder like diffraction ring of PCBM reveals, that PCBM clusters are randomly orientated in the film and exhibit a smaller spacing (center to center spacing is around 10 \AA [60, 218]) in comparison to the P3HT Bragg peaks, which is expressed by the higher angle for constructive interference of the diffraction ring. P3HT exhibits three Bragg peaks in q_z direction, which are related to the (h00) lamella stacking with a spacing of around 16.5 \AA . The existence of three diffraction order peaks indicates long range ordering in this crystalline direction. The wing-like shape of the (100) Bragg peak indicates an orientation distribution of the P3HT crystallites which are mainly oriented in edge-on orientation. The high background intensity, which appears in green in Figure 4.5 surrounding the P3HT (100) Bragg peak, originates from randomly oriented P3HT crystallites. In the in-plane q_{xy} direction another Bragg peak appears, which is related to the P3HT (020) π - π -stacking exhibiting a spacing of about 3.8 \AA .

For each Bragg peak 2D GIXD provides the following information about crystallinity

- spacing in-between scattering planes, which is here the molecular stacking distance
- mosaicity, which is a measure of the orientation distribution of crystalline domains with respect to the substrate

- relative amount of crystallites, which can give a measure of the ratio between two crystalline directions according to the respectively integrated peak intensity

This amount of information can be obtained within a few seconds of integration time (about 3s in this work) for each 2D diffraction image by the utilization of high intense synchrotron radiation. This fast acquisition time and huge amount of structural information makes GIXD appropriate for the real time observation of polymer-fullerene blend crystallization in thin films during drying.

4.3 Real time observation of morphology formation¹

In preceding chapters, the solubility limits and phase transitions of the used soluble organic semiconductors are discussed for the solvent 1,2-dichlorobenzene. This chapter comprises the in-situ measurement of P3HT:PCBM blend crystallization in solution cast films by grazing incidence X-ray diffraction (GIXD), which is accomplished simultaneously with laser reflectometry. Figure 4.6 depicts schematically the combination of GIXD and reflectometry, whereas GIXD reveals structural information and laser reflectometry provides the evolution of film composition as discussed in chapter 2.2. After the proof of principle of this experimental approach at the synchrotron facility Ångströmquelle Karlsruhe (ANKA) in 2009 all further experiments have been carried out at the European Synchrotron Radiation Facility (ESRF, Grenoble, France) which provides higher X-ray intensity for reduced integration time of each measurement.

¹ The essence of this section is published in [58, 81].

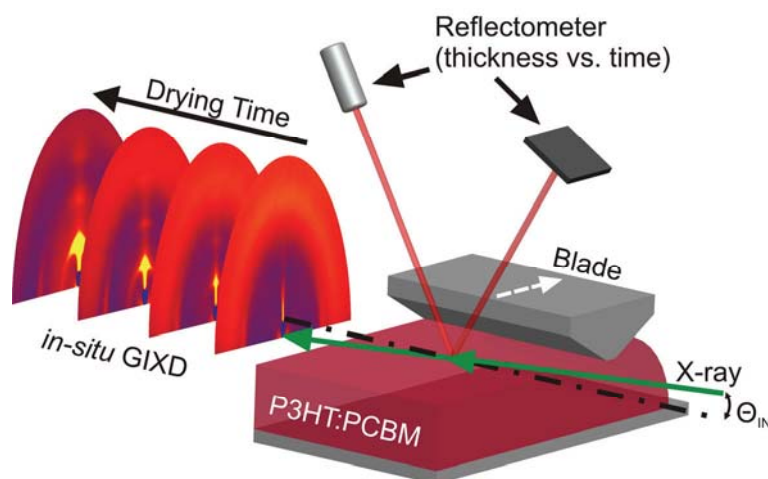


Figure 4.6: Scheme of in-situ drying experiments of knife cast P3HT:PCBM films simultaneously monitored by GIXD and laser reflectometry. [58]

Experimental The real-time GIXD study was done at beamline ID10B with 12.3 keV (wavelength $\lambda \approx 1 \text{ \AA}$) photon energy in the European Synchrotron Radiation Facility (ESRF, Grenoble, France) during the evaporation of the solvent in a temperature controlled drying channel (Figure 2.1) with X-ray transparent aluminum windows. Figure 4.7 depict photographs of the experimental hutch and the coating and drying setup. As substrates glass slides coated with PEDOT:PSS or native silicon wavers were used. To enable slow drying, the film was dried at 25°C without airflow. The X-ray diffraction patterns of the drying blend film were taken with an area detector (MarCCD) with 3 seconds of integration time in intervals of 50 seconds. After taking an image, the sample was moved horizontally in the direction of coating by 0.6 mm (the horizontal beam size was determined by the horizontal slit width which was 0.5 mm) to measure a section of the film not previously exposed to direct radiation. The 2D MAR-CCD images were corrected and translated into undistorted reciprocal space maps. The analysis of all GIXD experiments of this work has been conducted by Monamie Sanyal within her thesis.

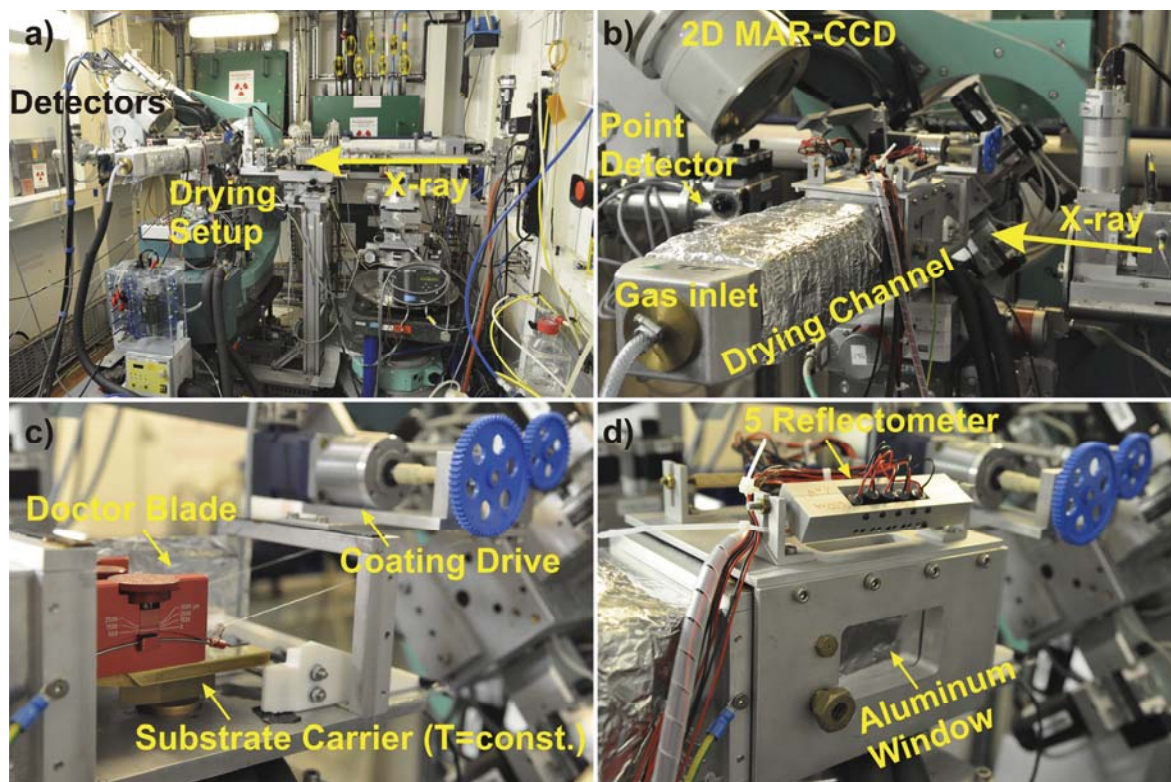


Figure 4.7: a) Overview of the experimental hutch. b) Drying channel mounted at the goniometer with horizontal incident X-ray. c) Coating knife (doctor blade) at temperature controlled substrate carrier with its step motor based drive. d) Closed drying channel with five reflectometers on top.

Results and Discussion With the combined experimental approach of GIXD and laser reflectometry the real time observed phase transitions shall be compared to the expected phase transitions according to the superposition of the binary phase diagrams (see chapter 3.4 and 3.5). The phase transitions according to the binary phase diagrams are depicted in the ternary P3HT-PCBM-DCB phase diagram as star symbols in Figure 4.8a. For improved readability an enlarged inset of the upper corner of the ternary phase diagram is additionally shown. The position of the freshly coated wet film is indicated by the first open circle in the upper corner. The position of each GIXD measurement obtained during film drying of a P3HT:PCBM (1:0.8) film is also depicted in the ternary phase diagram (open circles in Figure 4.8a). The appearance of different diffraction features are denoted in the ternary phase diagram, but shall be evaluated more concisely later. The star symbols indicate the position of the binary solubility limits at the binary axis.

4.3 Real time observation of morphology formation

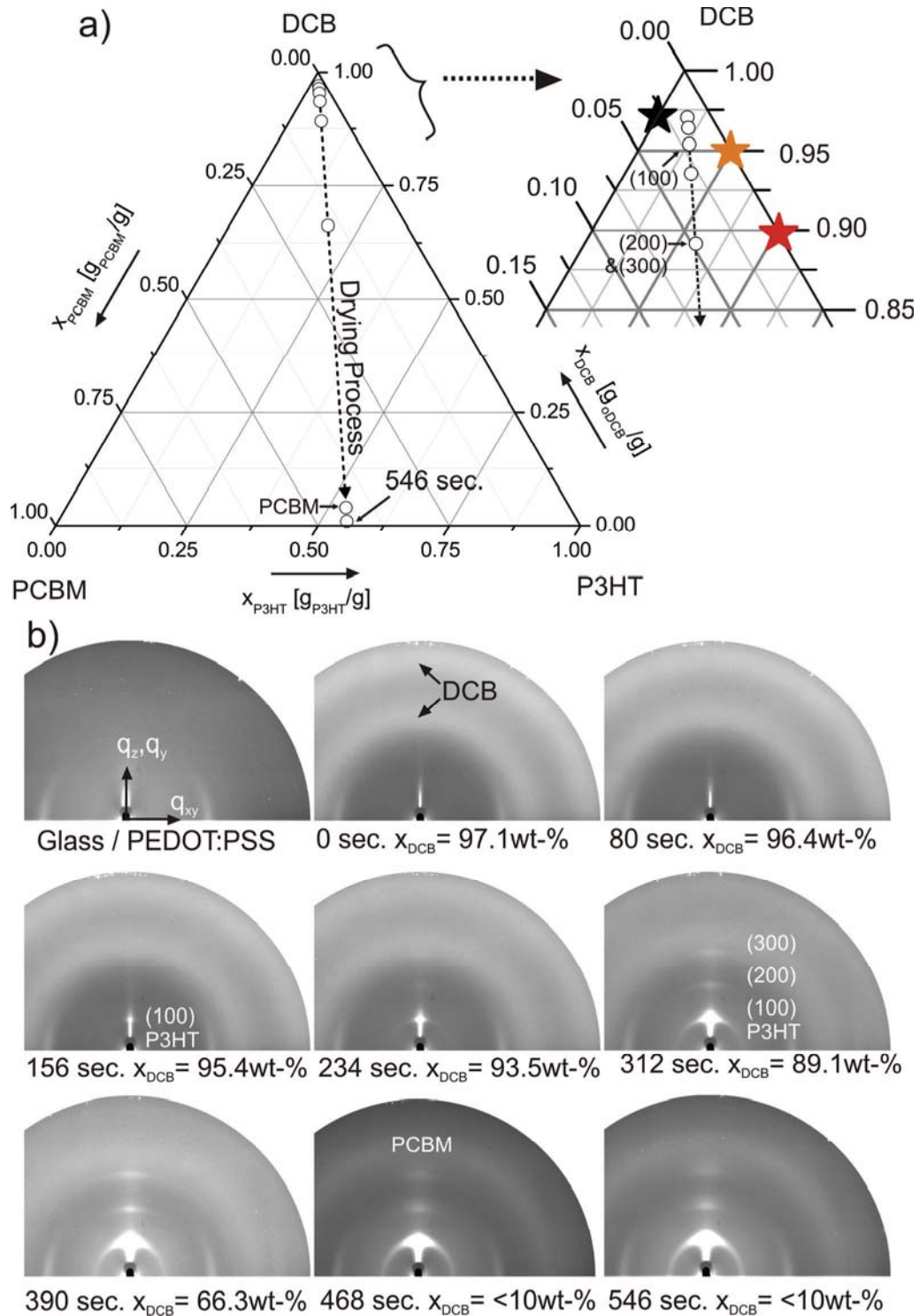


Figure 4.8: a) Ternary phase diagram of P3HT-PCBM-DCB; the star symbols denote phase transitions in the binary cases. Each open circle symbol indicates a frame of GIXD measurements shown in figure b). The first image is of the neat PEDOT:PSS/glass substrate and the following images show the evolution of film drying and crystallization. Below each image, the drying time and actual solvent fraction is given. [81]

4 Morphology formation in polymer-fullerene films

A first inspection of the diffraction patterns in Figure 4.8b already indicates the evolution of the (100) Bragg peak of P3HT starting from a spot-like shape (indicating an edge-on configuration) and ending as the often reported wing-like shaped peak (larger orientation distribution) of the solid film [75, 219]. The film composition at each instant of GIXD measurement is mentioned below each image.

In order to quantify the dynamics of blend crystallization, a measure for PCBM and P3HT relative crystallinity must be defined. For the powder like diffraction ring of PCBM we chose an integrated annular section of the diffraction ring (s. Figure 4.5). In the case of the anisotropic structure and diffraction pattern of P3HT, we use the annular integrated area of the (100) Bragg peak in order to take all the crystallite orientations into account. This is indicated by the area enclosed by two dashed lines in the inset of Figure 4.9. However, the amount of P3HT crystallites is not the only information we can obtain from the 2D images, since the mosaic spread obtained from the annular peak width provides information about the orientation distribution of P3HT crystallites.

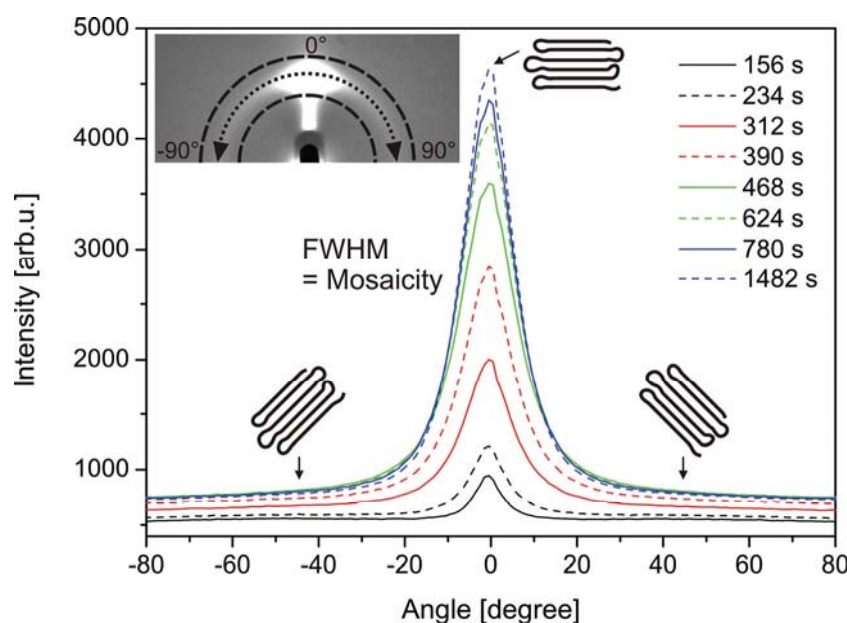


Figure 4.9: Evolution of the annular intensity profiles of the P3HT (100) Bragg peak. The inset depicts the (100) Bragg peak integration area and the annular geometry for the determination of mosaicity. The FWHM of the shown Gaussian fits to the intensity distribution is called mosaicity.

The intensity is expressed as a function of the annular angle as shown in Figure 4.9, where the intensity profile is integrated in-between the indicated dashed semi circles. These profile plots, which are Gaussian fits to the measured data, depict the orientation distribution of P3HT crystallites with respect to the substrate. A common measure for this distribution is the full width at half maximum (FWHM), which is called mosaicity.

In the following the evolution of PCBM and P3HT crystallinity, as well as the mosaicity of P3HT crystallites is discussed in relation to the evolution of film composition during drying. The time evolution of the film composition is plotted in Figure 4.10a. To cover the entire evolution of the solvent fraction, a model of constant gas phase mass transfer coefficient for the film drying kinetics was adapted to the experimental data [56]. In high diluted solutions, the decrease of solvent mass fraction x_{DCB} proceeds slowly in the beginning, leading to a long residence time at solvent fractions > 85 wt.%. As the solid fraction becomes significant, the solvent fraction x_{DCB} reduces rapidly and a wide range in the phase diagram is crossed quickly, offering little time for further molecular ordering. Nevertheless, the thickness decreases almost linearly over the constant rate period (drying period I) due to an almost constant evaporation rate. In the falling rate period (period II), at high solid fractions, the evaporation rate decreases due to the increased diffusional limitation of solvent being trapped in the film. This provides less mobility for solvent transport to the surface. In this period no interference patterns are observed anymore due to very low changes in film thickness, but the reflectometer signal changes until the optical properties remain constant. This state is defined as dry. Hence, experimentally we are able to determine the time range of the falling rate period. The thickness evolution in this range can be resolved by ellipsometry (see appendix section A 1.4 and [57]).

The bars in Figure 4.10a labeled with PCBM, P3HT (sol-gel) and P3HT (gel) indicate the instants when the solubility limits/phase transitions of each component are reached for the binary cases. The width of each bar originates from two cases of transferring the binary phase diagrams to the ternary system. Denoted as case i), we assume that the solvent is distributed between both solid constituents with respect to their weight ratio (here 1:0.8). For case ii) we assume that the entire solvent is available for each solid compound.

4 Morphology formation in polymer-fullerene films

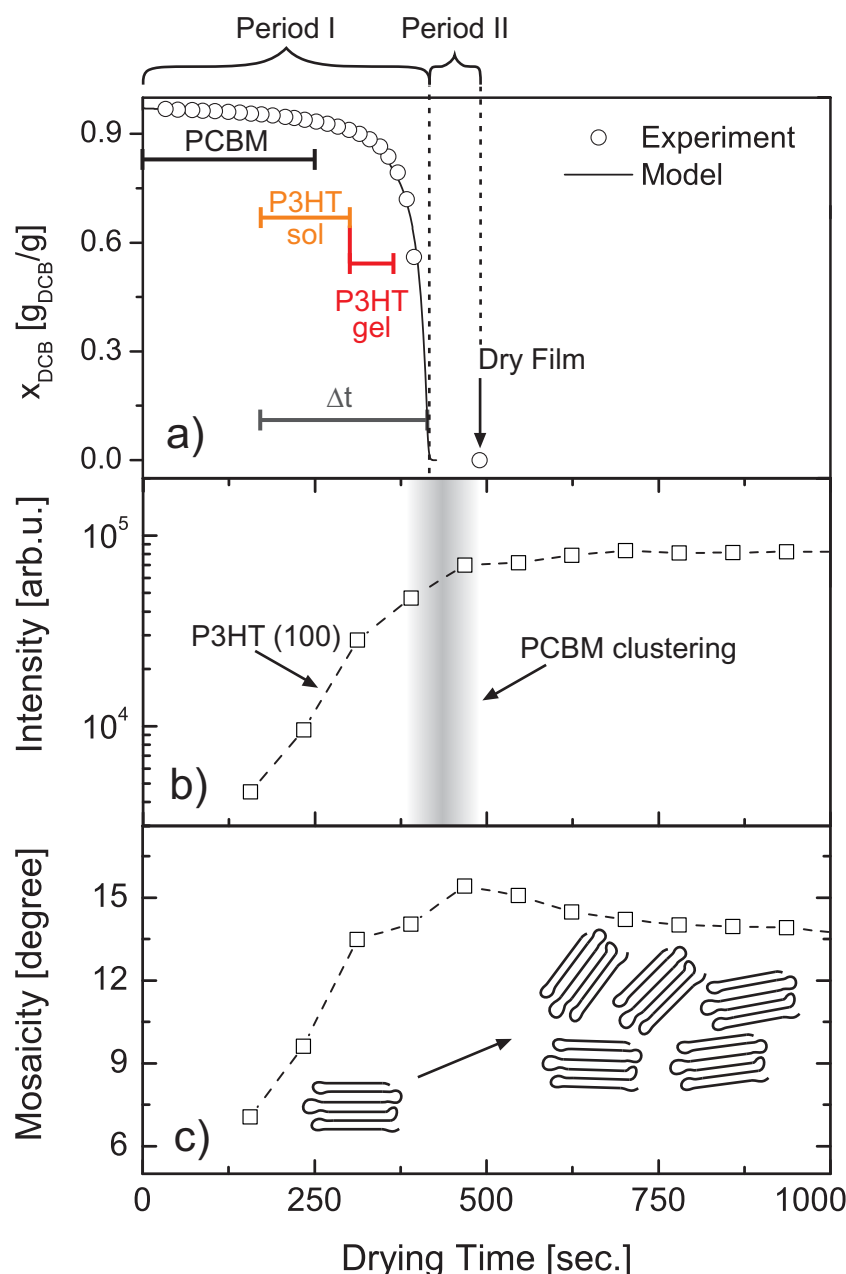


Figure 4.10: a) Evolution of film composition (solvent mass fraction x_{DCB}) during film drying of P3HT:PCBM films on PEDOT:PSS/Glass as obtained from laser reflectometry (data - symbols, fit from model - line). The labeled bars indicate ranges of phase transitions as expected from the superposition of the binary phase diagrams. b) To obtain the measure of overall P3HT crystallinity in the blend film, the integrated area of the P3HT (100) Bragg peak is plotted versus drying time. c) Evolution of P3HT mosaicity during film drying. [81]

These expected transitions of Figure 4.10a are compared with the in real time observed evolution of P3HT crystallinity (Figure 4.10b), obtained from the

integrated intensity of the P3HT (100) Bragg peak. For P3HT, we initially expect a delay in crystallization until the solubility limit is reached. Regarding the marginally decreasing solvent fraction in this period, the expected instant of delayed P3HT nucleation at the solubility limit (according to case i and ii the P3HT solubility range is about $x_s = 5.1 - 9.1$ wt.% which is equivalent to $x_{DCB} = 90.9 - 94.9$ wt.%) is confirmed by the appearance of the P3HT (100) Bragg peak after 156 s of film drying at $x_s = 4.6$ wt.%. The integrated Bragg-Peak intensity of P3HT is low at this phase of nucleation. Subsequently the intensity increases and near the range of complete gelation, the second and third order Bragg peaks appear, indicating further solidification and ordering. When the film is dry, the intensity of the P3HT (100) Bragg peak also remains almost constant. A slight intensity increase afterwards may be attributed to “solvent annealing” from the remnant solvent vapor in the atmosphere. Note that there was no gas flow in the drying channel to ensure slow drying conditions. In contrast to the expectations, PCBM crystallizes at a later stage of drying, which will be discussed later.

The spot-like P3HT (100) Bragg peak, or in other words low mosaicity, in Figure 4.8b at 156s indicates the initially formed P3HT nuclei to be very well aligned in edge-on configuration [71, 75, 220]. This implies that the nucleation is induced by a planar interface. Our measurements do not prove whether the nucleation takes place at the film surface or the buried film/substrate interface, but the most reasonable case shall be discussed in the following. In literature strong influence of substrate surface energy on the final dry film crystallinity is reported [94, 102, 221, 222], which suggests the morphology formation to take place at the film/substrate interface. Furthermore, a solvent concentration gradient with increased solid fraction at the air/film interface can be excluded as driving force for crystallization at such an early stage of about 95 wt.% solvent fraction for the low volatile DCB. We deduce therefore, that P3HT nuclei most probably form at the buried film/substrate interface. From the well oriented layer, further polymer crystallites are growing, whereby the subsequently formed P3HT crystallites exhibit an increasing disorder, which can be seen in an increasing wing-like (100) Bragg peak shape with proceeding solvent evaporation in Figure 4.8b and an increasing mosaicity in Figure 4.10c.

Now we retake the discussion of initially suppressed PCBM crystallization. Though the DCB and PCBM diffraction peaks nearly overlap, profile plots in Figure 4.11 show the emergence of the diffraction peaks of PCBM

4 Morphology formation in polymer-fullerene films

after DCB diffraction peaks have largely depleted. The overlap of PEDOT:PSS and PCBM diffraction peak, makes it difficult to decipher the appearance of the PCBM peak following the disappearance of DCB diffraction peaks. Hence, the profile plots in Figure 4.11 were taken with a bare silicon substrate. The P3HT (100) Bragg peak at $q_z = 0.4 \text{ \AA}^{-1}$ appears in this experiment at 702 s drying time ($x_s = 14 \text{ wt.}\%$), while the PCBM diffraction peak at $q_z = 1.36 \text{ \AA}^{-1}$ starts to form at 864 s ($x_s = 46 \text{ wt.}\%$). Even in comparison to the highest published PCBM solubility of 7.7 wt.% (see Table 3.1) our observations give evidence to a foremost polymer crystallization followed by a PCBM clustering at a later stage of drying.

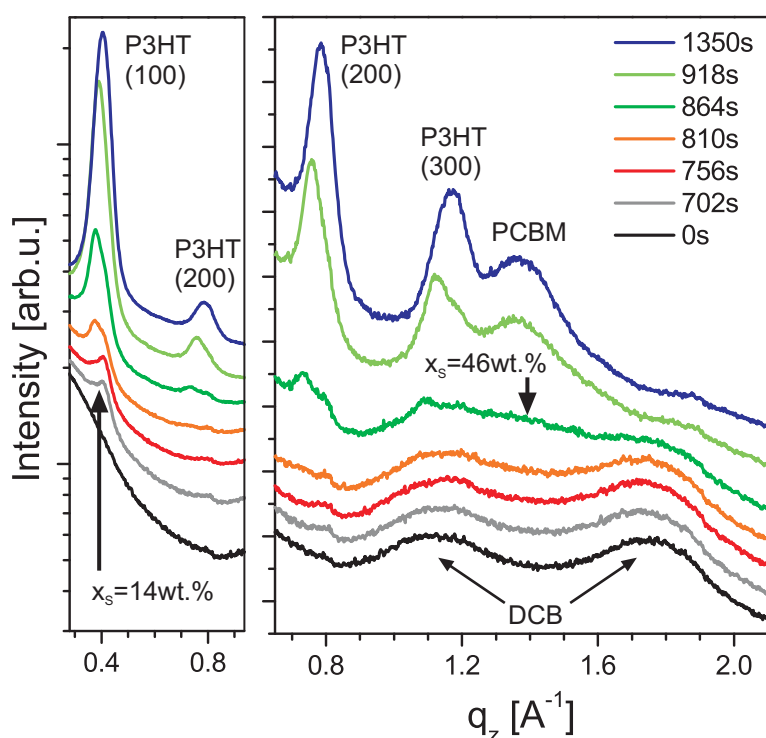


Figure 4.11: Selected profile plots at increasing drying times showing the emergence of the diffraction peaks of PCBM, P3HT (h00) Bragg peaks and disappearance of the diffraction peaks of the evaporating solvent DCB on a silicon dioxide/silicon substrate (log scale left, linear right). Vertical offset accomplished for clarification. [81]

According to these observations of oppressed PCBM crystallization, strong interactions between the fullerene and polymer molecules may be deduced. Hence, the polymer-fullerene interactions prevail over the fullerene-fullerene forces that should facilitate a solubility driven PCBM crystallization at the beginning of drying. This is supported by the observation of large

4.3 Real time observation of morphology formation

micrometer sized PCBM crystallites if the polymer is absent [223]. Further, it is remarkable that the dimensions of phase separated P3HT-PCBM structures in the range of a few tens of nanometers are very small, even for very long drying times in comparison to less miscible and hence less interacting blends [101, 223, 224].

The spacing of P3HT alkyl chains does not offer enough space for intercalating PCBM molecules in-between the side chains [225]. Collins et al. showed that in thermodynamic equilibrium P3HT crystallites only comprise 3-4 % PCBM [44]. Accordingly PCBM molecules must be squeezed out of the area where the polymer crystallizes. There are many hints in literature that this step of P3HT crystallization is a slow process as for example slow drying promotes crystallinity [109, 110, 192]. Selectively PCBM solvating additives [55, 207] reduce these strong interactions and promote polymer crystallization.

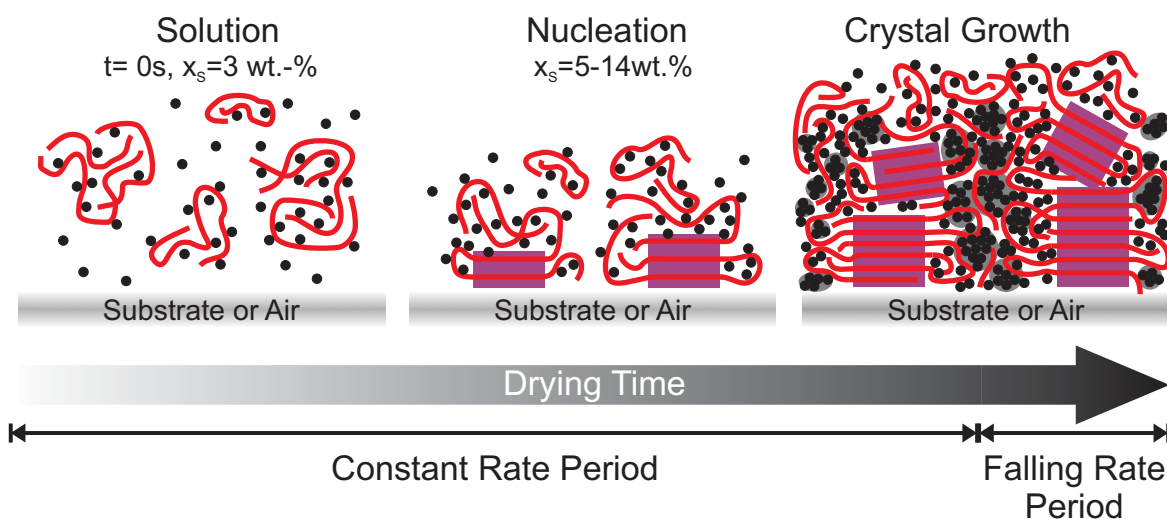


Figure 4.12: Schematic of the stages of molecular arrangement during solvent evaporation with nucleation at the substrate or air interface. Lines represent P3HT chains, purple boxes P3HT crystallites, dots PCBM molecules and grey circles PCBM aggregates. [81]

The above discussed structure evolution is schematically shown in Figure 4.12, where PCBM is symbolized as dots, PCBM aggregates as grey circles, P3HT as lines and purple rectangles symbolizing crystalline P3HT domains. Blend crystallization proceeds with the following steps: i) P3HT crystallization at the substrate surface followed by ii) polymer crystal growth in (100) direction with increasing mosaicity. Subsequently iii) PCBM is

squeezed out of the lamellae and aggregates in a final drying period. The π - π -stacking is normal to the image plane and is therefore not illustrated. The novel insights into morphology formation of this work provide a fundamental understanding of the molecular assembly during film drying.

In comparison to a low PCBM solubility of only 3-4 % in crystalline P3HT, Collins et al. observed a solubility of about 16 % in amorphous P3HT regions [44]. This confirms the image of mainly pure crystalline P3HT domains comprising very few PCBM inclusions, amorphous P3HT regions containing higher amounts of PCBM molecules and PCBM clusters partly intermixed in the amorphous P3HT regions.

4.4 Influence of polymer-fullerene blending ratio¹

The powerful approach of real time observation of structure formation shall now be applied to investigate the structure dependence on donor-acceptor blending ratio, which is known to be crucial for efficient polymer solar cells. It is known from literature that the optimized P3HT:PCBM blending ratio is close to 1:0.8 [31]. The ratio dependence of device performance has been investigated in relation to the binary P3HT:PCBM phase diagram by calorimetry [147, 165] and dynamic mechanical analysis [141]. Optimum device performance is reported to be in slight hypoeutectic composition (slight excess of PCBM), which is assumed to increase the PCBM network that acts as conductive electron pathways [165]. The available reports focus on the investigation of equilibrium states generated by heating the blend films up to the melting point. The focus of our work is on the ratio dependent structural evolution during film drying as it proceeds in the fabrication process of OPV.

Experimental P3HT:PCBM films were cast on PEDOT:PSS/Glass substrates by doctor-blade (70 μ m slit width and 5mm/s coating speed) in the ratios 1:0, 1:0.5, 1:0.8 and 1:2 from $x_s=3$ wt.% DCB solution. Final film thicknesses were 200 nm (1:0.5), 135 nm (1:0.8) and 70 nm (1:2), due to the decreasing fraction of higher viscous polymer. Pure PCBM was drop cast and

¹ The essence of this section is published in [80].

dried under vacuum in order to prevent large scale crystallization. For the real time observation, the drying gas flow in the setup was switched off for realizing slow drying conditions. In-situ GIXD measurements were obtained at ID10B beamline at ESRF as described before (wavelength $\lambda = 0.934 \text{ \AA}$) with 3 seconds integration time in intervals of 50 seconds. The 2D MAR-CCD images (Figure 4.13) were corrected and translated into undistorted reciprocal space maps. Ex-situ GIXD measurements at PEDOT:PSS/ITO/Glass substrates were done at the MPI-MF beamline of the synchrotron facility Ångströmquelle in Karlsruhe (ANKA) at 8 keV energy ($\lambda = 1.55 \text{ \AA}$) with a point detector. The absorption was measured in transmission with a spectrophotometer (Perkin Elmer, Lambda 1050) using a blank PEDOT:PSS/ITO/glass substrate as reference.

Results and Discussion Figure 4.13 depicts four 2D X-ray scattering frames for the drying process of each blending ratio. The top image shows the as cast state of the wet film. The next image shows the appearance of the first P3HT Bragg peak, followed by the appearance of second and third Bragg peak. The bottom image depicts the state of the final film structure in the dry state. At the beginning the diffraction images only comprise both DCB diffraction rings. The appearance of the P3HT (100) Bragg peak shows for all cases a spot-like shape, which indicates a surface induced nucleation of well aligned crystallites in edge-on configuration. In the succeeding drying process it is notable that the shape remains spot-like for the 1:2 blending ratio. A deeper analysis of the final film structure in the dry film shows an increasing mosaicity from the ratio 1:2 over 1:0.8 to 1:0.5 [80]. The average P3HT spacing of 16.5 \AA associated with the P3HT (h00) peaks does not show any dependency on blending ratio. These images do not give insights into the quality of P3HT (020) π - π stacking, which will be discussed below.

A summary of the observed structural evolution is given in relation to the position in the phase diagram in Figure 4.14a. The related drying kinetics are depicted as evolution of film thickness and solvent mass fraction in Figure 4.14b. The drying kinetics could only be measured for 1:0.8 blending ratio due to the low optical contrast for PEDOT:PSS/Glass substrates. A constant mass transfer coefficient was fitted to the 1:0.8 ratio drying experiment according to reference [56] and served for the simulation of the other blending ratios. The crystallization kinetics are in reasonable agreement with the simulated evolution of solvent evaporation, which is shown in reference [80].

4 Morphology formation in polymer-fullerene films

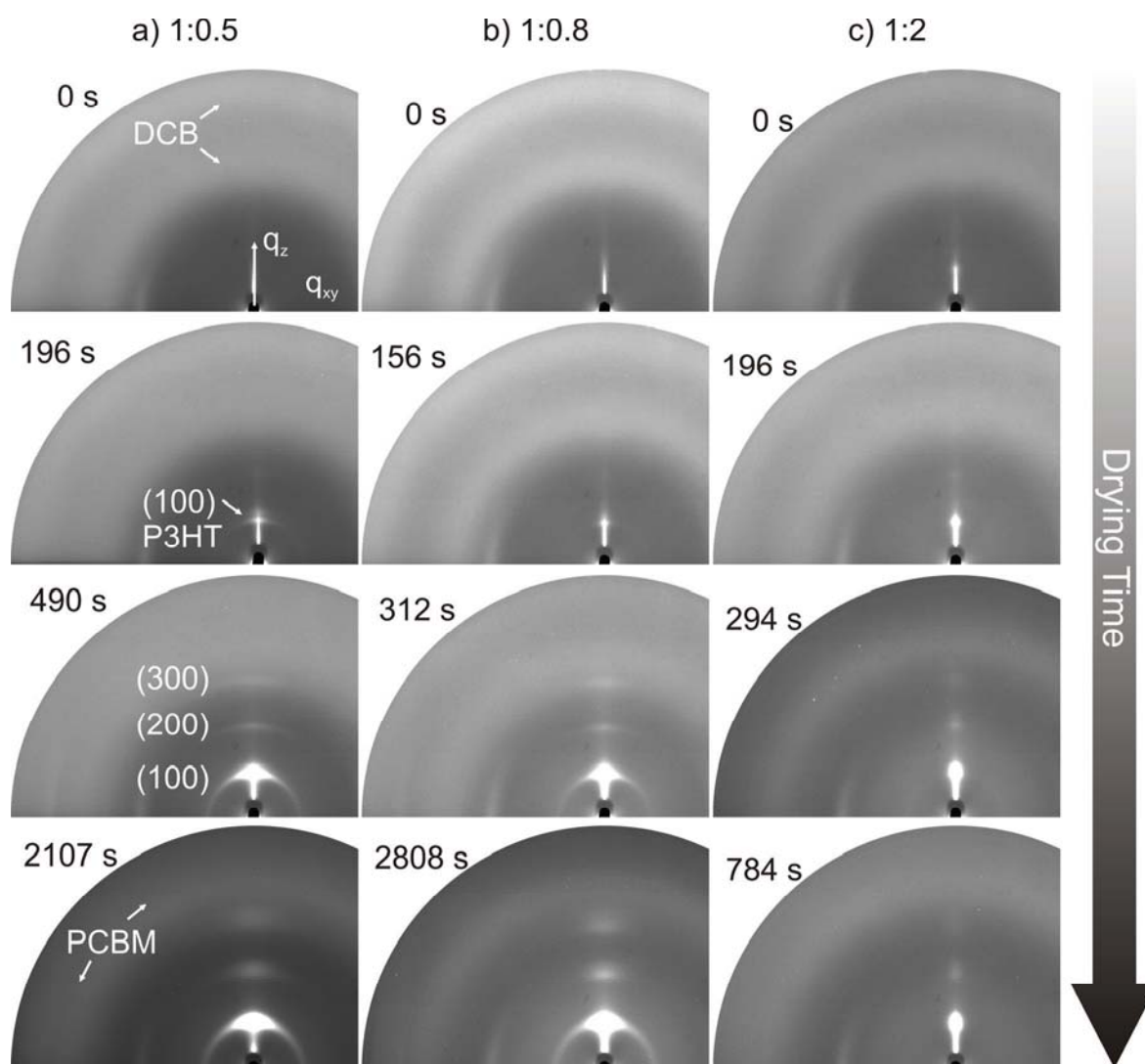


Figure 4.13: 2D x-ray diffraction patterns at different instants of drying for P3HT:PCBM blend ratios (a) 1:0.5, (b) 1:0.8 and (c) 1:2. The stages of drying are from top to bottom: initial instant of drying, first observation of the P3HT (100) peak, observation of the P3HT (200) and (300), observation of PCBM diffraction ring. [80]

Again we observe final long term crystallization after the solvent has largely depleted, as discussed before in Figure 4.10. The comparison of both Figure 4.14a and b demonstrates the difference between the position in the phase diagram and the time scale. This is due to the strong nonlinear decrease of the mass fraction in the drying process. As it was already shown in the preceding chapter 4.3, we observe for all blending ratios a delay of crystallization until the solubility limit of P3HT is reached (after 150-200 s drying time). The delay of P3HT (100) Bragg peak appearance (symbols at highest

4.4 Influence of polymer-fullerene blending ratio

solvent fraction) is stronger for the 1:2 blending ratio, which might be due to the comparatively high amount of present PCBM. The appearance of the higher order P3HT Bragg peaks proceeds for the ratio of 1:0.8 first, followed by the ratio 1:0.5 and at last 1:2.

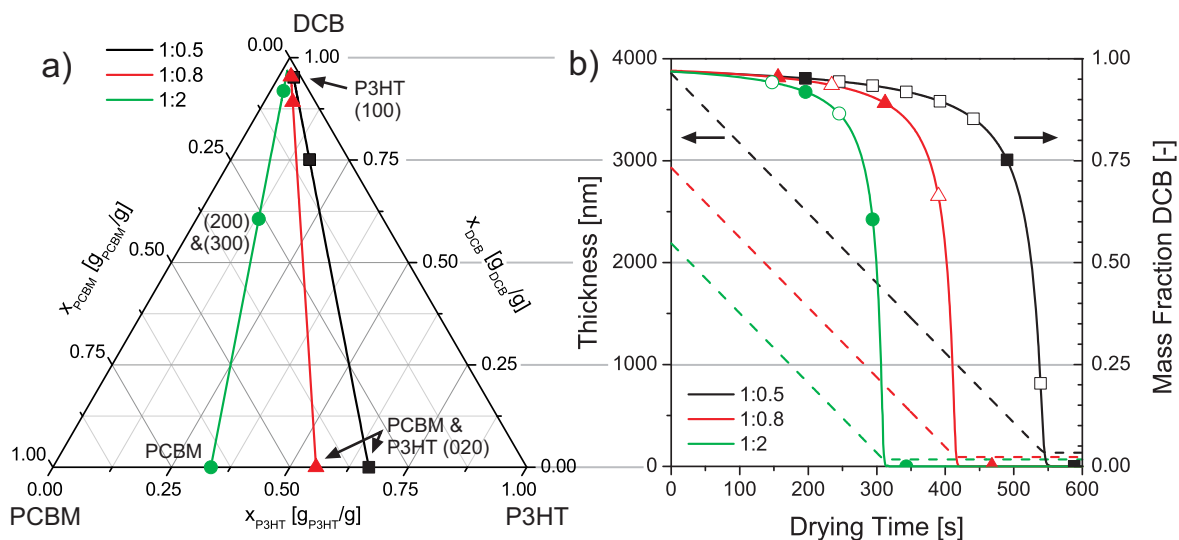


Figure 4.14: a) Drying path through the phase diagram of different P3HT:PCBM blending ratios at 25°C. Symbols indicate the appearance of P3HT (100) Bragg peak, (200) and (300) and the PCBM diffraction ring in order of appearance from top to bottom. b) Drying kinetics of the investigated films. Each symbol represents a GIXD measurement. Filled symbols are related to the instants of structural changes indicated in the ternary phase diagram

PCBM aggregation takes place in the final stage of drying, which is indicated by the symbols that represent the dry state at the binary P3HT-PCBM axis (bottom axis of triangle diagram). Because of the steep drop of solvent mass fraction in the final drying stage and the overlapping diffraction peaks of PCBM, DCB and PEDOT:PSS, it is not possible to determine the exact instant of PCBM aggregation for these substrates. However, for native silicon substrates we could derive the late PCBM aggregation close to the dry state of the film. Further point detector analysis of the dry films reveal a strong impact of P3HT:PCBM blending ratio on the (020) packing direction as it is shown in the in-plane intensity profiles along q_{xy} in Figure 4.15a. For pure P3HT and the ratios 1:0.5 and 1:0.8 (data not shown) a strong P3HT (020) Bragg peak is observed, which corresponds to the π - π -stacking of polymer

4 Morphology formation in polymer-fullerene films

backbones. This is an important issue, since this crystalline direction provides a high hole mobility for charge extraction over wide distances [45].

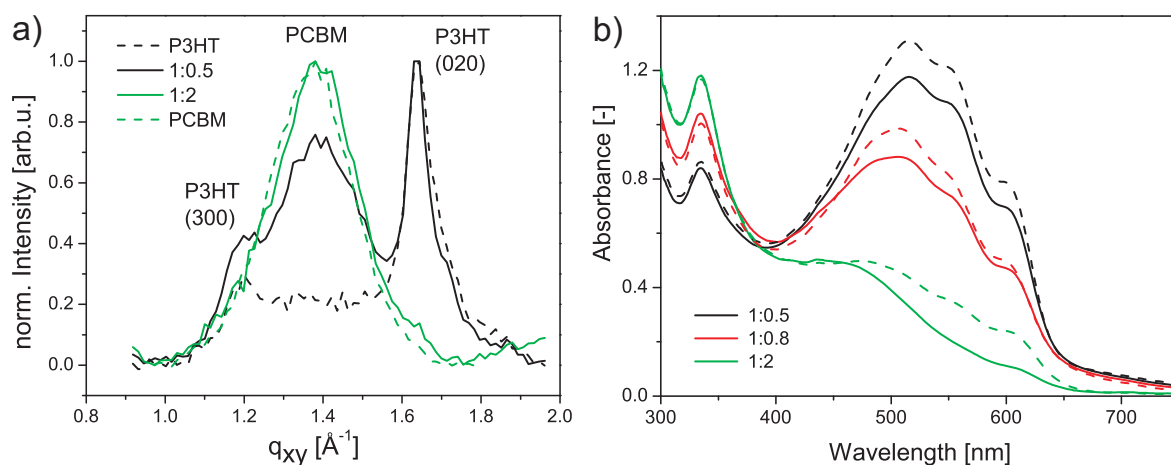


Figure 4.15: a) In-plane profile plots from GIXD point detector measurements and b) Absorption spectra of doctor bladed P3HT:PCBM films of different blending ratios for as cast film (solid line) and thermally annealed films for 5 min at 150°C (dashed line). [80]

For the highest amount of PCBM (1:2), the (020) peak disappears completely. This indicates that the P3HT π - π -stacking is broken by intercalating PCBM molecules in-between the polymer backbones. This is confirmed by the disappearance of the vibronic shoulders at 560 and 605 nm in the absorption spectra (Figure 4.15b), which are also related to P3HT π - π -stacking. Thermal annealing promotes the diffusion of PCBM out of the π - π -stacking area in-between the lamellae and allows for an improvement of π - π -stacking. This is expressed by the increasing shoulders in the absorption spectra. It should be noted that the logarithmic character of the absorbance may lead to an over interpretation of the improved absorption due to annealing.

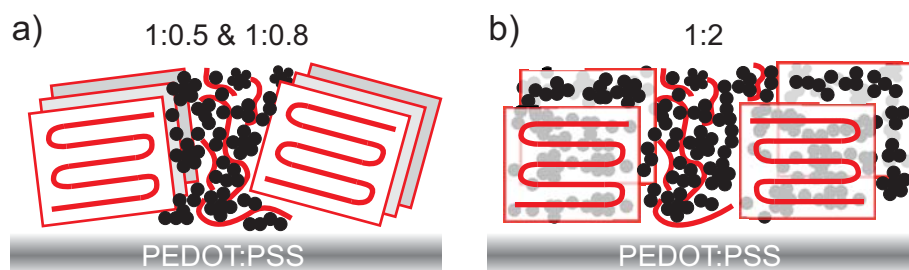


Figure 4.16: Cartoon depicting the P3HT:PCBM blend structure in ratios of a) 1:0.5 and 1:0.8 and b) 1:2 for PEDOT:PSS covered substrates. [80]

Figure 4.16 schematically summarizes the impact of blending ratio on film morphology: mosaicity increases with the P3HT fraction and π - π -stacking is hampered by excessive amount of PCBM as it could be shown here for the blending ratio 1:2.

4.5 Influence of drying temperature¹

Since the optimized donor-acceptor blending ratio is mostly fixed for a distinct material system, we focus in the following on other methods for the manipulation of film structure. Accessible and precisely tunable parameters for controlling the drying process are the drying temperature and the drying gas velocity. Temperature influences several parameters like solvent vapor pressure, solubility and the diffusion kinetics in gas and liquid phase. In contrast to this, drying gas velocity only influences the mass transfer coefficient in the gas phase, which is proportional to the evaporation rate of solvent. This section investigates the impact of these two parameters on structure evolution and explores the possibilities for solar cell efficiency improvement due to optimized drying conditions.

4.5.1 In-situ observation of molecular ordering

Experimental In order to investigate the effect of drying temperature P3HT:PCBM films are fabricated under different drying conditions in the range of 10°C-80°C drying temperature and 0.15 m/s and 0.5 m/s gas velocity. Drying conditions are precisely defined in the drying channel with integrated doctor blade (see Figure 2.1). The solid fraction of the blend-solution film was kept constant, in order to start the drying process at the same position in the phase diagram. The final thicknesses were 68 nm, 95 nm, 119 nm, 191 nm for drying temperatures of 80°C, 40°C, 25°C and 10°C respectively. The thickness decreases with increasing coating and drying temperature due to the lower viscosity of the wet film for a constant solid fraction and similar coating conditions (70 μ m slit width and 5mm/s coating speed). In order to exclude the thickness influence on the final film morphology, equal film thicknesses are fabricated for the ex situ morphology and solar cell characterization as shown in sections 4.5.2 and 4.5.3 respectively.

¹ Benedikt Brenneis [268] dedicated his diploma thesis the investigation of the drying temperature influence on film structure. The essence of this chapter is published in [58, 81]

The real-time GIXD study was done at beamline ID10B with energy 12.3 keV in the European Synchrotron Radiation Facility (ESRF), Grenoble, France during the evaporation of the solvent in a temperature controlled environment utilizing PEDOT:PSS (H.C. Starck, Clevios VP Al 4083) coated glass slides or native silicon wavers as substrates. The x-ray diffraction patterns of the drying blend film were taken with an area detector (MarCCD) with 3 seconds of integration time in intervals of 50 seconds. The 2D MAR-CCD images were corrected and translated into undistorted reciprocal space maps.

Results and Discussion A first inspection of 2D GIXD diffraction patterns obtained from P3HT:PCBM films that were dried at different temperatures, allows a first structural interpretation (Figure 4.17).

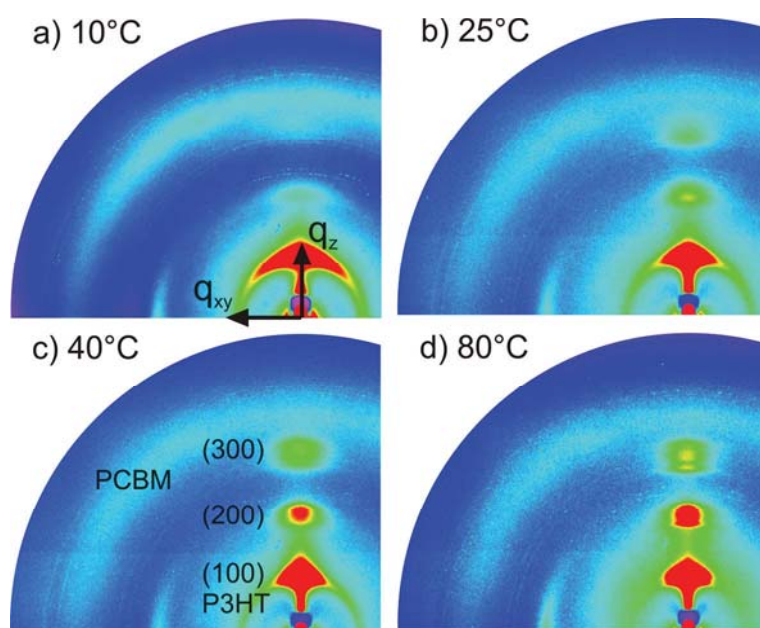


Figure 4.17: GIXD diffraction patterns of the final P3HT:PCBM films dried at 10°C, 25°C, 40°C and 80°C cast from DCB at PEDOT:PSS/glass substrates. [58]

At all drying temperatures, P3HT (h00) Bragg diffraction peaks are observed along q_z in out-of-plane direction, indicating that P3HT is mainly oriented in edge-on configuration (s. Figure 4.2). The wing-like shape of the P3HT (100) Bragg peak decreases with increasing temperature revealing a lower mosaicity (narrower orientation distribution). The higher order Bragg

peaks are more pronounced at higher drying temperatures, suggesting that P3HT ordering in (h00) direction increases for higher drying temperatures. Furthermore, the estimated P3HT (100) crystallinity increases with drying temperature. It is about three times higher¹ for films dried at 80°C than at 10°C. The evolution of these different structural properties and their optoelectronic performance are investigated in the following.

As previously described, GIXD is utilized for monitoring the blend crystallization during solvent evaporation by 2D detector measurements. The integrated (100) Bragg peak area gives a measure for overall P3HT crystallinity, regardless of the crystallites orientation. Figure 4.18a depicts the evolution of P3HT overall crystallinity in the course of film drying at different drying temperatures. To ensure slow drying, the drying channel was operated without airflow. All plots are normalized to each maximum value of intensity.

The crystallization kinetics show a faster increase of crystallinity for higher drying temperatures as well as the drying proceeds faster at higher temperatures. Hence, crystal growth is related to the evolution of solid fraction in the film. According to reference [57] the Avrami equation 4.1 [194-196, 226] – which is frequently used to describe isothermal crystallization processes – is fitted to the normalized crystallization kinetics as obtained by in-situ GIXD. The S-shape of the Avrami fits originates from a sequence of mechanisms of crystal growth. i) Initially the crystal growth is low because of the low amount of nuclei which increases with time. ii) Subsequently, the crystallization rate increases due to a dominating growth based on the previously formed nuclei. iii) In the final phase the decrease of crystallization rate is caused by the impingement of grains upon each other and the cessation of growth in the overlapping regions [194]. The exponent n of the equation is used for exploring the type of crystallization. Wang et al reported a value for n of 1.8 ± 0.1 for P3HT:PCBM films cast from chlorobenzene [57]. The drying time was about 15 s at 30°C drying temperature. In our case the exponents exhibit values of $n(10^\circ\text{C}) = 2.0 \pm 0.1$, $n(25^\circ\text{C}) = 3.2 \pm 0.4$, and $n(40^\circ\text{C}) = 3.4 \pm 3.5$. The strong standard deviation at 40°C drying temperature originates from the strong mismatch of decreasing intensity after reaching the

¹ The measured intensity may be slightly underestimated for films with a larger amount of edge-on orientation on the surface (e.g. 80°C) since the exact Bragg condition (scattering angle = $2 \times$ incidence angle at (100) P3HT Bragg peak) is not met in this geometry. [58]

4 Morphology formation in polymer-fullerene films

maximum crystallinity. It is important to note that each curve was normalized to its maximum value. The final crystallinity is not 100% and it differs for the different drying temperatures. Highest P3HT (100) crystallinity is achieved at 40°C which decreases with temperature exhibiting lowest (100) crystallinity at 10°C.

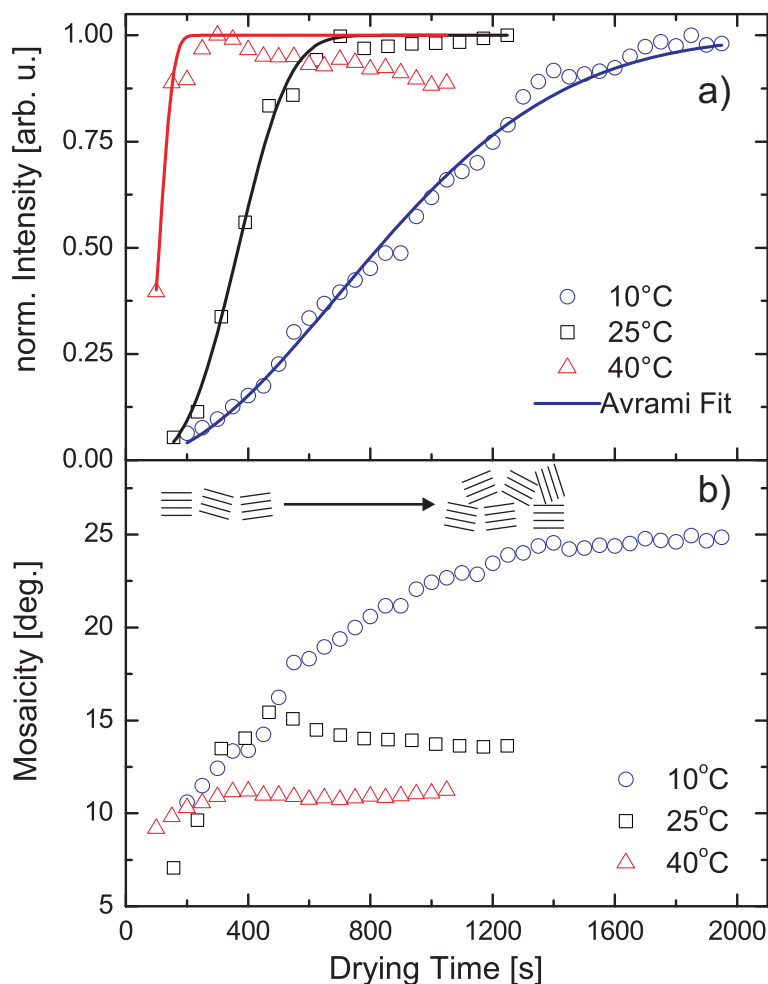


Figure 4.18: a) Evolution of normalized P3HT (100) Bragg peak intensity at 10°C, 25°C and 40°C drying temperature. Symbols indicate in-situ GIXD measurements and lines the Avrami fits. b) Evolution of mosaicity obtained from the same in-situ GIXD measurements. [58]

A deeper analysis of the Avrami parameters of this fairly simple approach is not undertaken due to many experimental limitations such as [227-230]:

- constant volume during crystallization
- constancy in shape of growing (disc, rod or sphere)

- no induction time
- unique nucleation mode (thermal or athermal but not both)
- complete sample crystallinity
- constant value of radial density in growing structures

Figure 4.18b depicts the evolution of P3HT mosaicity (orientation distribution), which is related to the wing-like shape of P3HT (100) Bragg peak. It is remarkable that all curves start at a similar low mosaicity in the initial stage of drying. The evolution of mosaicity coincides for all drying temperatures with increasing drying time until each film has mostly dried. The highest value is reached for the longest drying experiment at the lowest drying temperature of 10°C. This suggests that the state of high orientation distribution is preferred and aspired if sufficient drying time is provided.

Since hole transport is only provided along the polymer backbone and in π - π -stacking direction the orientation of P3HT crystallites should affect the direction of hole conductivity. Therefore we assume that an increased mosaicity provides an increased hole transport in the vertical direction. This will be discussed based on solar cell devices below. Solar cells have been fabricated in collaboration with Michael Klein at the Light Technology Institute at KIT. Further dependencies of structural properties from molecular to macroscopic scale on drying conditions are discussed in the subsequent section.

4.5.2 Ex-situ characterization of film structure

Experimental Films discussed in this section have all been fabricated in the coating and drying setup used for the in situ experiments. Investigated drying process parameters were again gas flow velocity and drying temperatures. At low drying temperatures, the final films show high roughness which can partly lead to peak-valley distances of around 200 nm. Hence, films were prepared at comparatively high thicknesses of 350 ± 28 nm in order to prevent local shortcuts because of too low active layer thickness. In this thickness range, the absorption and solar cell efficiency exhibit a broad plateau [231] diminishing the influence of thickness fluctuations.

AFM measurements were done in tapping mode with a Veeco Dimension Icon. The root mean square roughness analysis was done on $10 \mu\text{m} \times 10 \mu\text{m}$ images of the final films.

Results and Discussion A more detailed investigation of different aspects of film morphology is discussed in conjunction with the drying history of the samples. Such exemplary constant rate period drying kinetics of the following discussed conditions are given in Figure 4.19a where the solvent mass fraction is plotted versus drying time. Both parameters temperature and gas flow rate affect the overall drying time for film formation. The influence of film thickness on drying time is shown in Figure 4.19b. This shall point out, that thickness variations may contribute to structural changes induced by changes of film formation time. The drying time after crossing a solubility limit, which is denoted as Δt changes with film thickness. We assume that this time is crucial for the molecular self-assembly. Hence, low fluctuations of film thickness are crucial for reliable interpretation of the structural investigations. Henceforth, we relate the observed structural changes to the drying time after crossing P3HT solubility as described previously as case I in section 4.3.

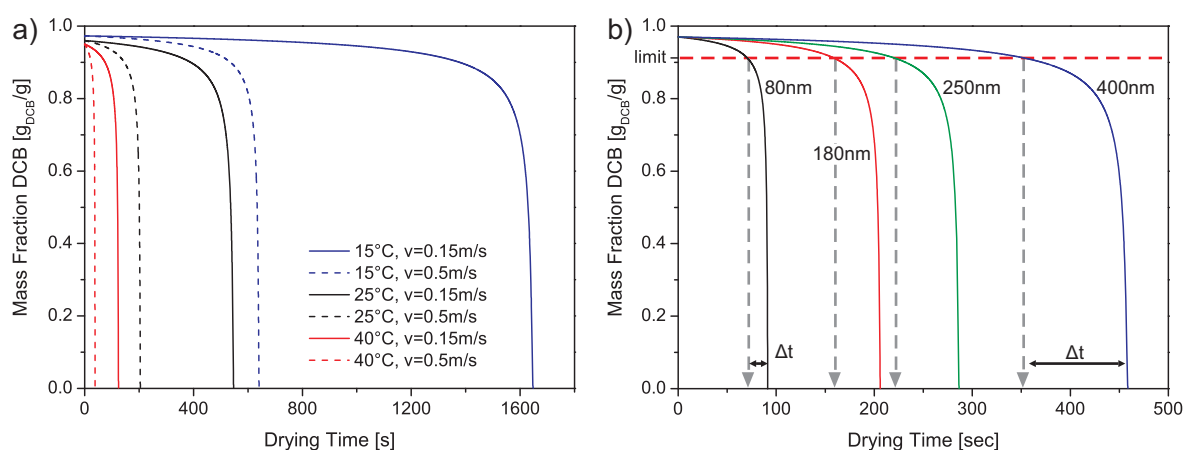


Figure 4.19: a) Exemplary drying kinetics of solution cast P3HT:PCBM films at different drying conditions. Coating and drying temperature and drying gas velocity are mentioned in the legend. b) Influence of film thickness on the drying kinetics calculated at 20°C, $v=0.3\text{m/s}$ drying conditions. The time after crossing the P3HT solubility limit (indicated as dashed red line) is marked as Δt , which increases with film thickness. [81]

P3HT:PCBM films are fabricated by doctor-blading and subsequent drying at the mentioned drying conditions in the dedicated drying channel (Figure 2.1). The structure of these films is investigated by AFM (surface) and HAADF-STEM (transmission). AFM measurements give evidence of the existence of two different structure length scales by comparing the topogra-

phy (Figure 4.20a) with the phase image (Figure 4.20b). While the dominating lateral structures of film topography measure up to several hundred nanometers, we observe a smaller substructure in the phase image which resembles the fibril/whisker structure of P3HT [46, 203, 232]. Further HAADF-STEM and AFM data is available in the appendix in Figure 10.18 and Figure 10.19. The drying condition's impact on the fibril structure is not as strong as on film topography, which is discussed in the following.

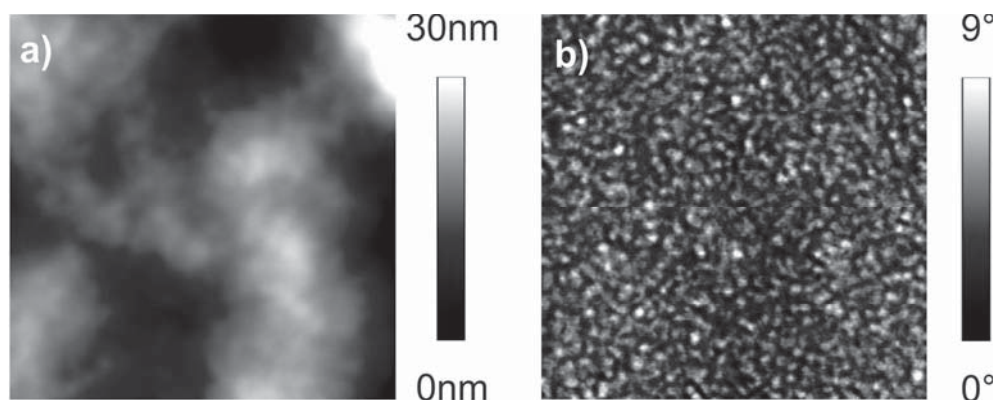


Figure 4.20: Different aspects of P3HT:PCBM film structure with respect to a) topography and b) the fibril structure in the AFM phase image for 25°C, $v = 0.5$ m/s drying conditions. The image dimensions are $1 \mu\text{m} \times 1 \mu\text{m}$. [81]

For explaining the origin of film topography, the identification of the driving force for structure formation in relation to the drying conditions and phase behavior is crucial. Kim et al. proposed for the drying process of other organic semiconductors the film structure to originate from spinodal demixing [101]. This process was further investigated by Heriot et al. observed in polymer-polymer blends a bilayer formation with subsequent stratification during film drying, leading to a phase separated structure [127]. Likewise, P3HT:PCBM blends were investigated with laser reflectometry which did not show such interference features as expected for a bi- or multilayer formation [56]. Hence, we assume the observed structures to form by growing polymer aggregates, whereby the aggregate size seems to depend on drying time after entering the unstable two-phase region of the polymer-solvent phase diagram (Figure 3.4). Lateral and vertical dimensions of topological features increase as it is manifested in the morphology of the films dried under different temperature and drying rate conditions as shown in Figure 4.21. This is quantitatively depicted by the increasing film roughness (root mean square

4 Morphology formation in polymer-fullerene films

value) with drying time after crossing P3HT solubility. The increasing roughness at slow drying gas velocity and decreasing temperature is induced by lower solubility and longer aggregation time (filled symbols). In the absence of PCBM, neat P3HT-films (open symbols) resulted in similar roughness as blended with PCBM, demonstrating that the film topography is mainly governed by P3HT. AFM images of these films can be found in Figure 10.19.

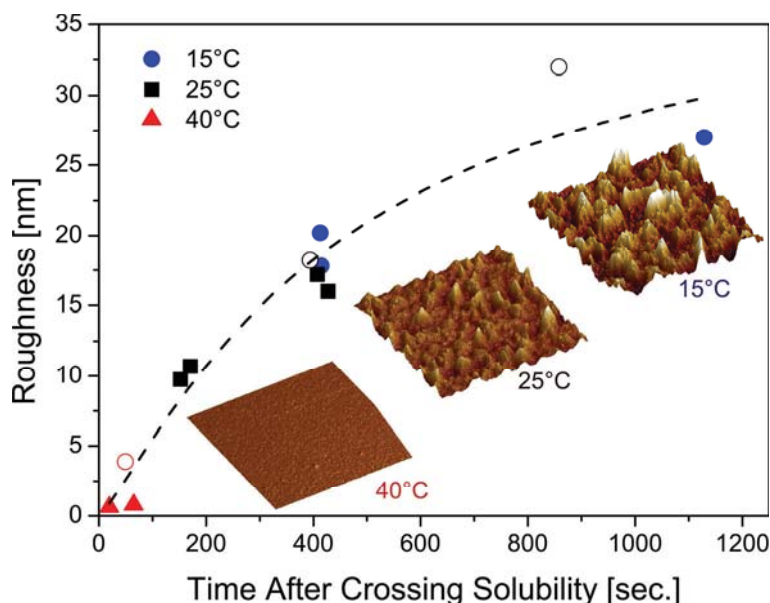


Figure 4.21: Influence of overall drying time after crossing P3HT solubility on final film root mean square (rms) roughness for pure P3HT (open symbols) and P3HT:PCBM (filled symbols) films dried at different temperatures, gas flow velocities and measured at different substrate positions. The AFM insets are $10\ \mu\text{m} \times 10\ \mu\text{m}$ with a height scale of 150 nm. The film thicknesses are $350\ \text{nm} \pm 8\%$ on top of PEDOT:PSS and ITO. [81]

Although Figure 4.20 already reveals two different kinds of structure scales, these images cannot serve for the interpretation of the quality of P3HT:PCBM phase segregation. A simple method for obtaining a rough insight into the phase segregated substructure is the determination of blend film structure before and after removing one component with a selective solvent. In this case we chose octanethiol for the removal of PCBM by washing the film three times in this solvent [99]. Figure 4.22 confirms that PCBM has mostly been removed from the blend film, which can be seen by the disappearance of the characteristic PCBM absorption peak at 333 nm.

Further changes in the absorption around 705 nm could be due to interference effects or PCBM absorption.

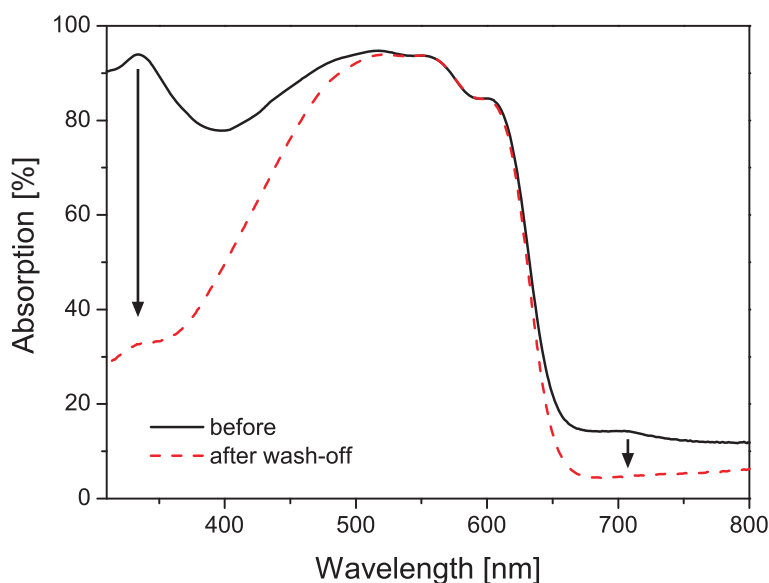


Figure 4.22: Absorption spectra of P3HT:PCBM films before (solid line) and after (dashed line) washing off PCBM with octanethiol. Arrows indicate absorption feature which are altered upon the removal of PCBM.

AFM images of P3HT:PCBM films before and after this treatment are shown in Figure 4.23. The rough film fabricated at 15°C drying temperature (Figure 4.23a left) is compared with the smooth film from 40°C drying temperature (Figure 4.23b left). This comparison shall elucidate the correlation between surface roughness and degree of P3HT:PCBM phase segregation. After PCBM removal from the 15°C processed film, the topology in Figure 4.23a remains mainly the same, while a smaller substructure appears. In the case of the smooth film processed at 40°C we see comparatively large features upon PCBM removal.

Hence, we conclude, that the size of PCBM clusters increases with drying temperature, as it is more quantitatively depicted in the AFM profile plots of Figure 4.24. The profiles were obtained at the same area before and after PCBM removal. Figure 4.24a shows that the large scale topography remains mostly unaltered, while small portions of PCBM with a peak to peak distance of 45 ± 22 nm are removed from the surface. In the case of 40°C drying temperature PCBM removal generates surface defects with a much larger peak to peak distance of 218 ± 55 nm.

4 Morphology formation in polymer-fullerene films

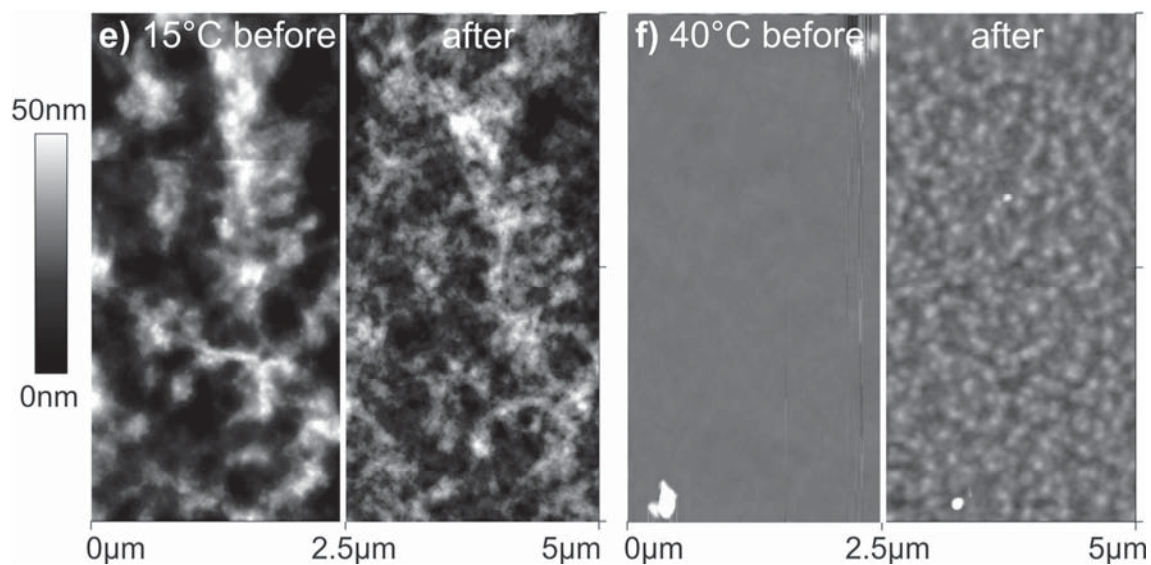


Figure 4.23: Atomic force microscope topography images of P3HT:PCBM films doctor bladed at a) 15°C and b) 40°C (represented with the same topographical scale). In both cases, the left image shows the untreated blend film and the right image shows the film topography after washing off PCBM with octanethiol. [58]

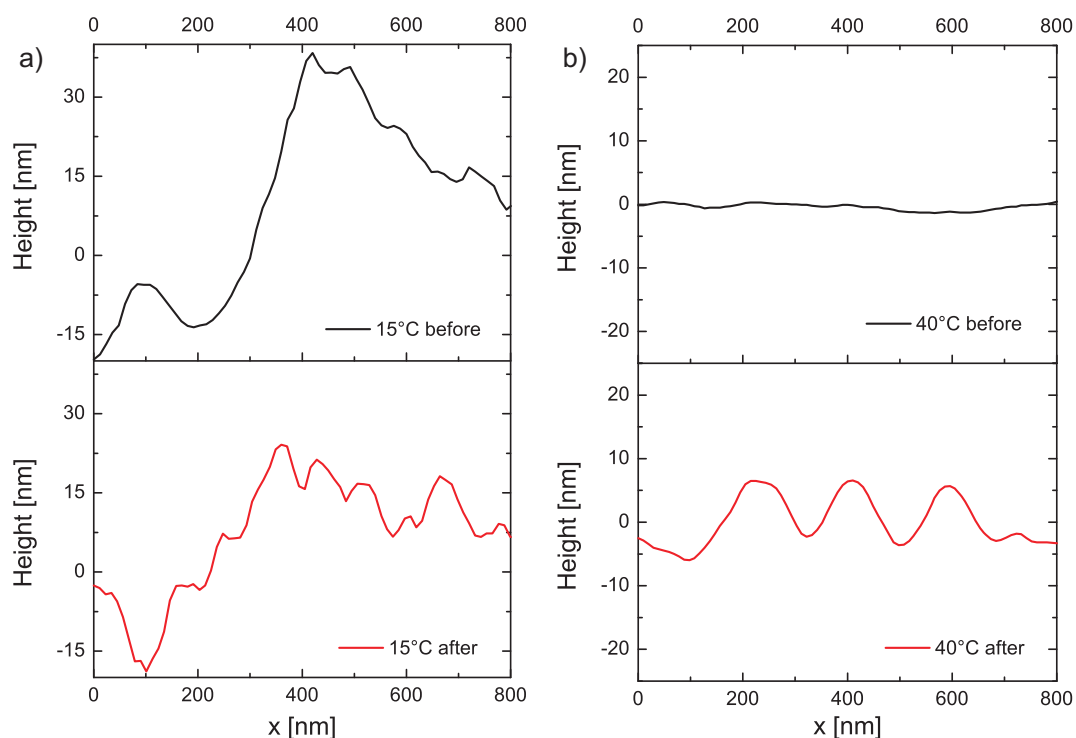


Figure 4.24: (top) AFM profiles of P3HT:PCBM films dried at a) 15°C and b) 40°C and the films after washing off PCBM (bottom) measured at the same area. [58]

These observations are in agreement with increasing PCBM correlation length at higher temperatures as obtained from GIXD [58]. It seems likely that this effect originates from the stronger increase of PCBM solubility in comparison to P3HT at higher temperatures. In fact PCBM solubility increases by a factor of 2.7 from 10°C to 40°C in comparison to a factor of 2.4 for P3HT. This reduces the polymer fullerene interaction and promotes PCBM aggregation.

The elaborated mechanisms of structure formation during film drying are summarized in Figure 4.25. Figure 4.25a shows schematically the formation of an even film without large scale P3HT aggregation, which can be due to fast drying at high temperatures and/or high airflow rates. Drying at higher temperatures leads to large scale PCBM clusters, high P3HT (100) crystallinity and domain size, but poor (020) crystallinity and domain size. Figure 4.25b depicts the formation of P3HT aggregates during the slow drying process, which leads to turbidity of the solution and subsequently to a rough surface. This is in agreement with observations of Koppe et al. [189]. Such films also exhibit high P3HT mosaicity, which forms in the course of film shrinkage. This large scale rough topography comprises a smaller substructure of i) P3HT fibrils and ii) amorphous P3HT regions intermixed with PCBM and iii) PCBM clusters dispersed in the amorphous P3HT regions. The lamellar (020) π - π -stacking is normal to the image plane and not illustrated here. P3HT exhibits a higher amount of (020) π - π -stacked molecules, but lower (100) crystallinity for lower temperatures [58]. Additionally, PCBM cluster sizes decrease with lower drying temperatures resulting in finer donor-acceptor interpenetration with increased interface area. The increasing roughness at lower drying temperatures can be used for the enlargement of the active layer/metal electrode contact area and for improved light absorption [233] without any additional processing steps.

Beside the structural factors coating quality (thickness homogeneity at cm scale in lateral direction) by doctor blading was best at 15°C. This is probably caused by higher solution viscosity which oppresses dewetting effects due to inertial forces. Instead of decreasing temperature, Koppola et al. observed an improvement of film homogeneity by increasing the solid fraction to 8-12 wt.% at room temperature [23]. This is most probably due to the same effect of increased viscosity or even a gel formation prior to coating by entering the two phase region for P3HT (Figure 3.4).

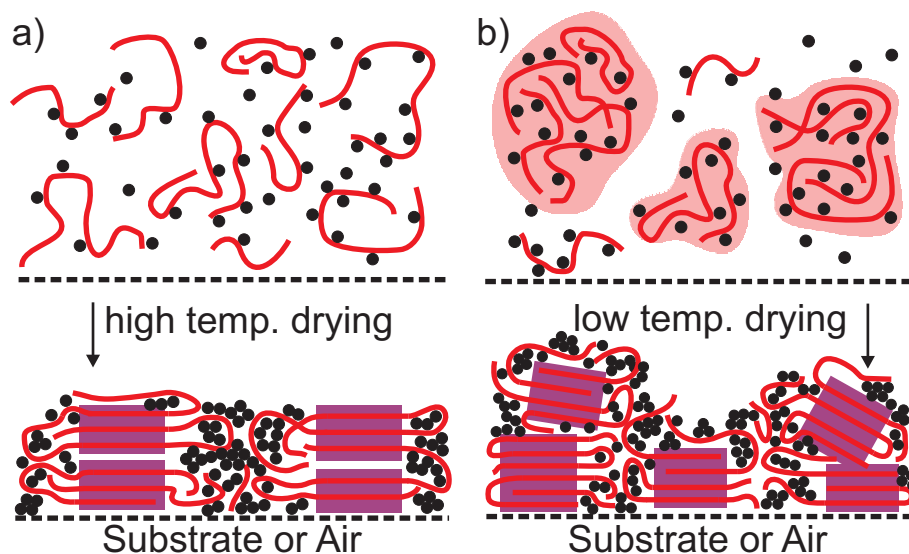


Figure 4.25: a) Schematic of molecular ordering for fast drying at high temperatures in comparison to b) slow drying at lower temperatures with macroscopic polymer aggregation leading to high film roughness. The P3HT-PCBM phase segregation results in a smaller substructure within the film topography. [81]

4.5.3 Optoelectronic properties¹

Experimental For sample preparation, we used 48mm x 60mm ITO/glass substrates ($12 \Omega/\square$, Visiontek). The substrates were cleaned by sonication in acetone and isopropanol, followed by a 2 min oxygen plasma treatment at 160 W and 40 kHz (Pico, Diener electronic). Subsequently the PEDOT:PSS (VPAI4083, Clevios, H.C. Starck) dispersion was coated by doctor blading in ambient conditions. 40 μl PEDOT:PSS dispersion (diluted 1:1 by volume with water) were cast with a blade slit width of 70 μm and a blade speed of 5 mm/s resulting in 20-40 nm dry film thickness. This layer was subsequently heated at 120°C for 20 min in a glovebox under nitrogen atmosphere. P3HT (Rieke Metals 4002E, $M_w \approx 48900 \text{ g/mol}$, polydispersity 1.7) and PCBM (Solenne, purity >99%) with weight ratios of 1:0.8 were dissolved in 2.7 to 5 wt.% solid fraction (depending on the coating temperature) in DCB (anhydrous 99%, Sigma Aldrich) and cast using the same parameters as for the PEDOT:PSS layer in the setup shown in Figure 2a. The coating parameters

¹ The characterization of optoelectronic properties has been carried out in collaboration with Michael Klein, Alexander Colsmann and Uli Lemmer of the organic photovoltaic group at the Light Technology Institute at KIT.

and setup were the same for in-situ GIXD measurements and solar cell preparation. After cutting the substrates into 16 mm×16 mm pieces, a calcium (50 nm) / aluminum (200 nm) cathode was deposited. The current density-voltage characteristics were measured under a spectrally monitored ORIEL solar simulator (1 sun according to ASTM-G173-03e1) under nitrogen atmosphere. The active area was 0.24 cm². After the characterization of the as cast devices the substrates were thermally annealed at a 150°C hot plate for 5 min in a nitrogen glovebox and subsequently put at an aluminum plate which had room temperature.

The absorption was measured in transmission with a spectrophotometer (Perkin Elmer, Lambda 1050) using a blank PEDOT:PSS/ITO/glass substrate as reference. The absorption spectra were normalized to the PCBM absorption peak at 333 nm.

Results and Discussion To correlate the discussed structural observations with optoelectronic properties, solar cell devices were built under same coating and drying conditions and thicknesses as the above investigated films. Decreasing drying temperature and increasing drying time shifts the P3HT main absorption peak to longer wavelength and enhances the vibronic shoulders in the absorption spectra (Figure 4.26a).

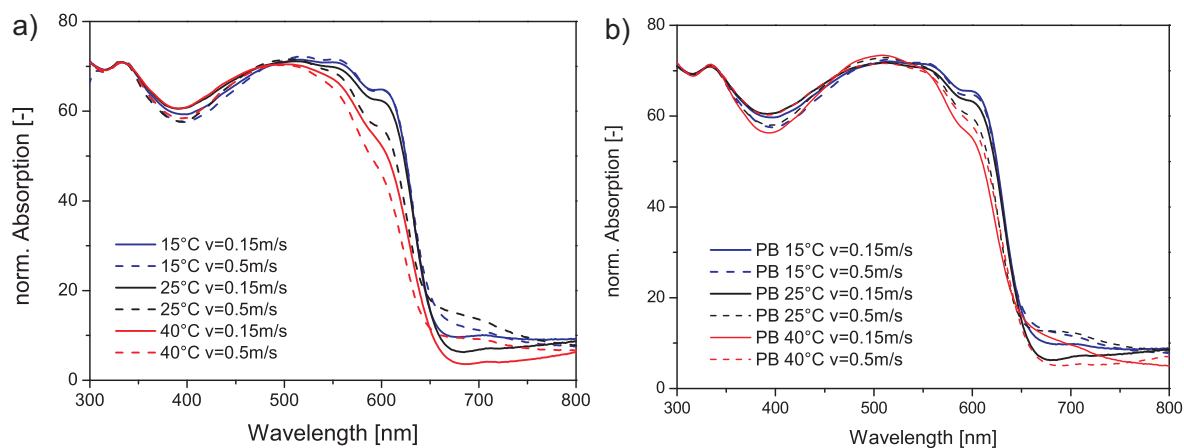


Figure 4.26: Absorption spectra of a) as cast and b) annealed (150°C, 5 min) P3HT:PCBM films dried at 15°C (blue), 25°C (black), 40°C (red) drying temperature at a nitrogen flow of 0.15m/s (solid lines) and 0.5 m/s (dashed lines). The spectra are normalized to the PCBM peak at 333 nm. [81]

Thermal annealing at 150°C for 5 min promotes the formation of vibronic shoulders, but does not equalize the absorption characteristic generated by different drying conditions (Figure 4.26b).

For a deeper analysis the position of the P3HT main absorption peak and the degree of π - π -stacking is discussed in the following. The position of the P3HT main absorption peak is plotted against the drying time after crossing P3HT solubility in Figure 4.27a. Two drying rates were realized for each temperature by two different nitrogen flow rates. A shift to longer wavelength originates from a higher correlation length of the polymer backbone; hence more stretched polymers, which is stronger for slowly dried films. Additional thermal annealing reduces the temperature influence but does not compensate it. After annealing, the position of the P3HT main absorption peak is independent from the drying gas velocity at each temperature leading to the assumption that the correlation length is merely related to drying temperature. As a measure of the vibronic shoulders, which correlate with the amount of π - π -stacked P3HT molecules [58, 234], we chose the ratio of the π - π absorption at 605 nm and the PCBM absorption 333 nm. The amount of π - π order increases with overall drying time after crossing P3HT solubility (Figure 4.27b), but approaches a saturation for 15°C drying temperature. This implies that π - π ordering is one parameter that increases with crystallization time that reaches saturation after a certain time. Additional thermal annealing enhances the shoulder for fast dried films, but this effect gets negligible for longer drying times.

Corresponding current density-voltage characteristics of equally fabricated solar cells are shown in Figure 4.28a for the “as cast” devices. The results after additional annealing for 5 min at 150°C are given in Figure 4.28b. The substrate size was 28.8 cm², which was cut into smaller substrates with a solar cell size of 0.24 cm². All layers except the cathode were prepared in ambient conditions which causes drawbacks in open-circuit voltage and power conversion efficiency (PCE).

The highest PCE of 2.1% for the untreated, doctor bladed solar cells was achieved at 15°C and 0.15m/s drying gas velocity. The efficiency of solar cells increases with lower drying temperature and slower drying according to longer crystallization time after crossing P3HT solubility (Table 4.1).

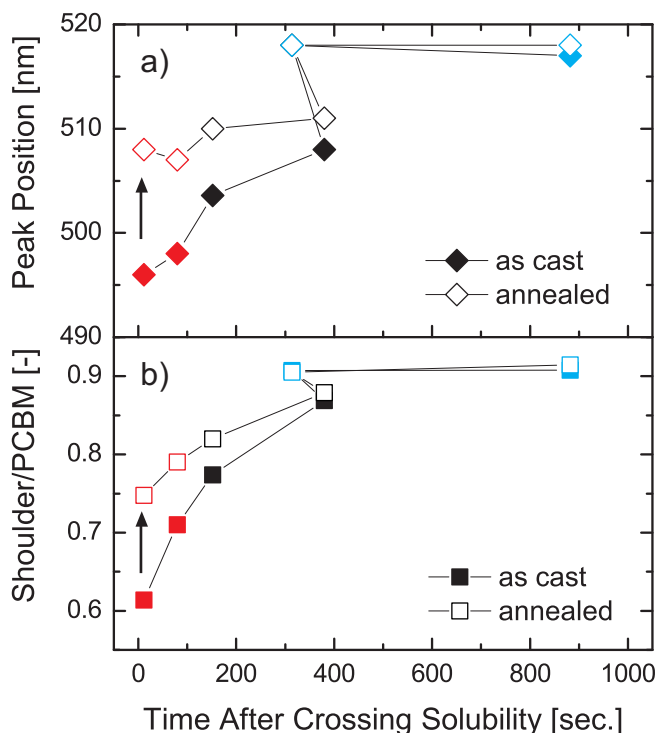


Figure 4.27: a) Position of the P3HT main absorption peak and b) absorption ratio of the vibronic shoulder at 605nm related to the constant PCBM absorption at 333nm for the as cast (filled symbols) and annealed (150°C, 5 min, open symbols) films plotted against the drying time after crossing P3HT solubility. [81]

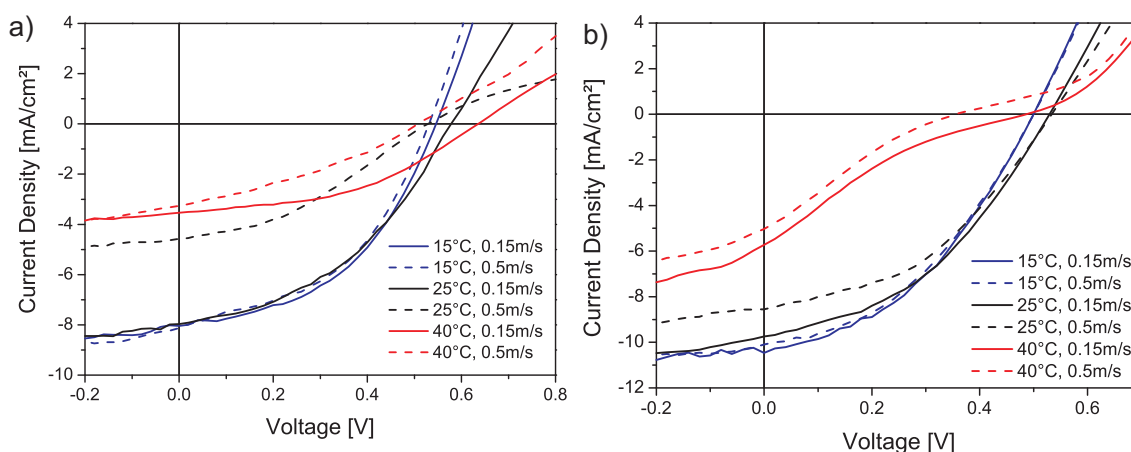


Figure 4.28: Current density-voltage characteristics of (a) the best untreated and (b) annealed P3HT:PCBM devices dried at 15°C (blue), 25°C (black), 40°C (red) drying temperature at a nitrogen flow of 0.15m/s (solid lines) and 0.5m/s (dashed lines). [81]

4 Morphology formation in polymer-fullerene films

Table 4.1: Device performance of the untreated, P3HT:PCBM films fabricated by doctor blading in ambient conditions at different drying scenarios. The average film thickness was 310 ± 90 nm. Device characterization was performed in an N_2 atmosphere at room temperature. [81]

As cast	d	J_{sc}	V_{oc}	FF	η	η_{max}
Drying Conditions	[nm]	[mA/cm ²]	[V]	[%]	[%]	[%]
15°C, v=0.15m/s	308	-7.6±0.3	0.52±0.02	44.2±2.3	1.8±0.2	2.1
15°C, v=0.5m/s	262	-7.2±0.5	0.52±0.02	45.2±4.1	1.7±0.2	2.0
25°C, v=0.15m/s	362	-7.5±0.3	0.55±0.04	41.3±1.9	1.7±0.2	2.0
25°C, v=0.5m/s	346	-4.6±0.5	0.44±0.07	34.8±3.8	0.7±0.1	0.9
40°C, v=0.15m/s	439	-3.6±0.1	0.53±0.12	37.1±7.0	0.7±0.3	1.0
40°C, v=0.5m/s	151	-3.2±0.1	0.35±0.14	30.1±3.7	0.4±0.2	0.6

The gain in efficiency is mainly due to an increased short-circuit current (Figure 4.29a). It is remarkable that this trend is still existent after annealing for 5 minutes at 150°C (see attachment Table 10.1). As depicted in Figure 4.29a and b, the short-circuit current and PCE of both 15°C and the slowly dried 25°C solar cells are very similar. This depicts the same trend of reaching a saturation state as discussed before for the optical properties. It could be associated with an equilibrium state of morphology, which is reached after a distinct period of crystallization and assembly time. The crystallization time after crossing the solubility limit for reaching this equilibrium is in this case about 300s.

Additionally, the high surface roughness promotes the PCE with increased light trapping and contact area to the cathode layer. As shown before, lower drying temperature also causes a finer P3HT-PCBM phase separation and a higher orientation distribution with increased vertical crystalline orientation [58]. In contrast to this, at fast drying conditions, the higher evaporation rate reduces the time for structure formation, leading to the lowest degree of π - π ordering, the lowest surface roughness and according to this the lowest PCE. The higher degree of P3HT (100) crystallinity achieved at 40°C drying temperatures does not seem to be beneficial for the device performance. For these drying conditions, the worst PCE was observed. This also effects an increasing series resistance for fast dried P3HT:PCBM layers

as it can be seen by an decreasing slope of the current density-voltage curve in the forward operation regime in Figure 4.28a.

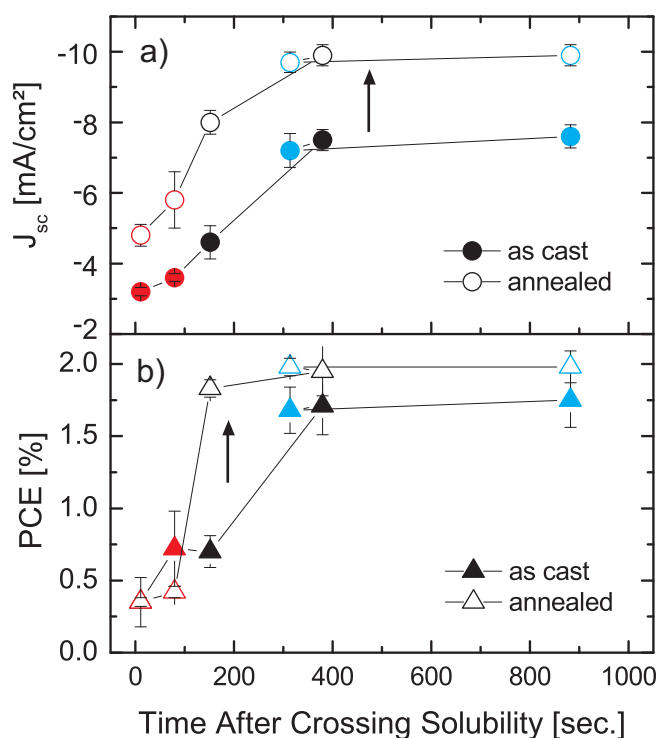


Figure 4.29: a) Short-circuit current density and b) power conversion efficiency of the untreated (filled symbols) and for 5 min at 150°C annealed (open symbols) solar cells plotted against the drying time after crossing P3HT solubility. [81]

Annealing reduces the series resistance for 25°C drying temperature processed devices, but causes for 40°C a strong S-shape (Figure 4.28b). The background of the S-shape is often related to unbalanced charge carrier mobility [235, 236]. As shown before, PCBM clusters increase with temperature and P3HT crystallites loose π - π conjugation. This could cause increased electron mobility in the PCBM, but decreased hole mobility in the polymer phase leading to an unbalanced charge carrier mobility. Recently, it was shown that annealing affects the vertical distribution of P3HT and PCBM [92] which could furthermore be associated with this effect. The improved power conversion efficiency (Figure 4.29) due to thermal annealing comprises an almost constant increase of short-circuit current at all drying conditions. For the 15°C processed devices this is not due to changes in the optical properties, as they remain constant. A possible explanation could be an improved active

4 Morphology formation in polymer-fullerene films

layer-cathode contact after the thermal treatment and the removal of residual solvent or humidity [237].

After thermal annealing, the trend of higher PCE at lower temperatures and drying rates remains, proofing the drying process as an additional key for the manipulation of film morphology and hence solar cell properties. The low sensitivity of PCE on the drying gas flow at 15°C is attractive for application in large area roll-to-roll (R2R) fabrication, where an inhomogeneous airflow in the drying unit could affect lateral film inhomogeneity.

5 Influence of solvent mixtures on film properties

In the preceding chapter it could be shown that high device performance of solar cells requires a minimum drying time which was for the chosen material system and fabrication conditions in the order of 300 s. In terms of high throughput fabrication of large area OPV it is desirable to reduce this time in order to generate higher productivity and lowering the manufacturing costs. The difficulty is to accelerate the fabrication speed by remaining solar cell efficiency high. In the following, two solvent strategies are discussed.

First, small amounts of low volatile and selectively PCBM solvating additive are added to the polymer-fullerene solution. We assume that the additive facilitates structure formation even at reduced drying time.

Second, we mix the low volatile host solvent (commonly DCB) with a distinct amount of higher volatile solvent in order to accelerate drying at the beginning until we reach the first solubility limit, since we assume that this initial period is not relevant for structure formation.

5.1 Low volatile and selectively solvating additives¹

During this thesis alkanethiols have been identified as selective solvents for PCBM by not solvating P3HT [55, 87, 100, 207, 208]. 1,8-octandithiol (ODT, bp=270°C) exhibits a lower vapor pressure as for example DCB and remains therefore in the film until DCB has largely evaporated. Hence, ODT evaporation determines the final drying period. Yao et al. determined PCBM solubility in ODT to 19 mg/ml ($x_s \approx 2\text{wt.}\%$) at room temperature [100]. In section 4.3 we have shown that PCBM molecules are not completely dissolved in a molecular disperse solution if blended with P3HT in DCB. PCBM merely strongly interacts with P3HT chains. ODT on the other hand selectively interacts with PCBM which weakens the interaction between PCBM and P3HT. This effect keeps PCBM partially in molecular disperse solution and forces P3HT in an aggregated state, since it is insoluble in ODT. This has

¹ Mareike Kowalski dedicated her student research project to selectively solvating additives [238].

been shown to be beneficial for structure formation in P3HT:PCBM solar cells.

Experimental In this section PEDOT:PSS/ITO/glass substrates have been prepared as described previously. P3HT:PCBM (1:0.8) films were cast from 2 wt.%, 3 wt.% and 4.5 wt.% solid fractions for 15°C, 25°C and 40°C coating and drying temperature respectively. The ODT to solid ratio was 1:4 by weight as used by Yao et al. [100]. Films were fabricated at coating and drying conditions as described in the previous chapters. The average film thickness of the investigated solar cells was $220 \text{ nm} \pm 46 \text{ nm}$. For the analysis of the reflectometry measurements the influence of ODT refractive index on the solution was neglected.

Results and Discussion In this section it is investigated whether the beneficial effect of ODT incorporated into P3HT:PCBM solution in DCB compensates the structural drawbacks of faster drying at higher temperatures. Fast drying at elevated temperatures has been demonstrated in section 4.5 to result in less efficient solar cells.

First of all, the impact of low amounts of ODT on thin film drying kinetics was investigated. The evaporation kinetics is exemplarily shown in Figure 5.1 for a drying P3HT:PCBM film cast from DCB solution at 3 wt.% solid and ODT fraction. After the constant rate period of DCB evaporation the drying temperature was slowly increased from 20°C to 60°C in order to accelerate ODT evaporation. After ODT has largely been removed we still see a slight decrease in reflectometer photovoltage indicating changes in the optic film properties. It is likely that this is due to the evaporation of residual solvent in the film although this state would be indicated as “dry” by the naked eye. It was also recognized that films in this state are very sensitive to mechanic influences such as scratching. Finally all films exhibit a similar roughness in contrast to pure DCB processed films where the roughness was a function of drying time (see appendix Figure 10.22)

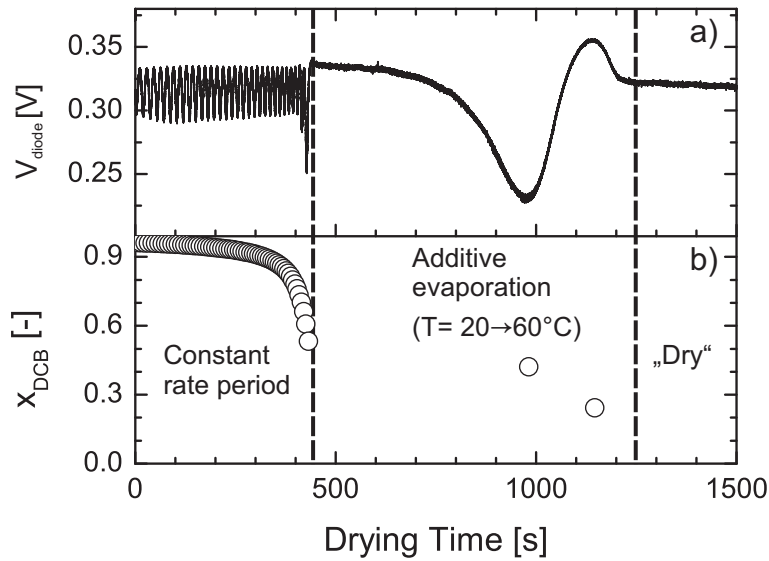


Figure 5.1: Exemplary drying kinetics of a drying P3HT:PCBM film cast from DCB and ODT at 20°C. After the constant rate period the drying temperature was slowly increased to 60°C for enhanced ODT evaporation. a) Reflectometer signal which was transferred to b) the evolution of solvent mass fraction x_{DCB} .

Hence, the incorporation of even very low amounts of additive increases the overall drying time enormously. In the following it is discussed if the structural and solar cell performance benefits justify the usage of ODT in comparison to low temperature drying with pure DCB which gave the best solar cell performance (see section 4.5.3).

The absorption characteristics of the ODT processed P3HT:PCBM films are summarized in Figure 5.2. In comparison to films processed without additives Figure 5.2a shows stronger pronounced vibronic shoulders even for higher drying temperatures. The shoulder height correlates with the amount of π - π -stacked P3HT chains.

The position of the P3HT main absorption peak is shown in Figure 5.2b for the as cast and annealed devices. For comparison the same scale is used as in Figure 4.27 of films fabricated without ODT. Additive processing causes a comparatively constant peak position which indicates a similar conjugation length of P3HT chains for all drying temperatures. In terms of morphology this shows that P3HT are stretched in a similar degree such that the range of π -electron delocalization is extended over the same length. Annealing only slightly reduces the conjugation length indicated by a slight blueshift of the peak.

5 Influence of solvent mixtures on film properties

As already seen in the absorption spectra Figure 5.2c shows the relative height of the vibronic shoulders in relation to the constant PCBM absorption. As we could evidence before, the shoulder height is associated with the amount of π - π -stacked P3HT chains which is also comparatively constant over all drying conditions. Annealing has a marginal effect. Hence, the usage of small amounts of ODT causes that the peak position and shoulder height are almost independent from drying conditions and additional thermal treatment. This depicts a strong improvement in comparison to film processing without additive.

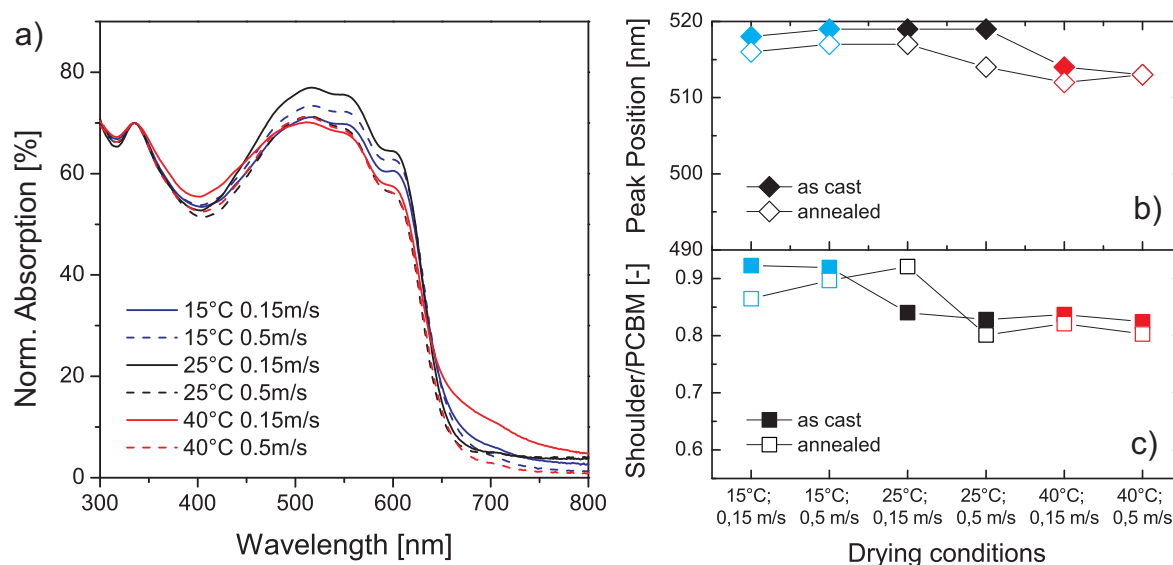


Figure 5.2: a) Normalized absorption spectra of P3HT:PCBM films cast under different drying temperatures and gas flow velocities from DCB and ODT. Films have been thermally treated at 150°C for 5min. b) Position of the P3HT main absorption peak and c) ratio of vibronic side band absorption at 605nm and PCBM absorption at 333nm for as cast and thermally annealed films. [238]

Regarding the optical properties we expect high power conversion efficiencies for the associated devices cast with ODT independent from the drying conditions. Figure 5.3a depicts the current density-voltage characteristics of the ODT processed solar cells after an additional thermal annealing. Before thermal annealing no reasonable power conversion efficiency could be measured which we assign to residual ODT and humidity. As cathode we used in this case pure aluminum which shows less damage caused by the evaporation of residual solvent during thermal annealing. After thermal annealing it turns out that drying conditions clearly have an impact on device

performance. This is surprising since all films exhibit a similar light absorption behavior and exhibit similar structures as investigated by AFM (see appendix Figure 10.20 and Figure 10.21) due to the usage of ODT.

Figure 5.3b shows the systematic increase of short-circuit current with decreasing drying temperature. The PCE follows this trend (Figure 5.3c). The previously observed S-shape at 40°C drying temperature also appears after annealing for the ODT processed solar cells. This effect is usually related to unbalanced charge carrier mobility.

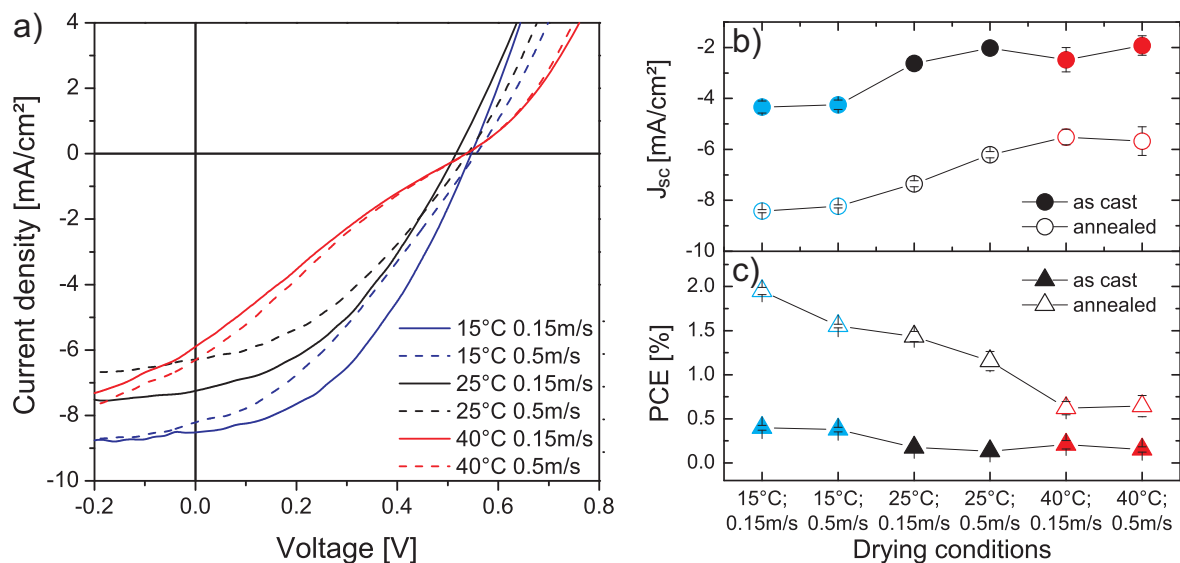


Figure 5.3: a) Current density-voltage characteristics of P3HT:PCBM solar cells cast under different drying temperatures and gas flow velocities from DCB and ODT added in 1:1 weight ratio. b) Short-circuit current density and c) averaged power conversion efficiency (PCE) for as cast and thermally annealed solar cells. [238]

Absolute device efficiencies do not show an improvement for ODT processing in comparison to low temperature drying without additive. The same can be found in literature where no superior efficiencies could be reached for P3HT:PCBM and ODT in comparison to an optimized processing without additive. One might argue if further optimization of the P3HT:PCBM:ODT:DCB blending ratio would improve the PCE, but so far this has not been reported. One beneficial factor of ODT is the reduced standard deviation in PCE. This implies that the film structure is much more reproducible.

However, the usage of an additional volatile component signifies for the fabrication process that this substance has to be removed out of the drying air and must be separated from the host solvent subsequently. For P3HT:PCBM this does not seem reasonable although we earn reproducibility in device performance.

5.2 Mixture of solvents with different volatility¹

Another strategy for the acceleration of the drying process without drawbacks in device performance is the incorporation of a high volatile solvent. In the scope of high throughput and environmentally friendlier manufacturing it is further desirable to use non-halogenated solvents. Therefore, in this section we replaced the established solvent 1,2-dichlorobenzene with the environmentally friendlier indane. In the following the importance of the ratio between high and low volatile solvent will be discussed.

5.2.1 Solvent mixture drying kinetics

Numerical approach Calculations are done for horizontal plate geometry in forced convection by a two dimensional mass transfer model including a moving drying front as described in section 2.4.2 and published in [56, 135]. The calculations are carried out with an initial uncoated offset of $x_0=10$ mm which are followed by 60 mm wet film of $x_{solid} = 2$ wt.% solid fraction of P3HT:PCBM ($x_{solvent} = 98$ wt.%) and 200 nm dry film thickness. Drying kinetics are shown for the centered position of the wet film, i.e. at $x = 30$ mm. Drying conditions are 20°C and $v = 0.3$ m/s drying gas velocity. P3HT and PCBM solubility have been determined as describe in section 3.3 and published in [81].

Results and Discussion In section 4.3 it could be shown for DCB solution that the P3HT:PCBM blend crystallization proceeds with foremost P3HT crystallization at solvent fractions of $x_{solvent}=85-95$ wt.% followed by PCBM clustering in the final drying period at low solvent fractions $x_{solvent} < 55$ wt.% [81]. The observation of the delay in crystallization leads to the assumption that this period before crossing solubility limits possibly does not contribute

¹ The essence of this section was published in [239].

to structure formation. In the case of DCB the solubility of P3HT and PCBM at 20°C is 3.8 wt.% and 2.6 wt.% respectively. For indane P3HT and PCBM solubility at 20°C was determined to 2.9 wt.% and 5.5 wt.% respectively.

Hence, it seems likely that the dry film structure after skipping this initial phase by faster drying before crossing solubility - followed by a final slow drying step - will be equal in comparison to an overall slow drying process. This consideration was undertaken more quantitatively for the combination of higher volatile solvents chloroform (bp = 61°C), toluene (bp = 111°C) and o-xylene (bp = 144°C) with the less volatile host solvent indane (bp = 178°C). Vapor pressure of indane and its solubility of P3HT and PCBM is comparable to the well known ideal solvent DCB (bp = 179°C). As structure formation is not only governed by drying kinetics but also strongly depends on the solid-solvent interactions, we will discuss the dry film structures of the used solvent combinations later. Figure 5.4 depicts the drying kinetics of different solvent mixtures and solvent blending ratios. For easier readability, the mass fractions of the solvent mixtures are mentioned as a single solvent.

Figure 5.4a-c depict the evolution of solvent mass fraction $x_{solv.} = (m_{solv.1} + m_{solv.2}) / (m_{solv.1} + m_{solv.2} + m_{solid})$ of drying P3HT:PCBM films. From Figure 5.4a-c the difference in vapor pressure in-between both mixed solvents decreases. In the top row it gets quantitatively clear, how the drying time can be influenced by the type of solvent combination and the solvent blending ratio. The transition from the more or less fast initial drying period to the finally slower drying period governed by the host solvent is depicted in the bottom row of Figure 5.4a-c. Note that the less volatile solvent indane also evaporates at the beginning with an evaporation rate proportional to the partial pressure which depends on the pure component vapor pressure and the molar solvent fraction. In other words, the evaporation rate increases with both, the vapor pressure and the molar fraction of a component in a mixture. Due to lower differences in the vapor pressure of the mixture o-xylene-indane here no abrupt change in the evaporation kinetics can be detected.

The idea behind using solvent mixtures in this work was the reduction of retention time in that area of the phase diagram, where no crystallization processes are proceeding. In Figure 5.4a-c (bottom) it can be seen that for the 1:1 solvent blending ratio the transition from fast to slower indane dominated drying kinetics has largely completed at 95-96 wt.% overall solvent fraction.

5 Influence of solvent mixtures on film properties

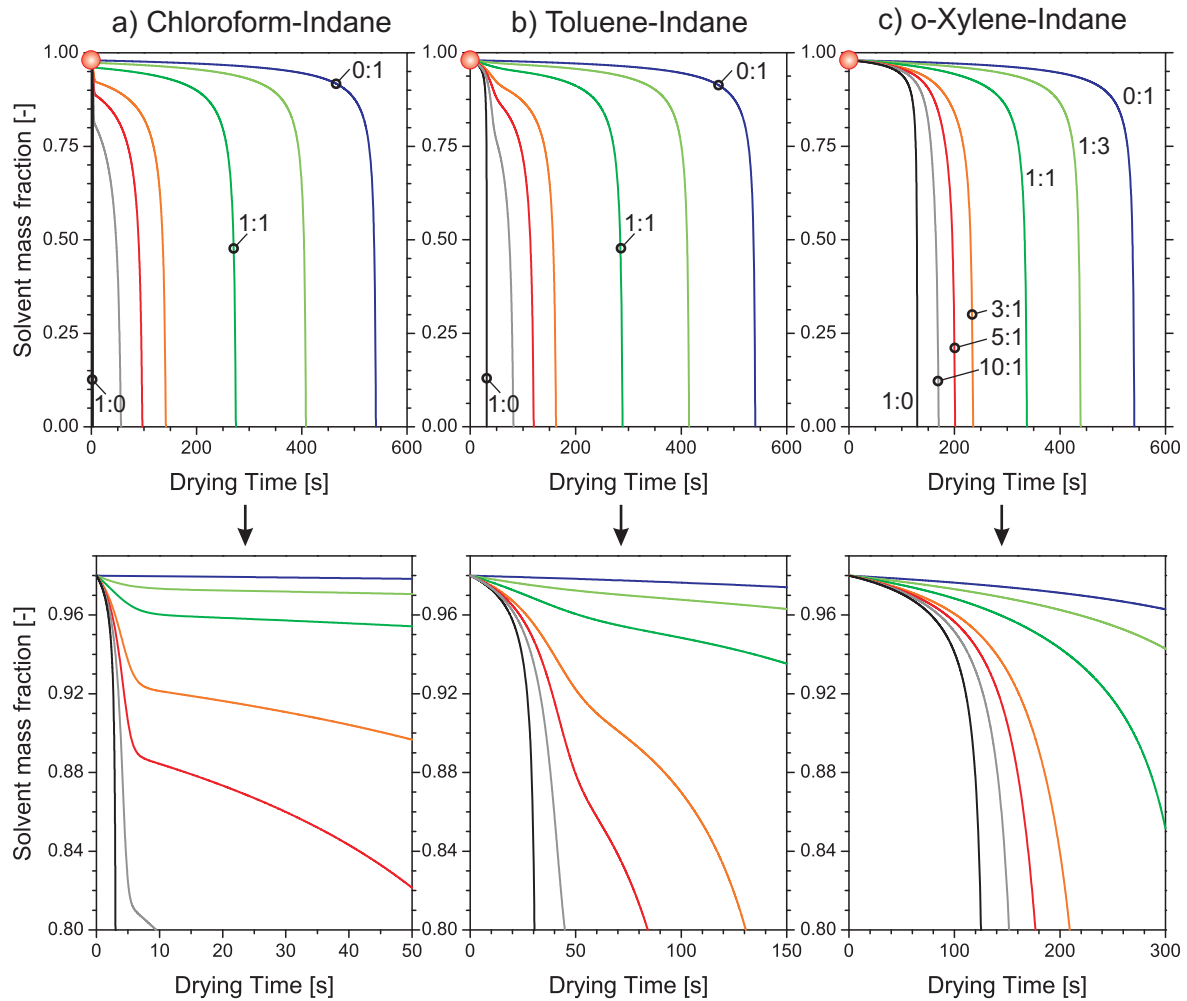


Figure 5.4 Calculated drying kinetics (constant rate period) of the solvent mixtures a) chloroform-indane, b) toluene-indane and c) o-xylene-indane for different solvent blending ratios which are indicated in c). The top row shows the entire evolution while the bottom row depicts a zoomed view of the composition evolution. [239]

This secures that the indane dominated slow drying period is roughly reached at the P3HT:PCBM solubility limit. From chloroform to toluene and o-xylene one can see the strong difference in the “sharpness” of the transition from initially fast to slower final drying period due to the decreasing vapor pressure. In terms of fabrication speed, the lowest drying time of the combination chloroform-indane would be the best. In the following we will discuss how far the choice of solvent mixtures for the 1:1 ratio in combination with their evaporation kinetics influences the film structure and the corresponding optoelectronic properties of solar cells.

5.2.2 Impact of solvent mixtures on film structure

Experimental In order to investigate the influence of the different drying kinetics of the 1:1 blended solvents on film structure, we conducted GIXD and AFM measurements of the final films. These measurements were done at P3HT:PCBM solar cells whose optoelectronic properties will be discussed below. X-ray reflectivity and GIXD measurements were done on the P3HT:PCBM solar cell devices in the synchrotron facility ANKA (Karlsruhe, Germany), using a point detector with 8 keV photon energy. AFM measurements were done in tapping mode with a Veeco Dimension Icon.

Results and Discussion The 2D GIXD diffraction pattern of all P3HT:PCBM films cast from the mentioned solvent mixtures on a glass/ITO/PEDOT:PSS substrate look similar on first sight (see appendix Figure 10.23). The equal P3HT (100) Bragg peak shape in Figure 10.23 indicates a similar angular orientation distribution of P3HT crystallites, known as mosaicity, for all solvent combinations. The crystallites orientation can therefore not account for differences in device performance.

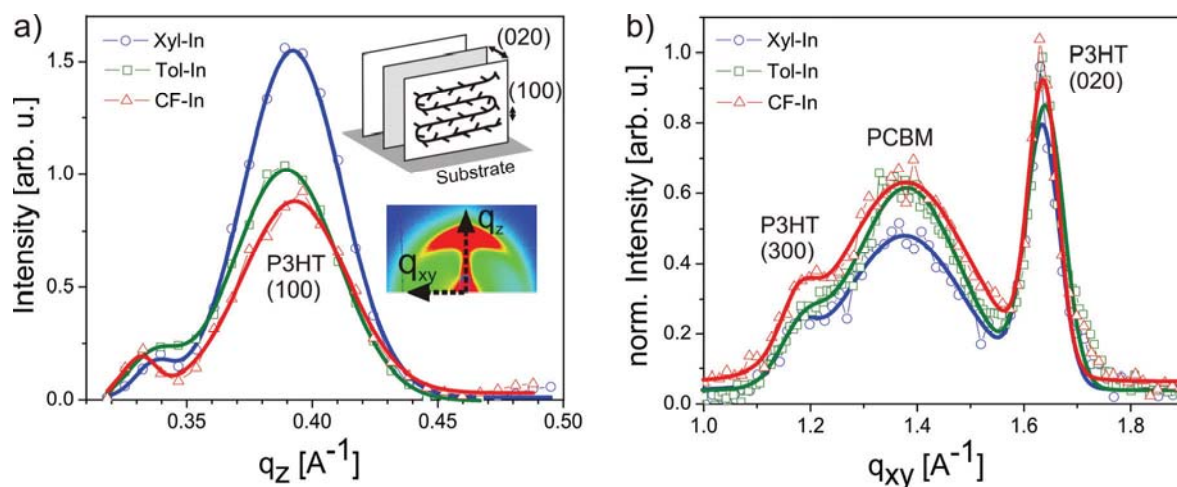


Figure 5.5: a) Out-of-plane and b) in-plane X-ray diffraction profiles of P3HT:PCBM films cast from different solvent mixtures obtained by point detector measurements. Symbols represent experimental data and lines the appropriate fits. The solvent blending ratios were for all combinations 1:1 by volume. [239]

The P3HT structure is well oriented in (h00) direction perpendicular to the substrate as well as in (020) direction along the substrate (see inset of

5 Influence of solvent mixtures on film properties

Figure 5.5a for explanation). In order to determine the associated spacing and coherence length (measure of the domain size) of PCBM aggregates and P3HT structure, point detector measurements were obtained. The diffraction profiles in out-of-plane direction along q_z and in-plane profiles along q_{xy} are depicted in Figure 5.5a and Figure 5.5b respectively. Figure 5.5a comprises the P3HT (100) Bragg peak which reveals similar d_{100} spacing for all solvent mixtures as well as a similar correlation length L_{100} which is slightly higher for the o-xylene-indane case (see appendix Table 10.2).

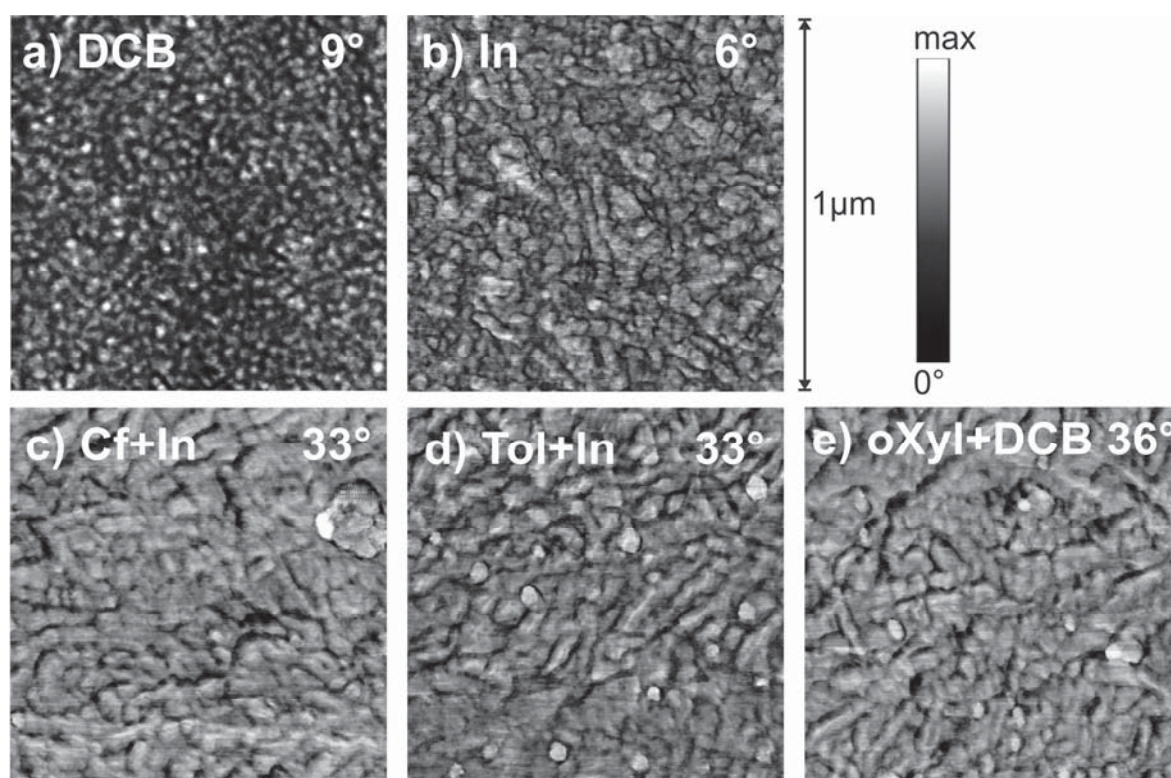


Figure 5.6: AFM phase images of P3HT:PCBM films cast by doctor blade from different solvents such as a) o-dichlorobenzene, b) indane, c) chloroform-indane, d) toluene-indane and e) o-xylene-indane at room temperature. The solvent blending ratio was for all cases 1:1 by volume. For clarification the image scale was adapted for each image differently as indicated in each image. [239]

This similarity of well pronounced crystallinity can also be found in the in-plane data of Figure 5.5b, which reveals the same d_{020} spacing and the same correlation length L_{020} in π - π -stacking direction except for the o-xylene-indane case where it is slightly lower. The difference in the intensity of the specular Bragg peaks is due to the difference in thickness of the films. Hence,

GIXD measurements show very similar crystallinity for all solvent mixtures regardless of the differences in initial evaporation kinetics.

In order to cover a larger scale of film morphology we investigated the P3HT:PCBM blend surface by AFM. Figure 5.6 shows $1 \times 1 \mu\text{m}^2$ phase images of the reference solvent DCB, pure indane and the solvent mixtures of chloroform, toluene and o-xylene with indane. The structures resemble those of P3HT lamellar fibrils [46, 203, 232]. While Figure 5.6a shows the finest structure of all films for DCB, the structure gets coarser for indane processed films (Figure 5.6b). For all solvent mixtures, which initially dry faster than pure indane or DCB, the structure exhibits even bigger structural features as for pure indane and DCB (Figure 5.6c-e).

Since the larger structure scale cannot be caused by longer assembly and crystallization times, they must originate from solvent specific properties that cause differences in the initial molecular conformation due to specific solid-liquid interaction forces.

5.2.3 Impact of solvent mixtures on optoelectronic properties

Experimental P3HT:PCBM solar cells were fabricated at Holst Centre (Eindhoven, Netherlands) and after their characterization investigated for their structural properties at Karlsruhe Institute of Technology. Solar cells were obtained by dissolving 1.5 wt.% of P3HT and 1.2 wt.% of PCBM at 70°C for 14 hours in several solvent systems, namely orthodichlorobenzene (DCB), indane, as well as 1:1 (by wt.) mixtures of indane/toluene, indane/o-xylene and indane/chloroform. Chloroform and toluene were purchased from Merck, whereas o-xylene (98%), DCB (99%), and indane (95%) were provided by Sigma-Aldrich. P3HT (the same batch as investigated in this thesis) was purchased from Rieke Metals and PCBM by Solenne.

After cleaning of the pre-patterned-ITO glass substrates (Philips polyLED), PEDOT:PSS (Clevios P VP AI 4083, H.C. Starck) was spin-coated, and annealed at 130°C for 5 minutes. The thickness of the resulting PEDOT:PSS layer was 50 nm. The photoactive layer was subsequently deposited by doctor blading (Coatmaster 509 MC-1). Solvent evaporation was allowed to proceed slowly by covering the just deposited wet film with a petri dish. Finally, the top electrode, made of 1 nm LiF and 100 nm Al, was thermally evaporated in a vacuum chamber (Rittal control unit) through a shadow mask.

Results and Discussion The structural investigation above revealed strong P3HT crystallinity in (100) direction perpendicular and in (020) π - π -stacking direction along the substrate. Thus we expect strong vibronic shoulders in the absorption spectra due to the high amount of P3HT π - π interaction. This expectation is confirmed by Figure 5.7 where the normalized absorption is plotted for pure DCB and indane as well as for all solvent mixtures. All absorption spectra feature strong vibronic shoulders and a similar position of the main absorption peak that indicates a similar conjugation length of the P3HT chains.

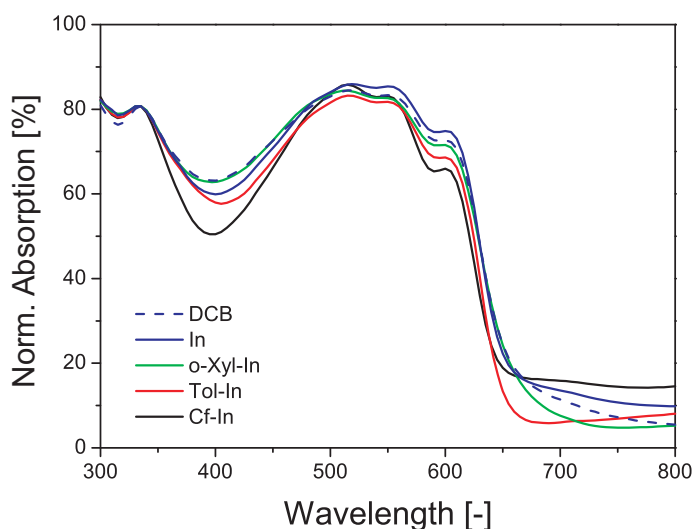


Figure 5.7: Normalized absorption spectra of P3HT:PCBM (1:0.8) films cast from *o*-dichlorobenzene (DCB), indane (In), *o*-xylene-indane (*o*-Xyl-In), toluene-indane (Tol-In) and chloroform-indane (Cf-In). The solvent blending ratios were for all combinations 1:1 by volume. Spectra are normalized to the PCBM absorption peak at 333 nm. [239]

To what extent the above discussed structural and optic properties influence the solar cell device properties can be seen in Figure 5.8. Here current density-voltage characteristics of P3HT:PCBM solar cells are depicted for the fabrication from different solvent mixtures. The combination toluene-indane led to the highest power conversion efficiency (Figure 5.8a). Reasons for the dramatic difference in short-circuit current density between chloroform, toluene and *o*-xylene as higher volatile solvent component, cannot be found in GIXD and AFM results. We do not expect strong differences in the vertical gradients of P3HT:PCBM composition for the solvent mixtures driven by differences in the solvents surface tensions. The higher volatile solvents

exhibit similar surface tensions of 27.5mN/m, 28-28.5mN/m and 29.5mN/m for chloroform, toluene and o-xylene respectively. The initial solvent specific molecular conformation in the solution state is unlikely to account for these differences since the molecular structure as investigated by GIXD is similar for all solvent mixtures.

A possible reason for the very low short-circuit current and S-shape of the chloroform-indane processed device could be caused by an enrichment of hole conducting polymer at the cathode interface. This would act as a barrier for electron extraction and would result in such a performance characteristic. Ruderer et al. observed an enrichment of P3HT at the film/cathode interface by using pure chloroform as solvent [240], which might explain this effect. Furthermore, we can only speculate that the three dimensional multiple scales ordering of polymer fibers and fullerene clusters could also be responsible for the observed differences in electronic properties.

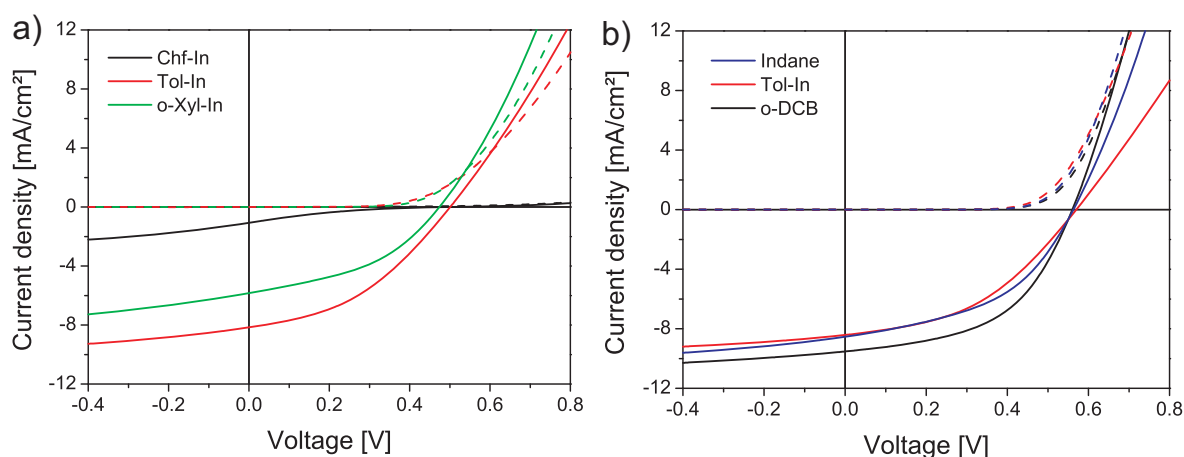


Figure 5.8: a) Representative JV-characteristics of P3HT:PCBM (1:0.8) solar cells fabricated by doctor blading and slow drying conditions from the solvent mixtures chloroform-indane (Cf-In), toluene-indane (Tol-In) and o-xylene-indane (o-Xyl-In) in 1:1 ratio for all solvents. b) Best JV-characteristics of equally fabricated solar cells from pure indane (In), o-dichlorobenzene (o-DCB) and toluene-indane (Tol-In). The solar cells were treated for 5 min at 130°C. Solid lines represent conditions under illumination while dashed lines are measured at dark conditions. [239]

Another set of solar cells was fabricated for the comparison of the most promising solvent mixture toluene-indane, the pure host solvent indane and the ideal reference solvent DCB (Figure 5.8b). Although DCB still provides the highest power conversion efficiency after annealing (Table 5.1) indane

5 Influence of solvent mixtures on film properties

leads to comparable results. The practical disadvantage of pure indane is the poor wetting behavior, which can be improved by mixing with the discussed solvents.

Table 5.1: Current density-voltage characteristics of P3HT:PCBM solar cells fabricated by doctor blading under ambient conditions from different solvents. TA denotes the performance after additional thermal annealing of the same cells for 5 min at 130°C. [239]

Solvent	d	J _{sc}	V _{oc}	FF	PCE	PCE _{max}
	[nm]	[mA/cm ²]	[V]	[-]	[%]	[%]
Tol-In	225±60	5.5±3.0	0.41±0.03	0.32±0.25	1.0±0.6	2.0
Tol-In + TA	225±60	7.4±1.0	0.53±0.06	0.41±0.05	1.5±0.4	2.1
DCB	265±150	3.8±1.8	0.48±0.03	0.53±0.03	1.0±0.55	1.9
DCB + TA	265±150	7.9±1.1	0.57±0.02	0.41±0.08	1.9±0.6	2.7

In combination with toluene the drying time can be reduced about 40% by generating a similar P3HT:PCBM crystallinity, absorption behavior and solar cell performance in comparison to DCB. A slight drawback is the increased series resistance which can be derived from the decreasing slope of the current density-voltage curve in the forward operation regime in Figure 5.8b. Overall this indicates the solvent mixture toluene-indane as a suitable replacement of DCB for high throughput and large area fabrication of organic solar cells.

6 Structure formation of low band gap polymers

After the fundamental and extensive investigation of the well known material system P3HT:PCBM it is at the end of thesis of interest to examine the transferability of the obtained knowledge to other material systems. For this purpose we replaced P3HT by the low band gap polymers PSBTBT and PCPDTBT (Figure 1.5). The C₆₁-PCBM was additionally replaced by C₇₁-PCBM (Figure 1.6). The asymmetric C₇₁ fullerene was chosen because of its increased absorption in the visible region, which leads to better overlap with the solar spectrum relative to that obtained with the C₆₁ analogue [207, 241, 242].

For these material systems power conversion efficiencies of about 5.5% have been reached [87, 207, 242-246]. One interesting advantage is the broad absorption of these polymer-fullerene systems which allows for the fabrication of color neutral, semi-transparent solar cells [247, 248]. This has already been realized in large area building integrated photovoltaics [249].

6.1 In-situ observation of molecular ordering

Experimental Both polymers were provided by Konarka Technologies and used as received. PC₇₁BM (>99%) was purchased from Solenne. The solutions have been prepared in a 1:2 and 1:3.4 ratio by weight for PSBTBT:PC₇₁BM and PCPDTBT:PC₇₁BM respectively at 1wt.% polymer in DCB and have been stirred at 80°C for at least 48h after preparation under nitrogen atmosphere in a glovebox. In the case of PCPDTBT 3wt.% of ODT were added for additive processing. Knife coating parameters were 400 µm slit width at 10 mm/s coating speed with 60 µl solution.

Laser reflectometry ($\lambda = 650\text{nm}$) drying process measurements were accomplished at low laser intensities since these material systems strongly absorb light at this wavelength. The experiments were carried out at 40°C and 0.15 m/s drying gas velocity. The analysis of the reflectometry measurement was conducted with the refractive index of P3HT and PC₆₁BM because of the limited material availability. This slightly affects the obtained thickness values of the last interference peaks where the solid fraction and its refractive index is significant (see section A 1.2). In situ GIXD images were taken at intervals of 18 s at beamline ID10B at ESRF as described before.

Results and Discussion for PSBTBT:PC₇₁BM In this section the previously discussed crystallization behavior of P3HT:PCBM blends is compared with the assembly process as observed in situ by GIXD at solution cast PSBTBT:PC₇₁BM films.

For the comparison with device performance in solar cells, it would be the best to apply the films at commonly used PEDOT:PSS coated substrates. On the other hand, the diffraction patterns are more pronounced if native silicon is used as a more ideal substrate which is beneficial for accurate X-ray analysis. Figure 6.1a and b show that silicon substrates are a reasonable compromise between well-defined GIXD pattern and reasonable comparability of the diffraction features for PEDOT:PSS covered substrates as used for the fabrication of solar cells.

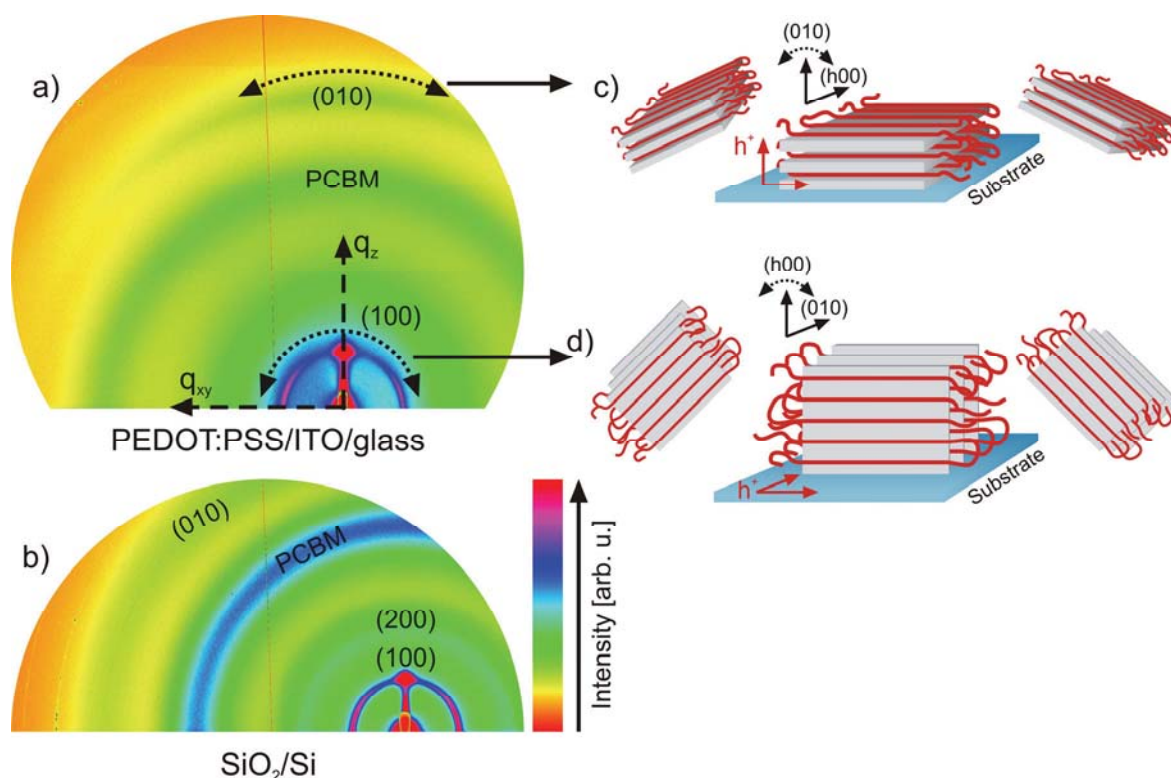


Figure 6.1: GIXD diffraction patterns of PSBTBT:PC₇₁BM (1:2) films cast from DCB by doctor blade at a) PEDOT:PSS/ITO/glass and b) native silicon substrates. Drying was accomplished at 40°C. c) Scheme of the face-on configuration related to the out-of-plane (010) Bragg reflection and d) edge-on configuration related to the out-of-plane (h00) Bragg reflection with high hole mobility along the polymer backbones and along the π - π -stacking direction.

The main diffraction features of PSBTBT:PC₇₁BM films are mentioned in Figure 6.1a and with a stronger diffraction signal on silicon substrates in Figure 6.1b assuming a similar polymer unit cell as for P3HT (see Figure 4.2) [243]. The diffraction peak associated with the PSBTBT (010) π - π -stacking is more intense in out-of-plane direction. For PEDOT:PSS substrates it is therefore only visible in out-of-plane direction due to the lower signal intensity and the chosen color scale. According to Sirringhaus et al. this indicates a π - π -stacking direction oriented normal to the substrates with the polymer lamellae in face-on configuration to the substrate [75] as depicted in Figure 6.1c. The angular intensity distribution of the (010) Bragg reflection is associated with the orientation distribution as indicated in Figure 6.1c. For this orientation we expect high hole mobility in the in-plane along the polymer backbones and perpendicular to the substrate along the direction of π - π -stacking.

Chen et al. on the other hand suggest for a similar diffraction pattern edge-on orientation of PSBTBT due to the observation of the (h00) out-of-plane Bragg peaks [243]. The higher signal to noise ratio in Figure 6.1b also shows the (200) Bragg peak as a powder like ring, which indicated a broad orientation distribution of the edge-on orientation as illustrated in Figure 6.1d. For edge-on orientation we expect high hole mobility along the polymer backbones and along the direction of π - π -stacking both in the in-plane direction. However, the high mosaic spread of both, the (h00) and (010) Bragg reflection indicates a broad orientation distribution in all orientations. This is beneficial for the required vertical hole transport along the polymer backbones and along the overlapping p_z orbitals in π - π -stacking direction [45]. This very broad orientation distribution which is beneficial for solar cell performance is in contrast to previous observations for P3HT:PCBM films investigated in this work which were mainly oriented in edge on orientation.

For an investigation of the mentioned structural properties during film drying we accomplished real time GIXD measurements at PSBTBT:PCBM blends cast from DCB solution by knife coating (doctor blade). Simultaneously the film thickness was measured by reflectometry in the previously shown setup (Figure 2.1). The reflectometry measurement provides indirectly the film composition at the instant of each GIXD measurement. Figure 6.2a depicts the reflectometer raw signal. Based on the interference fringes we can calculate the evolution of solvent mass fraction x_{DCB} (see section 2.2).

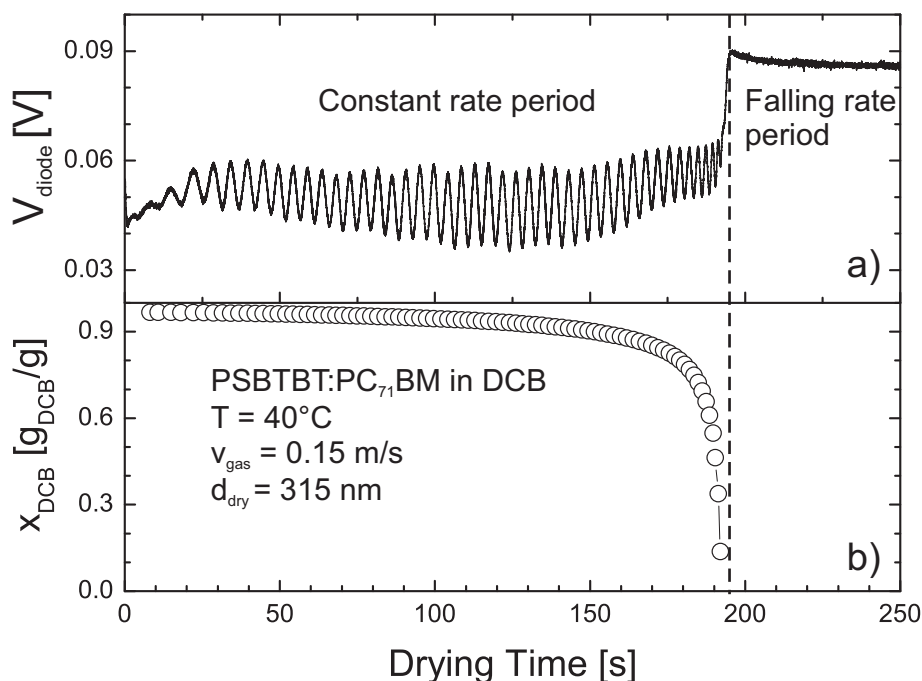


Figure 6.2: a) Reflectometer raw data of the PSBTBT:PC₇₁BM in situ GIXD drying experiment indicating the constant and falling rate period. Solvent was pure DCB. b) Calculated evolution of solvent mass fraction based on the reflectometer measurement.

Up to about 10wt.% DCB the film thickness decreases with a constant evaporation rate. Subsequently the drying rate drops strongly which is commonly attributed to a diffusional mass transfer limitation of the residual solvent in the film. These low amounts of solvent provide molecular mobility which can lead to slight ordering processes in this stage. Chang et al. have shown that residual solvent is even by thermal annealing hard to remove entirely [237].

The simultaneously obtained GIXD measurements are shown in Figure 6.3. The first image depicts the freshly cast PSBTBT:PC₇₁BM film from DCB solution. The sharp ring at lower q than DCB can be treated as background signal, since it is also observed for the bare substrate. Within the first measurements we do not observe any changes in diffraction features. At 90 s drying time and 95 wt.% solvent, GIXD reveals the first indication of PSBTBT (h00) crystallinity. The (h00) Bragg reflection is partly of a spot like shape indicating well-oriented nucleation at the interface. But we also observe another portion of randomly oriented polymer (h00) crystallinity at this early stage of nucleation. This indicated that PSBTBT not only partly crystallizes at

6.1 In-situ observation of molecular ordering

an interface as P3HT, but also crystallizes with random orientation. The PSBTBT (100) Bragg Peak and randomly orientated powder like diffraction ring do not change their shape in the course of drying as it was observed for P3HT:PCBM. The broad orientation distribution is also featured by the (010) π - π -stacking peak.

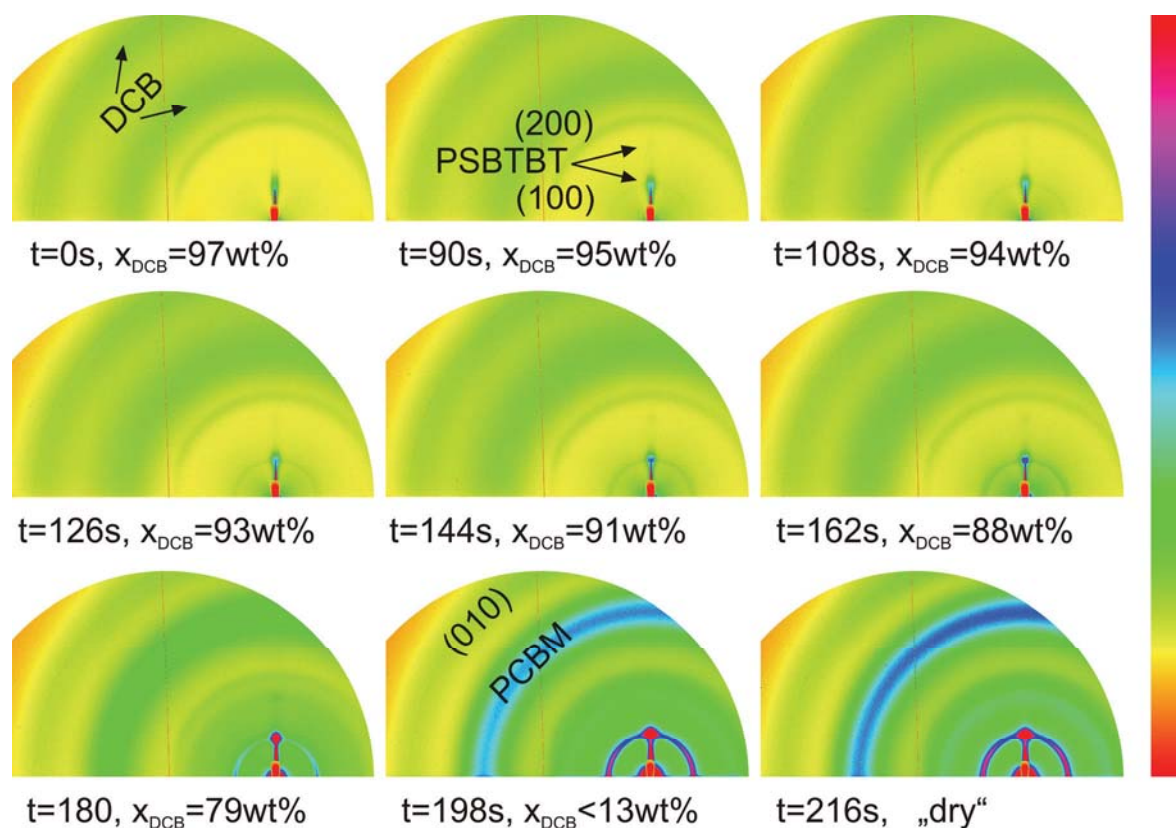


Figure 6.3: Evolution of GIXD diffraction patterns during the drying of a PSBTBT:PC₇₁BM (1:2) film cast from DCB solution by doctor blade at 40°C on native silicon substrate. While the first image is of the freshly coated film, the second image shows the first indication of crystallinity. Following images show the evolution of film drying and crystallization. Below each image, the drying time and actual solvent fraction is mentioned.

At a later stage PCBM aggregation sets in. The exact determination of PCBM aggregation needs further analysis of the profile plots. The important fact is that strong PCBM diffraction signals appear at the very end of the drying process which is similar in comparison to the behavior of P3HT:PCBM. For P3HT:PCBM, fullerene aggregation was observed at the transition from constant rate to falling rate period although the solubility limit

of PCBM was reached much earlier. It is likely that PC₇₁BM strongly interacts with PSBTBT which also leads to oppressed fullerene aggregation for this material combination. In the falling rate period the 2D diffraction pattern remains qualitatively uniform. Slight reorganization of the blend structure due to residual solvent probably leads to changes in peak intensities, but the main structure is settled after 216 s.

The diffraction feature associated with the PSBTBT (010) π - π -stacking overlaps with those of DCB. This also requires a deeper analysis of the profile plots which is beyond the scope of this work. The existence of well pronounced π - π -stacking should be visible in the absorption spectra and promotes hole mobility.

Results and Discussion for PCPDTBT:PC₇₁BM As demonstrated in the preceding section, PSBTBT behaves in its crystallization behavior in several aspects similar to P3HT. If the silicon bridging atom is exchanged with a carbon atom, the π - π -stacking is sterically hindered and reduces the crystallization ability of the carbon bridged polymer PCPDTBT (see Figure 1.5) [87, 243, 244, 250]. For particular this polymer the processing additive ODT shows a strong impact on the crystallization behavior. The mechanisms during the drying process have not yet been investigated in detail which is presented in this section.

Drying experiments with simultaneous in situ GIXD and laser reflectometry provide structural information and the associated film composition for processing without additive and with 3 wt.% ODT in the host solvent DCB. Figure 6.4 depicts the reflectometry measurement of the PCPDTBT:PC₇₁BM drying experiment in pure DCB. The dry film thickness is in the order as for the previously investigated PSBTBT experiment. The overall drying time for the PCPDTBT:PC₇₁BM films is shorter due to the higher solid fraction of 4.4 wt.% in comparison to 3 wt.% for PSBTBT:PC₇₁BM. However, the drying curve also features a constant rate period (\approx 110 s) followed by a long falling rate period extended over several hundred seconds. This second period is much stronger pronounced as in the case of PSBTBT.

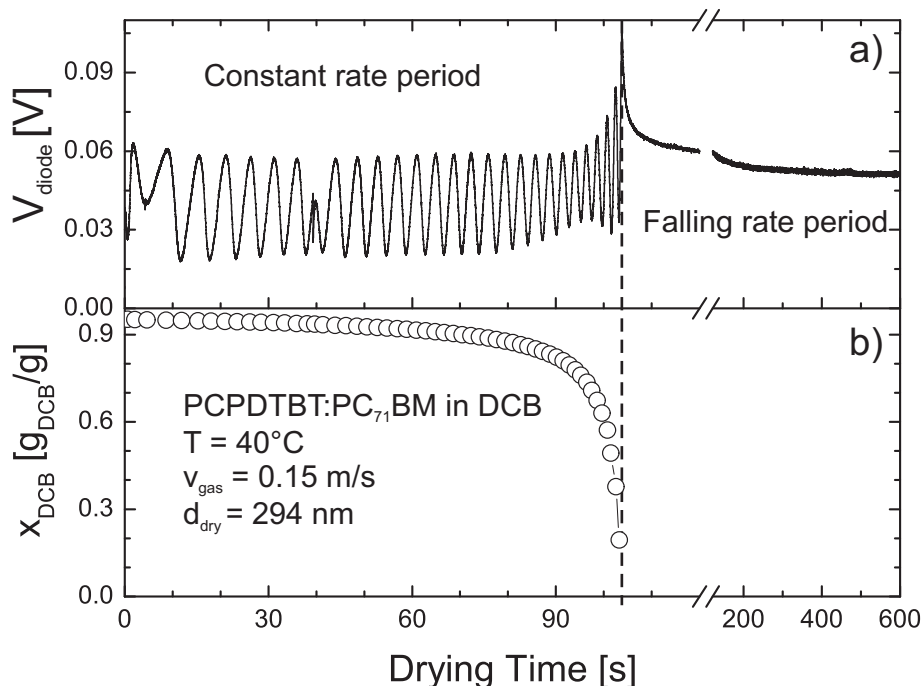


Figure 6.4: a) Reflectometer raw data of the PCPDTBT:PC₇₁BM in situ GIXD drying experiment indicating the constant and falling rate period. Solvent was pure DCB. b) Calculated evolution of solvent mass fraction based on the reflectometer measurement.

In the drying process of PCPDTBT:PC₇₁BM films processed without ODT diffraction patterns show the disappearance of DCB diffraction and the evolution of the powder like diffraction ring of PC₇₁BM (Figure 6.5). The polymer does not give a single indication of crystallinity. We only observe a very intense and broad background at low q which probably corresponds to randomly oriented PCPDTBT lamellae. Hence, on the one hand PC₇₁BM is allowed for aggregation. On the other hand PC₇₁BM hinders polymer crystallization. In the absence of fullerene Rogers et al. observed partial crystallinity for this polymer [250].

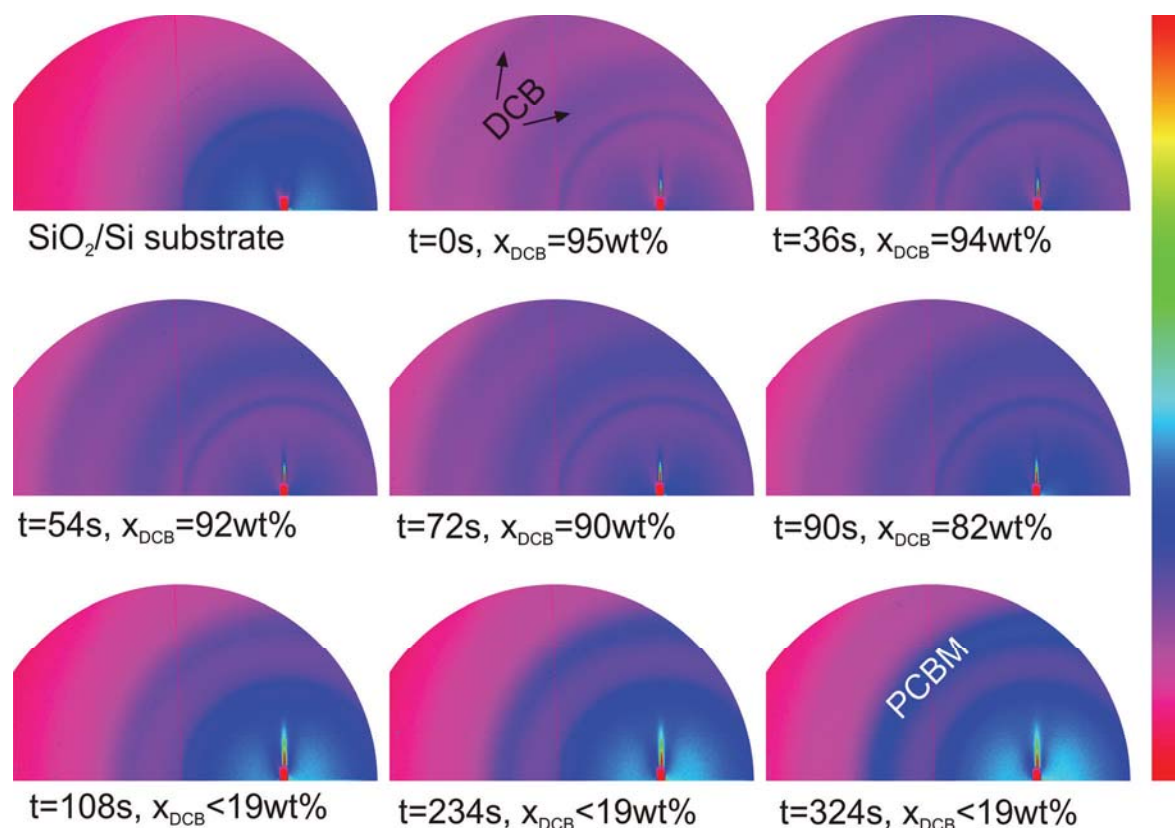


Figure 6.5: Evolution of GIXD diffraction patterns during the drying of a PCPDTBT:PC₇₁BM (1:3.4) film cast from DCB solution by doctor blade at 40°C on native silicon substrate. While the first image is of the bare substrate, the second image shows the freshly coated film. Following images show the evolution of film drying and PCBM aggregation. Below each image, the drying time and actual solvent fraction is mentioned.

Consequently, the crystallization ability should improve if selectively PCBM solvating additive is incorporated into the solution. We assume that ODT weakens the polymer-fullerene interactions by dissolving PCBM and providing more freedom for polymer assembly. Therefore the PCPDTBT:PC₇₁BM films have been investigated for DCB solutions with 3 wt.% ODT. Figure 6.6 depicts the drying behavior of such films. As already shown several times, we observe a DCB controlled constant rate period initially. Thereafter ODT evaporation controls the drying rate until the amount of ODT gets as low such that the film enters the falling rate period of diffusional limited ODT and DCB evaporation. Due to the extremely low vapor pressure of ODT we still observe a small change in reflectometry signal due to changes in the optical thickness after several thousand seconds which is likely to originate from residual solvent.

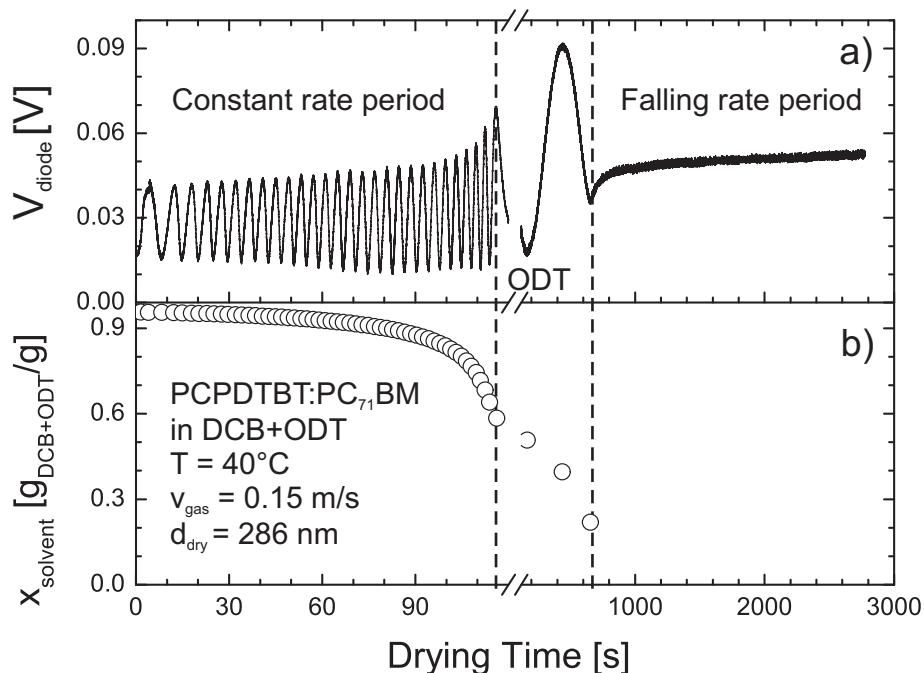


Figure 6.6: a) Reflectometer raw data of the PCPDTBT:PC₇₁BM in situ GIXD drying experiment indicating i) the DCB constant rate period followed by ii) ODT determined drying and finally iii) the falling rate period. Solvent was DCB with 3wt.% ODT. b) Calculated evolution of solvent mass fraction (DCB and ODT) based on the reflectometer measurement.

In order to obtain insights into the working principles of ODT in real time during drying, we investigated the structural evolution of PCPDTBT:PC₇₁BM dissolved in DCB and ODT. The drying film was monitored by in situ GIXD simultaneously to the above mentioned reflectometry measurement as depicted in Figure 6.7. The first image was obtained directly after film coating by doctor blade. In the first drying period no changes in the diffraction patterns can be observed. After 90 s the inner DCB ring at lower q gets more intense which is probably the first indication of PC₇₁BM aggregation. The powder like diffraction ring associated to PC₇₁BM clusters gets clearly visible in the subsequent image at 108 s. It is important to note that at this instant no PCPDTBT crystallization is observed. Since the solution contains selectively PC₇₁BM solvating ODT which should facilitate polymer crystallization and keep the fullerene in solution the opposite effect of foremost polymer crystallization was proposed. However, PC₇₁BM solubility is limited to about 19 mg/ml ($x_s \approx 2$ wt.%) in ODT at room temperature [100] which might have been crossed already at this stage of drying at 23 wt.%

6 Structure formation of low band gap polymers

overall solid fraction. A possible explanation could be the reduction of PC₇₁BM interactions with PCPDTBT due to ODT, which allows PC₇₁BM to get partly dissolved. This amount of PC₇₁BM molecules is not anymore hindered by interactions with the polymer and undergoes aggregation after the film has crossed fullerene solubility. The much higher diffraction intensity of PC₇₁BM in the ODT processed film also indicates an overall increased amount of fullerene clusters due to the effect of ODT.

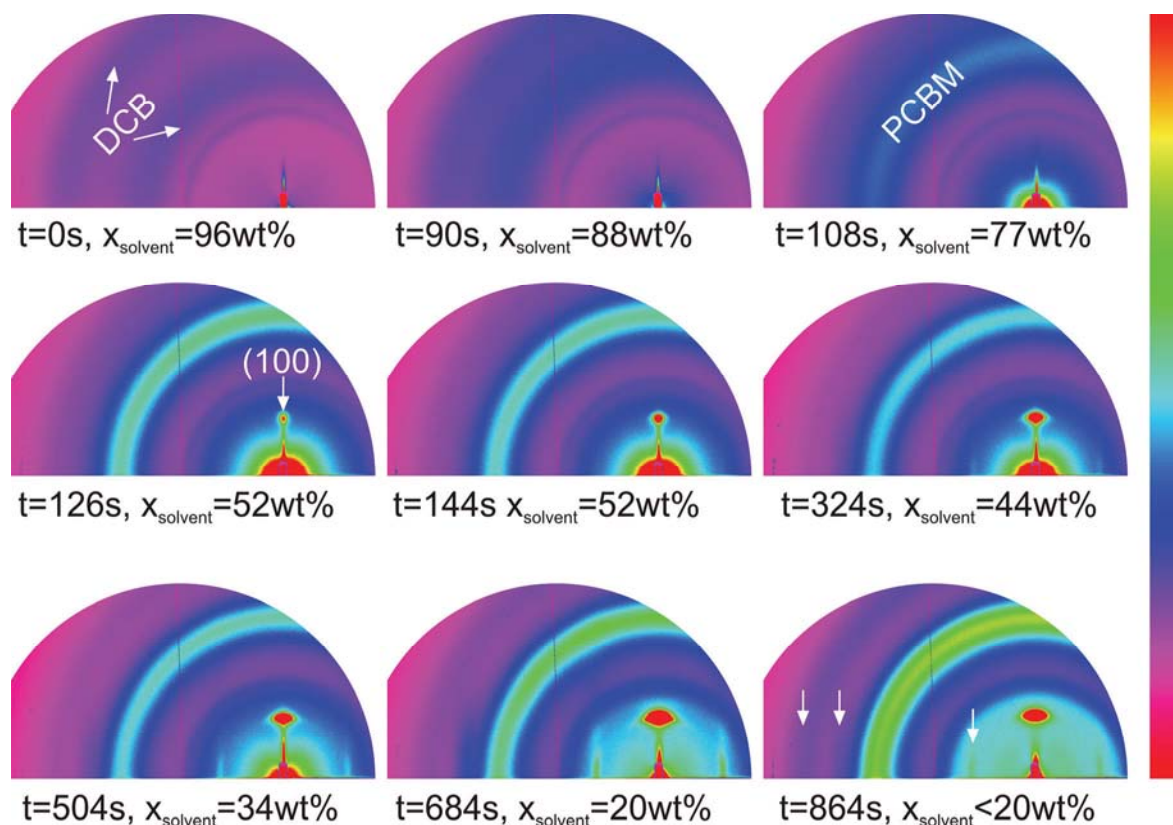


Figure 6.7: Evolution of GIXD diffraction patterns during the drying of a PCPDTBT:PC₇₁BM (1:3.4) film cast from DCB and 3wt.% ODT solution by doctor blade at 40°C on native silicon substrate. While the first image is of the freshly coated film, the second image shows the first indication of PCBM aggregation. Following images show the evolution of film drying and crystallization. Below each image, the drying time and actual solvent fraction is mentioned.

The polymer on the other hand crystallizes with nucleation at the interface (spot like (100) Bragg peak shape) at about 48 wt.% overall solid fraction which corresponds to the transition period from DCB controlled drying to ODT determined drying. In the following the PCPDTBT (100) Bragg reflec-

tion intensity and hence the amount of polymer crystallites grows. During the process of crystal growth many in-plane peaks (indicated by arrows) appear which indicates a much more complex structure for the carbon bridged PCPDTBT as for the silicon bridged PSBTBT. Rogers et al. attributed the different peaks to two polymorphs of this polymer [250]. The exact crystal-line structure of this molecule is not exhaustively understood and requires a deeper analysis of this data. It is notable that PCPDTBT crystallinity still increases strongly in the mainly ODT determined drying process starting at about 120 s and 52 wt.% solvent, although the polymer is insoluble in the additive. At the transition from ODT determined drying to the falling rate period a strong increase in background intensity close to the direct beam can be observed. This probably corresponds to randomly oriented PCPDTBT lamellae. The Bragg reflections exhibit much lower mosaicity in comparison to PSBTBT.

In conclusion, it could be shown that the usage of ODT allows for a well pronounced PCPDTBT crystallization and also promotes PC₇₁BM aggregation. In contrast to PSBTBT the nucleation is predominantly induced at the air or substrate interface as observed for P3HT and leads to a low mosaicity of the dry film polymer structure. It is important to mention that PC₇₁BM undergoes clustering before PCPDTBT crystallizes. This is probably due to the ODT promoted undisturbed fullerene aggregation in solution after crossing fullerene solubility which is not hampered anymore by the interaction with PCPDTBT.

6.2 Film structure and optoelectronic properties¹

Experimental AFM and absorption measurements as well as the solar cell fabrication are accomplished as described above. The average film thickness for the investigated solar cells was 86 ± 11 nm. Owing to the low solubility PSBTBT:PC₇₁BM solutions were prepared at 90°C. From literature it is known that 2 wt.% PSBTBT solutions in chlorobenzene already show solid state light absorption features [208]. This also demands processing temperatures above room temperature in order to prevent large scale crystallization and gelation. Therefore PSBTBT:PC₇₁BM solar cells were fabricated at 40-

¹ The work of this section was accompanied by the student research project of Timo Basile [252].

85°C coating and drying temperature and 0.15 m/s gas flow velocity in the previously introduced experimental setup (Figure 2.1).

Results and Discussion The in situ investigation of PSBTBT:PC₇₁BM blends revealed comparable crystallization mechanisms as previously observed for P3HT. Consequently one might expect the same process-structure dependencies as previously studied for P3HT. Hence, it is of interest to investigate the process-structure-property relationship of this material system for different drying conditions.

First, the active layer of solar cell devices was investigated by AFM. Figure 6.8a exemplarily shows the film topography for 60°C drying conditions. More AFM and STEM images can be found in the appendix in Figure 10.24. As for P3HT:PCBM we observe a large scale topography which comprises a finer substructure in the phase image (Figure 6.8b). The shape of the phase image features resembles those of polymer fibrils due to π - π -stacked polymer chains [46, 203, 232] as also observed for P3HT:PCBM (see Figure 4.20 and Figure 5.6). In contrast to P3HT the roughness of PSBTBT:PC₇₁BM films does not change with drying temperature. This indicates that the dynamics of PSBTBT assembly proceed faster than the drying process which is not capable of limiting the structural ordering of the PSBTBT:PC₇₁BM blend.

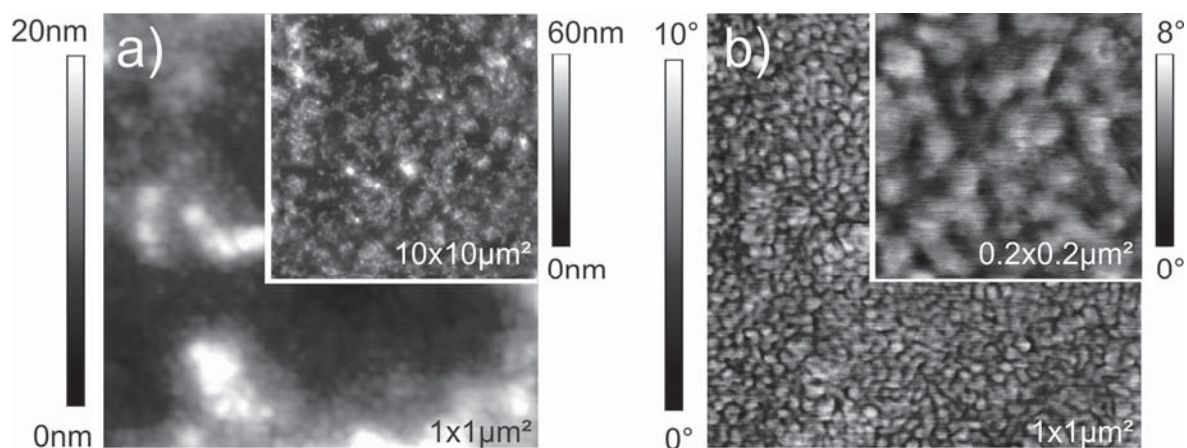


Figure 6.8: Representative AFM a) topography and b) phase images of a PSBTBT: PC₇₁BM (1:2) film cast from DCB at PEDOT:PSS/ITO/glass and dried at 60°C, $v = 0.15$ m/s gas flow. The film thickness was 90 nm.

Deeper insights into the degree of phase separation by the selective removal of PC₇₁BM could not be obtained since the PSBTBT:PC₇₁BM is mechanically unstable after washing off PC₇₁BM and collapses during sample preparation. The reduced mechanical stability of the remaining polymer network suggests that a finer interpenetrating polymer-fullerene network is present in this case. The scheme in Figure 6.10 might indicate a possible explanation for the reduced mechanical stability. In P3HT, the hexyl side chains are placed in a spacing minor to the C₆₀ diameter at the polymer backbone [225]. This prevents fullerene intercalation into P3HT crystallites [44] and gives best device performance for roughly 1:1 polymer-fullerene ratios. Cates et al. investigated intercalated poly(2,5-bis(3-hexadecylthiophen-2-yl)thieno[3,2-b]thiophene (pBTTT):fullerene blends [251]. In their case the device performance was very low at a 1:1 blending ratio due to the incorporation of fullerene into the polymer structure, but could considerably be increased by increasing the PC₇₁BM ratio to 1:4 due to the formation of continuous PC₇₁BM electron pathways.

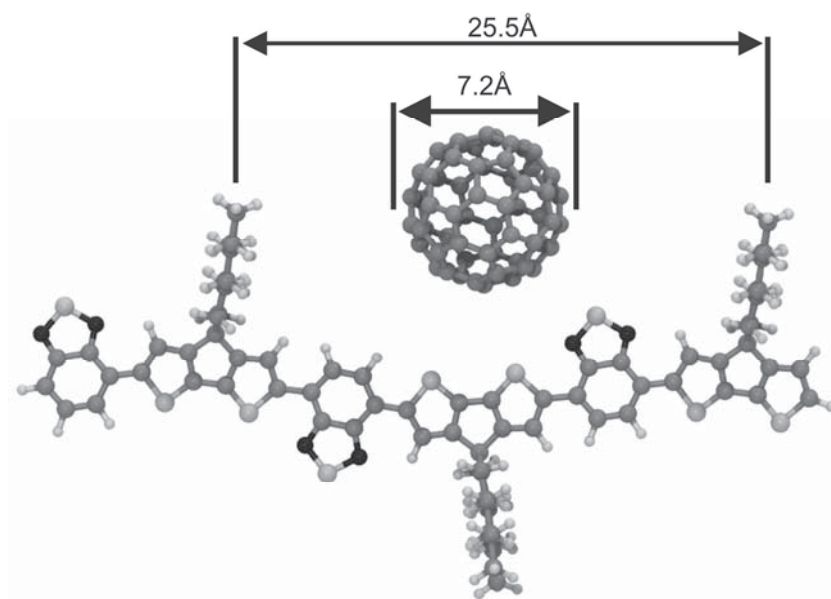


Figure 6.9: This scheme illustrates the side chain spacing of PCPDTBT in comparison to the size of a non functionalized C₆₀ fullerene.¹

¹ This image was provided by Robert Maul of the Institute of Nanotechnology (INT) at KIT.

6 Structure formation of low band gap polymers

In the case of PSBTBT and PCPDTBT the optimum blending ratios for efficient solar cells are 1:2 and 1:3.4 respectively. This is also superior to 1:1 which might also be an indication for fullerene intercalation that requires superior amounts of PCBM for the formation of continuous electron pathways through the bulk heterojunction layer. Such high blending ratios result in largely hindered π - π -stacking in P3HT:PCBM blends as mentioned above in section 4.4 if no fullerene intercalation takes place.

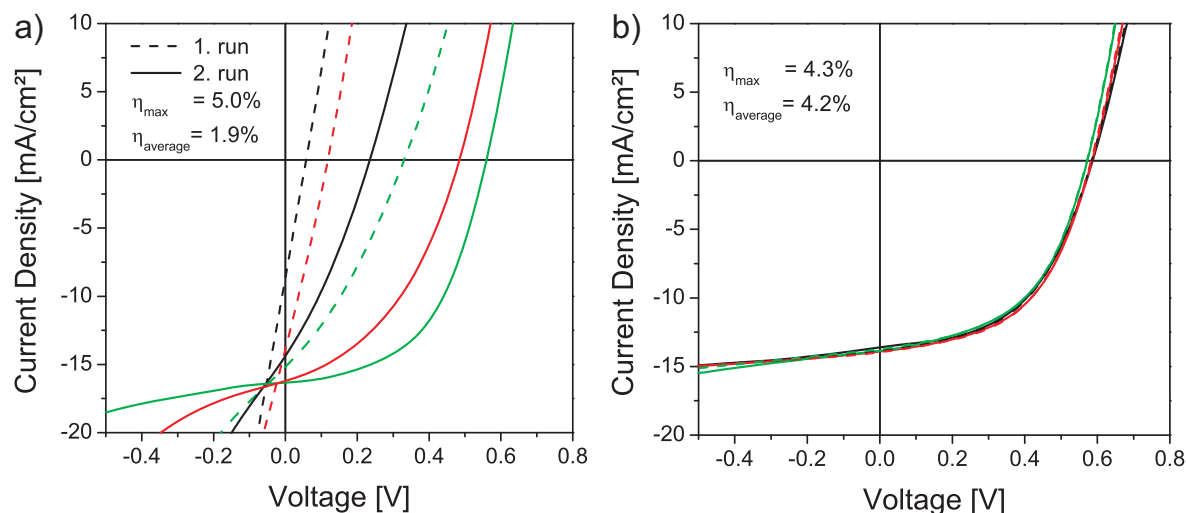


Figure 6.10: Current density – voltage (JV) characteristics of (1:2) PSBTBT:PC₇₁BM solar cells cast by doctor blade from DCB at 40°C drying temperatures under ambient conditions. a) JV-curves of three solar cells after the first and second characterization run for a) an as cast device and b) the same but subsequently thermally treated device (5min at 150°C). Maximum and average efficiencies are mentioned in each graph. [252]

Prior to a thermal treatment of as cast PSBTBT:PC₇₁BM solar cells the devices show on the one hand a strong performance deviation and on the other hand a strong instability of the JV-characteristics. Figure 6.10a depicts exemplary JV-curves for a 40°C processed sample. In comparison to the first characterization run the PCE increases with device characterization time. In the second characterization run one solar cell of the 40°C processed substrate exhibited 5% power conversion efficiency while other solar cells at the same substrate showed quite poor performance. It is important to note that the JV-curves are pinned at a constant J_{sc} during these changes. This implies that the morphology is in a sufficiently efficient state, such that charge carriers can be transported to the interface. The strong increase in V_{oc} on the other hand

suggests that interface effects are responsible for initially reduced solar cell efficiency. These suggestions are in agreement with Lu et al. who showed recently the increase of PCBM concentration at the BHJ film-cathode interface due to thermal annealing after cathode deposition [253].

Figure 6.10b shows the same sample after thermal treatment at 150°C for 5 min. After the annealing step no difference in-between both characterization runs exists anymore and all JV-curves coincide precisely. Hence, the thermal treatment led to a sort of equilibration of the film-cathode interface which results in a very homogeneous device performance. The average PCE strongly increased while the maximum value decreased. This could originate from an improved state at the interface but slightly worsened bulk morphology due to increased PC₇₁BM cluster size upon annealing [83].

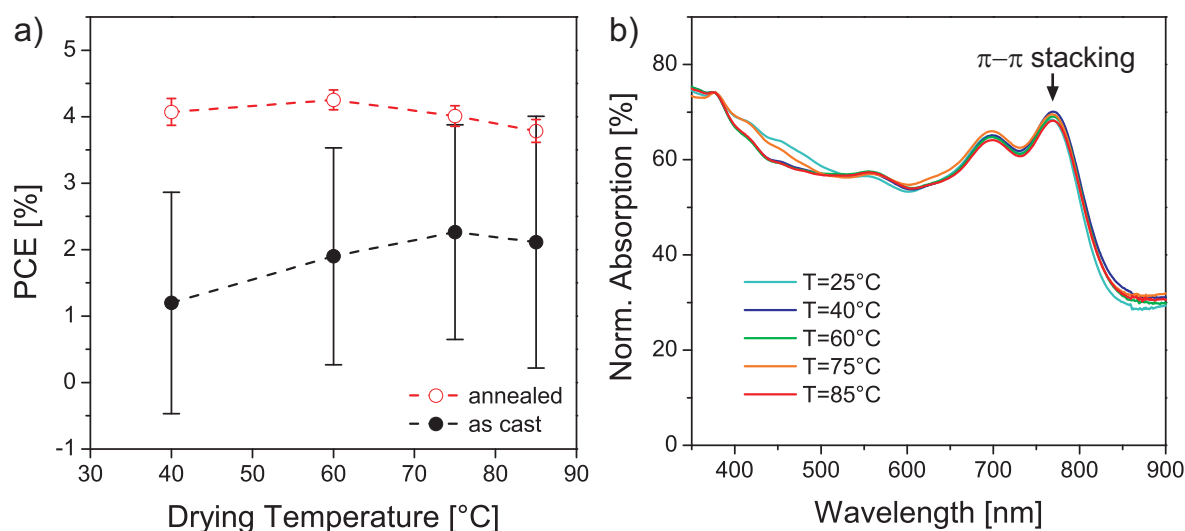


Figure 6.11: a) Average power conversion efficiencies for the as cast solar cells (filled symbols) and after subsequent thermally treatment (open symbols) of solar cells dried at different temperatures. b) Normalized absorption spectra of PSBTBT:PC₇₁BM films taken from the same substrates as the solar cells and were measured as cast. [252]

The comparison of as cast and annealed solar cells is shown for all investigated drying conditions in Figure 6.11a. A summary of device performance can be found in the appendix (Table 10.3 and Table 10.4). The strong decrease of performance deviation after annealing occurs for all drying temperatures. Additionally, the annealing step results in an increased but still roughly constant average PCE for all temperatures. Within the deviation of device performance no correlation between PCE and drying temperature can be

observed. This is in further agreement with the light absorption behavior of the presented solar cells as shown in Figure 6.11b. The spectra are normalized to the absorption peak at 375 nm. While the absorption peak at 700 nm is already present in neat PSBTBT solutions the peak at 760 nm is attributed to polymer chain π - π interaction [243]. All spectra are similar regardless of the film processing temperature from 25°C to 85°C indicating a similar conjugation length and similar amount of π - π packed polymer chains.

In conclusion, we identified PSBTBT as an efficient polymer with fast crystallization kinetics which could not be altered by means of different drying temperatures in the range of 25°C-85°C. This is beneficial for large area OPV fabrication where inhomogeneous drying rates and a broad temperature distribution can occur. P3HT:PCBM is very sensitive to processing conditions which could lead to laterally inhomogeneous device performance in large area devices. The discovery of the independence of PSBTBT:PC₇₁BM film morphology and optoelectronic properties from coating and drying process parameters allows for an independent process optimization in terms of coating quality and fabrication throughput without drawbacks in solar cell performance. Reduced fullerene concentration at the BHJ layer-cathode interface is possibly one reason for the requirement of thermal annealing that provides an enrichment of fullerene at the cathode. Prior to this step strong performance deviations and poor performance stability was observed.

7 Conclusion

7.1 Summary of the obtained results

Starting point of this work was the hypothesis that drying process parameters are suitable for systematically tuning the structure formation during drying of solution cast polymer-fullerene films in order to generate optimized structures with improved photovoltaic performance. For the evaluation of this hypothesis the structure formation of the polymer-fullerene material system P3HT:PCBM was investigated incorporating i) thin film drying kinetics, ii) phase behavior of polymer-fullerene solutions, iii) structure formation and iv) the drying process-structure-property relationship of P3HT:PCBM solar cells. The generality of the obtained results has been studied in comparison with the behavior of low band gap polymers namely PSBTBT and PCPDTBT.

Drying kinetics Within this thesis a dedicated coating and drying setup was developed which afforded precisely defined coating and drying process conditions as prerequisite for all obtained results. For the first time, the drying behavior of finally a few hundred nanometer thin films could be investigated at five measurement positions with laser reflectometry simultaneously. This allowed the elaboration of a spatially resolved numerical thin film drying model. The model includes a gas phase mass transfer as a function of time and space, ideal solution behavior with respect to solid-liquid and liquid-liquid interaction of the multiple components and neglects diffusional resistance within the film. In conjunction with drying experiments this model showed to be capable of describing the effect of a moving drying front in drying gas flow direction if the mass transfer resistance is governed by the gas phase. The drying front causes a local acceleration of the drying rate as the drying front approaches.

The drying behavior of solvent mixtures as measured spatially resolved could also be described reasonably with the elaborated model under the mentioned simplifications. In the course of these investigations it could be demonstrated that for such thin films in the sub micrometer range the drying process also comprises a constant rate period (constant evaporation rate) and a falling rate period (decreasing evaporation rate). The latter was observed even

at film thicknesses below 100 nm where solvent diffusion distances to the film surface are very short.

Thermodynamics of polymer-fullerene solutions In conjunction with the measurement and simulation of the evolution of film composition it was of interest to determine important instants of phase transitions during the film formation such as solubility limits. Therefore a method for the determination of the binary solutions phase diagrams was elaborated. Oversaturated solutions of pure P3HT and PCBM solutions were prepared and agitated at a constant temperature. In a temperature controlled centrifugation step and further resting in order to diminish the shearing forces from centrifugation, a sufficiently clear phase separated state was achieved. In a subsequent step the composition of each phase was determined via refractive index measurements. With this method the binodal region of P3HT solutions could be determined in the temperature range of 0°C-60°C. Within the unstable region P3HT solutions phase separate into a sol and a gel phase. We suggest that the onset of gel formation, which represents the formation of a physically cross-linked network over macroscopic dimensions within the solution phase, governs the formation of the semi crystalline BHJ morphology. The fullerene PCBM exhibits only a simple solubility limit. If PCBM solubility is crossed, solid aggregates precipitate. Furthermore the temperature related increase of solubility is stronger for PCBM as for P3HT in the investigated range from 0-60°C.

Structure formation After being able to control and describe thin film drying kinetics and to know the solubility limits of donor and acceptor molecules it was possible to draw the drying path through the phase diagram. According to the superposition of the binary phase diagrams PCBM is expected to form clusters before P3HT undergoes partial gelation because of the higher solubility of P3HT.

However, we were only able to determine the binary phase diagrams and had to develop another technique for the investigation of the ternary system as applied for solar cell fabrication. Therefore the above mentioned coating and drying setup with spatially resolved thickness measurement was combined with synchrotron based grazing incidence X-ray diffraction (GIXD) measurements. This novel method allowed the in situ observation of the ternary

polymer-fullerene-solvent crystallization process during solvent evaporation in real time. This gave us unique insights into the mechanisms and dynamics of polymer-fullerene blend crystallization. Each GIXD measurement could be related to the current film thickness and composition due to the simultaneously accomplished reflectometry measurement. With this experimental approach the structural evolution in the ternary blend could be associated with the position in the ternary phase diagram. After reaching P3HT solubility the crystallization proceeded with i) well oriented P3HT nucleation at the air or substrate interface followed by ii) P3HT crystal growth with increasing orientation distribution of the crystallites and finally iii) PCBM aggregation in the final drying period. The strongest structural changes proceed in the final part of the constant rate drying period, where the solid fraction undergoes the strongest increase and crosses a wide range in the phase diagram. The onset of P3HT crystallization coincided with the instant of crossed P3HT solubility which is equivalent to the onset of gelation. The comparison with the binary phase diagrams furthermore suggested the fullerene to crystallize before the polymer. The contradictory experimental results deliver the information of strong polymer-fullerene interaction forces. These strong interactions suppress PCBM aggregation because PCBM interacts stronger with P3HT as with molecules of its own kind. If P3HT is absent, PCBM forms micrometer to millimeter large crystals which supports this hypothesis.

By increasing the PCBM fraction it could be shown for the 1:2 P3HT:PCBM ratio that PCBM molecules brake the (020) π - π -stacking of P3HT lamellae which signifies a dramatic loss of hole mobility and consequently reduced device performance. Thermal annealing promotes PCBM diffusion and the thermodynamically preferred π - π -stacking squeezes PCBM out of the subsequently formed P3HT crystallites.

It is further notable that increasing drying temperature reduces the amount of (020) π - π -stacked P3HT molecules but leads to an increased amount of P3HT (100) crystallinity. Hence, drying temperature determines the preferred direction of crystal growth.

Drying process-structure-property relationship As mentioned before, PCBM solubility increases stronger with temperature than P3HT solubility in DCB. This signifies reduced polymer-fullerene interactions in solutions at higher temperatures. Consequently higher temperatures promote PCBM clustering resulting in a coarser P3HT:PCBM phase segregation. This was

confirmed independently by GIXD with a higher crystal correlation length of PCBM and AFM measurements after selective PCBM removal which revealed larger PCBM domains. Besides a finer degree of phase separation, reduced drying temperatures also causes a higher amount of π - π -stacked polymers, longer polymer conjugation length, increased amount of vertical charge transport pathways and an increasingly rough topography due to larger polymer aggregates. These aggregates are on a superior scale to that of polymer-fullerene phase separation. Jointly this leads to improved power conversion efficiency at lower drying temperatures.

The beneficial effect of long drying times suggested that the strong polymer-fullerene interaction hinders P3HT crystallization. Therefore 3 wt.% of the selectively PCBM solvating and low volatile additive ODT was incorporated into the solution. This enhanced in particular the π - π -stacking capability of P3HT. Beside this, no further effect attributed to ODT could be observed. The solar cell efficiency of ODT processed devices also showed best performance for low temperature drying, but maximum efficiencies did not exceed those of ODT free processed solar cells fabricated at low temperatures. Hence, the incorporation of ODT did not compensate the deteriorating effect of higher drying temperatures. Thus, drying time could not be decreased by means of increased temperatures upon the usage of ODT. Moreover, the falling rate drying period increases strongly due to the low vapor pressure of ODT.

Another strategy for accelerating drying time with only small drawbacks in solar cell performance resulted upon the observation of the onset of crystallization at the solubility limit of P3HT. Depending on the formulation of the initial solution it can take about 50% of the constant rate period drying time until P3HT solubility is crossed. The incorporation of different “friendly” low volatile co-solvents provided a 40% reduction of drying time at similar solar cell performance as for the pure host solvent. The focus of reduced drying time was combined with the replacement of the halogenated solvent DCB. With slight drawbacks in device performance DCB could be replaced by the solvent mixture toluene-indane with 40% increased throughput at same drying conditions.

Transferability to other material systems Finally it was of interest to investigate the transferability of the obtained knowledge on molecular assembly in P3HT:PCBM films to other material systems. Attractive electron donor

molecules are for instance low band gap polymers such as PSBTBT and PCPDTBT because of their absorption in the low photon energy regions up to 800 nm. Both polymers are alternating donor-acceptor copolymers. Due to their large side chain spacing fullerene intercalation seems to be possible. This is in strong contrast to P3HT. The consequences for structure formation were investigated within this thesis. Furthermore, asymmetric PC₇₁BM fullerenes are interesting due to their stronger light absorption in comparison to their C₆₀ derivative PC₆₁BM as mainly investigated in this thesis.

On the one hand, the crystallization mechanism of PSBTBT:PC₇₁BM (1:2) blends show similarities to that of P3HT:PCBM with partly interface induced polymer nucleation and subsequent fullerene aggregation in the final drying stage. Non-orientated bulk crystallization was observed in parallel. On the other hand, we observed no correlation between drying conditions and film structure and consequently no impact on solar cell performance for this material system. This suggests that PSBTBT crystallization kinetics proceed fast enough such that the drying process cannot limit the structure formation.

PCPDTBT:PC₇₁BM (1:3.4) films show very poor crystallinity after regular processing due to the strong interaction between polymer and fullerene and further steric hindrance. If this blend is processed with selectively PCBM solvating additive ODT it undergoes crystallization. In this case PC₇₁BM crystallizes before the onset of polymer crystallization which is due to reduced polymer-fullerene interaction forces at a comparatively high amount of fullerene in solution. This allows for fullerene clustering because fullerene-fullerene interactions are not anymore that strong weakened by the presence of the polymer. As shown in literature this increase in crystallinity leads to a strong increase in device performance. This effect was also visible for P3HT:PCBM where the ODT effect was less, but revealed the same effect of promoted polymer crystallinity.

Summary In conclusion P3HT:PCBM is a very suitable polymer-fullerene model system for the investigation of the process-structure-property relationship due to its sensitivity to many process parameters. The real time investigations of the structure formation during film drying could be conducted with novel experimental methods developed within this thesis for the first time. This gave unique insights into molecular assembly mechanisms and their dynamics. The obtained results provide a fundamental understanding of molecular ordering during drying of solution cast films. In relation to the

obtained structural study different parameters such as the drying temperature, drying gas velocity and the choice of solvent could successfully been exploited for the manipulation of structure formation resulting in improved device performance. The elaborated film drying simulation could be exploited for the design of an initially accelerated drying process of halogen free solvent mixtures with only small drawbacks in device performance. The mechanisms of structure formation of chemically more complex systems showed similarities to those of P3HT:PCBM, although the dependency on the drying process was not observed. However, the developed powerful in situ techniques will provide access to a profound investigation of novel materials and other applications where film structure is of importance which facilitates the process optimization in future research.

7.2 Outlook

The strong impact of process conditions on the structure formation with implications on device performance, as investigated in this thesis, has already been expanded to other topics within our research group. It can be of importance for other materials which undergo structure formation during the fabrication process such as organic light emitting diodes (OLED), lithium ion battery materials, transparent conductive materials or membranes. A deeper investigation of the process-structure-property relationship for such applications could reveal new processing approaches towards increased material performance.

From the morphological point of view it will be important to investigate the impact of fabrication conditions, solvents and their mixtures on the vertical profile in polymer-fullerene composition. These might cause low device performance although an integral measurement of film morphology suggests the film structure to provide an efficient bulk heterojunction. For instance enrichment of the hole conducting polymer at the cathode or of electron conducting fullerene at the anode interface would act as barrier for charge carrier extraction. Up to now many suggestions for the driving force for such vertical gradients are reported, but the understanding remains incomplete. Understanding the governing mechanisms will provide novel approaches for the prevention or exploitation of vertical gradients in the desired spatial orientation.

A consequent step towards morphology control results from the observation of interface induced polymer nucleation and crystal growth (see section 4.3). If nuclei form at the substrate interface one can influence the nucleation and subsequent crystal growth by modifications of the interface. In situ GIXD is an appropriate technique for the investigation of the effectiveness of the chosen interface engineering approaches.

Beside the investigation of novel donor acceptor materials it would be important to investigate the transferability of structural investigations obtained for batch fabrication to large area fabrication processes. For this purpose a roll-to-roll plant is available in the Thin Film Technology research laboratory.

8 References

- [1] BP, “Statistical review of world energy, <http://www.bp.com/statisticalreview>,” June 2010.
- [2] V. Quaschnig, *Regenerative Energiesysteme*, vol. 5. Hanser Verlag München, 2009.
- [3] V. Smil, “Energy at the crossroads,” in *OECD Global Science Forum Conference on Scientific Challenges for Energy Research*, 2006.
- [4] C. Bankier and S. Gale, “Energy payback of roof mounted photovoltaic cells,” *Energy Bulletin*, vol. <http://energybulletin.net/print/17219>, 2006.
- [5] V. Fthenakis and E. Alsema, “Photovoltaics energy payback times, greenhouse gas emissions and external costs: 2004–early 2005 status,” *Prog. Photovolt: Res. Appl.*, vol. 14, p. 275–280, 2006.
- [6] A. Furman and M. Rashid, “Solar feasibility - can solar energy compete economically?,” *Electrical Communications and Computers (CONIELECOMP), 2011 21st International Conference, San Andres Cholula*, vol. 2, pp. 10 – 13, 2011.
- [7] F.C. Krebs, S.A. Gevorgyan, J. Alstrup, “A roll-to-roll process to flexible polymer solar cells: model studies, manufacture and operational stability studies,” *Journal of Materials Chemistry*, vol. 19, pp. 5442–5451, 2009.
- [8] R. Steim, P. Schilinsky, S.A. Choulis, C.J. Brabec, “Flexible polymer photovoltaic modules with incorporated organic bypass diodes to address module shading effects,” *Solar Energy Materials and Solar Cells*, vol. 93, p. 1963–1967, 2009.
- [9] S.C. Gong, S.K. Jang, S.O. Ryu, H. Jeon, H.H. Park, H.J. Chang, “Post annealing effect of flexible polymer solar cells to improve their electrical properties,” *Current Applied Physics*, vol. 10, pp. e192–e196, 2010.
- [10] Y. Galagan, J.E.J.M. Rubingh, R. Andriessen, C.C. Fan, P.W.M. Blom, S.C. Veenstra, J.M. Kroon, “Ito-free flexible organic solar cells with printed current collecting grids,” *Solar Energy Materials and Solar Cells*, vol. 95, pp. 1339–1343, 2011.
- [11] D.J. Lipomi, B.C.K. Tee, M. Vosgueritchian, Z. Bao, “Stretchable organic solar cells,” *Advanced Materials*, vol. 23, pp. 1771–1775, 2011.
- [12] M.C. Barr, J.A. Rowehl, R.R. Lunt, J. Xu, A. Wang, C.M. Boyce, S.G. Im, V. Bulovic, K.K. Gleason, “Direct monolithic integration of organic photovoltaic circuits on unmodified paper,” *Advanced Materials*, vol. 23, p. 3500–3505, 2011.
- [13] X. Fan, Z. Chu, F. Wang, C. Zhang, L. Chen, Y. Tang, D. Zou, “Wire-shaped flexible dye-sensitized solar cells,” *Advanced Materials*, vol. 20, p. 592–595, 2008.
- [14] B. O’Connor, K.P. Pipe, M. Shtein, “Fiber based organic photovoltaic devices,” *Applied Physics Letters*, vol. 92, p. 193306, 2008.

8 References

- [15] M.A. Green, K. Emery, Y. Hishikawa, W. Warta, “Solar cell efficiency tables (version 37),” *Prog. Photovolt: Res. Appl.*, vol. 19, p. 84–92, 2011.
- [16] ZSW Stuttgart, “New world record with efficient cigs solar cell, www.zsw-bw.de,” August 2010.
- [17] F. C. Krebs, “Polymer solar cell modules prepared using roll-to-roll methods: Knife-over-edge coating, slot-die coating and screen printing,” *Solar Energy Materials and Solar Cells*, vol. 93, pp. 465–475, 2009.
- [18] F. C. Krebs, “Fabrication and processing of polymer solar cells: A review of printing and coating techniques,” *Solar Energy Materials and Solar Cells*, vol. 93, no. 4, pp. 394–412, 2009.
- [19] F.C. Krebs, T. Tromholt, M. Jørgensen, “Upscaling of polymer solar cell fabrication using full roll-to-roll processing,” *Nanoscale*, vol. 2, pp. 873–886, 2010.
- [20] B. Zimmermann, H.-F. Schleiermacher, M. Niggemann, U. Würfel, “Ito-free flexible inverted organic solar cell modules with high fill factor prepared by slot die coating,” *Solar Energy Materials and Solar Cells*, vol. 95, no. 7, pp. 1587–1589, 2011.
- [21] F.C. Krebs, J. Alstrup, H. Spanggaard, K. Larsen, E. Kold, “Production of large-area polymer solar cells by industrial silk screen printing, lifetime considerations and lamination with polyethyleneterephthalate,” *Solar Energy Materials and Solar Cells*, vol. 83, pp. 293–300, 2004.
- [22] S.E. Shaheen, R. Radspinner, N. Peyghambarian, G.E. Jabbour, “Fabrication of bulk heterojunction plastic solar cells by screen printing,” *Applied Physics Letters*, vol. 79, no. 18, pp. 2996–2998, 2001.
- [23] P. Kopola, T. Aernouts, S. Guillerez, H. Jin, M. Tuomikoski, A. Maaninen, J. Hast, “High efficient plastic solar cells fabricated with a high-throughput gravure printing method,” *Solar Energy Materials and Solar Cells*, vol. 94, p. 1673–1680, 2010.
- [24] C. Girotto, D. Moia, B.P. Rand, P. Heremans, “High-performance organic solar cells with spray coated hole-transport and active layers,” *Advanced Functional Materials*, vol. 21, p. 64–72, 2010.
- [25] J.S. Kim, W.S. Chung, K. Kim, D.Y. Kim, K.J. Paeng, S.M. Jo, S.Y. Jang, “Performance optimization of polymer solar cells using electrostatically sprayed photoactive layers,” *Advanced Functional Materials*, vol. 20, p. 3538–3546, 2010.
- [26] L.M. Chen, Z. Hong, W.L. Kwan, C.H. Lu, Y.F. Lai, B. Lei, C.P. Liu, Y. Yang, “Multi-source/component spray coating for polymer solar cells,” *ACS Nano*, vol. 4, pp. 4744–4752, 2010.
- [27] R. Green, A. Morfa, A.J. Ferguson, N. Kopidakis, G. Rumbles, S.E. Shaheen, “Performance of bulk heterojunction photovoltaic devices prepared by airbrush spray deposition,” *Applied Physics Letters*, vol. 92, p. 033301, 2008.
- [28] S.Y. Park, Y.J. Kang, S. Lee, D.G. Kim, J.K. Kim, J.H. Kim, J.W. Kang, “Spray-coated organic solar cells with large-area of 12.25 cm²,” *Solar Energy Materials and Solar Cells*, vol. 95, p. 852–855, 2011.

- [29] A. Lange, M. Wegener, C. Boeffel, B. Fischer, A. Wedel, D. Neher, "A new approach to the solvent system for inkjet-printed p3ht:pcbm solar cells and its use in devices with printed passive and active layers," *Solar Energy Materials and Solar Cells*, vol. 94, pp. 1816–1821, 2010.
- [30] C.N. Hoth, S.A. Choulis, P. Schilinsky, C.J. Brabec, "High photovoltaic performance of inkjet printed polymer:fullerene blends," *Advanced Materials*, vol. 19, pp. 3973–3978, 2007.
- [31] G. Dennler, M.C. Scharber, C.J. Brabec, "Polymer-fullerene bulk-heterojunction solar cells," *Advanced Materials*, vol. 21, pp. 1323–1338, 2009.
- [32] R. Service, "Outlook brightens for plastic solar cells," *Science*, vol. 332, p. 293, 2011.
- [33] B. Gregg, "Excitonic solar cells," *Journal of Physical Chemistry B*, vol. 107, pp. 4688–4698, 2003.
- [34] C.W. Tang, "Two-layer organic photovoltaic cell," *Applied Physics Letters*, vol. 48, no. 2, pp. 183–185, 1986.
- [35] A. Haugeneder, M. Neges, C. Kallinger, W. Spirkl, U. Lemmer, J. Feldmann, U. Scherf, E. Harth, A. Gügel, K. Müllen, "Exciton diffusion and dissociation in conjugated polymer/fullerene blends and heterostructures," *Physical Review B*, vol. 59, pp. 15 346–15 351, 1999.
- [36] R.R. Lunt, N.C. Giebink, A.A. Belak, J.B. Benziger, S.R. Forrest, "Exciton diffusion lengths of organic semiconductor thin films measured by spectrally resolved photoluminescence quenching," *Journal of Applied Physics*, vol. 105, p. 053711, 2009.
- [37] L.G. Yang, H.Z. Chen, M. Wang, "Optimal film thickness for exciton diffusion length measurement by photocurrent response in organic heterostructures," *Thin Solid Films*, vol. 516, p. 7701–7707, 2008.
- [38] S. Hellström, F. Zhang, Olle Inganäs, M.R. Andersson, "Structure-property relationships of small bandgap conjugated polymers for solar cells," *Dalton Transactions*, vol. 45, p. 10032–10039, 2009.
- [39] J. J. M. Halls, J. Cornil, D. A. dos Santos, R. Silbey, D. H. Hwang, A. B. Holmes, J. L. Bredas, R. H. Friend, "Charge- and energy-transfer processes at polymer/polymer interfaces: A joint experimental and theoretical study," *Physical Review B*, vol. 60, p. 5721–5727, 1999.
- [40] J.L. Brédas, D. Beljonne, V. Coropceanu, J. Cornil, "Charge-transfer and energy-transfer processes in δ -conjugated oligomers and polymers: A molecular picture," *Chemical Reviews*, vol. 104, pp. 4971–5003, 2004.
- [41] J. J. M. Halls, C.A. Walsh, N.C. Greenham, E.A. Marseglia, R.H. Friend, S.C. Moratti, A.B. Holmes, "Efficient photodiodes from interpenetrating polymer networks," *Nature*, vol. 376, pp. 498–500, 1995.

8 References

- [42] G. Yu, A. J. Heeger, “Charge separation and photovoltaic conversion in polymer composites with internal donor/acceptor heterojunctions,” *Journal of Applied Physics*, vol. 78, p. 45410, 1995.
- [43] S.E. Shaheen, C.J. Brabec, N.S. Sariciftci, F. Padinger, T. Fromherz, J.C. Hummelen, “2.5% efficient organic plastic solar cells,” *Applied Physics Letters*, vol. 78, pp. 841–843, 2001.
- [44] B.A. Collins, E. Gann, L. Guignard, X. He, C.R. McNeill, H. Ade, “Molecular miscibility of polymer-fullerene blends,” *J. Phys. Chem. Lett.*, vol. 1, p. 3160–3166, 2010.
- [45] J.A. Merlo, C.D. Frisbie, “Field effect conductance of conducting polymer nanofibers,” *Journal of Polymer Science: Part B: Polymer Physics*, vol. 41, p. 2674–2680, 2003.
- [46] R. Zhang, B. Li, M.C. Iovu, M. Jeffries-EL, G. Sauvé, J. Cooper, S. Jia, S. Tristram-Nagle, D.M. Smilgies, D.N. Lambeth, R.D. McCullough, T. Kowalewski, “Nanostructure dependence of field-effect mobility in regioregular poly(3-hexylthiophene) thin film field effect transistors,” *J. Am. Chem. Soc.*, vol. 128, pp. 3480–3481, 2006.
- [47] A.A. Virkar, S. Mannsfeld, Z. Bao, N. Stingelin, “Organic semiconductor growth and morphology considerations for organic thin-film transistors,” *Advanced Materials*, vol. 22, p. 3857–3875, 2010.
- [48] P. Würfel, *Physik der Solarzellen*. Spektrum Akademischer Verlag, Heidelberg-Berlin, 2 ed., 2000.
- [49] A. Colsmann, *Ladungstransportschichten für effiziente organische Halbleiterbauelemente*. PhD thesis, Universität Karlsruhe (TH), 2008.
- [50] Solenne. B.V., <http://www.solennebv.com/>, “<http://www.solennebv.com/>.”
- [51] A. Salleo, R.J. Kline, D.M. DeLongchamp, M.L. Chabinyc, “Microstructural characterization and charge transport in thin films of conjugated polymers,” *Advanced Materials*, vol. 22, p. 3812–3838, 2010.
- [52] J. Gierschner, H.-G. Mack, H.-J. Egelhaaf, S. Schweizer, B. Doser, D. Oelkrug, “Optical spectra of oligothiophenes: vibronic states, torsional motions, and solvent shifts,” *Synthetic Metals*, vol. 138, p. 311–315, 2003.
- [53] W.C. Tsoi, S.J. Spencer, L. Yang, A.M. Ballantyne, P.G. Nicholson, A. Turnbull, A.G. Shard, C.E. Murphy, D. D.C. Bradley, J. Nelson, J.S. Kim, “Effect of crystallization on the electronic energy levels and thin film morphology of p3ht:pcbm blends,” *Macromolecules*, vol. 44, p. 2944–2952, 2011.
- [54] M.M. Boumann, E.E. Havinge, R.A.J. Janssen, E.W. Meijer, “Chiroptical properties of regioregular chiral polythiophenes,” *Molecular Crystals and Liquid Crystals*, vol. 256, pp. 439–448, 1994.
- [55] J. Peet, N.S. Cho, S.K. Lee, G.C. Bazan, “Transition from solution to the solid state in polymer solar cells cast from mixed solvents,” *Macromolecules*, vol. 41, pp. 8655–8659, 2008.

- [56] B. Schmidt-Hansberg, M.F.G. Klein, K. Peters, F. Buss, J. Pfeifer, S. Walheim, A. Colsmann, U. Lemmer, P. Scharfer, W. Schabel, "In situ monitoring the drying kinetics of knife coated polymer-fullerene films for organic solar cells," *Journal of Applied Physics*, vol. 106, p. 124501, 2009.
- [57] T. Wang, A.D.F. Dunbar, P.A. Staniec, A.J. Pearson, P.E. Hopkinson, J.E. Macdonald, S. Lilliu, C. Pizzey, N.J. Terrill, A.M. Donald, A.J. Ryan, R.A.L. Jones, D.G. Lidzey, "The development of nanoscale morphology in polymer:fullerene photovoltaic blends during solvent casting," *Soft Matter*, vol. 6, p. 4128–4134, 2010.
- [58] M. Sanyal, B. Schmidt-Hansberg, M.F.G. Klein, A. Colsmann, C. Munuera, A. Vorobiev, U. Lemmer, W. Schabel, H. Dosch, E. Barrena, "In situ x-ray study of drying-temperature influence on the structural evolution of bulk-heterojunction polymer–fullerene solar cells processed by doctor-blading," *Advanced Energy Materials*, vol. 1, p. 363–367, 2011.
- [59] M. Reyes-Reyes, K. Kim, D.L. Carroll, "High-efficiency photovoltaic devices based on annealed poly(3-hexylthiophene) and 1-(3-methoxycarbonyl)-propyl-1-phenyl-(6,6)c61 blends," *Applied Physics Letters*, vol. 87, p. 083506, 2005.
- [60] X. Yang, J. Loos, S.C. Veenstra, W.J.H. Verhees, M.M. Wienk, J.M. Kroon, M.A.J. Michels, R.A.J. Janssen, "Nanoscale morphology of high-performance polymer solar cells," *Nano Letters*, vol. 5, no. 4, pp. 579–583, 2005.
- [61] W. Ma, C. Yang, X. Gong, K. Lee, A.J. Heeger, "Thermally stable, efficient polymer solar cells with nanoscale control of the interpenetrating network morphology," *Advanced Functional Materials*, vol. 15, pp. 1617–1622, 2005.
- [62] V.D. Mihailetschi, H. Xie, B. Boer, L.J.A. Koster, P.W.M. Blom, "Charge transport and photocurrent generation in poly(3-hexylthiophene):methanofullerene bulk-heterojunction solar cells," *Advanced Functional Materials*, vol. 16, pp. 699–708, 2006.
- [63] E. Verploegen, R. Mondal, C.J. Bettinger, S. Sok, M.F. Toney, Z. Bao, "Effects of thermal annealing upon the morphology of polymer–fullerene blends," *Advanced Functional Materials*, vol. 20, p. 3519–3529, 2010.
- [64] Y. Zhao, Z. Xie, Y. Qu, Y. Geng, L. Wang, "Solvent-vapor treatment induced performance enhancement of poly(3-hexylthiophene):methanofullerene bulk-heterojunction photovoltaic cells," *Applied Physics Letters*, vol. 90, p. 043504, 2007.
- [65] G.D. Sharma, P. Suresh, S.S. Sharma, Y.K. Vijay, J.A. Mikroyannidis, "Effect of solvent and subsequent thermal annealing on the performance of phenylenevinylene copolymer:pcbm solar cells," *Applied Materials and Interfaces*, vol. 2, p. 504–510, 2010.
- [66] S.S. van Bavel, E. Sourty, G. de With, J. Loos, "Three-dimensional nanoscale organization of bulk heterojunction polymer solar cells," *Nano Letters*, vol. 9, no. 2, pp. 507–513, 2009.
- [67] H. Hoppe, N.S. Sariciftci, "Morphology of polymer/fullerene bulk heterojunction solar cells," *J. Mater. Chem.*, vol. 16, pp. 45–61, 2006.

8 References

- [68] X. Yang, J. Loos, "Toward high-performance polymer solar cells: The importance of morphology control," *Macromolecules*, vol. 40, no. 5, pp. 1353–1362, 2007.
- [69] S. Günes, H. Neugebauer, N.S. Sariciftci, "Conjugated polymer-based organic solar cells," *Chemical Reviews*, vol. 107, pp. 1324–1338, 2007.
- [70] J.E. Slota, X. Hea, W.T.S. Huck, "Controlling nanoscale morphology in polymer photovoltaic devices," *Nano Today*, vol. 5, p. 231–242, 2010.
- [71] D.M. DeLongchamp, R.J. Kline, D.A. Fischer, L.J. Richter, M.F. Toney, "Molecular characterization of organic electronic films," *Advanced Materials*, vol. 23, p. 319–337, 2011.
- [72] E.I. Altman, U.D. Schwarz, "Mechanisms, kinetics, and dynamics of oxidation and reactions on oxide surfaces investigated by scanning probe microscopy," *Advanced Materials*, vol. 22, p. 2854–2869, 2010.
- [73] R. Giridharagopal, D.S. Ginger, "Characterizing morphology in bulk heterojunction organic photovoltaic systems," *Journal of Physical Chemistry Letters*, vol. 1, p. 1160–1169, 2010.
- [74] P. H. Fuoss, S. Brennan, "Surface sensitive x-ray scattering," *Annu. Rev. Mater. Sci.*, vol. 20, pp. 365–390, 1990.
- [75] H. Sirringhaus, P. J. Brown, R. H. Friend, M. M. Nielsen, K. Bechgaard, B. M. W. Langeveld-Voss, A. J. H. Spiering, R. A. J. Janssen, E. W. Meijer, P. Herwig, D. M. de Leeuw, "Two-dimensional charge transport in self-organized, high-mobility conjugated polymers," *Nature*, vol. 401, pp. 685–688, 1999.
- [76] R.J. Kline, M.D. McGehee, M.F. Toney, "Highly oriented crystals at the buried interface in polythiophene thin-film transistors," *Nature Materials*, vol. 5, pp. 222–228, March 2006.
- [77] S. Lilliu, T. Agostinelli, E. Pires, M. Hampton, J. Nelson, J.E. Macdonald, "Dynamics of crystallization and disorder during annealing of p3ht/pcbm bulk heterojunctions," *Macromolecules*, vol. 44, p. 2725–2734, 2011.
- [78] T. Agostinelli, S. Lilliu, J.G. Labram, M. Campoy-Quiles, M. Hampton, E. Pires, J. Rawle, O. Bikondoa, D.D. C. Bradley, T.D. Anthopoulos, J. Nelson, J.E. Macdonald, "Real-time investigation of crystallization and phase-segregation dynamics in p3ht:pcbm solar cells during thermal annealing," *Advanced Functional Materials*, vol. 21, p. 1701–1708, 2011.
- [79] A. Amassian, V.A. Pozdin, R. Li, D.M. Smilgies, G.G. Malliaras, "Solvent vapor annealing of an insoluble molecular semiconductor," *Journal of Materials Chemistry*, vol. 20, p. 2623–2629, 2010.
- [80] M. Sanyal, B. Schmidt-Hansberg, M.F.G. Klein, C. Munuera, A. Vorobiev, A. Colsmann, P. Scharfer, U. Lemmer, W. Schabel, H. Dosch, E. Barrena, "Effect of photovoltaic polymer/fullerene blend composition ratio on microstructure evolution during film solidification investigated in real time by x-ray diffraction," *Macromolecules*, vol. 44, p. 3795–3800, 2011.

- [81] B. Schmidt-Hansberg, M. Sanyal, M. F. Klein, M. Pfaff, N. Schnabel, S. Jaiser, A. Vorobiev, E. Mueller, A. Colsmann, P. Scharfer, D. Gerthsen, U. Lemmer, E. Barrena, and W. Schabel, "Moving through the phase diagram: Morphology formation in solution cast polymer-fullerene-blend films for organic solar cells," *ACS Nano*, vol. 5, p. 8579–8590, 2011.
- [82] J.W. Kiel, M.E. Mackay, B.J. Kirby, B.B. Maranville, C.F. Majkrzak, "Phase-sensitive neutron reflectometry measurements applied in the study of photovoltaic films," *Journal of Chemical Physics*, vol. 133, p. 074902, 2010.
- [83] J.W. Kiel, A.P.R. Eberle, M.E. Mackay, "Nanoparticle agglomeration in polymer-based solar cells," *Physical Review Letters*, vol. 105, p. 168701, 2010.
- [84] M. Pfaff, E. Müller, M.F.G. Klein, A. Colsmann, U. Lemmer, V. Krzyzanek, R. Reichelt, D. Gerthsen, "Low-energy electron scattering in carbon-based materials analyzed by scanning transmission electron microscopy and its application to sample thickness determination," *Journal of Microscopy*, vol. 243, no. 1, pp. 31–39, 2011.
- [85] J.C. Hindson, Z. Saghi, J.C. Hernandez-Garrido, P.A. Midgley, N.C. Greenham, "Morphological study of nanoparticle-polymer solar cells using high-angle annular dark-field electron tomography," *Nano Letters*, vol. 11, p. 904–909, 2011.
- [86] X. Yang, J.K.J. van Duren, R.A.J. Janssen, M.A.J. Michels, J. Loos, "Morphology and thermal stability of the active layer in poly(p-phenylenevinylene)/methanofullerene plastic photovoltaic devices," *Macromolecules*, vol. 37, pp. 2151–2158, 2004.
- [87] M. Morana, H. Azimi, G. Dennler, H.J. Egelhaaf, M. Scharber, K. Forberich, J. Hauch, R. Gaudiana, D. Waller, Z. Zhu, K. Hingerl, S.S. van Bavel, J. Loos, C.J. Brabec, "Nanomorphology and charge generation in bulk heterojunctions based on low-bandgap dithiophene polymers with different bridging atoms," *Advanced Functional Materials*, vol. 20, p. 1180–1188, 2010.
- [88] J.S. Moon, C.J. Takacs, Y. Sun, A.J. Heeger, "Spontaneous formation of bulk heterojunction nanostructures: Multiple routes to equivalent morphologies," *Nano Letters*, vol. 11, p. 1036–1039, 2011.
- [89] N. Kiriy, E. Jähne, H.J. Adler, M. Schneider, A. Kiriy, G. Gorodyska, S. Minko, D. Jehnichen, P. Simon, A.A. Fokin, M. Stamm, "One-dimensional aggregation of regioregular polyalkylthiophenes," *Nano Letters*, vol. 3, pp. 707–712, 2003.
- [90] S.S. van Bavel, M. Bärenklau, G. de With, H. Hoppe, J. Loos, "P3ht/pcbm bulk heterojunction solar cells: Impact of blend composition and 3d morphology on device performance," *Advanced Functional Materials*, vol. 20, p. 1458–1463, 2010.
- [91] A.J. Parnell, A.D.F. Dunbar, A.J. Pearson, P.A. Staniec, A.J.C. Dennison, H. Hamamatsu, M.W.A. Skoda, D.G. Lidzey, R.A.L. Jones, "Depletion of pcbm at the cathode interface in p3ht/pcbm thin films as quantified via neutron reflectivity measurements," *Advanced Materials*, vol. 22, p. 2444–2447, 2010.
- [92] K.H. Lee, P.E. Schwenn, A.R.G. Smith, H. Cavaye, P.E. Shaw, M. James, K.B. Krueger, I.R. Gentle, P. Meredith, P.L. Burn, "Morphology of all-solution-processed "bilayer" organic solar cells," *Advanced Materials*, vol. 23, p. 766–770, 2010.

8 References

- [93] M. Campoy-Quiles, T. Ferenczi, T. Agostinelli, P.G. Etchegoin, Y. KIM, T.D. Anthopoulos, P.N. Stavrinou, D.D.C. Bradley, J. Nelson, “Morphology evolution via self-organization and lateral and vertical diffusion in polymer:fullerene solar cell blends,” *Nature Materials*, vol. 7, pp. 158–164, 2008.
- [94] D.S. Germack, C.K. Chan, R.J. Kline, D.A. Fischer, D.J. Gundlach, M.F. Toney, L.J. Richter, D.M. DeLongchamp, “Interfacial segregation in polymer/fullerene blend films for photovoltaic devices,” *Macromolecules*, vol. 43, no. 8, p. 3828–3836, 2010.
- [95] C. M. Björström, S. Nilsson, A. Bernasik, A. Budkowski, M. Andersson, K. O. Magnusson, E. Moons, “Vertical phase separation in spin-coated films of a low bandgap polyfluorene/pcbm blend—effects of specific substrate interaction,” *Applied Surface Science*, vol. 253, pp. 3906–3912, 2007.
- [96] F.C. Krebs, K. Norrman, “Using light-induced thermocleavage in a roll-to-roll process for polymer solar cells,” *Applied Materials and Interfaces*, vol. 2, p. 877–887, 2010.
- [97] B.Y. Yu, W.C. Lin, W.B. Wang, S. Iida, S.Z. Chen, C.Y. Liu, C.H. Kuo, S.H. Lee, W.L. Kao, G.J. Yen, Y.W. You, C.P. Liu, J.H. Jou, J.J. Shyue, “Effect of fabrication parameters on three-dimensional nanostructures of bulk heterojunctions imaged by high-resolution scanning tof-sims,” *ACS Nano*, vol. 4, no. 2, p. 833–840, 2010.
- [98] J.Y. Oh, W.S. Jang, T.I. Lee, J.M. Myoung, H.K. Baik, “Driving vertical phase separation in a bulk-heterojunction by inserting a poly(3-hexylthiophene) layer for highly efficient organic solar cells,” *Applied Physics Letters*, vol. 98, p. 023303, 2011.
- [99] Z. Xu, L.M. Chen, G. Yang, C.H. Huang, J. Hou, Y. Wu, G. Li, C.S. Hsu, Y. Yang, “Vertical phase separation in poly(3-hexylthiophene): Fullerene derivative blends and its advantage for inverted structure solar cells,” *Advanced Functional Materials*, vol. 19, p. 1227–1234, 2009.
- [100] Y. Yao, J. Hou, Z. Xu, G. Li, Y. Yang, “Effects of solvent mixtures on the nanoscale phase separation in polymer solar cells,” *Advanced Functional Materials*, vol. 18, p. 1783–1789, 2008.
- [101] J.S. Kim, P.K.H. Ho, C.E. Murphy, R.H. Friend, “Phase separation in polyfluorene-based conjugated polymer blends: Lateral and vertical analysis of blend spin-cast thin films,” *Macromolecules*, vol. 37, pp. 2861–2871, 2004.
- [102] D.S. Germack, C.K. Chan, B.H. Hamadani, L.J. Richter, D.A. Fischer, D.J. Gundlach, D.M. DeLongchamp, “Substrate-dependent interface composition and charge transport in films for organic photovoltaics,” *Applied Physics Letters*, vol. 94, p. 233303, 2009.
- [103] W. Chen, D.C. Qi, H. Huang, X. Gao, A.T.S. Wee, “Organic–organic heterojunction interfaces: Effect of molecular orientation,” *Advanced Functional Materials*, vol. 21, p. 410–424, 2011.
- [104] G. Binnig, C.F. Quate, “Atomic force microscope,” *Physical Review Letters*, vol. 56, pp. 930–934, 1986.

- [105] C.R. McNeill, B. Watts, L. Thomsen, W.J. Belcher, N.C. Greenham, P.C. Dastoor, "Nanoscale quantitative chemical mapping of conjugated polymer blends," *Nano Letters*, vol. 6, pp. 1202–1206, 2006.
- [106] K.B. Burke, W.J. Belcher, L. Thomsen, B. Watts, C.R. McNeill, H. Ade, P.C. Dastoor, "Role of solvent trapping effects in determining the structure and morphology of ternary blend organic devices," *Macromolecules*, vol. 42, pp. 3098–3103, 2009.
- [107] S. Swaraj, C. Wang, H. Yan, B. Watts, J. Lüning, C.R. McNeill, H. Ade, "Nanomorphology of bulk heterojunction photovoltaic thin films probed with resonant soft x-ray scattering," *Nano Letters*, vol. 10, p. 2863–2869, 2010.
- [108] B. Watts, T. Schuettfort, C.R. McNeill, "Mapping of domain orientation and molecular order in polycrystalline semiconducting polymer films with soft x-ray microscopy," *Advanced Functional Materials*, vol. 21, p. 1122–1131, 2011.
- [109] G. Li, V. Shrotriya, J. Huang, Y. Yao, T. Moriarty, K. Emery, Y. Yang, "High-efficiency solution processable polymer photovoltaic cells by self-organization of polymer blends," *Nature Materials*, vol. 4, pp. 864–868, 2005.
- [110] V.D. Mihailetschi, H. Xie, B. Boer, L.M. Popescu, J.C. Hummelen, P.W.M. Blom, "Origin of the enhanced performance in poly(3-hexylthiophene):[6,6]-phenyl c61-butyric acid methyl ester solar cells upon slow drying of the active layer," *Applied Physics Letters*, vol. 89, p. 012107, 2006.
- [111] W. Schabel, *Trocknung von Polymerfilmen - Messung von Konzentrationsprofilen mit der Inversen-Mikro-Raman-Spektroskopie*. PhD thesis, Universität Karlsruhe (TH), 2004.
- [112] P. Scharfer, *Zum Stofftransport in Brennstoffzellenmembranen - Untersuchungen mit Hilfe der konfokalen Mikro-Raman-Spektroskopie*. PhD thesis, Karlsruhe Institute of Technology, 2009.
- [113] C.S. Lu, O. Lewis, "Investigation of film-thickness determination by oscillating quartz resonators with large mass load," *Journal of Applied Physics*, vol. 43, pp. 4385–4390, 1972.
- [114] D.A. Buttry, M.D. Ward, "Measurement of interfacial processes at electrode surfaces with the electrochemical quartz crystal microbalance," *Chem. Rev.*, vol. 92, pp. 1355–1379, 1992.
- [115] R.A. Cairncross, J.G. Becker, S. Ramaswamy, R. O'Connor, "Moisture sorption, transport, and hydrolytic degradation in polylactide," *Applied Biochemistry and Biotechnology*, vol. 129–132, pp. 774–785, 2006.
- [116] S. J. Martin, "Closing remarks," *Faraday Discuss.*, vol. 107, pp. 463–476, 1997.
- [117] W. Schabel, P. Scharfer, M. Müller, I. Ludwig, M. Kind, "Messung und simulation von konzentrationsprofilen bei der trocknung binärer polymerlösungen," *Chemie Ingenieur Technik*, vol. 75, pp. 1336–1344, 2003.

8 References

- [118] W. Schabel, "Inverse mikro-raman-spektroskopie-eine neue messmethode zur untersuchung lokaler stofftransportvorgänge in dünnen filmen, folien und membranen," *Chemie Ingenieur Technik*, vol. 77, pp. 1915–1926, 2005.
- [119] I. Ludwig, W. Schabel, M. Kind, J.-C. Castaing, P. Ferlin, "Drying and film formation of industrial waterborne latices," *AIChE Journal*, vol. 53, pp. 549–560, 2007.
- [120] P. Scharfer, W. Schabel, M. Kind, "Mass transport measurements in membranes by means of in situ raman spectroscopy—first results of methanol and water profiles in fuel cell membranes," *Journal of Membrane Science*, vol. 303, pp. 37–42, 2007.
- [121] S. Jeck, P. Scharfer, M. Kind, "Water sorption in physically crosslinked poly(vinyl alcohol) membranes: An experimental investigation of schroeder's paradox," *Journal of Membrane Science*, vol. 337, pp. 291–296, 2009.
- [122] H. Fujiwara, *Spectroscopic Ellipsometry - Principles and Applications*. John Wiley & Sons, Ltd, 2007.
- [123] M. Campoy-Quiles, M. Sims, P.G. Etchegoin, D.D.C. Bradley, "Thickness-dependent thermal transition temperatures in thin conjugated polymer films," *Macromolecules*, vol. 39, pp. 7673–7680, 2006.
- [124] A.M.C. Ng, K.Y. Cheung, M.K. Fung, A.B. Djuriscic, W.K. Chan, "Spectroscopic ellipsometry characterization of polymer–fullerene blend films," *Thin Solid Films*, vol. 517, pp. 1047–1052, 2008.
- [125] A. Ng, C. Li, M. Fung, A. Djuriscic, J. Zapien, W. Chan, K. Cheung, and W.-Y. Wong, "Accurate determination of the index of refraction of polymer blend films by spectroscopic ellipsometry," *Journal of Physical Chemistry C*, vol. 114, no. 35, pp. 15094–15101, 2010.
- [126] P.C. Jukes, S.Y. Heriot, J.S. Sharp, R.A. L. Jones, "Time-resolved light scattering studies of phase separation in thin film semiconducting polymer blends during spin-coating," *Macromolecules*, vol. 38, pp. 2030–2032, 2005.
- [127] S.Y. Heriot, R.A.L. Jones, "An interfacial instability in a transient wetting layer leads to lateral phase separation in thin spin-cast polymer-blend films," *Nature Materials*, vol. 4, pp. 782–786, 2005.
- [128] I. Mamaliga, W. Schabel, and M. Kind, "Measurements of sorption isotherms and diffusion coefficients by means of a magnetic suspension balance," *Chemical Engineering and Processing*, vol. 43, no. 6, pp. 753 – 763, 2004.
- [129] W. Schabel, I. Mamaliga, M. Kind, "Messungen von sorptionsisothermen und diffusionskoeffizienten in polymerlösungen," *Chem. Ing. Tech.*, vol. 75, pp. 36–41, 2003.
- [130] R.A. Cairncross, C.J. Durning, "A model for drying of viscoelastic polymer coatings," *AIChE*, vol. 42, pp. 2415–2425, 1996.
- [131] J.S. Vrentas, J.L. Duda, "Diffusion of small molecules in amorphous polymers," *Macromolecules*, vol. 9, pp. 785–790, 1976.
- [132] J.S. Vrentas, C.M. Vrentas, "Drying of solvent-coated polymer films," *Journal of Polymer Science: Part B: Polymer Physics*, vol. 32, pp. 187–194, 1994.

- [133] S. Alsoy, J.L. Duda, "Modeling of multicomponent drying of polymer films," *AIChE*, vol. 45, pp. 896–905, 1999.
- [134] E. B. Perez and M. S. Carvalho, "Drying of thin films of polymer solutions coated over impermeable substrates," *Heat Transfer Engineering*, vol. 28, no. 6, pp. 559–566, 2007.
- [135] B. Schmidt-Hansberg, M. Baunach, J. Krenn, S. Walheim, U. Lemmer, P. Scharfer, W. Schabel, "Spatially resolved drying kinetics of multi-component solution cast films for organic electronics," *Chemical Engineering and Processing*, vol. 50, pp. 509–515, 2011.
- [136] J. Pfeifer, "Oberflächenwelligkeit und zeitaufgelöste Schichtdickenmessung bei dünnen Polymerfilmen," Master's thesis, Institute of Nanotechnology, Karlsruhe Institute of Technology, 2007.
- [137] E. Hecht, *Optik*. Oldenbourg, 5. ed., 2009. ISBN: 978-3-486-58861-3.
- [138] W. Heller, "Remarks on refractive index mixture rules," *Journal of Physical Chemistry*, vol. 69, pp. 1123–1129, 1965.
- [139] M. Baunach, "Lateral aufgelöste Messung der Schichtdickenabnahme von flüssig prozessierten Polymer-Fulleren-Filmen mit Lösungsmittel-gemischen für organische Elektronik," Master's thesis, Institut für Thermische Verfahrenstechnik, Karlsruhe Institute of Technology, 2010.
- [140] T. Wang, A.J. Pearson, D.G. Lidzey, R.A.L. Jones, "Evolution of structure, optoelectronic properties, and device performance of polythiophene:fullerene solar cells during thermal annealing," *Advanced Functional Materials*, vol. 21, p. 1383–1390, 2011.
- [141] P.E. Hopkinson, P.A. Staniec, A.J. Pearson, A.D.F. Dunbar, T. Wang, A.J. Ryan, R.A. L. Jones, D.G. Lidzey, A.M. Donald, "A phase diagram of the p3ht:pcbm organic photovoltaic system: Implications for device processing and performance," *Macromolecules*, vol. 44, p. 2908–2917, 2011.
- [142] S. Bertho, G. Janssen, T.J. Cleij, B. Conings, W. Moons, A. Gadisa, J. D'Haen, E. Goovaerts, L. Lutsen, J. Manca, D. Vanderzande, "Effect of temperature on the morphological and photovoltaic stability of bulk heterojunction polymer:fullerene solar cells," *Solar Energy Materials & Solar Cells*, vol. 92, pp. 753–760, 2008.
- [143] Y. Kim, S.A. Choulis, J. Nelson, D.D.C. Bradley, S. Cook, J.R. Durrant, "Device annealing effect in organic solar cells with blends of regioregular poly(3-hexylthiophene) and soluble fullerene," *Applied Physics Letters*, vol. 86, p. 063502, 2005.
- [144] J.Y. Kim, C.D. Frisbie, "Correlation of phase behavior and charge transport in conjugated polymer/fullerene blends," *J. Phys. Chem. C*, vol. 112, pp. 17726–17736, 2008.
- [145] S. Hugger, R. Thomann, T. Heinzl, T. Thurn-Albrecht, "Semicrystalline morphology in thin films of poly(3-hexylthiophene)," *Colloid. Polym. Sci.*, vol. 282, pp. 932–938, 2004.
- [146] Y. Zhao, G. Yuan, P. Roche, M. Leclerc, "A calorimetric study of the phase transitions in poly(3-hexylthiophene)," *Polymer*, vol. 36, pp. 2211–2214, 1995.

8 References

- [147] J. Zhao, A. Swinnen, G. Van Assche, J. Manca, D. Vanderzande, B. Van Mele, “Phase diagram of p3ht/pcbm blends and its implication for the stability of morphology,” *J. Phys. Chem. B*, vol. 113, pp. 1587–1591, 2009.
- [148] R.B. Bird, W.E. Stuart, E.N. Lightfoot, *Transport Phenomena*. John Wiley and Sons Inc., New York, 1960.
- [149] E.-U. Schlünder, *Einführung in die Stoffübertragung*. Georg Thieme Verlag, Stuttgart, 1984.
- [150] E.N. Fuller, P.D. Schettler, J.C. Giddings, “A new method for prediction of binary gas - phase diffusion coefficients,” *Industrial and Engineering Chemistry*, vol. 58, pp. 19–27, 1966.
- [151] M. Kraume, *Transportvorgänge in der Verfahrenstechnik - Grundlagen und apparative Umsetzungen*. Springer Verlag, Berlin, Heidelberg, 2004.
- [152] H. Brauer, D. Sucker, “Stoff- und warmeubergang an umstromten platten, zylindern und kugeln,” *Chemie Ingenieur Technik*, vol. 48, pp. 737–741, 1976.
- [153] H. Brauer, D. Sucker, “Umströmung von platten, zylindern und kugeln,” *Chemie Ingenieur Technik*, vol. 48, pp. 665–671, 1976.
- [154] H. Brauer and D. Mewes, *Stoffaustausch einschließlich chemischer Reaktionen*. Aarau; Frankfurt am Main: Sauerländer, 1971. ISBN 3-7941-0008-5.
- [155] T.A. Ameel, “Average effects of forced convection over a flat plate with an unheated starting length,” *Int. Comm. Heat Mass Transfer*, vol. 24, pp. 1113–1120, 1997.
- [156] F. P. Incropera, D. P. DeWitt, T. L. Bergmann, A. S. Lavine, *Fundamentals of Heat and Mass Transfer*. John Wiley & Sons, Ltd, 2007.
- [157] P. Scharfer, Y. Zhou, J. Krenn, M. Kind, and W. Schabel, “Influence of local gas phase mass transport coefficients on the drying rate of polymer films – a fundamental study,” in *14th International Coating Science and Technology Symposium*, 2008.
- [158] W. Schabel, P. Scharfer, M. Kind, I. Mamaliga, “Sorption and diffusion measurements in ternary polymer–solvent–solvent systems by means of a magnetic suspension balance—experimental methods and correlations with a modified flory–huggins and free-volume theory,” *Chemical Engineering Science*, vol. 62, p. 2254 – 2266, 2007.
- [159] K. Stephan, F. Mayinger, *Thermodynamik: Mehrstoffsysteme und chemische Reaktionen*. Springer-Verlag: Berlin, 1999.
- [160] V. G. V. und Chemieingenieurwesen, *VDI-Wärmeatlas*, vol. 9. Springer-Verlag: Berlin, 2002.
- [161] J. Krenn, S. Baesch, B. Schmidt-Hansberg, M. Baunach, P. Scharfer, W. Schabel, “Numerical investigation of the local mass transfer on flat plates in laminar flow,” *Chemical Engineering and Processing*, vol. 50, pp. 503–508, 2011.
- [162] A.J. Moulé, K. Meerholz, “Controlling morphology in polymer–fullerene mixtures,” *Advanced Materials*, vol. 20, pp. 240–245, 2008.

- [163] C.S. Kim, L.L. Tinker, B.F. DiSalle, E.D. Gomez, S. Lee, S. Bernhard, Y.L. Loo, "Altering the thermodynamics of phase separation in inverted bulk-heterojunction organic solar cells," *Advanced Materials*, vol. 21, p. 3110–3115, 2009.
- [164] C. L. Yaws, *Chemical Properties Handbook*. McGraw-Hill, 1999.
- [165] C. Müller, T.A.M. Ferenczi, M. Campoy-Quiles, J.M. Frost, D.D.C. Bradley, P. Smith, N. Stingelin-Stutzmann, J. Nelson, "Binary organic photovoltaic blends: A simple rationale for optimum compositions," *Advanced Materials*, vol. 20, pp. 3510–3515, 2008.
- [166] L. Li, H. Tang, H. Wu, G. Lu, X. Yang, "Effects of fullerene solubility on the crystallization of poly(3-hexylthiophene) and performance of photovoltaic devices," *Organic Electronics*, vol. 10, pp. 1334–1344, 2009.
- [167] B. Walker, A. Tamayo, D.T. Duong, X.D. Dang, C. Kim, J. Granstrom, T.Q. Nguyen, "A systematic approach to solvent selection based on cohesive energy densities in a molecular bulk heterojunction system," *Advanced Energy Materials*, vol. 1, p. 221–229, 2011.
- [168] J. Hildebrand, R. L. Scott, *The Solubility of Nonelectrolytes*. Reinhold, New York, 3rd ed., 1950.
- [169] C. M. Hansen, *Hansen solubility parameters : a user's handbook*. CRC Press, Boca Raton, FL, 2nd ed., 2007.
- [170] C.M. Hansen, A.L. Smith, "Using hansen solubility parameters to correlate solubility of c60 fullerene in organic solvents and in polymers," *Carbon*, vol. 42, p. 1591–1597, 2004.
- [171] S. Abbott, C.M. Hansen, "Hansen Solubility Parameters in Practice, (software) www.hansen-solubility.com."
- [172] C. Qian, S.J. Mumby, B.E. Eichinger, "Phase diagrams of binary polymer solutions and blends," *Macromolecules*, vol. 24, pp. 1655–1661, 1991.
- [173] J. J. Michels, "Surface-directed spinodal decomposition of solvent-quenched organic transistor blends," *Chem.Phys. Chem.*, vol. 12, p. 342–348, 2011.
- [174] M. Huggins, "Solutions of long chain compounds," *Journal of Chemical Physics*, vol. 9, p. 440, 1941.
- [175] P.J. Flory, "Thermodynamics of high polymer solutions," *Journal of Chemical Physics*, vol. 9, pp. 660–661, 1941.
- [176] P.J. Flory, "Thermodynamics of high polymer solutions," *Journal of Chemical Physics*, vol. 10, pp. 51–61, 1942.
- [177] J.W. Cahn, D.J.E. Hilliard, "Free energy of a nonuniform system. i. interfacial free energy," *The Journal of Chemical Physics*, vol. 28, pp. 258–267, 1958.
- [178] J.W. Cahn, "On spinodal decomposition," *Acta Metallurgica*, vol. 9, pp. 795–801, 1961.
- [179] B. Tieke, *Makromolekulare Chemie - Eine Einführung*. Wiley-VCH, Weinheim, 2005.

8 References

- [180] M.D. Lechner, K. Gehrke, E.H. Nordmeier, *Makromolekulare Chemie - Ein Lehrbuch für Chemiker, Physiker, Materialwissenschaftler und Verfahrenstechniker*. Birkhäuser, Basel-Boston-Berlin, 2003.
- [181] K. Kamide, S. Matsuda, “A method for determining the Flory theta temperature and entropy parameter of single- or multicomponent-polymer–single solvent systems from the critical solution point data,” *Polymer Journal*, vol. 16, pp. 825–837, 1984.
- [182] K. Kamide, S. Matsuda, M. Saito, “Evaluation of concentration dependence of χ -parameter, Flory temperature and entropy parameter for polymer–solvent system from their critical solution temperature and concentration data,” *Polymer Journal*, vol. 17, pp. 1013–1027, 1985.
- [183] R. Koningsveld, L.A. Kleintjens, A.R. Shultz, “Liquid–liquid phase separation in multicomponent polymer solutions. ix. concentration-dependent pair interaction parameter from critical miscibility data on the system polystyrene–cyclohexane,” *Journal of Polymer Science Part A-2: Polymer Physics*, vol. 8, pp. 1261–1278, 1970.
- [184] K.S. Siow, G. Delmas, D. Patterson, “Cloud-point curves in polymer solutions with adjacent upper and lower critical solution temperatures,” *Macromolecules*, vol. 5, pp. 29–34, 1972.
- [185] S. Matsuda, “Phase equilibria of quasi-ternary systems consisting of multicomponent polymers in a binary solvent mixture v. effects of concentration dependence of thermodynamic interaction parameters,” *Polymer Journal*, vol. 12, pp. 993–1016, 1986.
- [186] J. S. Gutmann, *Strukturbildung in dünnen Filmen aus Mischungen statistischer Copolymerer*. PhD thesis, Johannes Gutenberg-Universität Mainz, 2000.
- [187] M. Wünsch, *Ternäre polymerhaltige Lösungen – Phasenverhalten und Grenzflächenspannung*. PhD thesis, Johannes-Gutenberg-Universität Mainz, 2001.
- [188] K. Fuchs, *Entwicklung und Charakterisierung thermotroper Polymerblends*. PhD thesis, Albert-Ludwigs-Universität Freiburg i.Br., 2001.
- [189] M. Koppe, C.J. Brabec, S. Heiml, A. Schausberger, W. Duffy, M. Heeney, I. McCulloch, “Influence of molecular weight distribution on the gelation of p3ht and its impact on the photovoltaic performance,” *Macromolecules*, vol. 42, no. 13, p. 4661–4666, 2009.
- [190] S. Jaiser *Beschreibung von Phasengleichgewichten halbleitender organischer Materialien*, Studienarbeit, Institut für Thermische Verfahrenstechnik, Karlsruhe Institute of Technology, 2009.
- [191] N. Schnabel, “Untersuchung der Phasengleichgewichte halbleitender organischer Materialien in der Flüssigphase,” Master’s thesis, Institut für Thermische Verfahrenstechnik, Universität Karlsruhe (TH), 2008.
- [192] B. Schmidt-Hansberg, H. Do, A. Colsmann, U. Lemmer, W. Schabel, “Drying of thin film polymer solar cells,” *European Physical Journal - Special Topics*, vol. 166, pp. 49–54, 2009.

- [193] S. Malik, T. Jana, A.K. Nandi, "Thermoreversible gelation of regioregular poly(3-hexylthiophene) in xylene," *Macromolecules*, vol. 34, pp. 275–282, 2001.
- [194] M. Avrami, "Kinetics of phase change. i," *Journal of Chemical Physics*, vol. 7, pp. 1103–1112, 1939.
- [195] M. Avrami, "Kinetics of phase change. ii - transformation-time relations for random distribution of nuclei," *Journal of Chemical Physics*, vol. 8, pp. 212–224, 1940.
- [196] M. Avrami, "Granulation, phase change, and microstructure kinetics of phase change. iii," *Journal of Chemical Physics*, vol. 9, pp. 177–184, 1941.
- [197] C.Y. Chen, S.H. Chan, J.Y. Li, K.H. Wu, H.L. Chen, J.H. Chen, W.Y. Huang, S.A. Chen, "Formation and thermally-induced disruption of nanowhiskers in poly(3-hexylthiophene)/xylene gel studied by small-angle x-ray scattering," *Macromolecules*, vol. 43, p. 7305–7311, 2010.
- [198] H. Xin, F.S. Kim, S.A. Jenekhe, "Highly efficient solar cells based on poly(3-butylthiophene) nanowires," *Journal of the American Chemical Society*, vol. 130, p. 5424–5425, 2008.
- [199] H. Xin, G. Ren, F.S. Kim, S.A. Jenekhe, "Bulk heterojunction solar cells from poly(3-butylthiophene)/ fullerene blends: In situ self-assembly of nanowires, morphology, charge transport, and photovoltaic properties," *Chemistry of Materials*, vol. 20, p. 6199–6207, 2008.
- [200] J. Liu, M. Arif, J. Zou, S.I. Khondaker, L. Zhai, "Controlling poly(3-hexylthiophene) crystal dimension: Nanowhiskers and nanoribbons," *Macromolecules*, vol. 42, pp. 9390–9393, 2009.
- [201] S. Berson, R. DeBettignies, S. Bailly, S. Guillerez, "Poly(3-hexylthiophene) fibers for photovoltaic applications," *Advanced Functional Materials*, vol. 17, p. 1377–1384, 2007.
- [202] S. Samitsu, T. Shimomura, S. Heike, T. Hashizume, K. Ito, "Effective production of poly(3-alkylthiophene) nanofibers by means of whisker method using anisole solvent: Structural, optical, and electrical properties," *Macromolecules*, vol. 41, pp. 8000–8010, 2008.
- [203] W.D. Oosterbaan, J.C. Bolsee, A. Gadisa, V. Vrindts, S. Bertho, J. DHaen, T.J. Cleij, L. Lutsen, C.R. McNeill, L. Thomsen, J.V. Manca, D. Vanderzande, "Alkyl-chain-length-independent hole mobility via morphological control with poly(3-alkylthiophene) nanofibers," *Advanced Functional Materials*, vol. 20, pp. 792–802, 2010.
- [204] J.S. Kim, J.H. Lee, J.H. Park, C. Shim, M. Sim, K. Cho, "High-efficiency organic solar cells based on preformed poly(3-hexylthiophene) nanowires," *Advanced Functional Materials*, vol. 21, p. 480–486, 2010.
- [205] J.H. Kim, J.H. Park, J.H. Lee, J.S. Kim, M. Sim, C. Shima, K. Cho, "Bulk heterojunction solar cells based on preformed polythiophene nanowires via solubility-induced crystallization," *Journal of Materials Chemistry*, vol. 20, p. 7398–7405, 2010.

8 References

- [206] B.G. Kim, M.S. Kim, J. Kim, “Ultrasonic-assisted nanodimensional self-assembly of poly-3-hexylthiophene for organic photovoltaic cells,” *ACS Nano*, vol. 4, p. 2160–2166, 2010.
- [207] J. Peet, J.Y. Kim, N.E. Coates, W.L. Ma, D. Moses, A. J. Heeger, G.C. Bazan, “Efficiency enhancement in low-bandgap polymer solar cells by processing with alkane dithiols,” *Nature Materials*, vol. 6, pp. 497–500, 2007.
- [208] H.Y. Chen, H. Yang, G. Yang, S. Sista, R. Zadoyan, G. Li, Y. Yang, “Fast-grown interpenetrating network in poly(3-hexylthiophene): Methanofullerenes solar cells processed with additive,” *J. Phys. Chem. C*, vol. 113, p. 7946–7953, 2009.
- [209] S.H. Chan, Y.S. Hsiao, L.I. Hung, G.W. Hwang, H.L. Chen, C. Ting, C.P. Chen, “Morphology evolution of spin-coated films of poly(thiophene-phenylene-thiophene) and [6,6]-phenyl-c71-butyric acid methyl ester by solvent effect,” *Macromolecules*, vol. 43, p. 3399–3405, 2010.
- [210] D.J.D. Moet, M. Lenes, M. Morana, H. Azimi, C.J. Brabec, P.W.M. Blom, “Enhanced dissociation of charge-transfer states in narrow band gap polymer:fullerene solar cells processed with 1,8-octanedithiol,” *Applied Physics Letters*, vol. 96, p. 213506, 2010.
- [211] J. Peet, M.L. Senatore, A.J. Heeger, G.C. Bazan, “The role of processing in the fabrication and optimization of plastic solar cells,” *Advanced Materials*, vol. 21, p. 1521–1527, 2009.
- [212] M. Tolin, *X-Ray Scattering from Soft-Matter Thin Films: Materials Science and Basic Research*. Springer-Verlag: Berlin, 1999.
- [213] R.-J. Roe, *Methods of X-Ray and Neutron Scattering in Polymer Science*. Oxford University Press: New York, 2000.
- [214] M. L. Chabiny, “X-ray scattering from films of semiconducting polymers,” *Polymer Reviews*, vol. 48, p. 463–492, 2008.
- [215] M. Sanyal, *In-situ study of Real time Structural Evolution during Polymer/Fullerene Bulk Heterojunction Thin Film Formation*. PhD thesis, Max Planck Institut für Metallforschung, Universität Stuttgart, 2011.
- [216] D.W. Breiby, O. Bunk, J.W. Andreasen, H.T. Lemked, M.M. Nielsen, “Simulating x-ray diffraction of textured films,” *Journal of Applied Crystallography*, vol. 41, p. 262–271, 2008.
- [217] J. Mardalen, E.J. Samuelsen, O.R. Gautun, P.H. Carlsen, “X-ray scattering from oriented poly(3-alkylthiophenes),” *Synthetic Metals*, vol. 48, pp. 363–380, 1992.
- [218] M.T. Rispens, A. Meetsma, R. Rittberger, C.J. Brabec, N.S. Sariciftci, “Influence of the solvent on the crystal structure of pcbm and the efficiency of mdmo-ppv:pcbm plastic solar cells,” *Chem. Commun.*, vol. 7, pp. 2116–2118, 2003.
- [219] Y. Kim, S. Cook, S.M. Tuladhar, S.A. Choulis, J. Nelson, J.R. Durrant, D.D.C. Bradley, M. Giles, I. McCulloch, C.-S. Ha, M. Ree, “A strong regioregularity effect in self-

organizing conjugated polymer films and high-efficiency polythiophene:fullerene solar cells,” *Nature Materials*, vol. 5, pp. 197–203, 2006.

[220] M. Brinkmann, C. Contal, N. Kayunkid, T. Djuric, R. Resel, “Highly oriented and nanotextured films of regioregular poly(3-hexylthiophene) grown by epitaxy on the nanostructured surface of an aromatic substrate,” *Macromolecules*, vol. 43, p. 7604–7610, 2010.

[221] B. Meredig, A. Salleo, R. Gee, “Ordering of poly(3-hexylthiophene) nanocrystallites on the basis of substrate surface energy,” *ACS Nano*, vol. 3, p. 2881–2886, 2009.

[222] H. Li, S. Yan, “Surface-induced polymer crystallization and the resultant structures and morphologies,” *Macromolecules*, vol. 44, p. 417–428, 2011.

[223] X. Yang, J.K.J. van Duren, M.T. Rispens, J.C. Hummelen, R.J.A. Janssen, M.A.J. Michels, J. Loos, “Crystalline organization of a methanofullerene as used for plastic solar-cell applications,” *Advanced Materials*, vol. 16, pp. 802–806, 2004.

[224] S. Walheim, M. Ramstein, U. Steiner, “Morphologies in ternary polymer blends after spin-coating,” *Langmuir*, vol. 15, pp. 4828–4836, 1999.

[225] M. Koppe, M. Scharber, C. Brabec, W. Duffy, M. Heeney, I. McCulloch, “Polyterthiophenes as donors for polymer solar cells,” *Advanced Functional Materials*, vol. 17, p. 1371–1376, 2007.

[226] D.W. van Krevelen, K. Te Nijenhuis, *Properties of Polymers: Their Correlation with Chemical Structure; Their Numerical Estimation and Prediction from Additive Group Contributions*. Elsevier Science, 4. ed., 2009.

[227] F. Price, “Some comments on the "avrami" equation,” *Journal of Applied Physics*, vol. 36, p. 3014, 1965.

[228] D. Grenier, RE. Prud’ Homme, “Avrami analysis: Three experimental limiting factors,” *Journal of Polymer Science: Polymer Physics Edition*, vol. 18, p. 1655–1657, 1980.

[229] J. Tomka, “Note on the use of the avrami equation for the interpretation of the primary crystallization of polymers,” *European Polymer Journal*, vol. 4, pp. 237–240, 1968.

[230] I. Hillier, “Modified avrami equation for the bulk crystallization kinetics of spherulitic polymers,” *Journal of Polymer Science Part A*, vol. 3, pp. 3067–3078, 1965.

[231] L. Zeng, C.W. Tang, S.H. Chen, “Effects of active layer thickness and thermal annealing on polythiophene: Fullerene bulk heterojunction photovoltaic devices,” *Applied Physics Letters*, vol. 97, p. 053305, 2010.

[232] E.J.W. Crossland, K. Rahimi, G. Reiter, U. Steiner, S. Ludwigs, “Systematic control of nucleation density in poly (3-hexylthiophene) thin films,” *Advanced Functional Materials*, vol. 21, pp. 518–524, 2011.

8 References

- [233] H.K. Lee, J.H. Jeon, D.H. Wang, O.O. Park, J.K. Kim, S.H. Im, J.H. Park, “Enhanced charge collection via nanoporous morphology in polymer solar cells,” *Applied Physics Letters*, vol. 96, p. 103304, 2010.
- [234] U. Zhokhavets, T. Erb, G. Gobsch, M. Al-Ibrahim, O. Ambacher, “Relation between absorption and crystallinity of poly(3-hexylthiophene)/fullerene films for plastic solar cells,” *Chemical Physics Letters*, vol. 418, pp. 347–350, 2006.
- [235] W. Tress, A. Petrich, M. Hummert, M. Hein, K. Leo, M. Riede, “Imbalanced mobilities causing s-shaped iv curves in planar heterojunction organic solar cells,” *Applied Physics Letters*, vol. 98, p. 063301, 2011.
- [236] W. Tress, K. Leo, M. Riede, “Influence of hole-transport layers and donor materials on open-circuit voltage and shape of i-v curves of organic solar cells,” *Advanced Functional Materials*, vol. 21, no. 11, pp. 2140–2149, 2011.
- [237] L. Chang, H.W.A. Lademann, J.B. Bonekamp, K. Meerholz, A.J. Moulé, “Effect of trace solvent on the morphology of p3ht:pcbm bulk heterojunction solar cells,” *Advanced Functional Materials*, vol. 21, p. 1779–1787, 2011.
- [238] M. Kowalski *Einfluss von Additiven auf die Nanomorphologie von Polymer-Fulleren-Schichten für organische Solarzellen*, Studienarbeit, Institut für Thermische Verfahrenstechnik, Karlsruhe Institute of Technology, 2010.
- [239] B. Schmidt-Hansberg, M. Sanyal, N. Grossiord, Y. Galagan, M. Baunach, M. F. Klein, A. Colmann, P. Scharfer, U. Lemmer, H. Dosch, J. Michels, E. Barrena, and W. Schabel, “Investigation of non-halogenated solvent mixtures for high throughput fabrication of polymer-fullerene solar cells,” *Solar Energy Materials and Solar Cells*, vol. 96, pp. 195–201, 2012.
- [240] M. Ruderer, S. Guo, R. Meier, H.Y. Chiang, V. Körstgens, J. Wiedersich, J. Perlich, S.V. Roth, P. Müller-Buschbaum, “Solvent-induced morphology in polymer-based systems for organic photovoltaics,” *Advanced Functional Materials*, vol. 21, p. 3382–3391, 2011.
- [241] M.M. Wienk, J.M. Kroon, W.J.H. Verhees, J. Knol, J.C. Hummelen, P.A. van Hal, R.A.J. Janssen, “Efficient methano[70]fullerene/mdmo-ppv bulk heterojunction photovoltaic cells,” *Angewandte Chemie International Edition*, vol. 42, p. 3371 – 3375, 2003.
- [242] D. Mühlbacher, M. Scharber, M. Morana, Z. Zhu, D. Waller, R. Gaudiana, C. Brabec, “High photovoltaic performance of a low-bandgap polymer,” *Advanced Materials*, vol. 18, p. 2884–2889, 2006.
- [243] H.Y. Chen, J. Hou, A.E. Hayden, H. Yang, K.N. Houk, Y. Yang, “Silicon atom substitution enhances interchain packing in a thiophene-based polymer system,” *Advanced Materials*, vol. 22, no. 3, pp. 371–375, 2010.
- [244] M.C. Scharber, M. Koppe, J. Gao, F. Cordella, M.A. Loi, P. Denk, M. Morana, H.J. Egelhaaf, K. Forberich, G. Dennler, R. Gaudiana, D. Waller, Z. Zhu, X. Shi, C.J. Brabec, “Influence of the bridging atom on the performance of a low-bandgap bulk heterojunction solar cell,” *Advanced Materials*, vol. 22, no. 3, pp. 367–370, 2010.

- [245] A. Maurano, R. Hamilton, C.G. Shuttle, A.M. Ballantyne, J. Nelson, B. O'Regan, W. Zhang, I. McCulloch, H. Azimi, M. Morana, C.J. Brabec, J.R. Durrant, "Recombination dynamics as a key determinant of open circuit voltage in organic bulk heterojunction solar cells: A comparison of four different donor polymers," *Advanced Materials*, vol. 22, p. 4987–4992, 2010.
- [246] J. Hou, H.Y. Chen, S. Zhang, G. Li, Y. Yang, "Synthesis, characterization, and photovoltaic properties of a low band gap polymer based on silole-containing polythiophenes and 2,1,3-benzothiadiazole," *Journal of the American Chemical Society*, vol. 130, p. 16144–16145, 2008.
- [247] A. Colsmann, A. Puetz, A. Bauer, J. Hanisch, E. Ahlswede, U. Lemmer, "Efficient semi-transparent organic solar cells with good transparency color perception and rendering properties," *Advanced Energy Materials*, vol. 1, p. 599–603, 2011.
- [248] T. Ameri, G. Dennler, C. Waldauf, H. Azimi, A. Seemann, K. Forberich, J. Hauch, M. Scharber, K. Hingerl, C.J. Brabec, "Fabrication, optical modeling, and color characterization of semitransparent bulk-heterojunction organic solar cells in an inverted structure," *Advanced Functional Materials*, vol. 20, p. 1592–1598, 2010.
- [249] Konarka Technologies Inc., <http://www.konarka.com/>, June 2011.
- [250] J.T. Rogers, K. Schmidt, M.F. Toney, E.J. Kramer, G.C. Bazan, "Structural order in bulk heterojunction films prepared with solvent additives," *Advanced Materials*, vol. 20, p. 2284–2288, 2011.
- [251] N.C. Cates, R. Gysel, Z. Beiley, C.E. Miller, M.F. Toney, M. Heeney, I. McCulloch, M.D. McGehee, "Tuning the properties of polymer bulk heterojunction solar cells by adjusting fullerene size to control intercalation," *Nano Letters*, vol. 9, no. 12, pp. 4153–4157, 2009.
- [252] T. Basile *Prozess-Struktur-Wechselbeziehung von amorphen und semikristallinen Polymer-Fulleren-Schichten für organische Solarzellen*, Studienarbeit, Institut für Thermische Verfahrenstechnik, Karlsruhe Institute of Technology, 2011.
- [253] H. Lu, B. Akgun, and T. P. Russell, "Morphological characterization of a low-bandgap crystalline polymer:pcbm bulk heterojunction solar cells," *Advanced Energy Materials*, vol. 1, no. 5, pp. 870–878, 2011.
- [254] C.R. Wilke, P. Chang, "Correlation of diffusion coefficients in dilute solutions," *AIChE*, vol. 1, no. 2, pp. 264–270, 1955.
- [255] H. Burrell, "Official digest," *Fed. Soc. Paint Technol.*, vol. 27, p. 726, 1955.
- [256] R. L. Scott and M. Magat, "Thermodynamics of high-polymer solutions. iii. swelling of cross-linked rubber," *Journal of Polymer Science*, vol. 4, no. 5, pp. 555–571, 1949.
- [257] R. Blanks and J. Prausnitz, "Thermodynamics of polymer solubility in polar and nonpolar systems," *Industrial and Engineering Chemistry Fundamentals*, vol. 3, pp. 1–8, 1964.

8 References

- [258] K. Peters, J. Braun, B. Schmidt-Hansberg, P. Scharfer, and W. Schabel, “Phase equilibrium of water in different types of pedot:pss,” *Chemical Engineering and Processing*, vol. 50, no. 5-6, pp. 555 – 557, 2011.
- [259] P. Dupeyrat, “Kraftmikroskopie an heterogenen leitfähigen Probensystemen,” Master’s thesis, Institut of Nanotechnology, Karlsruher Institut für Technologie, 2009.
- [260] O. Sahin, S. Magonov, C. Su, C.F. Quate, O. Solgaard, “An atomic force microscope tip designed to measure time-varying nanomechanical forces.,” *Nature Nanotechnology*, vol. 2, pp. 507–514, 2007.
- [261] J. Stöhr, *NEXAFS Spectroscopy*. Springer-Verlag: Berlin, 1996.
- [262] C. Wohlfarth, M. D. Lechner, *Landolt-Börnstein: Numerical Data and Functional Relationships in Science and Technology - New Series*, vol. 38. Springer Verlag, Berlin, Heidelberg, 1996.
- [263] J.Y. Lee, S.T. Connor, Y. Cui, P. Peumans, “Semitransparent organic photovoltaic cells with laminated top electrode,” *Nano Letters*, vol. 10, p. 1276–1279, 2010.
- [264] R. Søndergaard, M. Helgesen, M. Jørgensen, F.C. Krebs, “Fabrication of polymer solar cells using aqueous processing for all layers including the metal back electrode,” *Advanced Energy Materials*, vol. 1, p. 68–71, 2011.
- [265] W. Gaynor, J.Y. Lee, P. Peumans, “Fully solution-processed inverted polymer solar cells with laminated nanowire electrodes,” *ACS Nano*, vol. 4, no. 1, pp. 30–34, 2010.
- [266] K. Peters, “Messung und Modellierung der Trocknungskinetik photoaktiver Polymerschichten organischer Polymersolarzellen,” Master’s thesis, Institut für Thermische Verfahrenstechnik, Universität Karlsruhe (TH), 2008.
- [267] F. Buss *Parameterstudie zur Trocknungskinetik photoaktiver Schichten für Polymersolarzellen mit einem Lösemittelgemisch*, Studienarbeit, Institut für Thermische Verfahrenstechnik, Universität Karlsruhe (TH), 2009.
- [268] B. Brenneis, “Charakterisierung und Kontrolle der Nanomorphologie von Polymer-Fulleren-Schichten,” Master’s thesis, Institut für Thermische Verfahrenstechnik, Karlsruhe Institute of Technology, 2010.

9 List of Publications

Student research projects (Studienarbeiten) and Diploma theses conducted in conjunction with this thesis:

- [1] Natalie Schnabel, „Untersuchung der Phasengleichgewichte halbleitender organischer Materialien in der Flüssigphase“, Diploma thesis, Universität Karlsruhe (TH), 2008.
- [2] Katharina Peters, „Messung und Modellierung der Trocknungskinetik photoaktiver Polymerschichten organischer Polymersolarzellen“, Diploma thesis, Universität Karlsruhe (TH), 2008.
- [3] Helge Geisler, „Simulation der Grenzschichtausbildung an überströmten Polymerstrukturen“, Studienarbeit, Universität Karlsruhe (TH), 2009.
- [4] Felix Buss, „Parameterstudie zur Trocknungskinetik photoaktiver Schichten für Polymersolarzellen mit einem Lösemittelgemisch“, Studienarbeit, Universität Karlsruhe (TH), 2009.
- [5] Stefan Jaiser, „Beschreibung von Phasengleichgewichten halbleitender organischer Materialien“, Studienarbeit, Karlsruhe Institute of Technology, 2009.
- [6] Jens Buzengeiger, „Einfluss der Trocknungsbedingungen auf die Eigenschaften von Polymer-Solarzellen“, Studienarbeit, Universität Karlsruhe (TH), 2009.
- [7] Michael Baunach, „Lateral aufgelöste Messung der Schichtdickenabnahme von flüssig prozessierten Polymer-Fulleren-Filmen mit Lösungsmittel-gemischen für organische Elektronik“, Diploma thesis, Karlsruhe Institute of Technology, 2010.
- [8] Benedikt Brenneis, „Charakterisierung und Kontrolle der Nanomorphologie von Polymer-Fulleren-Schichten“, Diploma thesis, Karlsruhe Institute of Technology, 2010.
- [9] Mareike Kowalski, „Einfluss von Additiven auf die Nanomorphologie von Polymer-Fulleren-Schichten für organische Solarzellen“, Studienarbeit, Karlsruhe Institute of Technology, 2010.
- [10] Timo Basile, „Prozess-Struktur-Wechselbeziehung von amorphen und semikristallinen Polymer-Fulleren-Schichten für organische Solarzellen“, Studienarbeit, Karlsruhe Institute of Technology, 2011.

Publications:

- [1] B. Schmidt-Hansberg, M. Sanyal, N. Grossiord, Y. Galagan, M. Baunach, M.F.G. Klein, A. Colsmann, P. Scharfer, U. Lemmer, H. Dosch, J. Michels, E. Barrena, W. Schabel, “Investigation of non-halogenated solvent mixtures for high throughput fabrication of polymer-fullerene solar cells” *Solar Energy Materials and Solar Cells* 96, 195-201, 2012
- [2] B. Schmidt-Hansberg, M. Sanyal, M.F.G. Klein, M. Pfaff, N. Schnabel, S. Jaiser, A. Vorobiev, E. Müller, A. Colsmann, P. Scharfer, D. Gerthsen, U. Lemmer, E. Barrena,

9 List of Publications

W. Schabel, "Moving through the phase diagram: morphology formation in solution cast polymer–fullerene blend films for organic solar cells" *ACS Nano* 5, 8579–8590, 2011

[3] M. Sanyal, B. Schmidt-Hansberg, M.F.G. Klein, C. Munuera, A. Vorobiev, A. Colsmann, P. Scharfer, U. Lemmer, W. Schabel, H. Dosch, E. Barrena, "Effect of Photo-voltaic Polymer/Fullerene Blend Composition Ratio on Microstructure Evolution during Film Solidification Investigated in Real Time by X-ray Diffraction" *Macromolecules* 44, 3795–3800, 2011

[4] M. Sanyal, B. Schmidt-Hansberg, M.F.G. Klein, A. Colsmann, C. Munuera, A. Vorobiev, U. Lemmer, W. Schabel, H. Dosch, E. Barrena "In Situ X-Ray Study of Drying-Temperature Influence on the Structural Evolution of Bulk-Heterojunction Polymer–Fullerene Solar Cells Processed by Doctor-Blading" *Advanced Energy Materials* 1, 363-367, 2011

[5] B. Schmidt-Hansberg, M. Baunach, J. Krenn, S. Walheim, U. Lemmer, P. Scharfer, W. Schabel "Spatially resolved drying kinetics of multi-component solution cast films for organic electronics" *Chemical Engineering and Processing* 50, 509-515, 2011

[6] J. Krenn, S. Baesch, B. Schmidt-Hansberg, M. Baunach, P. Scharfer, Wilhelm Schabel "Numerical investigation of the local mass transfer on flat plates in laminar flow" *Chemical Engineering and Processing* 50, 503-508, 2011

[7] L. Wengeler, B. Schmidt-Hansberg, K. Peters, P. Scharfer, W. Schabel "Investigations on knife and slot die coating and processing of polymer nanoparticle films for hybrid polymer solar cells" *Chemical Engineering and Processing* 50, 478-482, 2011

[8] K. Peters, J. Braun, B. Schmidt-Hansberg, P. Scharfer, W. Schabel "Phase equilibrium of water in different types of PEDOT:PSS" *Chemical Engineering and Processing* 50, 555-557, 2011

[9] B. Schmidt-Hansberg, M. F. G. Klein, K. Peters, F. Buss, J. Pfeifer, S. Walheim, A. Colsmann, U. Lemmer, P. Scharfer, W. Schabel "In-situ monitoring the drying kinetics of knife coated polymer-fullerene films for organic solar cells" *Journal of Applied Physics* 106, 124501, 2009

Feature article in *Virtual Journal of Nanoscale Science & Technology* 21, 1, 2010

[10] B. Schmidt-Hansberg, H. Do, A. Colsmann, U. Lemmer, W. Schabel „Drying of thin film polymer solar cells" *European Physical Journal Special Topics* 166, 49-53, 2009

[11] Y. Serfert, S. Drusch, B. Schmidt-Hansberg, M. Kind, K. Schwarz "Process engineering parameters and type of n-octenylsuccinate-derivatised starch affect oxidative stability of microencapsulated long chain polyunsaturated fatty acids" *Journal of Food Engineering* 95, 386-392, 2009

[12] S. Drusch, Y. Serfert, M. Scampicchio, B. Schmidt-Hansberg, K. Schwarz "Impact of Physicochemical Characteristics on the Oxidative Stability of Fish Oil Microencapsulated by Spray-Drying" *Journal of Agricultural and Food Chemistry* 55, 11044, 2007

Conference contributions:

- [1] B. Schmidt-Hansberg, F. Buss, M. Klein, M. Sanyal, A. Colsmann, U. Lemmer, E. Barrena, P. Scharfer und W. Schabel „Tuning polymer-fullerene blend nanomorphology by controlled film drying conditions” *9th European Coating Symposium*, 08.-10.06. 2011, Åbo/Turku, Finland, (Talk)
- [2] B. Schmidt-Hansberg, M. Sanyal, M. Klein, A. Colsmann, U. Lemmer, E. Barrena, P. Scharfer, W. Schabel “In-situ observation and manipulation of polymer-fullerene self-assembly during thin film drying for organic solar cells” *MRS Spring Meeting*, 25.-29.04.2011, San Francisco, USA, (Poster)
- [3] B. Schmidt-Hansberg, M. Kowalski, M. Klein, M. Sanyal, A. Colsmann, U. Lemmer, E. Barrena, P. Scharfer, W. Schabel „Phasengleichgewichte und Stofftransport in organischen Halbleitern: Selbstanordnungsprozesse in Polymersolarzellen“ *ProcessNet-Fachausschuss Wärme- und Stofftransport*, 21.-22.03. 2009, Frankfurt, Germany, (Talk)
- [4] B. Schmidt-Hansberg, M. Baunach, M. Klein, M. Sanyal, C. Walsh, A. Colsmann, U. Lemmer, E. Barrena, P. Scharfer, W. Schabel, „Kontrolle der Morphologie in organischen Solarzellen“ *Processnet Jahrestagung*, 21.-23.09.2010, Aachen, Germany, (Poster)
- [5] B. Schmidt-Hansberg, M. Baunach, M. Klein, M. Sanyal, C. Walsh, A. Colsmann, U. Lemmer, E. Barrena, P. Scharfer, W. Schabel „In-situ monitoring the film formation of solution cast polymer-fullerene blends for organic solar cells” *15th International Coating Science and Technology (ISCST) Symposium*, 13.-15.09.2010, St. Paul, USA, (Talk)
- [6] B. Schmidt-Hansberg, J. Krenn, M. Baunach, S. Baesch, P. Scharfer, W. Schabel „Theoretical and experimental investigation of the gas phase mass transport on flat plates in laminar flow” *15th International Coating Science and Technology (ISCST) Symposium*, 13.-15.09.2010, St. Paul, USA, (Poster)
- [7] B. Schmidt-Hansberg, M. Sanyal, M. Klein, A. Colsmann, U. Lemmer, E. Barrena, P. Scharfer, W. Schabel, „Morphology formation in solution cast polymer-fullerene blends for organic photovoltaics” *1st International Conference on Materials for Energy*, 04.-08.07.2010, Karlsruhe, Germany, (Talk)
- [8] B. Schmidt-Hansberg, M. Sanyal, M. Klein, A. Colsmann, U. Lemmer, E. Barrena, P. Scharfer, W. Schabel „In-situ Monitoring the Morphology Formation During Drying of Knife Coated Polymer-Fullerene Films for Organic Solar Cells” *MRS Spring Meeting*, 05.-09.04.2010, San Francisco, USA, (Talk)
- [9] B. Schmidt-Hansberg, M.F.G. Klein, F. Pasker, H. Wettach, B. Brenneis, A. Colsmann, U. Lemmer, S. Höger, P. Scharfer, W. Schabel, “Morphology formation during drying of solution cast polymer-fullerene blends for solar cell applications” *Workshop of the DFG Priority Program 1355 "Organic Photovoltaics"*, 30.10. 2009, Dresden, Germany, (Talk)
- [10] B. Schmidt-Hansberg, B. Brenneis, S. Jaiser, M. Klein, A. Colsmann, U. Lemmer, J. Pfeifer, S. Walheim, M. Sanyal, E. Barrena, P. Scharfer, W. Schabel, „Phase behavior of solution cast polymer-fullerene blends during drying for organic solar cells“ *5th Plastic Electronics Europe*, 27.-29.10. 2009, Dresden, Germany, (Poster)

9 List of Publications

- [11] B. Schmidt-Hansberg, F. Buss, K. Peters, J. Pfeifer, S. Walheim, M.F.G. Klein, A. Colsmann, U. Lemmer, M. Sanyal, E. Barrena, P. Scharfer, W. Schabel, "Morphology formation during drying of solution cast polymer-fullerene blends for solar cell applications" *8th European Coating Symposium*, 07.-09.09. 2009, Karlsruhe, Germany, (Talk)
- [12] F. Buss, S. Jaiser, B. Schmidt-Hansberg, J. Pfeifer, S. Walheim, P. Scharfer, W. Schabel, "Moving through the phase diagram: Drying of solution cast polymer-fullerene films" *8th European Coating Symposium*, 07.-09.09. 2009, Karlsruhe, Germany, (Poster)
- [13] K. Peters, B. Schmidt-Hansberg, L. Wengeler, P. Scharfer, W. Schabel, "Feasibility Studies on Solution-processed Hole Injection Layers for Organic LEDs" *8th European Coating Symposium*, 07.-09.09. 2009, Karlsruhe, Germany, (Poster)
- [14] L. Wengeler, B. Schmidt-Hansberg, P. Scharfer, W. Schabel, "Roll to roll production of nano-particle based polymer solar cells on flexible substrates" *8th European Coating Symposium*, 07.-09.09. 2009, Karlsruhe, Germany, (Poster)
- [15] B. Schmidt-Hansberg, F. Buss, S. Jaiser, P. Scharfer, M. Klein, A. Colsmann, U. Lemmer, J. Pfeifer, S. Walheim, M. Kind, W. Schabel, "Phase separation during drying of polymer-fullerene-solutions for polymer solar cells" *Frontiers in Polymer Science*, 7.-9.06. 2009, Mainz, Germany, (Poster)
- [16] A. Bauer, A. Colsmann, U. Lemmer, J. Hanisch, E. Ahlswede, M. Sanyal, C. Munuera, E. Barrena, B. Schmidt-Hansberg, W. Schabel, F. Pasker, S. Höger, "Towards transparent and multijunction polymer solar cells with improved optoelectronic properties" *Annual Meeting of the DFG Priority Program 1355 "Organic Photovoltaics"*, 13.-14.05. 2009, Wuppertal, Germany, (Talk & Poster)
- [17] B. Schmidt-Hansberg, N. Schnabel, K. Peters, P. Scharfer, W. Schabel, "Phasenseparation von Polymer-Fulleren-Lösungen photoaktiver Schichten organischer Polymersolarzellen" *ProcessNet-Fachausschuss Kristallisation*, 12.-13.03. 2009, Dortmund, Germany, (Poster)
- [18] B. Schmidt-Hansberg, N. Schnabel, K. Peters, P. Scharfer, U. Lemmer, M. Kind, W. Schabel, "Phase separation during the drying process of the photoactive layer in polymer solar cells" *14th International Coating Science and Technology Symposium*, 07.-10.09 2008, Los Angeles, USA, (Talk)
- [19] W. Schabel, P. Scharfer, M. Müller, J. Krenn, B. Schmidt-Hansberg, "Drying issues and process scale up of solvent casted films for flat panel displays and organic electronics" *14th International Coating Science and Technology Symposium*, 07.-10.09 2008, Los Angeles, USA, (Talk)
- [20] B. Schmidt-Hansberg, J. Buzengeiger, M. Kind, A. Colsmann, U. Lemmer, W. Schabel, "Trocknung der Absorptionsschicht organischer Polymersolarzellen" *ProcessNet-Fachausschuss Trocknungstechnik/Kristallisation*, 05.-07.03 2008, Halle, Germany, (Poster)
- [21] B. Schmidt-Hansberg, H. Do, A. Colsmann, U. Lemmer, W. Schabel, "Drying of thin film polymer solar cells" *7th European Coating Symposium*, 12.-14.09 2007, Paris, France, (Poster)

Invited talks:

- [1] B. Schmidt-Hansberg, Structure formation of organic semiconductors, *9th European Coating Symposium*, invited short course lecture, 07.06. 2011, Åbo/Turku, Finland
- [2] B. Schmidt-Hansberg, M. Sanyal, M. Baunach, B. Brenneis, M. Klein, A. Colsmann, U. Lemmer, E. Barrena, P. Scharfer, W. Schabel, „In-situ monitoring the morphology formation during drying of knife coated polymer-fullerene blends“, *PV group meeting, Cavendish Laboratory*, 26.11.2009, Cambridge, UK
- [3] B. Schmidt-Hansberg, N. Schnabel, K. Peters, P. Scharfer, W. Schabel, “Phase separation during the drying process of the photoactive layer in polymer solar cells (PSCs)”, *Holst Centre*, 3.11.2008, Eindhoven, Netherlands
- [4] B. Schmidt-Hansberg, Drying of Polymer Solar Cells, *Merck OLED-Division*, 8.03.2008, Darmstadt, Germany

10 Appendix

A 1 Drying kinetics.....	174
A 1.1 Estimation of gas phase limitation of film drying	174
A 1.2 Error discussion of laser reflectometry	175
A 1.3 Experimental setup.....	176
A 1.4 Real Time Spectroscopic Ellipsometry (RTSE)	177
A 2 Phase diagrams.....	179
A 2.1 Solubility parameter concept	179
A 2.2 Calibration.....	180
A 2.3 Phase diagrams of other solvents	182
A 2.4 Water sorption into PEDOT:PSS.....	183
A 3 Morphology of polymer-fullerene blends	184
A 3.1 Fabrication of organic solar cells.....	184
A 3.2 Atomic Force Microscopy (AFM).....	187
A 3.3 Scanning Transmission Electron Microscopy (STEM).....	188
A 3.4 STXM and NEXAFS measurements	188
A 3.5 Influence of drying temperature	189
A 3.6 Influence of 1,8-octanedithiol on film structure	193
A 3.7 Influence of solvents on film structure	195
A 3.8 Structure formation of low band gap polymers	196
A 4 Material properties	199
A 4.1 Density	201
A 4.2 Vapor pressure	203
A 4.3 Gas phase diffusion coefficient.....	203
A 4.4 Refractive index	204
A 4.5 Phase equilibrium of solvent-solvent mixtures.....	205

A 1 Drying kinetics

A 1.1 Estimation of gas phase limitation of film drying

For the estimation of the degree of gas phase mass transfer domination the Biot number is used in analogy to heat transfer as a measure of the ratio between gas phase mass transfer and mass transfer within the film in the form

$$Bi = \frac{\beta_{1,g}}{D_{1,l}/d} \quad 10.1$$

with $\beta_{1,g}$ as the gas phase mass transfer coefficient of the solvent, $D_{1,l}$ as the solvent diffusion coefficient in the wet film and d as the film thickness. For comparatively low Biot numbers we would expect analog to heat transfer that the gas phase mass transfer is the dominating mechanisms for the drying process. As reference for diffusional limitation, values for Bi were taken from film drying data for the system toluene-polyvinyl acetate from reference [111]. At 40°C drying temperature and $\beta_{1,g} = 0.002 \text{ m/s}$ measurements and simulations show only weakly pronounced concentration profiles and mainly gas phase determined mass transfer of solvent up to solvent contents of 0.5 with $D_{1,l} \approx 3 \cdot 10^{-11} \text{ m}^2/\text{s}$ at $d \approx 35 \mu\text{m}$. This results in $Bi = 2520$. As drying proceeds Schabel obtained $D_{1,l} \approx 4 \cdot 10^{-13} \text{ m}^2/\text{s}$ for solvent contents of 0.1 which results at $d \approx 25 \mu\text{m}$ in increased values of $Bi = 135000$. Integral drying curves also express the additional mass transfer resistance in the film.

In this thesis we receive for exemplary values of $\beta_{1,g} = 0.003 \text{ m/s}$ (see Figure 2.12), $D_{1,l} = 1 \cdot 10^{-9} \text{ m}^2/\text{s}$ (according to Wilke and Chang [254] at room temperature for DCB) and an initial film thickness of $d = 4 \mu\text{m}$ a Biot number of 12. This is considerably less than for the cases of diffusional limitation as mentioned above. It is notable that the solvent content of the photoactive layer is larger than 30 initially. However, the drying of the final few weight percent of solvent at thicknesses around 200 nm most likely will be determined by diffusional limitation in the film. Assuming a comparable diffusion coefficient for residual DCB in the photoactive layer as for toluene in polyvinyl acetate at room temperature and a solvent content of 0.1 ($D_{1,l} = 5 \cdot 10^{-14} \text{ m}^2/\text{s}$), we receive a $Bi = 12000$. This is in the range of Biot where Schabel observed diffusional limitation in the film.

A 1.2 Error discussion of laser reflectometry

In the following the influence of small uncertainties in refractive index, dry film thickness and angle of incidence α on the interference analysis is undertaken. The crucial parameter in the analysis of the interference fringes obtained by reflectometry during film drying is the slope of the decrease in film thickness $\Delta d/\Delta t = (d_k - d_{k-1})/\Delta t$ where $k = [1, 2, \dots]$ is the number of interference condition. Since $\Delta d/\Delta t$ is directly proportional to the gas phase mass transfer coefficient the below discussed impact on $\Delta d/k$ directly influences the obtained values of the mass transfer coefficient.

In Figure 10.1a the thickness difference between two interference conditions Δd is plotted against the number of interference conditions. Film thickness is increasing with k . Hence, the influence of uncertainties in dry film thickness only has an impact on Δd in the final drying phase. At the beginning of film drying (high values of k) where the mass transfer coefficient was determined, the influence gets negligible. For uncertainties in the angle of incidence of $\pm 2^\circ$ leads to a constant deviation of Δd below 0.75%.

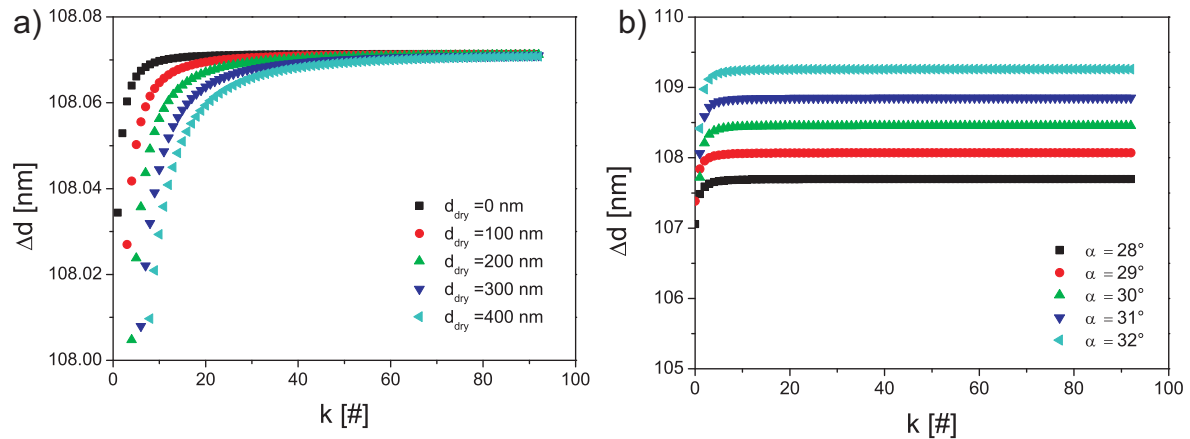


Figure 10.1: Influence of a) dry film thickness and b) angle of incidence on Δd per interference condition k . [139]

The influence of the refractive index of dissolved solid constituents is even with deviations of 10% negligible from the beginning of drying (high number of k = high film thickness) over a broad range of drying. Uncertainties in the solvents refractive index are more effective and cause with a deviation of 1% a change of 1.1% in Δd . This is due to the low mass fraction from 0.02 to 0.05 of dissolved solid components. At the beginning of drying one can therefore assume $n_1 \approx n_{solvent}$. In conclusion, the angle of incidence

and the solvent refractive index are the critical parameters that can strongly alter the measurement accuracy.

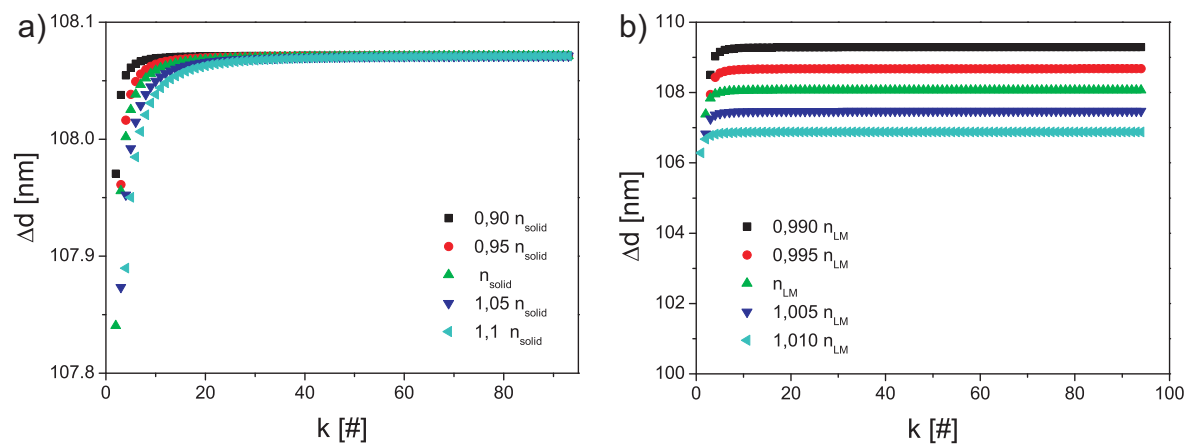


Figure 10.2: Influence of the refractive index of a) the dissolved solid and b) the liquid constituents (solvents or their mixtures) on Δd per interference condition k . [139]

A 1.3 Experimental setup

The coating and drying setup for real time GIXD was the same as for the fabrication of all other samples and solar cells. It is shown in more detail in Figure 4.7. Figure 10.3 depicts a technical drawing of the liquid temperature controlled substrate carrier.

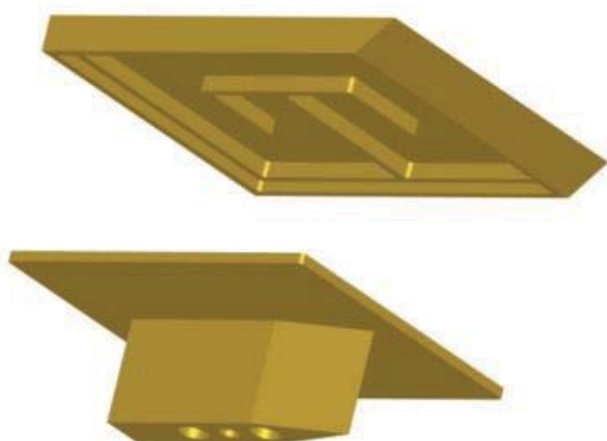


Figure 10.3: Liquid temperature controlled substrate carrier of the drying channel. [139]

A 1.4 Real Time Spectroscopic Ellipsometry (RTSE)

Spectroscopic ellipsometry (SE) measures the change in light polarization that a reflected light beam undergoes during interaction with a thin film. The elliptic state of polarization is described with the two parameters Ψ and Δ (see [122] for more details). The drying process of P3HT:PCBM films cast from DCB at room temperature was monitored with a rotating polarizer ellipsometer (GES5E, SOPRALAB) in situ under an incident angle of 65° . During drying 4 spectra per second were obtained from 200-1000 nm (6.5-1.2 eV).

Figure 10.4a depicts some exemplary spectra of $\cos(\Delta)$ during the drying process of P3HT:PCBM (1:0.8) films. At 0 s high film thickness causes many interference fringes that reduce in the course of drying. Spectra undergo the strongest change from about 200 s to 355 s. Figure 10.4b shows the evolution of $\cos(\Delta)$ during drying in a higher time resolution for two exemplary wavelengths. The numbered positions are associated to the spectra in Figure 10.4a.

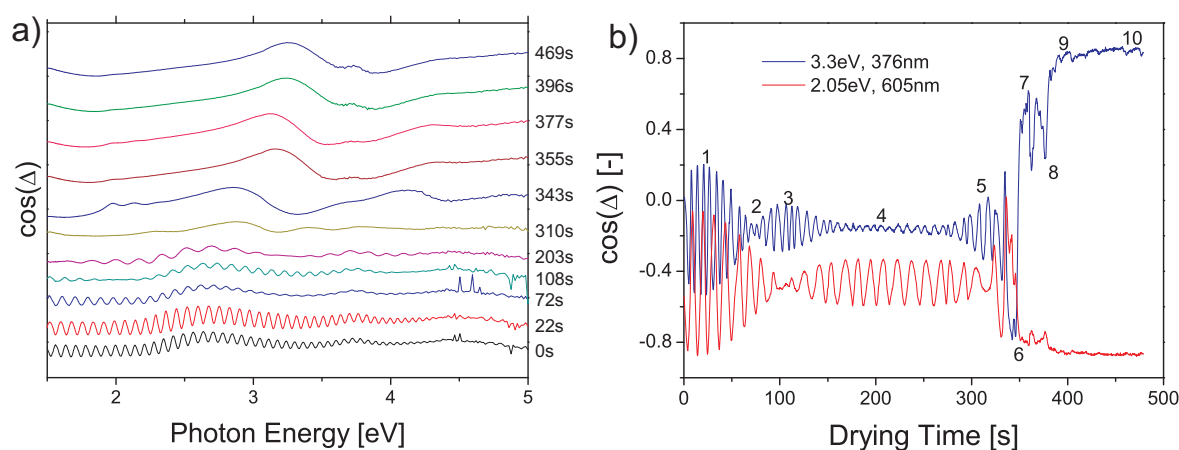


Figure 10.4: a) Real time spectroscopic ellipsometry $\cos(\Delta)$ spectra of some snapshots during film drying after doctor blading a P3HT:PCBM (1:0.8) film from DCB. b) Evolution of $\cos(\Delta)$ for two light wavelengths. The spectra of the numbered instants during the evolution of $\cos(\Delta)$ are plotted in a).

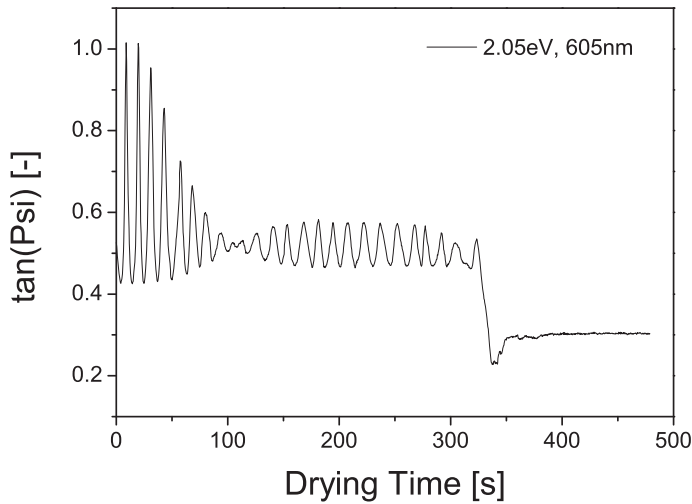


Figure 10.5: Evolution of $\tan(\Psi)$ as obtained by real time spectroscopic ellipsometry during drying of a solution cast P3HT:PCBM film. The wavelength of 605 nm is associated with the characteristic vibronic side-band absorption due to P3HT π - π interaction.

In particular the evolution at 605 nm is of interest because it is related to the vibronic sideband absorption induced by π - π -stacking of P3HT. Therefore the evolution of $\tan(\Psi)$ is also given in Figure 10.5. However, the extraction of information on the structural evolution such as the increase of π - π -stacking requires a thorough data analysis and modeling of the complex refractive index for each spectrum. This is beyond the scope of this thesis but showed the feasibility and potential of this experimental approach.

Another advantage of SE is the high thickness resolution which allows for the thickness monitoring in the falling rate drying period of P3HT:PCBM films which are transparent at wavelength higher than about 650 nm (1.9 eV). Hence the refractive index simplifies to its real part in the near infrared and the spectra can be fitted with a Cauchy model. In this model, the refractive index dispersion is given by a polynomial expression: $n = A + B/\lambda^2 + C/\lambda^4$ where A, B and C are coefficients obtained after a fitting procedure. This approach consists in minimizing an error function which is equal to the absolute difference between the measurement and the model values using a Levenberg Marquardt algorithm. Figure 10.6 depicts an excerpt of the obtained thickness evolution in the falling rate period of P3HT:PCBM (1:2) films. 100 measurements correspond to about 25 s.

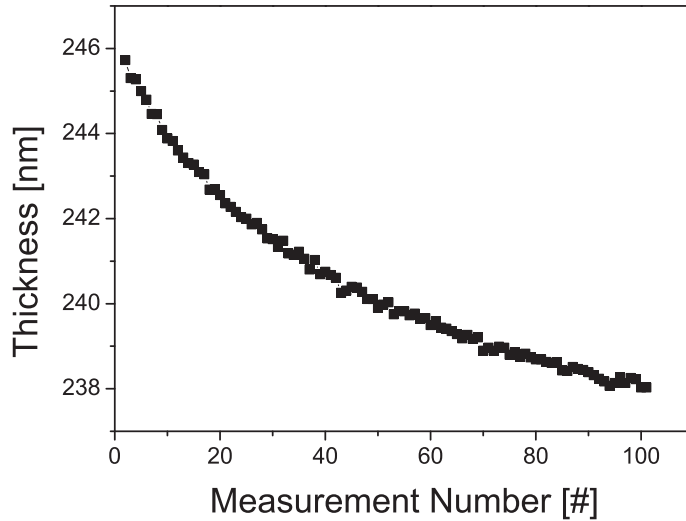


Figure 10.6: Thickness evolution obtained by applying a Cauchy model in the range of 700-1000 nm to a part of the falling rate period of a drying P3HT:PCBM (1:2) film.

A 2 Phase diagrams

A 2.1 Solubility parameter concept

The enthalpy of mixing in equation 3.1 can also be described by the solubility parameter concept

$$\Delta h_M = \frac{\Delta H_M}{V_{solvent}} = \varphi_1 \cdot \varphi_2 (\delta_1 - \delta_2)^2 \quad 10.2$$

where $V_{solvent}$ is the molar volume of solvent and δ_i the solubility parameter of each substance. The solubility parameter δ_i of a substance in a condensed state can be determined from the cohesive energy $E_{coh} \approx \Delta H_{vap} - RT$ [J/mol] with the molar volume V .

$$\delta = \left(\frac{E_{coh}}{V} \right)^{1/2} \quad [(J/cm^3)^{1/2}] \quad 10.3$$

Solvent with similar values of δ show similar solubility which can be refined by separate consideration of degree of hydrogen bonding [255]. This model for the cohesive energy can be refined by dividing the contributions into dispersion forces, polar forces and hydrogen bonding.

$$\delta^2 = \delta_d^2 + \delta_p^2 + \delta_h^2 \quad 10.4$$

each parameter can be assumed to depend on temperature. With this extension the enthalpy of mixing for the solubility parameter concept reads

$$\Delta h_M = \varphi_1 \cdot \varphi_2 \left[(\delta_{d1} - \delta_{d2})^2 + (\delta_{p1} - \delta_{p2})^2 + (\delta_{h1} - \delta_{h2})^2 \right] \quad 10.5$$

where “1” stands for the polymer and “2” for the solvent. The Flory-Huggins interaction parameter χ , which is considered to be the sum of entropic and enthalpic contributions $\chi = \chi_S + \chi_H$ and the solubility parameter are correlated with the following expression

$$\chi \approx \underbrace{0.34}_{\chi_S} + \underbrace{\frac{V_S}{RT} (\delta_1 - \delta_2)}_{\chi_H} \quad 10.6$$

The entropic contribution is usually set to $\chi_S = 0.34$ for non-polar systems [256, 257]. More detailed information and tabulated solubility parameters can be found in reference [226].

A 2.2 Calibration

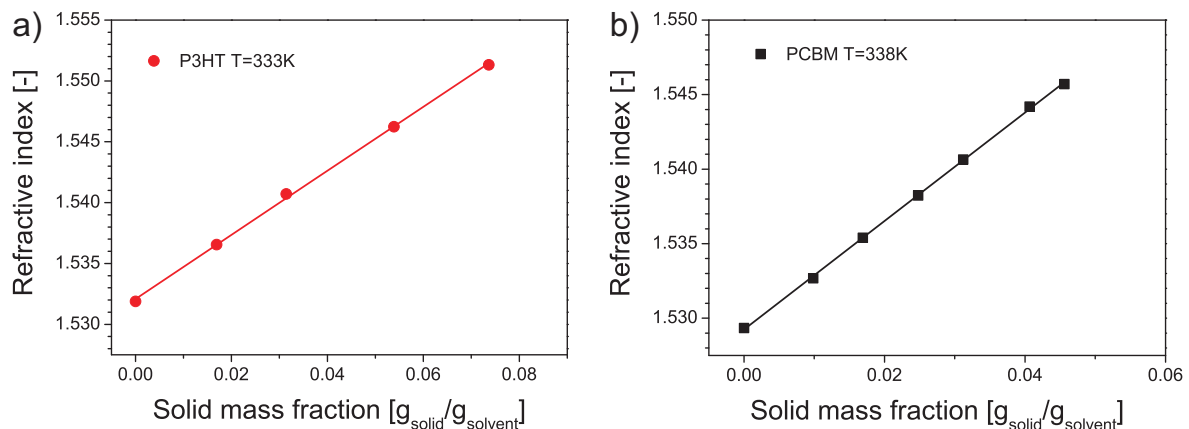


Figure 10.7: Calibration curves of the binary a) P3HT and b) PCBM solutions refractive index dissolved in DCB against the solid mass fraction. [81]

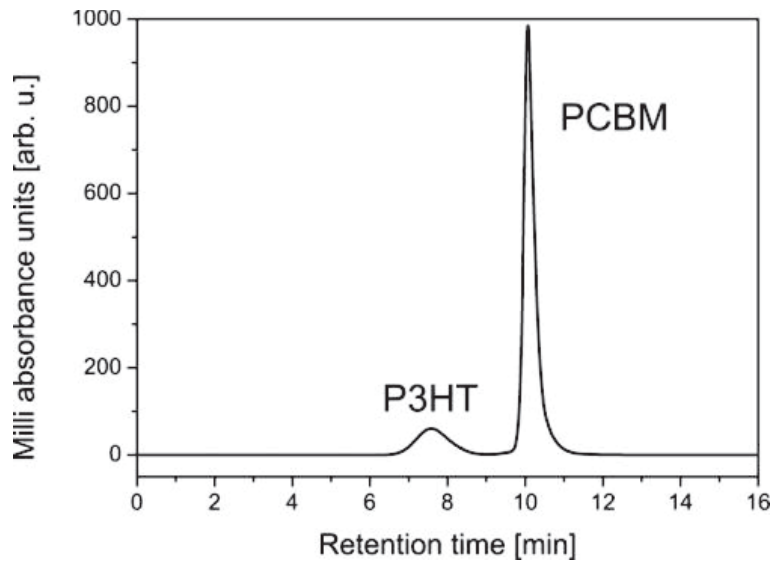


Figure 10.8: Exemplary plot of the diode array detector of a size exclusion chromatography (SEC) measurement for a P3HT-PCBM-DCB solution. [190]

A 2.3 Phase diagrams of other solvents

In addition to the discussed phase diagrams of DCB solutions, this section comprises measurements of further solvents.

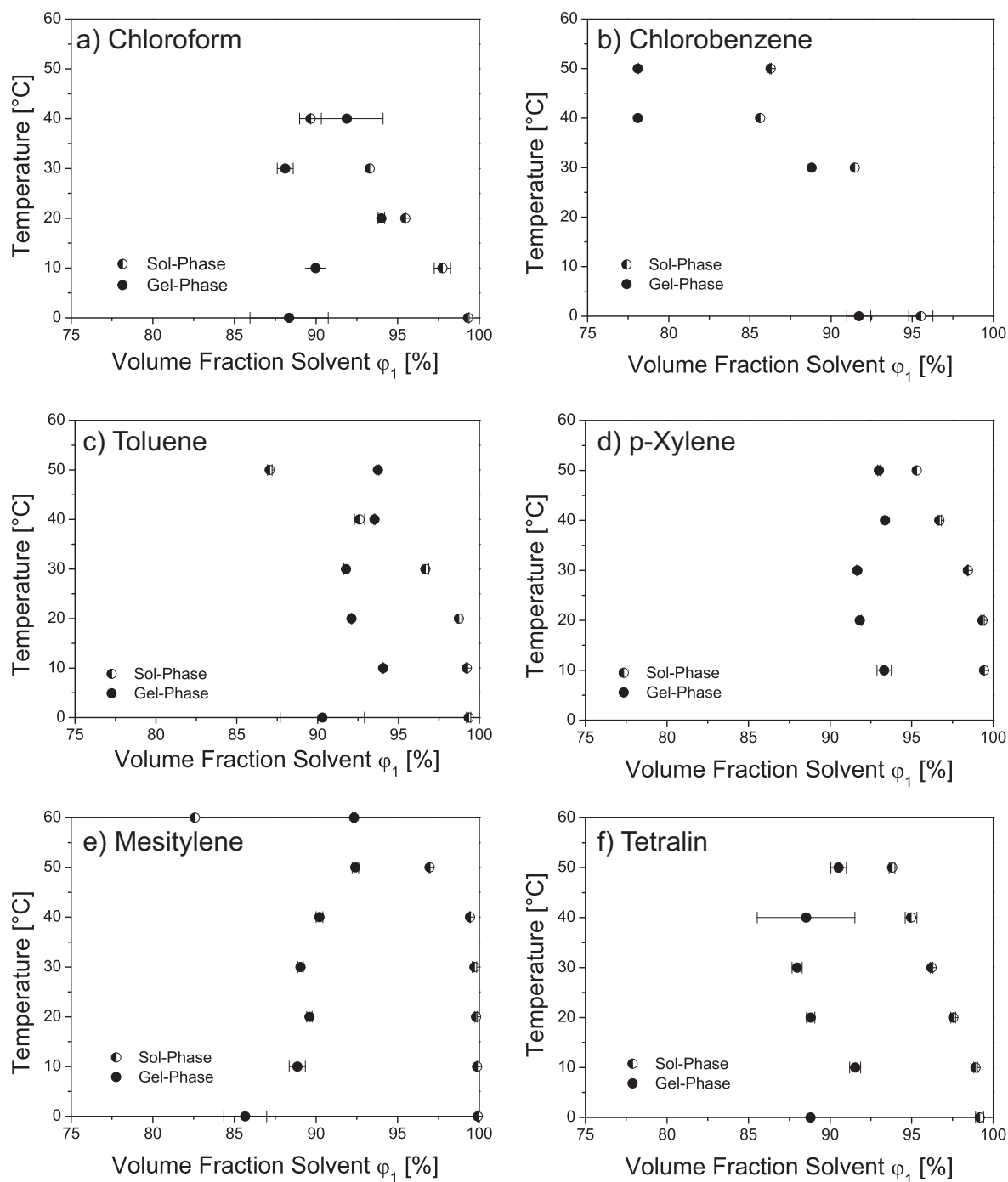


Figure 10.9: Solution phase diagrams of P3HT (Rieke Metals 4002E, $M_w \approx 48900$ g/mol, polydispersity 1.7) in different solvents. Each point was determined in two independent vials. [191]

Here each point was only determined twice in comparison to four independent samples as accomplished for DCB. For Flory-Huggins fitting the data is given in volume fractions.

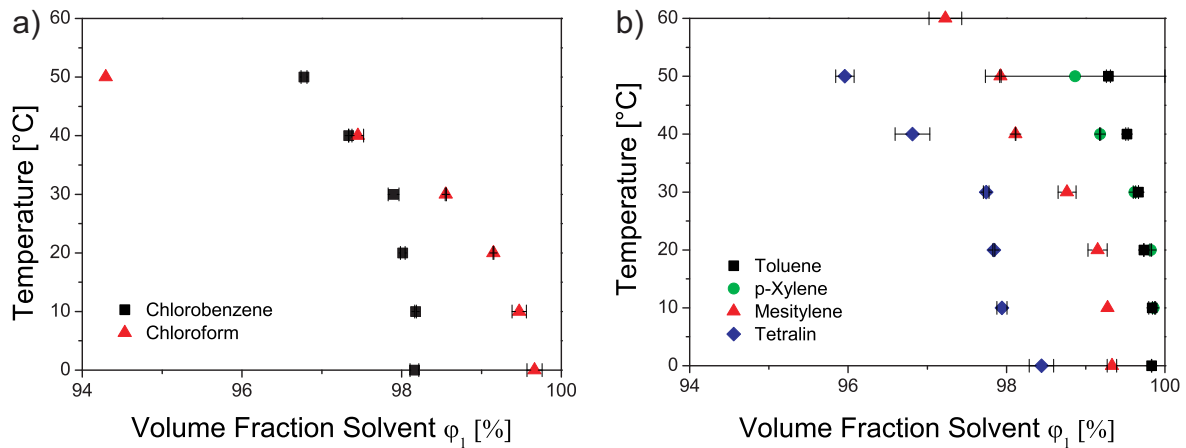


Figure 10.10: Solubility limits of PCBM in a) chlorinated and b) non-halogenated solvents. Each point was determined in two independent vials. [191]

A 2.4 Water sorption into PEDOT:PSS

The measurement of sorption isotherms as shown for P3HT:PCBM and DCB in section 2.3.2 can be very time and material consuming. For the investigated material systems the sorption measurement took several months for thick films of several micrometers. White light reflectometry allows an accurate and fast thickness measurement at much thinner film down to a few hundred nanometers. We used a NanoCalc-2000 (Mikropack GmbH) white light (250-1100 nm) reflectometer provided by the Institute of Nanotechnology. This technique was used for sorption experiments for the solvent water and the polymer blend PEDOT:PSS. Figure 10.11a depicts the experimental data and Cauchy fits for increasingly swollen PEDOT:PSS films under increasingly humid atmosphere. The Cauchy parameters (section A 1.4) were determined at dry films as well as the PEDOT:PSS density ($\rho_{VPAl4083} = 1.55 \text{ g/cm}^3$) by helium pycnometry. The neglect of changes in optical properties due to water sorption leads to an overestimation of absorbed water. This is shown in Figure 10.11 for reflectometry sorption and desorption measurements in comparison to measurements accomplished gravimetrically at about $20 \mu\text{m}$ thick films in a climate chamber [258]. However, the reflectometry sorption and desorption

isotherm could be measured within about one hour in comparison to the gravimetry experiment which took about 4 months. This shows the potential of this method which can be improved in accuracy by considering the evolution of the spectral refractive index

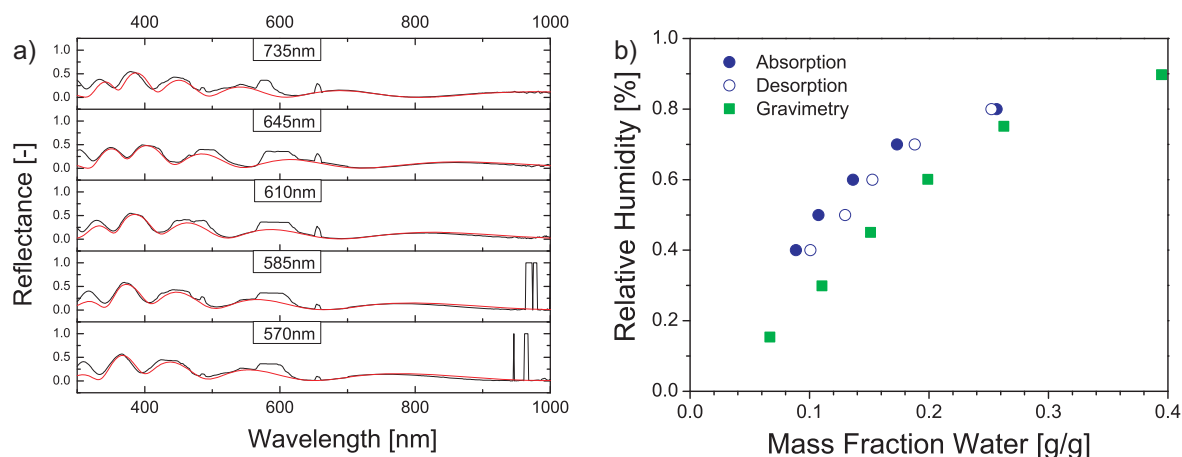


Figure 10.11: a) Measured reflectance (black) and fitted Cauchy model (red) with constant spectral refractive index to measurements of differently swollen PEDOT:PSS (VP AI 4083) film under water humidity. b) resulting sorption/desorption isotherm as obtained by white light reflectometry in comparison to gravimetric measurements. [190]

A 3 Morphology of polymer-fullerene blends

A 3.1 Fabrication of organic solar cells

The fabrication of solar cells starts with ITO/glass substrates ($48 \times 60 \text{ mm}^2$) as shown in Figure 10.12a. Subsequently these bare substrates are cut on the glass bottom side into a $16 \times 16 \text{ mm}^2$ pattern without braking (Figure 10.12b). In the following step three stripes of adhesive tape (12 mm width) are put on top of the ITO surface parallel to the long substrate edge. The tape protects the ITO layer in the succeeding etching step with smoking hydrochloric acid for 7 min until no conductivity can be measured anymore at those regions which were not covered by tape. The reason for ITO structuring will be explained below. After removing the adhesive tape, the structured substrate (Figure 10.12c) is cleaned carefully by repeating sonication treatments in toluene, acetone and isopropanol. Residual solvent is removed quickly by nitrogen air jet. The cleaned substrates are subsequently treated by oxygen

plasma (2 min, 160 W, 40 kHz) and directly used for coating of the hole conducting layer PEDOT:PSS by knife coating in a laminar flow box (Figure 10.12d). This layer is treated at 120°C for 20 min in a nitrogen glovebox. The in this thesis mainly discussed fabrication step – coating of the polymer-fullerene blend – is done in the above mentioned coating and drying setup in the following (Figure 10.12e).

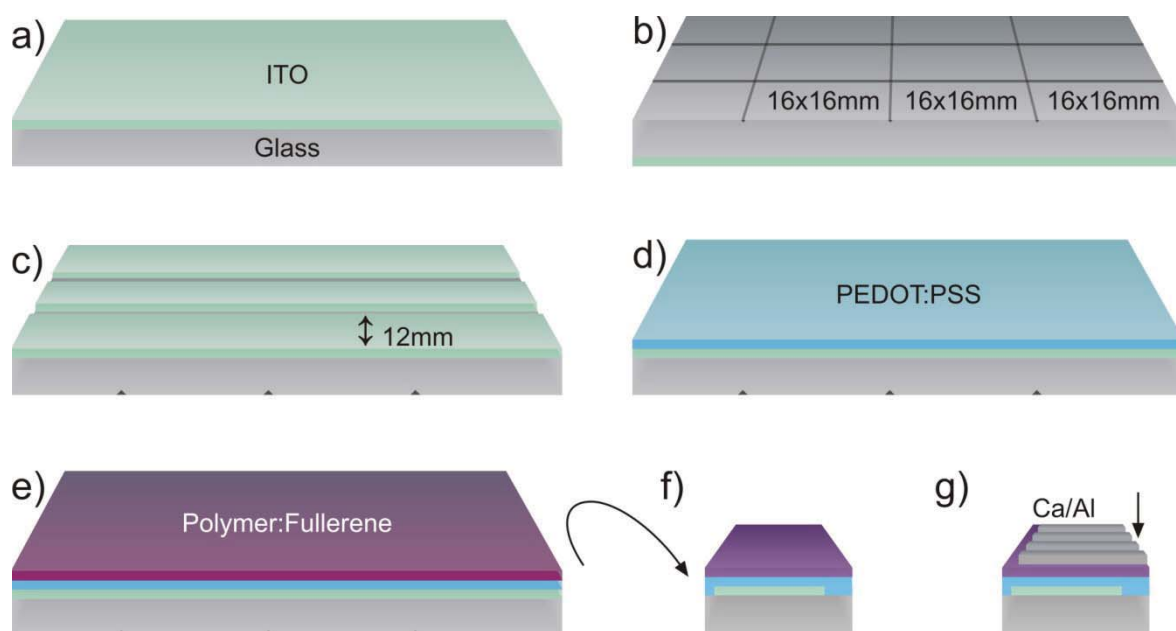


Figure 10.12: Process steps from the bare ITO/glass substrate to the final sub-substrates comprising three solar cells each.

After drying of the active layer, the substrate is broken into 9 pieces of $16 \times 16 \text{ mm}^2$ (Figure 10.12f). The smaller stripe of the substrate on the left in Figure 10.12b facilitates the coating and substrate splitting steps. In a final step metal electrodes (usually calcium and/or aluminum) are deposited on top of these $16 \times 16 \text{ mm}^2$ pieces through a shadow mask in a vacuum chamber (Figure 10.12g). Prior to the electrode deposition at one of these 4 electrode positions the films must be scratched mechanically in order to achieve electrical contact to the ITO anode on the bottom. Thus, each of the 3 deposited electrodes serve as cathodes for solar cells with a size of $12 \times 2 \text{ mm}^2$ which are connected via the ITO anode to the fourth electrode acting as anode contact. For the characterization of the 3 solar cells a multi contact clamp is put close to the in Figure 10.12g indicated edge and connects the solar cell device the characterization equipment. In order to prevent a shortcut between

cathodes which are deposited on top with the ITO anode underneath, the ITO had to be removed in the contact area of the contact clamp.

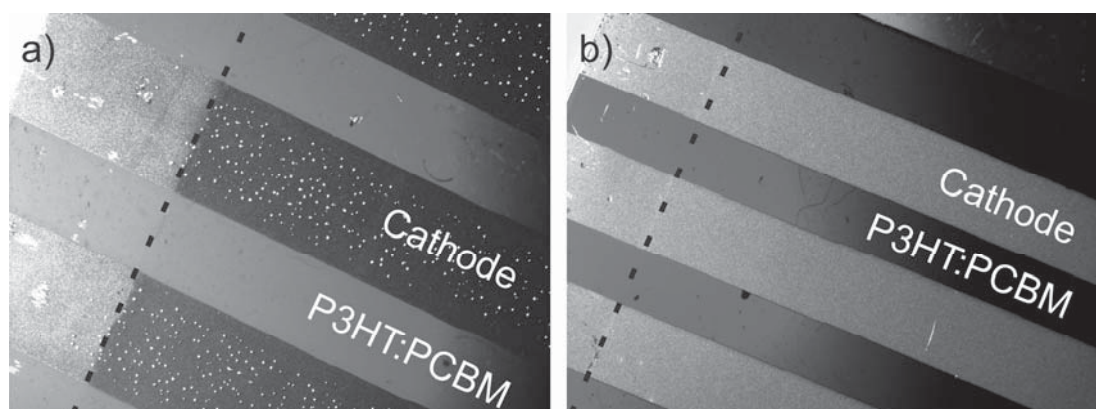


Figure 10.13: a) Residual solvent and/or ambient humidity penetrates metal cathode during thermal annealing at 150°C and causes holes in the cathode. b) Defect free cathode after previously desorbed humidity. [238]

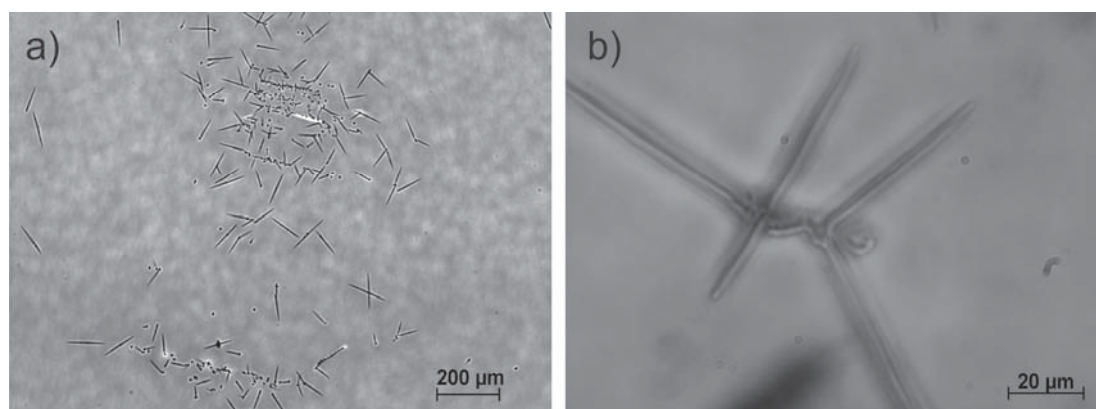


Figure 10.14: Excessive thermal annealing leads to large scale crystallites. [238]

If the samples contain residual solvent and/or humidity the metal electrode gets damaged in the thermal annealing step as shown exemplarily for an aluminum cathode in Figure 10.13a. It is remarkable that the electrodes are perforated only on top of the ITO covered regions (right side of dashed line). It is known that PEDOT:PSS tends to absorb ambient humidity (see section A 2.4), but since everything is covered by PEDOT:PSS the humidity damages must originate from ITO. If most of the remaining humidity was removed

prior to electrode deposition, no damages are generated during annealing (Figure 9.15b). Excessive thermal annealing leads to large scale crystals as depicted in optical microscope images in Figure 10.14.

A 3.2 Atomic Force Microscopy (AFM)

Atomic force microscopy (AFM) is a scanning surface sensitive technique, which probes the sample surface with a sharp tip (tip curvature is typically about 5 nm) [104]. Depending on the instrument, either the substrate or the tip is moved in order to realize the scanning process. For soft substances, such as polymeric and organic films it is common to operate in tapping mode, where the tip taps on the sample surface at a few hundred kHz. Interaction forces with the surface, which are mostly dominated by film topography induces deflection of the oscillating cantilever. The deflection is quantitatively detected by a tilt of the reflected laser beam causing a shift of the laser spot at the quadrant diode (Figure 10.15).

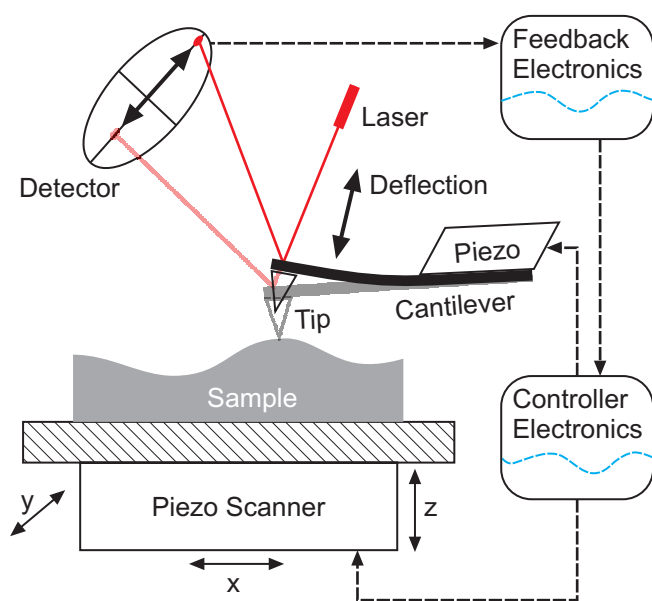


Figure 10.15: Scheme of an Atomic Force Microscope (AFM). The deflection of the tip is monitored on the basis of the shifted position of reflected laser light at a quadrant diode (According to [259]).

Tapping mode comprises two oscillating signals. First, the driving piezo oscillations for the generation of the tapping tip and second the real oscillation of the tip including all kinds of interaction with the sample. Hence, this mode provides additional information about the lateral surface properties through harmonic analysis, delivering the so called phase image. Contrast in

the phase image can originate from different material properties, such as differing elasticity, adhesion of the tip or hydrophilicity causing attractive and repulsive forces [260]. Although AFM might reveal crystalline and fibril structures in the phase images, it is not possible by solely this technique to distinguish amorphous and crystalline regions or different materials. Also the buried bulk structure of films cannot be accessed. Further applications of scanning probe techniques can be found in references [71, 72]. For the bulk film structure microscopic methods operating in transmission and for the determination of crystalline structures X-ray techniques are suitable.

A 3.3 Scanning Transmission Electron Microscopy (STEM)

In order to obtain an overall image of the bulk film structure, Scanning Transmission Electron Microscopy (STEM) was used in transmission normal to the surface which was previously investigated by AFM. As the name suggests, STEM is a combination of Scanning Electron Microscopy (SEM) and Transmission Electron Microscopy (TEM). The scanning electron beam is focused on the sample, which has been transferred onto a common copper grid. During penetration electrons interact with the sample. The transmitted and scattered electrons can be detected at different angles. The particular detectors are bright field (BF), annular dark field (ADF) and high angle annular dark field (HAADF) detectors from the center of the direct beam to wide angles.

The advantage of the HAADF detector is the higher sensitivity for low contrast samples in comparison to bright field TEM due to the detection of the scattered electrons, which contain more information about the sample structure than the direct image of transmission [84]. This is beneficial for organic semiconductors, which are mostly low contrast materials due to a very similar composition of mainly carbon and hydrogen.

A 3.4 STXM and NEXAFS measurements

Scanning Transmission X-ray Microscopy (STXM) and Near Edge X-Ray Absorption Fine Structure (NEXAFS) analysis was conducted in collaboration with Björn Bräuer at Stanford Synchrotron Radiation Lightsource (SSRL). The lateral resolution can be up to 30-50 nm. For details about this technique please see reference [261]. X-ray transparent samples have been prepared similar to STEM or TEM sample preparation by film transfer to a

common copper TEM grid. This was possible due to the water soluble PEDOT:PSS layer.

Figure 10.16a depicts the STXM image of a P3HT:PCBM film dried at 15°C. In correlation with AFM topography images the dark area can be identified as thick area (peak) and grey regions as thinner regions (valley). NEXAFS spectroscopy is sensitive to the chemical composition. Figure 10.16b shows the related NEXAFS spectra to the peak (black area) and valley (grey) regions. Beside the stronger absorption in the peak region due to higher film thickness, both spectra are similar. This indicates a similar chemical composition of peak and valley regions in the P3HT:PCBM topography.

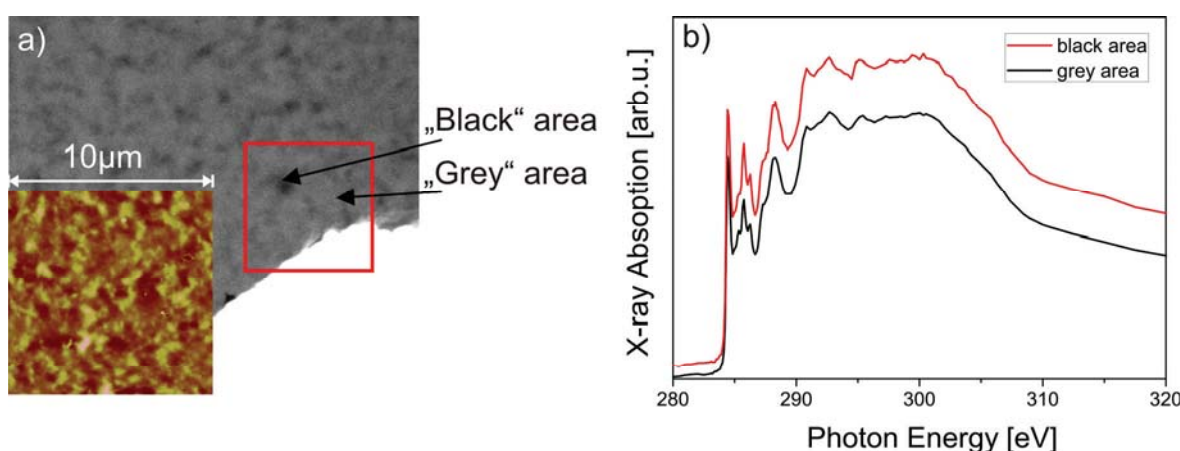


Figure 10.16: a) STXM image of a P3HT:PCBM (1:0.8) film processed from DCB at 15°C. The inset shows an AFM topography image of the same sample with a color topography scale of 100 nm. b) Associated NEXAFS spectra of the as “grey” and “black” denoted regions.

A 3.5 Influence of drying temperature

Figure 10.17 depicts drying kinetics for different drying temperatures. The lines are fitted to reflectometry measurements whereas the symbols indicate the estimated dry film state when the optical film properties remain constant. Since the calculations assume pure gas phase limitation of the drying, they only cover the constant rate drying period. The period of time between the end of the line plots and the symbol represents the falling rate period. It is remarkable that the offset between the end of constant rate period and the dry state increases with decreasing drying temperature.

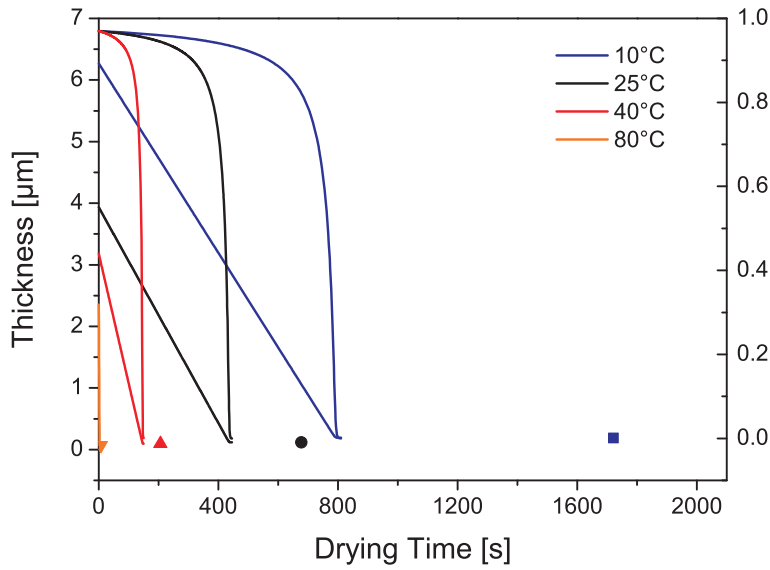


Figure 10.17: Fitted P3HT:PCBM film drying kinetics to reflectometry measurements at different drying temperatures (lines). Symbols indicate the instant of constant photovoltage, where the optical film properties remain constant. This instant is referred as dry state.

Table 10.1: Device performance of doctor bladed P3HT:PCBM films fabricated in ambient atmosphere at different drying conditions. An additional annealing step of 5 min at 150°C was applied. The average film thickness was about 310 nm ± 90nm. Device characterization was performed in N₂ atmosphere at room temperature.

Annealing 150°C, 5mins	J _{sc}	V _{oc}	FF	η	η _{max}
Drying Conditions	[mA/cm ²]	[V]	[%]	[%]	[%]
15°C, v=0.15m/s	-9.9±0.3	0.50±0.01	40.4±1.5	2.0±0.1	2.1
15°C, v=0.5m/s	-9.7±0.3	0.50±0.01	40.5±1.4	2.0±0.1	2.1
25°C, v=0.15m/s	-9.9±0.3	0.51±0.03	38.7±1.9	2.0±0.2	2.1
25°C, v=0.5m/s	-8.0±0.3	0.55±0.01	41.4±1.1	1.8±0.1	1.9
40°C, v=0.15m/s	-5.8±0.8	0.42±0.14	19.0±4.8	0.4±0.0	0.5
40°C, v=0.5m/s	-4.8±0.3	0.35±0.05	21.1±2.1	0.4±0.0	0.4

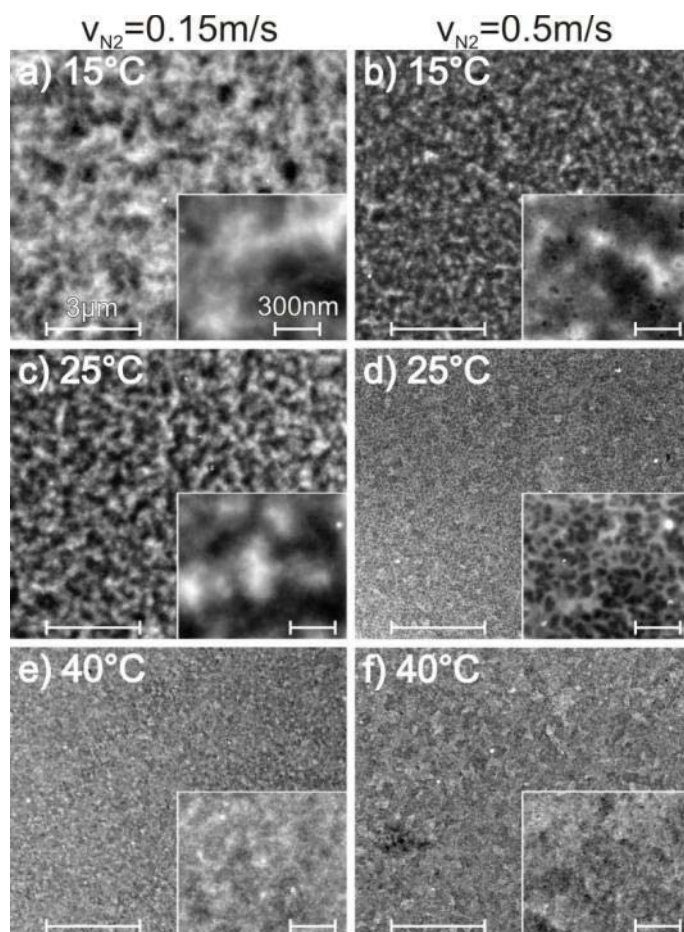


Figure 10.18: Low energy HAADF-STEM images taken at 15 keV of P3HT:PCBM films cast from DCB at different drying conditions. Average film thickness was 120nm. Scale bars are $3\mu\text{m}$ and 300nm for the main images and the insets respectively.

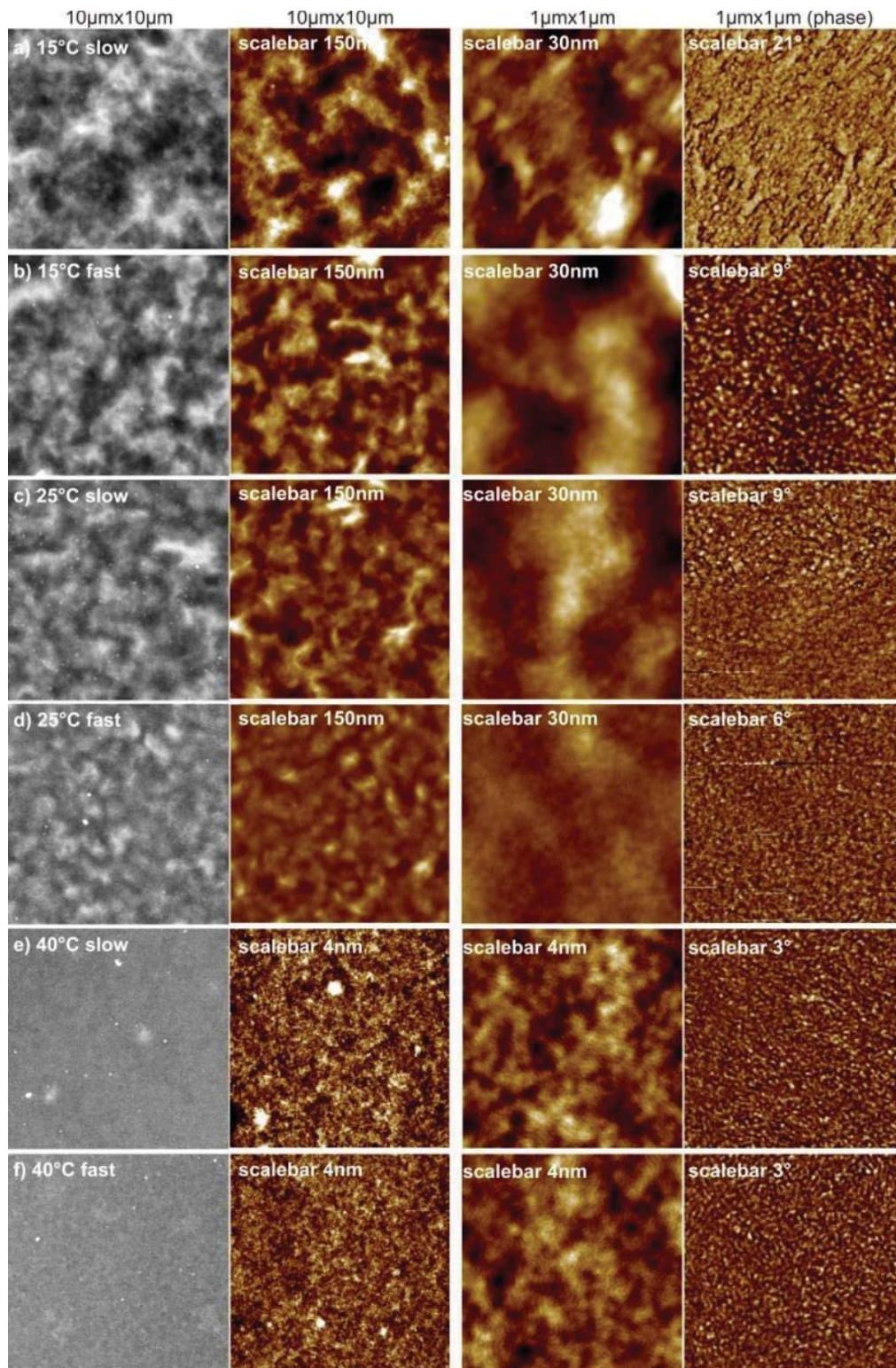


Figure 10.19: Series of 15 keV HAADF STEM ($10 \times 10 \mu\text{m}^2$) and AFM ($10 \times 10 \mu\text{m}^2$ and $1 \times 1 \mu\text{m}^2$) images. Among others these $10 \mu\text{m} \times 10 \mu\text{m}$ AFM images were used for the roughness analysis. The average film thickness is $350 \text{ nm} \pm 28 \text{ nm}$. [81]

A 3.6 Influence of 1,8-octanedithiol on film structure

While Figure 10.20 shows P3HT:PCBM films as cast after ODT processing Figure 10.21 shows the same samples after an additional thermal annealing step at 150°C for 5 min. Figure 10.22 summarizes the root mean square roughness obtained from 10×10 μm² AFM images of Figure 10.19, Figure 10.20 and Figure 10.21

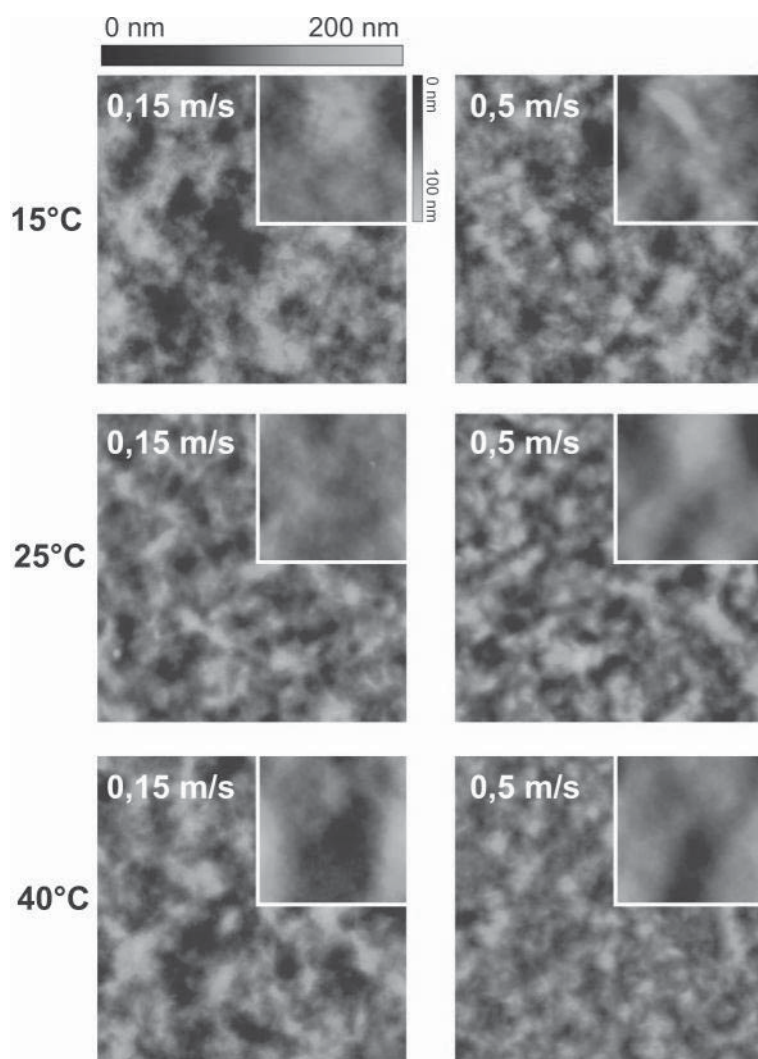


Figure 10.20: Overview of AFM topography images of ODT processed P3HT:PCBM films at different drying conditions. Large and inset image dimensions are 10×10 μm² and 1×1 μm² respectively. [238]

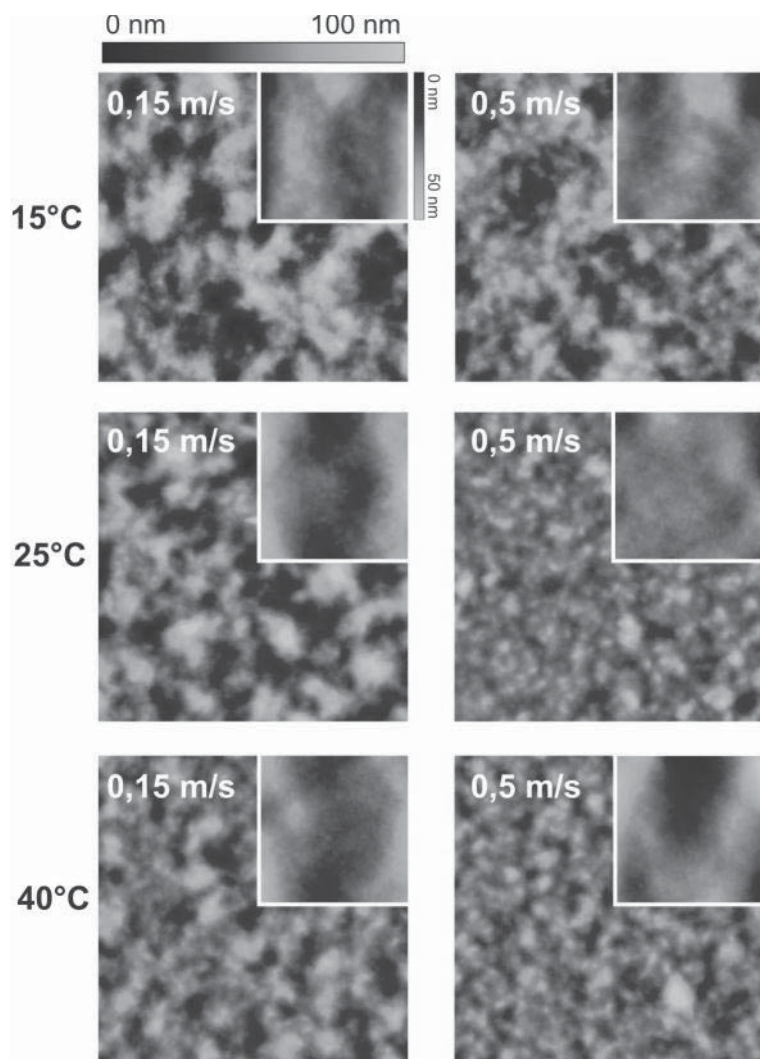


Figure 10.21: Overview of AFM topography images of ODT processed and subsequently thermally annealed (5min at 150°C) P3HT:PCBM films at different drying conditions. Large and inset image dimensions are $10 \times 10 \mu\text{m}^2$ and $1 \times 1 \mu\text{m}^2$ respectively. [238]

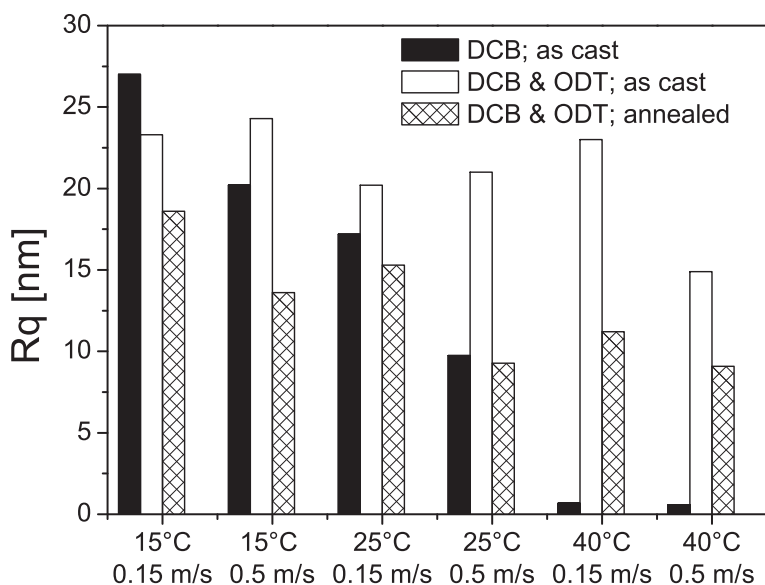


Figure 10.22: Root mean square roughness of P3HT:PCBM films cast from pure DCB (black bar) or DCB and ODT (white bar and patterned bar after 5 min, 150°C annealing) at different drying conditions determined at $10 \times 10 \mu\text{m}^2$ tapping mode AFM images. [238]

A 3.7 Influence of solvents on film structure

The structure of P3HT:PCBM films cast from the solvents indane, chloroform-indane, toluene-indane and o-xylene-indane gives similar 2D GIXD patterns as shown in Figure 10.23. The structural data obtained by point detector measurements of these films is listed in Table 10.2.

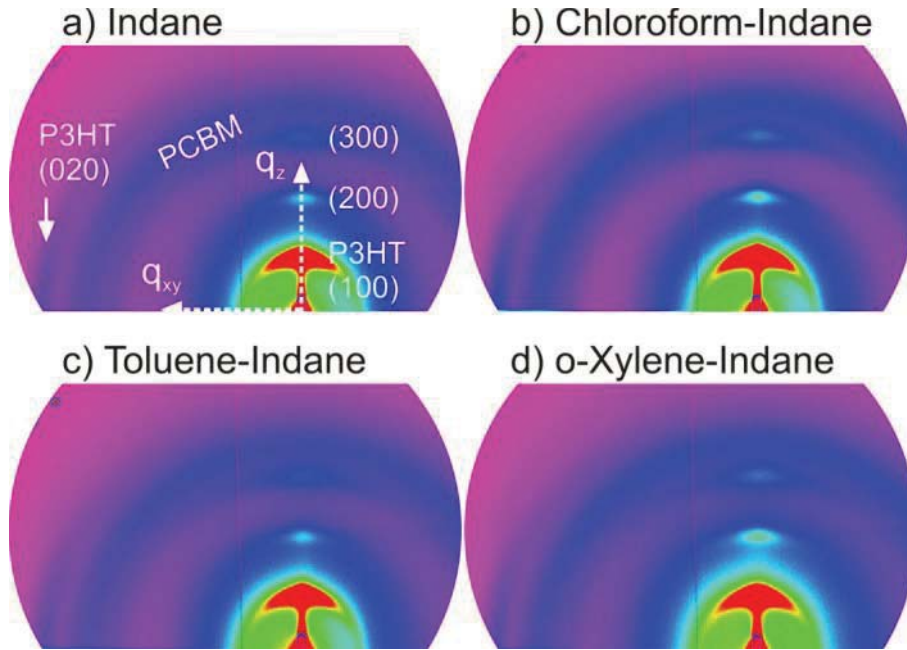


Figure 10.23: GIXD patterns of P3HT:PCBM films cast on PEDOT:PSS/ITO/glass substrates from a) indane, b) chloroform-indane, c) toluene-indane and d) o-xylene-indane. [239]

Table 10.2: Structural data for P3HT and PCBM obtained from the GIXD data for films cast from different solvent mixtures at room temperature: spacings d associated with the (100) and (020) Bragg reflections of P3HT and those of PCBM and mean coherence length L along those crystallographic directions. Film thicknesses were 170-180nm. [215]

Solvent	d_{100} [nm]	L_{100} [nm]	d_{020} [nm]	L_{020} [nm]	d_{PCBM} [nm]	L_{PCBM} [nm]
Chloroform-Indane	1.6	15.2	0.38	11.8	0.45	2.9
Toluene-Indane	1.6	15.2	0.38	11.8	0.45	2.9
o-Xylene-Indane	1.6	16.4	0.38	10.2	0.45	2.9

A 3.8 Structure formation of low band gap polymers

The structure of PSBTBT:PC₇₁BM films does not depend systematically on drying conditions as above discussed for P3HT:PC₆₁BM. Figure 10.24 summarizes AFM and STEM images conducted on the same samples as used

for solar cell fabrication. Film thicknesses and solar cell characteristics are given for the as cast devices in Table 10.3 and for annealed devices in Table 10.4.

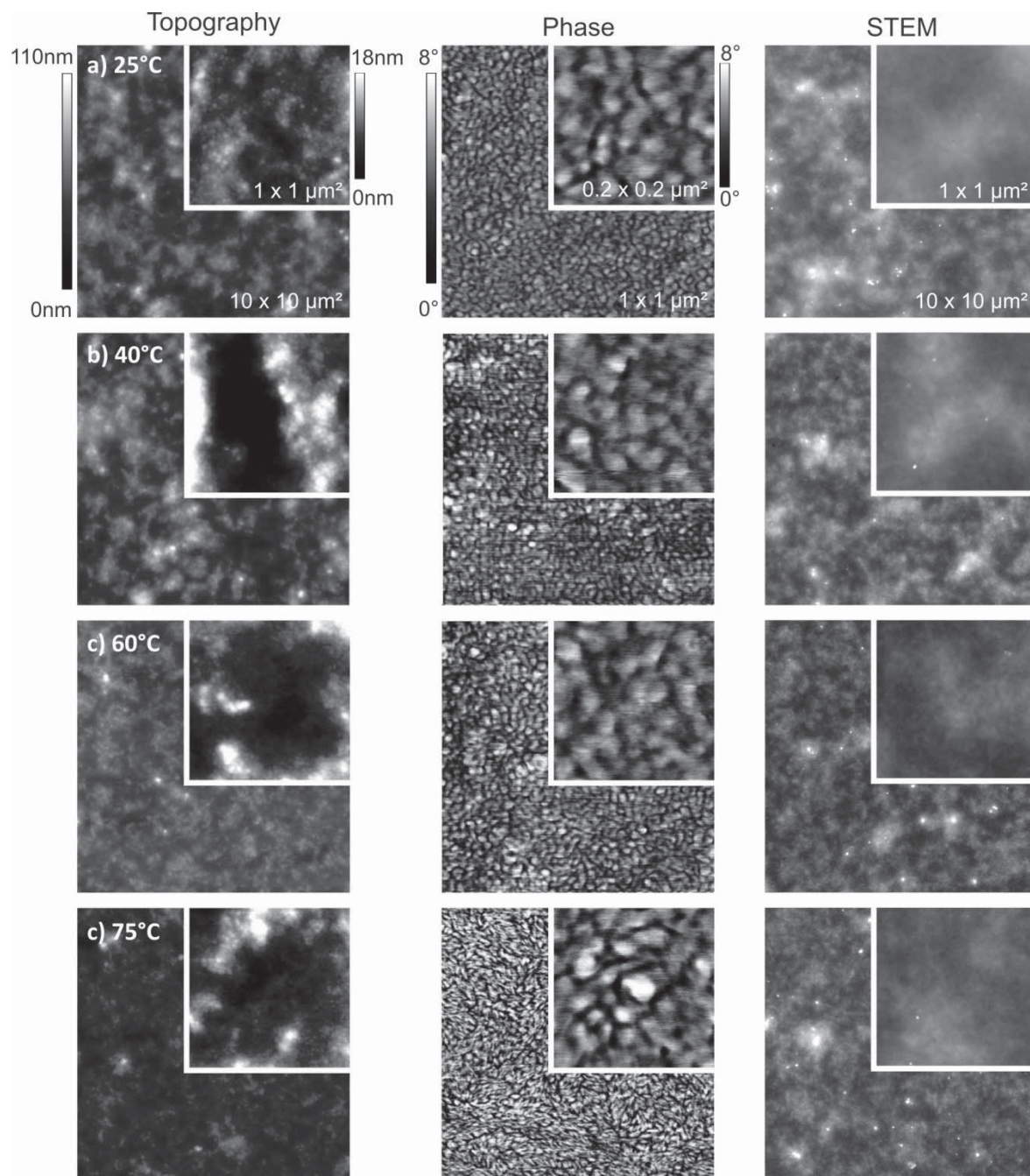


Figure 10.24: AFM images of PSBTBT:PC₇₁BM films of the investigated solar cells fabricated at different drying temperatures. AFM topography images (left column) are shown in comparison to the related phase images (middle column). The right column shows associated STEM images. The image scales are given in the first row. [252]

10 Appendix

Table 10.3: Device characteristics of PSBTBT:PC₇₁BM (1:2) solar cells as cast from DCB solution at different drying temperatures and 0.15 m/s drying gas flow. [252]

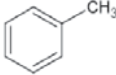
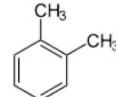
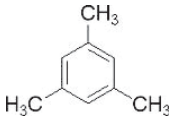
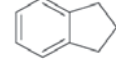
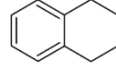
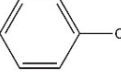
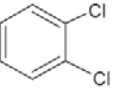
Drying Temp. °C	d nm	V _{OC} V	J _{SC} mA/cm ²	FF %	η %	η _{max} %
40°C	73	0.21±0.19	-12.7±3.4	19.3±19.7	1.2±1.7	5.0
60°C	90	0.32±0.19	-14.5±2.5	29.7±16.0	1.9±1.6	4.8
75°C	79	0.38±0.20	-14.0±1.4	33.0±15.7	2.3±1.6	4.6
85°C	101	0.34±0.24	-12.8±3.0	30.4±19.2	2.1±1.9	4.7

Table 10.4: Device characteristics of PSBTBT:PC₇₁BM (1:2) solar cells cast from DCB solution at different drying temperatures and 0.15 m/s drying gas flow and thermal treatment for 5 min at 150°C. The annealing was carried out after cathode deposition. [252]

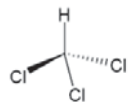
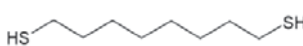
Drying Temp. °C	d nm	V _{OC} V	J _{SC} mA/cm ²	FF %	η %	η _{max} %
40°C	73	0.58±0.01	-13.5±0.4	51.6±2.0	4.1±0.2	4.3
60°C	90	0.60±0.00	-14.4±0.6	49.3±1.0	4.3±0.2	4.4
75°C	79	0.60±0.00	-13.3±0.5	50.1±1.1	4.0±0.2	4.3
85°C	101	0.60±0.01	-13.4±0.4	47.3±2.0	3.8±0.2	4.1

A 4 Material properties

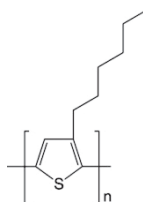
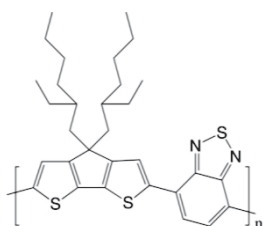
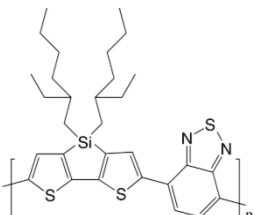
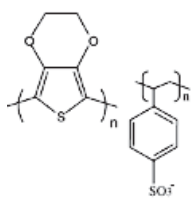
Used solvents

Substance	CAS number	Structure
Toluene Methylbenzene	108-88-3	
p-Xylene 1,4-Dimethylbenzene	106-42-3	
o-Xylene 1,2-Dimethylbenzene	95-47-6	
Mesitylene 1,3,5-Trimethylbenzene	108-67-8	
Indane Benzocyclopentane	496-11-7	
Tetralin 1,2,3,4-Tetrahydronaphthalene	119-64-2	
Chlorobenzene	108-90-7	
o-Dichlorobenzene 1,2-Dichlorobenzene	95-50-1	

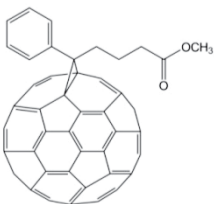
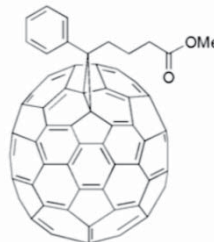
10 Appendix

Chloroform	67-66-3	
Trichloromethane		
1,8-Oktandithiol	1191-62-4	

Used polymers

Substance	CAS number	Structure
P3HT Poly(3-hexylthiophene-2,5-diyl) $M_w=40-60$ kg/mol, PDI= 1.7-1.9, 90-94% regio regular 4002E, Rieke Metals	104934-50-1	
PCPDTBT Poly{[4,4-bis(2-ethylhexyl)-cyclopenta-(2,1-b;3,4-b')dithiophene]-2,6-diyl-alt-(2,1,3-benzothiadiazole)-4,7-diyl} Konarka Technologies Inc.	920515-34-0	
PSBTBT Poly{[4,4-bis(2-ethylhexyl)dithieno(3,2-b;2',3'-d)silole]-2,6-diyl-alt-(2,1,3-benzothiadiazole)-4,7-diyl} Konarka Technologies Inc.	1160106-18-2	
PEDOT:PSS (1:6 by wt.) Poly(3,4-ethylenedioxythiophene) poly(styrenesulfonate) as aqueous dispersion Clevios P VP AI 4083, Heraeus	126213-51-2	

Used fullerene derivatives

Substance	CAS number	Structure
PC ₆₁ BM [6,6]-Phenyl C61-butyrlic acid methyl ester M _w = 910.9 g/mol, purity >99% Solenne B.V.	160848-22-6	
PC ₇₁ BM [6,6]-phenyl C71-butyrlic acid methyl ester M _w = 1031.0 g/mol, purity 99% Solenne B.V.	609771-63-3	

A 4.1 Density

The density of the used liquids can be calculated according to equation 10.7. Appropriate parameters are listed in.

$$\rho = A \cdot B^{-\left(1 - \frac{T_c}{T}\right)^n} \quad [g/cm^3] \quad 10.7$$

with T = Temperature in Kelvin
 A, B, T_c, n = fitted constants

10 Appendix

Table 10.5: Parameters for density calculation according to equation 10.7. Data is taken from [164].

Solvent	A	B	T _c [K]	n	Temp. range [K]	ρ(25°C) [g/cm ³]
Toluene	0.29990	0.27108	0.29889	591.79	178-592	0.8645
p-Xylene	0.27984	0.26003	0.27900	616.26	286-616	0.8577
o-Xylene	0.28381	0.26083	0.2741	630.37	248-630	0.8764
Mesitylene	0.27770	0.25909	0.27982	637.36	228-637	0.8614
Indane	0.31019	0.26117	0.30223	684.9	222-685	0.9599
Tetralin	0.29840	0.25750	0.26770	720.15	237-720	0.9671
Chlorobenzene	0.37818	0.27648	0.29036	632.35	228-632	1.1007
o-Dichlorbenzene	0.41887	0.26112	0.30815	705.00	256-705	1.3013
Chloroform	0.49807	0.25274	0.28766	536.40	210-536	1.4800
Trichlorethylen	0.50416	0.26952	0.28571	571.00	188-571	1.4577

Table 10.6: Solid densities of the used materials. [139]

Substance	15°C [g/cm ³]	25°C [g/cm ³]	30°C [g/cm ³]	40°C [g/cm ³]
P3HT	1.077 ^a	1.064 ^a / 1.111 ^b	1.056 ^a	1.026 ^a
PCBM	1.451 ^a	1.445 ^a / 1.596 ^b	1.442 ^a	1.438 ^a
PEDOT:PSS (VPAI 4083)	-	1.551 ^b	-	-

^a calculated from liquid densities of DCB solutions concentration series,

^b obtained in the solid state by helium pycnometry

A 4.2 Vapor pressure

The vapor pressure of the liquids used for film drying simulations can be calculated according to equation 10.8. Appropriate parameters are listed in Table 10.7.

$$\log_{10} p_i^* = A + \frac{B}{T} + C \cdot \log_{10} T + D \cdot T + E \cdot T^2 \quad 10.8$$

with p_i^* = vapor pressure of species i in Torr
 T = Temperature in Kelvin
 A, B, C, D, E = fitted constants

Table 10.7: Parameters for vapor pressure calculation according to equation 10.8. Data is taken from [164] except for 1,8-octanedithiol (ODT) which was taken from [262] and gives the pressure in Pascal.

Solvent	A	B	C	D	E	Temp. range °C	p(25°C) mbar
Toluene	34.0775	-3037.9	-9.1635	1.0289E-11	2.70E-06	-95-319	37.9
o-Xylene	37.2413	-3457.3	-10.126	9.07E-11	2.61E-06	-25-357	8.84
Indane	37.3577	-3733.7	-10.040	6.3179E-11	2.21E-06	-51-412	2.05
o-DCB	31.3614	-3522.6	-7.8886	-2.225E-10	1.1842E-06	-17-432	1.81
Chloroform	56.6178	-3246.2	-18.7	9.52E-03	1.16E-12	-64-263	262.9
1,8-ODT	6.22706	1881.086	-96.864	-	-	132-269	13.3*

**Due to the low vapor pressure of ODT at room temperature its vapor pressure is given for the lower validity limit of 132°C.*

A 4.3 Gas phase diffusion coefficient

The gas phase diffusion coefficient of component i in component j can be calculated by the group contribution method as suggested by Fuller et al. [150]

$$D_{ij} = \frac{0,00143 \cdot T^{1,75} [\tilde{M}_i + \tilde{M}_j]^{0,5}}{\sqrt{2} \cdot p \left[(\sum v_i)^{1/3} + (\sum v_j)^{1/3} \right]^2} \left[\text{cm}^2/\text{s} \right] \quad 10.9$$

with T = Temperature in Kelvin
 p = pressure in bar
 \tilde{M}_i = molar mass of component i in g/mol
 $\sum v_i$ = diffusion volumes

Table 10.8: Parameters for the calculation of gas phase diffusion coefficients according to equation 10.9. [150]

	Toluene	o-Xylene	Indane	o-DCB	Chloroform	1,8-ODT	Air
Molar Mass [g/mol]	92.1384	106.1650	118.2	147.0	119.4	178.4	28.96
Diffusion Volume	111.48	132.00	147.90	128.34	81.21	214.58	20.10

A 4.4 Refractive index

Table 10.9: Refractive indices at 589 nm used for the reflectometry analysis with the temperature T in degree centigrade. The solid refractive indices were determined from DCB solution concentration series. [139]

Substance	$n_i(20^\circ\text{C})$
Toluene	1.4937
o-Xylene	1.5023
Indane	1.5324
o-Dichlorobenzene	$-5 \cdot 10^{-4} \cdot T + 1.5617$
P3HT	$-0.0014 \cdot T + 1.8347$
PCBM	$3 \cdot 10^{-5} \cdot T^2 - 0.0034 \cdot T + 1.9816$

A 4.5 Phase equilibrium of solvent-solvent mixtures

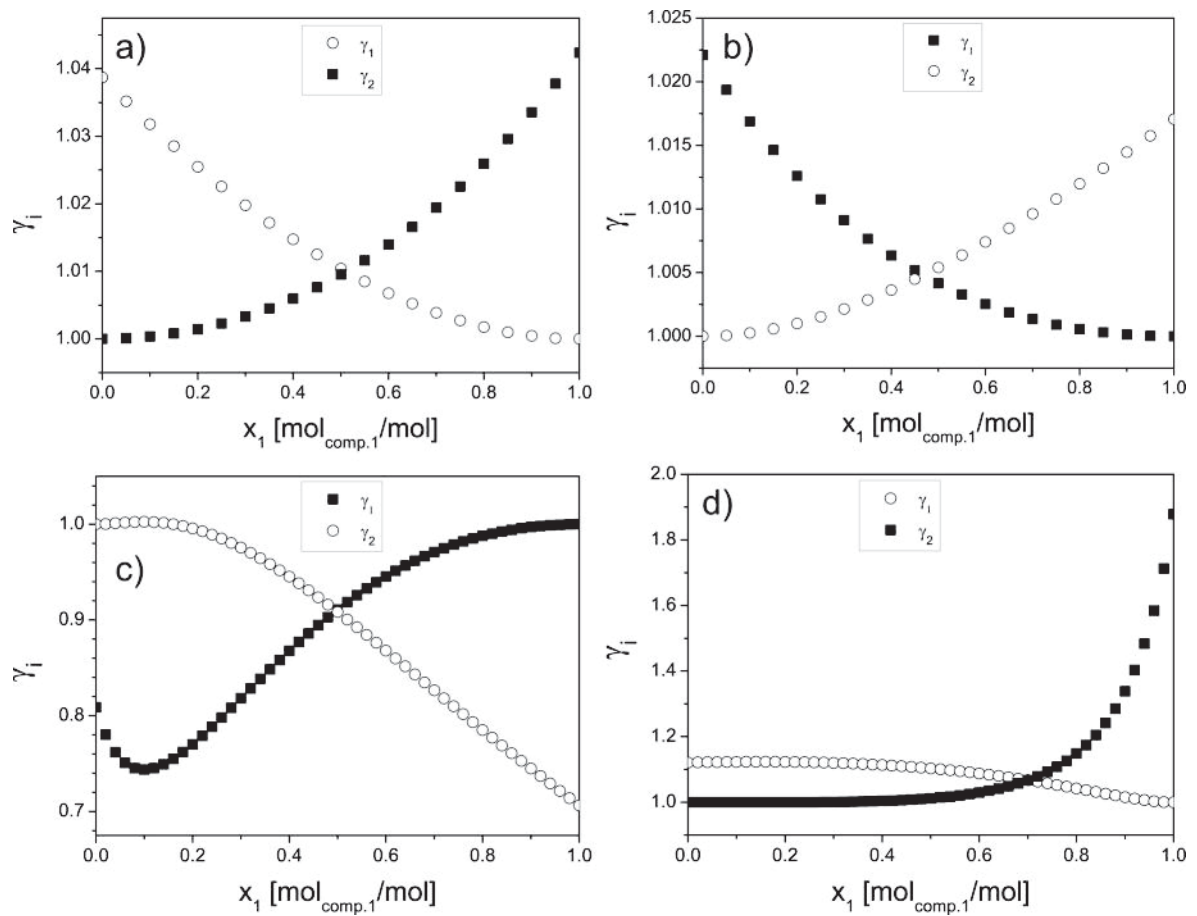


Figure 10.25: Activity coefficients of the mixtures a) o-xylene(1)-indane(2), b) toluene(1)-indane(2), c) chloroform(1)-indane(2) and d) chloroform(1)-o-dichlorobenzene according to UNIFAC. [139, 160]

